1064

OCT 19 1964

NEUTRON STAR MODELS

Sachiko Tsuruta

Submitted in partial fulfillment of the requirements
for the degree of Doctor of Philosophy
in the Faculty of Pure Science,
Columbia University

1964

CONTENTS

ABSTRACT i
ACKNOWLEDGMENTS iii
INTRODUCTION 1

CHAPTER I

RELATIVISTIC EQUATIONS OF HYDROSTATIC EQUILIBRIUM 6

1. PHYSICAL CONDITIONS IN STELLAR INTERIORS 6
2. RELATIVISTIC EQUATIONS OF HYDROSTATIC EQUILIBRIUM 11
   a. General Discussion 11
   b. A Summary of Some Fundamental Principles of the Theory of General Relativity 12
   c. Schwarzschild's Exterior Solution 15
   d. Schwarzschild's Interior Solution 17
   e. Derivation of the Relativistic Equations of Hydrostatic Equilibrium 18
3. UNITS TO BE USED IN RELATIVISTIC CALCULATIONS 19
4. GENERAL RELATIVISTIC QUANTITIES 20
   a. Physical Meaning of the Metric Tensor $g_{\mu\nu}$ 21
   b. Gravitational Mass and Proper Mass 25
   c. The Gravitational Binding Energy 26
   d. Schwarzschild Singularity 27
   e. Gravitational Red Shift 28
5. INTERPRETATION OF TERMS APPEARING IN RELATIVISTIC HYDROSTATIC EQUATIONS. 30

CHAPTER II

COMPOSITION OF SURFACE LAYERS 33

1. GENERAL REMARKS 33
2. SEMI-EMPIRICAL MASS FORMULA AND THE NUCLEAR BINDING ENERGY. . 38
3. EQUILIBRIUM CONFIGURATIONS FOR A COLD DENSE MATTER 43
   a. General Discussion 43
   b. Results of Others 45
   c. Results of this Research 47
4. STATISTICAL EQUILIBRIUM ABUNDANCES 53
5. THE ADJUSTMENT OF n_n AND n_p, AND THE ABUNDANCE CALCULATIONS, WITHOUT BETA PROCESSES 58
6. BETA REACTION RATES 65
   a. Terrestrial Beta Processes 65
   b. Beta Transition Rates in a Dense Stellar Interior 71
      i. Capture Rates of Continum Electrons 72
      ii. Electron Emission Rate in a Dense Plasma 74
      iii. Modified Fermi Function f for the Degeneracy Limit 76
   c. Discussion of the Results 78

(CHAPTER II cont'd)

7. PHOTO-BETA RATES 84
8. SELECTION OF BETA-REACTION NUCLEI 85
9. EQUILIBRIUM ABUNDANCE CALCULATIONS 96
    a. A Sample Calculation 96
    b. Final Abundance Calculations 97
        i. Nuclear Level Structure 97
        ii. Spin and Parity Distribution 103
        iii. Discussion of the Results 111
10. DETERMINATION OF SURFACE COMPOSITION 140

CHAPTER III

EQUATION OF STATE 143

1. INTRODUCTION 143
2. EQUILIBRIUM CONFIGURATION OF MATTER AT HIGH DENSITIES 145
    a. General Discussion 145
    b. Abundances of Various Components in a Highly Degenerate Baryon Gas . . . 148
    c. Number Densities at Different Phases 153
        i. Proton-electron Phase 153
        ii. Neutron Phase 154
        iii. Nucleon-muon-electron Phase 154
        iv. Hyperon Phase 155
        v. Pion Phase 162
    d. Summary 164
3. EQUATION OF STATE FOR A DEGENERATE IDEAL GAS 164
4. EQUATION OF STATE FOR A DEGENERATE REAL GAS 169
    a. General Discussion 169
    b. Skyrme Equation of State 172
    c. Saakyan's Equation of State for a Real Baryon Gas 173
    d. Salpeter's Equation of State 174
    e. Equation of State of Wheeler, Harrison and Wakano 176
    f. Levinger-Simmons Equation of State 177
    g. Results 185
5. RELATIVISTIC LIMITATIONS ON THE EQUATION OF STATE 188
6. COMPOSITE EQUATION OF STATE 194

CHAPTER IV

MODELS OF COLD NEUTRON STARS 201

1. GENERAL REMARKS 201
2. PREVIOUS WORK 203
    a. Models of White Dwarfs 203
    b. Original Work by Landau 205
    c. Limiting Mass by Oppenheimer and Serber 205
    d. Models of Neutron Cores by Oppenheimer and Volkoff 207

(CHAPTER IV cont'd.)

e. Models of Degenerate Stars by Wheeler, Harrison and Wakano 208
f. Cameron's Models of Neutron Stars 209
g. Models for Zero-temperature Stars by Hamada and Salpeter 214
h. Superdense Stars of Ambartsumyan and Saakyan 216
3. MODELS CONSTRUCTED IN THIS RESEARCH 221
a. General Remarks 221
b. Models With an Ideal Fermi Gas of Neutrons 222
c. Neutron Star Models with the Relativistic Skyrme Equation of State 229
d. Neutron Star Models of the Levinger-Simmons Type 233
e. Composite Models of the Levinger-Simmons Type 251
f. Final Models of Stable Neutron Stars 269
4. DISCUSSION 276
a. Chandrasekhar Mass Limit 276
b. Problem of Stability 278
c. Oppenheimer-Volkoff Mass Limit 280
d. Fate of Stars Exceeding the Maximum Mass Limit 280
e. Existence of the Third Maximum Mass 281
f. Central Singularity 282
g. Schwarzschild Singularity 283
h. Binding Energies 284
i. Effect of the Upper Limit Set by Relativity 287
j. Red Shift 288
5. CONCLUSIONS 289
6. SUMMARY 290

CHAPTER V

HOT NEUTRON STAR MODELS 295

1. INTRODUCTION 295
2. OPACITY 297
a. General Remarks 297
b. Cox's Opacity Code 299
c. Opacity Calculations 300
d. Results 301
e. Kramer's Formula for Bound-free Transitions 303
f. Electron Scattering 305
g. Electron Conduction 308
h. Discussion of the Results 309
3. ATMOSPHERIC CALCULATIONS 315
4. ENVELOPES OF NEUTRON STARS 319
a. Surface Integration 319
b. Atmospheric Temperatures 321
c. Temperature and Density Distribution Near the Surface 329
d. Diffusion, Convection, and the Composition of Envelopes 331

(CHAPTER V cont'd.)

5. ENERGY CONTENT OF A NEUTRON STAR 336
6. LUMINOSITY 342
   a. Optical Luminosity 342
   b. Neutrino Luminosity 349
7. COOLING TIMES 358
8. OBSERVATIONAL PROBLEMS — DETECTABILITY 367
   a. General Remarks 367
   b. X-ray Observations 370
   c. Discussion 372
9. CONCLUSION 380

APPENDIX 1 384
APPENDIX 2 387
APPENDIX 3 389

REFERENCES

FIGURES	PAGE
1	46
2	51
3	61
4	81
5	82
6	83
7	100
8	114
9	119
10	120
11	122
12	123
13	124
14	125
15	126
16	127
17	129
18	131
19	158
20	159
21	160
22	165
23	186
24	187
25	200
26	204

TABLES	PAGE
1a	45
1b	49
2	50
3	62, 63
4a	92
4b	93
5	112
6	137
7	163
8	213
9	220
10	226
11a	231
11b	231
12	233
13	239
14	240
15	241
16	254
17	255
18	256
19	271
20	272
21	272
22	291
23	292

FIGURES PAGE

27 206
28 211
29 217
30 224
31 225
32 230
33 234
34 242
35 243
36 244
37 260
38 263
39 265
40 267
41 273
42 302
43 326
44 327
45 330
46 332
47 339
48 350
49 354
50 360
51 361
52 362
53 363

TABLES PAGE

24 292
25 318
26 322
27 333
28 343
29 344
30 345
31 346
32 347
33 348

ABSTRACT

When this research was started the main objective was to construct hot neutron star models and to investigate the detectability of these stars. Since then there has arisen the possibility that some of the galactic x-ray sources recently discovered might be neutron stars. Hence both cold and hot models were constructed and their properties were investigated. For this purpose, equilibrium nuclear configurations of dense matter with densities in the range $10^6 \lesssim \rho \lesssim 10^{12}$ gm/cm^3 for (a), zero temperature and (b), temperatures in the range $2 \times 10^9 \lesssim T \lesssim 10^{10}$ °K were studied. Equilibrium concentrations of sub-atomic particles with densities in the range $10^{12} \lesssim \rho \lesssim 10^{17}$ gm/cm^3 at zero temperature were also studied, and then a number of different equations of state to be applied to a dense star were constructed.

In the temperature and density range considered, stability shifts to more neutron-rich nuclei with increase of density. Nuclei of smaller Z become more abundant and the abundances of nuclei near a peak tend to become comparable to that of the peak nucleus, with an increase of temperature. When $T \lesssim 5 \times 10^9$ °K, the transition from heavy nuclei to neutrons takes place at $\rho \sim 3 \times 10^{11}$ gm/cm^3. At higher temperatures this transition would occur at a lower density. The molecular weight per electron, μ_e, is rather insensitive to temperature changes. On the other hand its variation with density is somewhat larger ($\mu_e \sim 2$ for $\rho \sim 10^6$ gm/cm^3, while for $\rho \sim 3 \times 10^{11}$ gm/cm^3 $\mu_e \sim 3$). At higher densities ($\rho \gtrsim 10^{13}$ gm/cm^3) neutrons become contaminated with other baryons, mesons and leptons.

In "real" gas models the pressure is less than that for ideal gas models in the range $10^{12} \lesssim \rho < 10^{15}$ gm/cm^3, but the situation is reversed for $\rho > 10^{15}$ gm/cm^3. The relativistic limitation on the equation of state prevents the pressure from increasing too rapidly. The properties of neutron stars depend primarily on the mass and the interaction between the constituent particles, and the effects of hyperons and of the relativistic limit are minor. The envelope of electrons and heavy ions is important in some of the least massive neutron stars. The mass and radius of stable neutron stars range from about 0.2-2 $M_\odot$ and 25-5 km, respectively. The maximum mass of a neutron star can be as large as 2 $M_\odot$. All the models constructed develop a central singularity at a finite mass and radius, but all the stable models investigated in this research do not show the Schwarzschild singularity. A small local maximum above the Oppenheimer-Volkoff crushing point is observed. Red shifts are calculated to be from about 1% (least massive models) to 30% (most massive models) which indicates that general relativistic effects are not negligible even near the surface.

Surface properties, temperature effects and cooling are studied for six models of possible stable neutron stars. For this purpose the opacity is calculated by means of Cox's opacity code. Model atmospheres are constructed both for a pure iron and a pure magnesium composition. It is found that the non-degenerate layers are only a few meters thick and in no case exceed 1% of the stellar radius. When the surface temperature is about $10^{6 \sim 7}$ °K the internal temperature is about $10^{7.5 \sim 9}$ °K. For a surface temperature of $\sim 5 \times 10^7$ °K the internal energy and optical luminosity are $\sim 10^{50}$ ergs and $\sim 10^6$ $L_\odot$, while for the lower surface temperature of $\sim 2 \times 10^4$ °K these two values are $\sim 10^{40}$ ergs and 10^{-8} $L_\odot$. The cooling process is mainly

neutrino emission when $T > 10^9$ °K but at lower temperatures than this it is primarily optical radiation. The age of a neutron star of a given temperature depends on its mass, interaction potential and surface composition, among which the dependence on mass is the greatest. The cooling behavior is quite complicated. As a consequence, the possible age of a detectable neutron star can be anywhere from about 1 day to about 10^6 years. Low mass neutron stars would be almost impossible to detect, but intermediate and large mass neutron stars located even far away ($\sim 10^3$ parsec) can keep sufficiently luminous long enough to allow their detection by instruments above the earth's atmosphere, and it should not be too difficult to observe them, were the sensitivity of present detectors increased by a factor of, say, 100.

ACKNOWLEDGMENTS

I wish to extend my deepest gratitude to Dr. A. G. W. Cameron for accepting me as his student, for his excellent, patient guidance in the supervision of my doctoral research, for the enlightening discussions I have had with him, helpful advice and constructive criticism, and for making the special arrangements which enabled me to use extensively and efficiently various facilities in the Goddard Institute for Space Studies (especially the 7094 computer, its related machines such as the punching machine, and the xerox machine). Without his help, this research would have taken indefinitely longer.

My deepest appreciation is also due to Professor Henry M. Foley and other faculty members of Columbia University whose assistance and counsel were invaluable in time of need. I am indebted to the University and NASA for financial support. I wish to thank my committee members for their special interest in my work. I am grateful to Dr. H. Y. Chiu for the early part of my training in research in this field, to Dr. Robert Jastrow for his hospitality and others in the staff of the Goddard Institute for Space Studies (especially Dr. A. Levine and Mrs. E. Silva) for their kind cooperation. In addition, it is my pleasure to acknowledge with thanks the effort of the following persons: Mr. T. Psaropulos, for his painstaking, skillful drafting; Mr. B. Sacharoff, for making available the use of his integration and interpolation subroutine which improved the accuracy of my numerical work and for performing the calculation of Cox's opacity code; Dr. S. Kato for the interesting discussion of convection; Miss C. Federschmid for the time-consuming labor of typing my thesis; and Mrs. A. Bolton for her constant help with my problems as a student.

I should also like to thank Dr. E. E. Salpeter and other scientists who participated in the symposium on neutron stars and galactic x-ray sources held at the Goddard Institute for Space Studies in New York on March 20, 1964, which was a great stimulation and help to my work. Finally, I wish to express my gratitude to all of those whose encouragement meant a great deal in enabling me to continue.

INTRODUCTION

One of the major puzzles faced by people concerned with stellar structure problems in the late 1920's to early 1930's was the determination of the mechanism of energy generation processes within a star. The method commonly adopted in those days was to make convenient arbitrary assumptions about the energy sources. In 1932 Landau(1) proposed that some valuable insight might be obtained by first investigating the equilibrium configuration of a cold body of given mass with no energy generation. He argued that for a body of large mass, whose parts are kept together by gravitational attraction, there exist two possible equilibrium states - the electron-nuclear state and the neutronic state. It was also pointed out that if the mass is sufficiently large, the latter state would be more favorable. It was suggested about that time(2) that such a state of a neutronic configuration might be physically realized in the form of a neutron star, or a neutron core, at the last stage of the stellar evolution of a sufficiently massive star.

In 1933 Oppenheimer and Serber(3) estimated the possible minimum mass of a stable neutron core. The first extensive work on the construction of models of neutron stars was carried out by Oppenheimer and Volkoff,(4) who used general relativity in formulating the structure equations and assumed that the equation of state is that of a simple non-interacting Fermi gas of neutrons. Their results showed that the observable mass should have an upper limit of about 0.7 solar mass. Zwicky(5) suggested that a neutron star is a possible remnant of a supernova explosion. The problem of the behavior of a body with mass exceeding the maximum limit was first investigated by Oppenheimer and Snyder(6) in 1939, From the time of these investigations until rather recently, the study of neutron stars was somewhat neglected. The reason was that as a result of the progress made in nuclear physics, the theory of stellar evolution and the study of white dwarfs, it became generally believed that the end point of stellar evolution was a white dwarf star rather than a neutron star. The maximum mass of white dwarfs was calculated by Chandrasekhar(7) to be about 1.4 solar mass, larger than the limit for neutron stars calculated by Oppenheimer and Volkoff.

In 1958 Wheeler(8) pointed out that the subject of neutron stars would pose problems both interesting and stimulating in the fields of general relativity, gravitation theory and high energy physics. Since then the study of neutron stars has revived. In the work of Wheeler et al,(8) the properties of stellar configurations at zero-temperature from the white dwarf region to neutron star region was investigated, and a broad intermediate region where the configuration is unstable was found. The first effort to construct neutron star models of a real gas was made by Cameron(9) in 1959. In his models, a mean nuclear potential constructed by Skyrme(10) was used to take account of interaction forces among neutrons. The maximum observable mass of Cameron's models was about 2 solar masses. In 1960 Salpeter(11) investigated various kinds of equation of state for dense matter by a semi-empirical method and applied these to models of zero-temperature stars.(12) Both Cameron and Salpeter discussed the effect of hyperons but no quantitative calculations were given. During the period of 1960-1962 a series of papers were published by Ambartsumyan and Saakyan(13,14,15) on superdense hyperon stars.

This concludes a brief survey of the history of the study of neutron stars and other dense stars before research for this thesis was undertaken.

In studying the previous work, I noticed that all the models were constructed with zero-temperature and that the possible temperature effect of the surface layers was not investigated, with the exception of an interesting discussion in Cameron's paper. In his paper,(9) Cameron concluded that neutron stars are the probable end products of supernova processes and that such a star would, after its formation, cool off so rapidly that it would escape our observations. However, in an added note, he made a reservation concerning this conclusion and pointed out that, if a hot non-degenerate envelope is formed at the end of the evaporation stage when the gas at the stellar surface no longer has enough internal energy to expand to infinity, such an envelope might well retain a great deal of the internal heat of condensation for appreciable periods of time.

I was particularly interested in this suggestion which Cameron made. At the time this research was first undertaken no investigation of "hot neutron stars" with high-temperature, non-degenerate envelopes had yet been made, and it was not known whether there would be any hope for observation, even if they should exist. I thought that hot neutron star models might provide some insight into this problem, and decided to construct such models in the hope of determining the feasibility of directly observing these stars. Therefore, my objective when I started this research was mainly to construct hot neutron star models with hot non-degenerate outer layers and investigate their surface properties and the effect of these on cooling and detectability.

However, since then, the status of neutron star problems has undergone a considerable change because of the discovery of galactic x-ray sources and the possible identification of these sources with neutron stars. The recent development in this field is reviewed briefly below. In the summer of 1963, Saakyan's paper(16) was published where an improvement was applied to Cameron's models. Chiu(17) discussed the over-all problem of neutron stars, both dynamic and static, made rough estimates of temperature and cooling time, considered some observational problems, and concluded that while neutron stars are not observable on the earth they should be detectable above the earth's atmosphere owing to x-ray emission.

In recent years, it has been reported,(18,19,20) through rocket flights in outer space, that there exist x-ray sources outside the solar system. In December, 1963, Friedman(20) reported that two discrete galactic x-ray sources were detected, one in the constellation Scorpio with the measured flux of 10^{-7} ergs/cm^2-sec over the wave length range of 1.5 to 8 Å, and the other in the Crab Nebula with a flux about 8 times weaker than the former, and further proposed that they might be identified with neutron stars. Since then, interest in neutron stars appears to have grown rapidly, and many papers on neutron stars and galactic x-ray sources have been published (references 18(b), 19, 22, 23, 24, and 25). Some other alternative theories have also been proposed to explain the mechanism of these x-ray emissions.(21) The data on x-ray measurements are, however, too scarce at the present time to allow us to draw any definite conclusions and there is still no means of deciding against or in favor of some of these possibilities. The most recent experimental data(20') seems to indicate that the x-ray source in the Crab Nebula is not a neutron star but there is a possibility that the Scorpius source is a neutron star. I wish to emphasize that more detailed experimental data is quite badly needed, that the models based upon logical foundations and constructed in this research by straightforward application of physical principles, which are presented in detail in the following chapters, are consistent with all the information on x-ray measurements so far available, and that there is a good possibility that some of the galactic x-ray sources are indeed neutron stars.

Due to the recently increasing interest in the field, my work has become extended beyond the original modest plans. For instance, instead of using the existing cold models for neutron cores, an over-all re-investigation and reconstruction of cold models has been undertaken before constructing hot models, and model atmospheres with two possible surface compositions have been constructed to take the possible diffusion effect into account.

Chapter I introduces the basic physics governing the internal structure of neutron stars. Chapter II is devoted to the study of the equilibrium composition of surface layers. Various possible equations of state have been investigated in Chapter III. In Chapter IV, models constructed by others are introduced first, and then models constructed in this research are presented. The last chapter, V, is devoted to the problem of hot neutron stars, including the construction of model atmospheres, the study of surface properties, the calculation of total energy content, temperature, luminosity, and the investigation of the cooling behavior of various models of different ages, and finally the problems of observation and detection.

This research is confined to static problems of neutron stars and other dense stars under hydrostatic equilibrium. The stars are assumed to exhibit spherical symmetry with no rotation throughout.

CHAPTER I

RELATIVISTIC EQUATIONS OF HYDROSTATIC EQUILIBRIUM

I-1. PHYSICAL CONDITIONS IN STELLAR INTERIORS

In attacking the problems of the static structure of stars, there are four basic differential equations which govern the conditions in stellar interiors. These are generally expressed as:

$$\boxed{\begin{aligned}
\frac{dP}{dr} &= -\rho(r)\,\frac{GM_r}{r^2} \\
\frac{dM_r}{dr} &= 4\pi r^2 \rho(r) \\
\frac{dL_r}{dr} &= 4\pi r^2 \rho(r)\,\epsilon(r) \\
\frac{dT}{dr} &= -\frac{3}{4ac}\,\frac{\kappa\rho(r)}{T^3}\,\frac{L_r}{4\pi r^2} \text{ (radiative) or} \\
\frac{dT}{dr} &= \left(1-\frac{1}{\gamma}\right)\frac{T}{P}\,\frac{dP}{dr} \quad \text{(convective)}
\end{aligned}}
\qquad
\begin{aligned}
&(1\text{-}1)\\
&(1\text{-}2)\\
&(1\text{-}3)\\
&(1\text{-}4)\\
&
\end{aligned}$$

The first two are called equations of hydrostatic equilibrium. They result from the fact that for a star to be stable, all the forces acting on any part of the star must be in balance with each other. For a spherical body subject to a central gravitational force, this force directed inward must be balanced by the pressure force directed outward. The gravitational force acting on a volume element δv is given by $p(r)\,\frac{GM_r}{r^2}\,\delta v$, where $p(r)$ is the density at r, G is the constant of gravitation, r is the radial distance from the center to δv, and M_r is the mass inside a sphere of radius r. The pressure force on δv is $-\frac{dP}{dr}\delta v$. Equating the two we obtain (1-1). (1-2) is just a differential form of the definition of M_r

$$M_r = \int_0^r 4\pi r^2 \rho(r)\, dr \qquad (1\text{-}2')$$

The third equation is necessary to fulfill the condition of thermal equilibrium, that the total energy loss must be compensated by the net energy generation. The net energy loss per unit time can be characterized by the over-all luminosity or the energy flux through a sphere of radius r, L_r [by over-all, any type of energy loss (e.g. neutrino energy loss, etc.,) is meant]. The third equation (1-3) is then just the law of conservation of energy in differential form.

The two equations in (1-4) are related to the condition for the energy transport. There are three means by which energy is transported within a star: conduction, convection and radiation. In most of the stellar structure problems we encounter, either radiative transfer or convective transfer is most important. The equations in (1-4) are applicable to these problems. Here, dT/dr is the temperature gradiant, a is Stefan's radiation constant, c is the velocity of light, κ is the opacity of the material or the mass absorption coefficient usually expressed in cm^2/gm, and γ is the ratio of the specific heats C_p/C_v.

In the problem of model construction of hot neutron stars, radiation and electron conduction are more important than convection. This point will be discussed in Chapter V.

The four differential equations just introduced contain five variables P, M_r, L_r, T and r. One might, therefore, think that if one is chosen as the independent variable, the rest are determined by the four equations, provided that suitable boundary conditions are given. This is true if explicit relations are given through which $\rho(r)$, ϵ and κ can be eliminated. All of these quantities generally depend on the composition, density and temperature. That is, they can be expressed in the form:

$$\boxed{\begin{array}{l} P = P(\rho, T, C) \\ \kappa = \kappa(\rho, T, C) \\ \epsilon = \epsilon(\rho, T, C) \end{array}} \qquad \begin{array}{r} (1\text{-}5a) \\ (1\text{-}5b) \\ (1\text{-}5c) \end{array}$$

where composition is expressed symbolically by the letter C. The first is the equation of state. The three are called the "gas characteristic relations."(26)

The boundary conditions are generally given by

$$\boxed{\begin{array}{ll} M_r = 0,\ L_r = 0,\ P = P_c,\ T = T_c \text{ at } r = 0 \text{ (center)} & (1\text{-}6a) \\ M_r = M,\ L_r = L,\ P = 0,\ T = 0 \text{ at } r = R \text{ (surface)} & (1\text{-}6b) \end{array}}$$

where P_c and T_c are central pressure and temperature, M is the mass and R is the radius of the star.

For neutron stars, white dwarfs, or any stellar configuration of sufficiently high degeneracy and of no energy generation, the situation is far simpler. In the original form presented above the four differential equations are coupled together and it is necessary to carry out the numerical integration of four equations simultaneously. However, if there is no energy generation, ϵ in (1-3) is zero and the third equation drops out. Moreover, for a sufficiently high degeneracy, the temperature dependence of pressure drops out and the equation of state takes the form:

$$P = P(\rho) \quad \text{for a given composition .} \qquad (1\text{-}5a')$$

In this case, the hydrostatic and thermodynamic parts of the structure equations are decoupled and the first two and the last two equations in (1-1)-(1-4) can be treated separately.

In the core of a neutron star where the degeneracy is sufficiently high, the conduction process is so efficient that the temperature gradient dT/dr is practically zero and the last equation also drops out. The conclusion is that the structure problems of neutron stars boil down to the solution of the first two equations (1-1) and (1-2).

In the outermost part of the star where the density falls to the non-degenerate region (density low compared with temperature), the temperature effects also must be included in our hot neutron star models, but, as our results in Chapter V reveal, such non-degenerate regions occur only at about a meter or so from the surface, while the typical radius of a neutron star is about 10 kilometers, and in finding typical physical quantities of interest to us (mass, radius, internal distribution of matter, the maximum mass limit and many other general properties which are not sensitive to temperature), our cold-body approximation is perfectly valid; that is, the problem can be solved by integrating the two hydrostatic equations (1-1) and (1-2) under suitable boundary conditions and with the proper form of the equation of state (1-5a').

One correction to the above statement is necessary. That is, the equations of hydrostatic equilibrium (1-1) and (1-2) are derived from Newtonian mechanics. As it is to be fully demonstrated soon, however, the general relativistic effects become quite important for ultradense matter such as neutron stars. For instance, the deviation from Newtonian mechanics is characterized by the factor GM/RC^2, which, later, is identified with the gravitational red-shift of spectral lines. This quantity is about 0.01 to 0.3 for neutron stars (Chapter V), while the value of the same quantity for the sun and for the companion to Sirius (a typical white dwarf) is only 2.12×10^{-6} and approximately 6×10^{-5} respectively.

The conclusion is that for neutron star problems more general expressions for hydrostatic equilibrium, based on the general theory of relativity, must replace (1-1) and (1-2). The rest of this chapter is to be devoted to the derivation of such equations, their general properties and other general relativistic parameters which are to play important roles in the problem of neutron stars.

I-2. RELATIVISTIC EQUATIONS OF HYDROSTATIC EQUILIBRIUM

a. General Discussion

What is mentioned above can be seen also from the fact that the radius of a neutron star is comparable to the gravitational radius, $R_G = 2GM/c^2$. In such a case, it is not permissible to neglect the effects of general relativity and the calculations must be carried out with Einstein's gravitational equations.

The solution of Einstein's equations for the spherically symmetric distribution of matter is relatively simple and a complete solution of such problems for the static case was obtained by K. Schwarzschild as early as 1916.

The most general static line element exhibiting spherical symmetry is expressed as (p. 239, 241 of reference 27)

$$dS^2 = - e^{\lambda(r)} dr^2 - r^2 d\theta^2 - r^2 \sin^2\theta \, d\phi^2 + e^{\nu(r)} dt^2 \qquad (1-7)$$

If the matter supports no transverse stresses and if the macroscopic energy density ϵ and the pressure P are measured in proper coordinates, the following expressions are obtained as the general relativistic equations of hydrostatic equilibrium:

$$\frac{du(r)}{dr} = 4\pi\epsilon(P)r^2 \tag{1-8}$$

$$\frac{dP}{dr} = -\frac{(P+\epsilon(P))}{r(r-2u)}\left[4\pi r^3 P + u(r)\right] \tag{1-9}$$

In (1-8) and (1-9) a system of units is adopted which makes G = c = 1, where G is the gravitational constant, c is the velocity of light, u(r) is a quantity defined by

$$u(r) = \frac{1}{2}r\,(1 - e^{-\lambda}) \tag{1-10}$$

which characterizes the quantity of matter enclosed within a sphere of radius r, and its value at r = R is to be later identified with the mass of the star as perceived by a distant observer. The derivation of (1-8) and (1-9) is to be given below before going into further details.

b. A Summary of Some Fundamental Principles of the Theory of General Relativity

As in the case of many problems involving general relativity, we can start with(27)

$$ds^2 = g_{\mu\nu}\,dx^\mu dx^\nu \tag{1-11}$$

and

$$-8\pi T^{\mu\nu} = R^{\mu\nu} - \frac{1}{2}Rg^{\mu\nu} + \Lambda g^{\mu\nu} \tag{1-12}$$

where the first expression is the most general form of an interval in Riemannian space and the second is the field equation of Einstein.

$g_{\mu\nu}$ is the fundamental metrical tensor, $T^{\mu\nu}$ the energy-momentum tensor, $R^{\mu\nu}$ the contracted Riemann-Christoffel tensor, R the invariant obtained by further contraction of this tensor, and Λ is the cosmological constant. Here again, G and c are set equal to 1 .

The fundamental equation of mechanics in the language of general relativity is then given by

$$(T^{\mu\nu})_{\nu} = \frac{\partial T^{\mu\nu}}{\partial x^{\nu}} + \{\alpha\nu,\mu\}T^{\alpha\nu} + \{\alpha\nu,\nu\}T^{\mu\alpha} = 0 \qquad (1\text{-}13)$$

where

$$\{\mu\nu,\delta\} = \frac{1}{2} g^{\delta\lambda}\left\{\frac{\partial g_{\mu\lambda}}{\partial x^{\nu}} + \frac{\partial g_{\nu\lambda}}{\partial x^{\mu}} - \frac{\partial g_{\mu\nu}}{\partial x^{\lambda}}\right\} \qquad (1\text{-}14)$$

The contracted Riemann-Christoffel tensor is defined by

$$R_{\mu\nu} = \{\mu\delta,\alpha\}\{\alpha\nu,\delta\} - \{\mu\nu,\alpha\}\{\alpha\delta,\delta\} + \frac{\partial}{\partial x^{\mu}}\{\mu\delta,\delta\} - \frac{\partial}{\partial x^{\delta}}\{\mu\nu,\delta\} \qquad (1\text{-}15)$$

In proper coordinates the energy momentum tensor is written as$^{(27)}$

$$T_o^{\alpha\beta} = \begin{matrix} P_{xx}^{o} & P_{xy}^{o} & P_{xz}^{o} & 0 \\ P_{yx}^{o} & P_{yy}^{o} & P_{yz}^{o} & 0 \\ P_{zx}^{o} & P_{zy}^{o} & P_{zz}^{o} & 0 \\ 0 & 0 & 0 & c^2 \rho_{oo} \end{matrix} \qquad (1\text{-}16)$$

The transformation from the proper coordinates $(x_o^1, x_o^2, x_o^3, x_o^4)$, the coordinates so chosen that the matter in question is at rest with respect to the spatial axes, to other arbitrary coordinate systems (x^1, x^2, x^3, x^4) is provided by the relation

$$T^{\mu\nu} = \frac{\partial x^\mu}{\partial x_o^\alpha} \frac{\partial x^\nu}{\partial x^\beta} T_o^{\alpha\beta} \tag{1-17}$$

where the subscript zero denotes the quantities in proper coordinates.

Important simplifications are possible in the case of a perfect fluid, that is, for matter in which there are no transverse stresses and no mass motions. In that case it is known(27) that (1-16) reduces to a simpler form

$$T_o^{\alpha\beta} = \begin{matrix} -P & 0 & 0 & 0 \\ 0 & -P & 0 & 0 \\ 0 & 0 & -P & 0 \\ 0 & 0 & 0 & \epsilon \end{matrix} \tag{1-18}$$

where P is the pressure and ϵ is the energy density as measured by a local observer.

Using the definition of proper coordinates, with the help of (1-18), equation (1-17) reduces to

$$T^{\mu\nu} = (\epsilon + P) \frac{dx^\mu}{dS} \frac{dx^\nu}{dS} - g^{\mu\nu} P \tag{1-19}$$

The most general expression of a static line element in spherical symmetry is given by (1-7). Substituting the three-index symbols $\{\mu\nu, b\}$ of (1-14) (evaluated for the line element (1-7)) into the expression for $R_{\mu\nu}$ in (1-15), and substituting these $R_{\mu\nu}$ into the Einstein's field equation (1-12), we are led to

$$8\pi P = -8\pi T_1^1 = e^{-\lambda}\left(\frac{\nu'}{r} + \frac{1}{r^2}\right) - \frac{1}{r^2} \tag{1-20a}$$

$$\begin{aligned} 8\pi P &= -8\pi T_2^2 = -8\pi T_3^3 \\ &= e^{-\lambda}\left\{\frac{\nu''}{2} - \frac{\lambda'\nu'}{4} + \frac{\nu'^2}{4} + \frac{(\nu'-\lambda')}{2r}\right\} \end{aligned} \tag{1-20b}$$

$$8\pi\epsilon = 8\pi T_4^4 = e^{-\lambda}\left(\frac{\lambda'}{r} - \frac{1}{r^2}\right) + \frac{1}{r^2} \tag{1-20c}$$

as the only non-vanishing terms of the energy-momentum tensor, where the primes denote differentiation with respect to r. The cosmological constant Λ has been dropped in above derivations, because it is negligible in most stellar problems including neutron stars. From the above three relations, the following is easily deduced:

$$\frac{dP}{dr} + (\epsilon + P)\frac{\nu'}{2} = 0 \tag{1-21}$$

which is the relativistic analogue of the Newtonian expression (1-1), or $\frac{dP}{dr} + \frac{\rho\, d\varphi}{dr} = 0$ where φ is the Newtonian potential.

c. Schwarzschild's Exterior Solution

In the empty space surrounding a spherical distribution of matter, all components T_β^α should be zero. Applying this condition to (1-20a) and (1-20c), we obtain

$$\lambda' = -\nu' \qquad (1\text{-}22)$$

Combining this with (1-20b), we are led to

$$\nu'' + \nu'^2 + \frac{2\nu'}{r} = 0 \qquad (1\text{-}23)$$

Integrating this twice, we obtain

$$e^\nu = a + \frac{b}{r} \qquad (1\text{-}24)$$

where a and b are constants of integration.

Noting that the line element (1-7) must approach the special relativity form as r goes to infinity, $dS^2 \rightarrow -dr^2 - r^2\,d\theta^2 - r^2 \sin^2\theta\, d\phi^2 + dt^2$, and that $e^\lambda = e^\nu = 1$ in that case, a is set equal to 1. If further, the constant b is set equal to $-2M$, we have

$$e^{\nu(r)} = e^{-\lambda(r)} = 1 - 2M/r \quad \text{for } r \geq R \qquad (1\text{-}25)$$

Substituting (1-25) into (1-7) we obtain

$$dS^2 = -\frac{dr^2}{(1-\frac{2M}{r})} - r^2\,d\theta^2 - r^2 \sin^2\theta\, d\phi^2 + (1-\frac{2M}{r})dt^2 \qquad (1\text{-}26)$$

The constant M appearing in the above expression will soon be shown to be the total Newtonian mass of the star as calculated by a distant observer (Section I-4b).

d. Schwarzschild's Interior Solution

Under the condition that the pressure be zero at the surface and that the energy density ϵ be constant in the interior, (1-20c) can be integrated to give a result:

$$e^{-\lambda} = 1 - \frac{8\pi\epsilon}{3} r^2 \qquad (1-27)$$

where the constant of integration has been set equal to zero to remove singularities at the origin.

To obtain a solution for ν, we first integrate (1-21), eliminate ϵ and P through (2-20a) and (2-20c), eliminate λ through (1-27), and obtain

$$e^{\nu/2}\left(\frac{2}{r_o} + \frac{\nu'}{r} - \frac{r\nu'}{r_o^2}\right) = \text{const} \quad \text{where } r_o^2 = \frac{3}{8\pi\epsilon}$$

After integration, we get

$$e^{\nu/2} = A - B\,(1 - r^2/r_o^2)^{\frac{1}{2}} \qquad (1-28)$$

where A and B are constants of integration.

Making the pressure zero at the boundary r = R, and the interior solution fit smoothly at r = R to the exterior solution (obtained in sub-section c), the constants are evaluated. The results are

$$A = \frac{3}{2}\left(1 - r_1^{\,2}/r_o^{\,2}\right)^{\frac{1}{2}},\ B = \frac{1}{2} \text{ where } r_o \text{ and } r_1 \text{ are}$$

$$\text{defined by } r_o^{\,2} \equiv \frac{3}{8\pi\epsilon},\ M = \frac{4\pi}{3}\epsilon r_1^{\,3} \qquad (1\text{-}29)$$

With these values for the constants, the interior line element takes the form

$$ds^2 = -\frac{dr^2}{(1 - r^2/r_0^2)} - r^2 d\theta^2 - r^2 \sin^2\theta\, d\phi^2 + \left[A - B\left(1 - \frac{r^2}{r_0^2}\right)^{1/2}\right]^2 dt^2 \qquad (1\text{-}30)$$

In order for the solution to be real, the conditions that

$$r_1^2 < r_0^2 \text{ or } r_1^2 < \frac{3}{8\pi\epsilon} \text{ or } 2M < r_1 \qquad (1\text{-}31)$$

must be satisfied.

e. Derivation of the Relativistic Equations of Hydrostatic Equilibrium

By the use of the equation of state $\epsilon = \epsilon\ (P)$, equation (1-21) may be integrated:

$$\nu(r) = \nu\,(R) - \int_0^{P(r)} \frac{2\,dP}{P + \epsilon(P)} \qquad (1\text{-}32)$$

Taking the exponential of each term,

$$e^{\nu(r)} = e^{\nu(R)} \exp\left[-\int_0^{P(r)} 2\,dP/\{P + \epsilon(P)\}\right] \qquad (1\text{-}33)$$

The constant $e^{\nu(R)}$ is determined by making $e^{\nu(r)}$ continuous across the boundary. Then, from (1-25), we get $e^{\nu(R)} = 1 - 2M/R$. From the definition of $u(r)$ as expressed in (1-10), we have

$$e^{-\lambda} = 1 - 2u/r \tag{1-34}$$

Then (1-20c) becomes

$$\frac{du(r)}{dr} = 4\pi\epsilon(P)r^2$$

In (1-20a), $e^{-\lambda}$ and ν' are eliminated through (1-34) and (1-21), and it becomes:

$$\frac{dP}{dr} = \frac{-(P+\epsilon(P))}{r(r-2u)}[4\pi r^3 P + u]$$

The last two equations represent the relativistic analogue of the hydrostatic equations, which were already written down in (1-8) and (1-9).

I-3 UNITS TO BE USED IN RELATIVISTIC CALCULATIONS

In all the discussions above and hereafter, the system of units which makes $G = c = 1$ is to be used, unless otherwise indicated, so that energy and mass will have the same dimensionality. Furthermore, it is convenient if a system of units be used which gives the same dimensionality to both masses and distances. In this case $\hbar = 1$ also.

In addition, in actual calculations the numbers we are to deal with become enormously large ($M \sim 10^{33}$ gm, $R \sim 10^6$ cm, etc.) if c.g.s. units are used. Noting that the mass and radius of a neutron star are of order of magnitude of about 1 solar mass and 10 kilometers, numerical calculations are much simplified by the adoption of a system of units such that the distance, mass, pressure and density in c.g.s. units are obtained by multiplying the respective quantities obtained in this system of units R, M, P and ρ by conversion factors R_o, M_o, P_o, and ρ_o as defined by

$$\begin{aligned} R_o &= 2\sqrt{2\pi}\,\left(\frac{h}{M_n c}\right)^{3/2} \frac{c}{\sqrt{GM_n}} = 1.37 \times 10^{6} \text{ cm} = 13.7 \text{ km} \sim 10^{-5} R_{\odot} \\ M_o &= R_o c^2/G = 1.85 \times 10^{34} \text{ gm} = 9.29 \; M_{\odot} \\ P_o &= (M_n{}^4 c^5 / 32\pi^2\hbar^3)\, 4\pi = \kappa_n 4\pi = 6.45 \times 10^{36} \text{ dynes/cm}^2 \\ \rho_o &= (\kappa_n/c^2)\, 4\pi = P_o/c^2 = 7.15 \times 10^{15} \text{ gm/cm}^3 \end{aligned} \qquad (1\text{-}35)$$

where

$$\kappa_n = M_n{}^4 c^5/32\pi^2\hbar^3 = 5.12 \times 10^{35}$$

M_n is the mass of a neutron, $\hbar = h/2\pi$, h is Plank's constant.

I-4. GENERAL RELATIVISTIC QUANTITIES

There are several characteristic quantities of general relativity which are important in the problem of neutron stars. Some of these are introduced below.

a. Physical Meaning of the Metric Tensor $g_{\mu\nu}$

$g_{\mu\nu}$ was originally introduced as the components of the metric tensor in the most general expression of an interval in Riemannian space, as $dS^2 = g_{\mu\nu}\, dx^{\mu}\, dx^{\nu}$ (1-11). Its importance is, however, multiplied through the principle of equivalence which connects the metric and gravitation so that the metric for a flat space-time in the presence of any permanent gravitational field corresponds to the metric for a curved space-time without a gravitational field. Because of this, it is possible to regard $g_{\mu\nu}$ either as the components of the metric tensor in the form of (1-11) or as the gravitational potentials through the relation (1-12) in the Einstein theory of gravitation. A close connection between $g_{\mu\nu}$ and $\psi = -\frac{GM}{r}$, the Newtonian gravitational potential, is seen below.

The radial component of the metric and the time component, $g_{rr}(r)$ and $g_{44}(r)$ for a spherically symmetrical space are, from (1-7) and (1-11),

$$g_{rr}(r) = -e^{\lambda(r)} \quad \text{and} \quad g_{44}(r) = e^{\nu(r)} .$$

In an empty space outside a spherical distribution, they take the form

$$\left.\begin{aligned} g_{rr}(r) &= -(1 - 2M/r)^{-1} \\ g_{44}(r) &= (1 - 2M/r) = -\frac{1}{g_{rr}(r)} \end{aligned}\right\} \text{for } r \geq R \qquad (1\text{-}36)$$

as seen from equation (1-26). The radial component in the interior is found from (1-34) to be

$$g_{rr}(r) = -(1 - \frac{2u(r)}{r})^{-1} \quad \text{for } r < R \tag{1-37}$$

The time metric in the interior is obtained by applying the requirement that the chemical potential be constant under the statistical equilibrium.(63)

For a cold-body the chemical potential is simply the Fermi energy (including the rest mass). In the presence of a strong gravitational field, the energy, corresponding to the fourth component of the energy-momentum tensor, must be multiplied by a proper function of the fourth component of the metric to take care of the gravitational effect. We have namely the relation

$$\sqrt{g_{44}(r)}\ (M_k{}^2 + P_k{}^2(r))^{\frac{1}{2}} = \sqrt{g_{44}(R)}(M_k{}^2 + P_k{}^2(R))^{\frac{1}{2}} = \text{const}$$

for dense matter of spherical symmetry, where M_k is the mass and

P_k is the Fermi momentum of one of the particles, k, which constitute the body of interest and R is the radius of this body. For a pure neutron gas, the particles k are only neutrons, n. In this case, the above relation is simplified to

$$g_{44}(r) = (1 - \frac{2M}{R})\ (\cosh^2 \frac{t_n(r)}{4})^{-1} \quad \text{for } r \leq R \tag{1-38}$$

in the interior of a neutron star, where $t_n = 4 \sinh^{-1}(P_n/M_nC)$. In the above derivation, the relation $P_n(R) = 0$ was used.

The physical meaning of these expressions may become somewhat clearer if we note that in the system of units we are employing where $G = 1$ and $c = 1$, the Newtonian potential is just $\psi = -\frac{M}{r}$, and outside the star, we see from (1-36) that the radial component $g_{44}(r)$ and the time metric $g_{44}(r)$ become

$$\left.\begin{aligned} g_{rr}(r) &= -(1 + 2\psi)^{-1} \\ g_{44}(r) &= 1 + 2\psi \end{aligned}\right\} \quad r > R \qquad (1\text{-}39)$$

The last equation in (1-39) is identical with the relation between the time metric and Newtonian gravitational potential in a weak gravitational field (e.g. p. 199 of reference 27). In the absence of a gravitational field, the corresponding space-time is "flat", and $g_{rr} = -1$ and $g_{44} = 1$, $\psi = 0$. The above argument points out that the quantity $-2\psi = 2M/r$, or $2GM/rc^2$ in ordinary units, gives a measure of the deviation of the components of a metric tensor from their values in flat space-time, or the degree of curvature, which in turn gives the strength of the gravitational field. From the above expression, we see that the greater the mass for a fixed radius, in other words, the denser the body, the greater the deviation of g_{44} from unity. When finally $2M/R$ becomes 1, $g_{44} = 0$ and $g_{rr} = -\infty$. It was mentioned earlier that the quantity GM/Rc^2 is about 0.1 for a typical neutron star; in this case g_{44} is about 0.8 at the surface of the star and the 20% deviation is certainly not to be neglected. In the interior the deviation is larger still and this is why the problem of neutron stars must be treated by the theory of general relativity.

In a gravitational field actual distance and time intervals are determined from the same quantities measured in proper coordinates. In a spherically symmetrical body the length contraction occurs only radially and the actual radial distance and time intervals are determined by

$$dr_p = \sqrt{-g_{rr}}\, dr = e^{\lambda(r)/2}\, dr = (1 - 2U(r)/r)^{-1/2}\, dr \qquad (1\text{-}40)$$

and

$$d\tau = \sqrt{g_{44}}\, dt = e^{\nu(r)/2}\, dt \qquad (1\text{-}41)$$

The corresponding proper volume element is

$$dV_p = 4\pi r^2\, dr_p = 4\pi r^2 (1 - 2U(r)/r)^{-1/2}\, dr \qquad (1\text{-}42)$$

For instance, the actual stellar radius R_0 is found from

$$R_0 = \int_0^R \sqrt{-g_{rr}}\, dr \qquad (1\text{-}43)$$

and the total number of baryons in a spherical body of a baryon gas is found from

$$N = 4\pi \int_0^R \sqrt{-g_{rr}}\, n(r)\, r^2\, dr \qquad (1\text{-}44)$$

where $n(r) = \sum_k n_k(r)$ is the total baryon number density at r. In the above expressions R_o, the proper radius, is the actual radius of the star while R is defined as the radial distance from the center of the star to the boundary where the density become zero, which is the radius of a star as seen by a distant observer.

b. Gravitational Mass and Proper Mass

Equation (1-8) can be expressed as $u(R) = \int_0^R 4\pi\epsilon(P)r^2\,dr$; comparing this with a definition of the total Newtonian mass of a star $M = \int_0^R 4\pi\rho\, r^2\,dr$, we see that $u(R)$ in general relativity corresponds to the total Newtonian mass of the star as calculated by a distant observer. It includes not only the sum of the rest masses of the constituent particles, but also the Fermi energies of the constituent particles and the gravitational effect. This is clear from the fact that we are integrating over total energy density $\epsilon(P)$, rather than the sum of matter densities $\rho_m = \sum_k n_k M_k$.

Noting that the interior solution and the exterior solution of the field equations for spherical symmetry must be joined smoothly, equation (1-10) at the boundary $r = R$ is shown to become

$$u(R) = \tfrac{1}{2}R(1 - e^{-\lambda(R)}) = \tfrac{1}{2}R(1 - (1 - 2M/R)) = M$$

through the help of equation (1-25). That is, the so far undefined constant M introduced in (1-25) is indeed identified with the total Newtonian mass of the star as measured by a distant observer.

The mass M or u(R) obtained in this way is called the gravitational mass or the observable mass because it is the mass determined from its gravitational effect on a distant test particle, which is as the mass actually observed by a distant observer, for instance, the mass of a neutron star as seen from the earth.

Proper mass is defined as the mass measured by a local observer. It is obtained by integrating the proper matter density $\rho_m = \sum_k n_k M_k$ over the proper volume of the star $dv_p = 4\pi e^{\lambda/2} r^2\,dr$. In differential form it is written as

$$\frac{dM_p}{dr} = 4\pi \rho_m(P) r^2 \left[\frac{r}{r - 2u(r)}\right]^{1/2} \tag{1-45}$$

This corresponds to the mass the star would have if its particles were dispersed to infinity by the gravitational binding energy, in mass units.

c. The Gravitational Binding Energy

The gravitational binding energy M_B in mass units is the difference between the proper mass and gravitational mass, and may be obtained by integrating the following differential equation together with (1-9):

$$\frac{dM_B(r)}{dr} = 4\pi r^2 \left\{ \left[\frac{r}{r - 2U(r)}\right]^{1/2} \rho_m(P) - \epsilon(P) \right\} \tag{1-46}$$

$\rho_m(P)$ is matter density while $\epsilon(P)$ is energy density.

We know that the most stable configuration is the one with minimum total mass, and from that we see that no stable stellar configuration (in the form of a star of finite dimensions) can exist if the gravitational mass is greater than the proper mass. In that case, particles would be dispersed to infinity rather than being kept together in the form of a star.

d. Schwarzschild Singularity

Examining the expression of a line element such as equation (1-26), we note that for the solution to be real the following inequality must be fulfilled; $R > 2M$

or in ordinary units:

$$R > R_G = \frac{2GM}{c^2} \tag{1-47}$$

The limiting radius R_G is called the "gravitational radius." When $R = R_G$, a singularity occurs. This is called the Schwarzschild singularity. The Schwarzschild field, therefore, has a singular spherical surface at $r = \frac{2GM}{c^2}$ besides a singularity at the origin which is inherent in a Newtonian gravitational field also. On this surface, the component g_{44} vanishes and g_{rr} becomes infinite.

At least a part of this singularity appears to be attributed to the choice of the coordinate system. For instance, if the line element is expressed in isotropic form as (equation 82-14, p.205 of reference 27),

$$ds^2 = -\left(1+\frac{M}{2r}\right)^4 (dx^2+dy^2+dz^2) + \frac{(1-M/2r)^2}{(1+M/2r)^2}dt^2 \qquad (1\text{-}48)$$

the Schwarzschild singularity (a singularity other than that at the origin) does not occur.

When we use hydrostatic equations in the form (1-8) and (1-9), we have to be careful that the condition (1-47) be fulfilled always. For a star of about one solar mass, the gravitational radius is about 2.6 km. The radius of the sun is about 7 x 10^5 km and there is no danger of violating the condition (1-47). For a typical neutron star the radius can be less than about 10 km and for some of the models of densest neutron stars it may be worthwhile to keep this limitation in mind.

e. Gravitational Red Shift

One of the most powerful experimental varifications of the theory of general relativity was based upon the phenomenon known as the "red shift," which is the shift of spectral lines toward lower frequency due to the difference between the stronger gravitational field at the point where the light is emitted and the weaker field where it is received.

The proper period is seen from (1-26) to be

$$d\tau = \left(1-\frac{2M}{R}\right)^{1/2} dt \qquad (1\text{-}49)$$

The wavelength λ of light at the moment of emission at the surface of a star is $c\,d\tau$, where c is the velocity of light, while the wavelength of the same light ray at the moment of arrival at the observer on the earth will be $\lambda + \delta\lambda = c\,dt$, where $\delta\lambda$ is the difference in wavelength at those two moments, and dt is the coordinate period. Taking the ratio of these and using (1-49), we obtain

$$\frac{\lambda+\delta\lambda}{\lambda} = \frac{dt}{d\tau} = \left(1-\frac{2M}{R}\right)^{-\frac{1}{2}} \sim 1+\frac{M}{R} \text{ and } \frac{\delta\lambda}{\lambda} \sim \frac{M}{R} \qquad (1\text{-}50)$$

Or, converting to ordinary units,

$$\frac{\delta\lambda}{\lambda} \sim \frac{GM}{Rc^2} = \left|\frac{\Psi(R)}{c^2}\right| \cong 1.47 \frac{(M/M_\odot)}{R\ (km)}$$

where $M_\odot$ is the mass of the sun.

The shift is negligible in most of the stars but is quite important in the case of neutron stars as mentioned earlier. A detailed analysis of this effect is to be given in later chapters after the results of the models constructed in this research are presented.

More rigorous derivations of (1-50) are found in some standard textbooks on general relativity such as Tolman,(27) Bergman and Landau and Lifshitz.

I-5. INTERPRETATION OF TERMS APPEARING IN RELATIVISTIC HYDROSTATIC EQUATIONS

For this purpose, it is convenient to rewrite (1-9) as:

$$\frac{dP}{dr} = \left(- \frac{\rho(P)M(r)}{r^2}\right)\left(\frac{\rho(P)+P}{\rho(P)}\right)\left(\frac{1+\eta(r)}{1-2\varphi(r)}\right) \qquad (1\text{-}51)$$

where η and φ are defined as

$$\eta = 3P/\bar{\rho} \quad ; \quad \varphi(r) = M(r)/r \qquad (1\text{-}52)$$

$\bar{\rho}$ is the mean density of a star, that is, $M = \frac{4}{3}\pi R^3 \bar{\rho}$. $\varphi(R)$ is recognized to be a red shift as discussed on the preceding page. $u(R)$ or M has already been identified with the gravitational mass and in the above expression $u(r)$ has been replaced by an expression $M(r)$, also, the energy density $\epsilon(P)$ has been expressed as $\rho(P)$, so that the first term would take the form of the familiar expression of Newtonian mechanics.

Without the last two terms, (1-51) is identical with (1-1), noting that in our units $G = 1$ in (1-51). As it was noted, $\rho(P)$ in (1-51) is energy density but in a weak gravitational field where $\epsilon(P)$ is low, ϵ is practically the same as the rest mass density ρ_m. (The total energy may be expressed as the sum of rest mass energy, kinetic energy and potential energy but in the low density limit all the terms other than the sum of the rest mass energies of the constituent particles become negligible compared with the latter.)

The reason for the appearance of pressure P and energy density ρ (P) in the second term ($\rho(P) + P$) can be seen as follows. The energy-momentum tensor $T^{\mu\nu}$ was introduced into Einstein's field equation (1-12) to express the distribution of matter and energy in the theory of relativity, in the same way that matter density ρ was introduced into the Poisson's equation in the Newtonian theory of gravitation,

$$\frac{\partial^2 \psi}{\partial x^2} + \frac{\partial^2 \psi}{\partial y^2} + \frac{\partial^2 \psi}{\partial z^2} = 4\pi G\rho,$$

and, therefore, the gravitational potential in Newtonian mechanics ψ and the metric $g^{\mu\nu}$ in Einstein's theory correspond to each other. In a perfect fluid, as has been assumed in the above derivations, we have seen that the pressure and energy density appear as the components of $T^{\mu\nu}$, the same energy-momentum tensor:

$$T_1^{\ 1} = T_2^{\ 2} = T_3^{\ 3} = -P \text{ and } T_4^{\ 4} = \epsilon .$$

That is, the energy-momentum tensor is determined by the proper pressure and density. Furthermore, we note that in the absence of a gravitational field, the energy-momentum tensor reduces to $T_4^{\ 4} = \epsilon$ and all other components $=0$ (p. 200 in reference 27). That is, $\rho(P)$ in (1-51), the same as ϵ in the above, represents all the macroscopic energy densities as seen by a local observer in the absence of a gravitational field and the effect of the presence of a spherically symmetric gravitational field in a perfect fluid is represented by the non-vanishing components $T_1^{\ 1} = T_2^{\ 2} = T_3^{\ 3} = -P$, where P is the pressure as seen by a local observer. Therefore, it is quite natural that P appears together with energy density in the general relativistic expression (1-9). With a decrease of the strength of a gravitational field P becomes much less than $\rho(P)$ and the second term approaches unity. With a decrease in the pressure term as compared with the density term, we see from the first of equations (1-52) that η goes to zero. $\mathcal{G}$, the red-shift, has been seen to be proportional to the gravitational potential ψ (1-50), and this term also vanishes in the limit of weak potentials. Therefore, the last term also approaches unity as the gravitational field is decreased, and the expression (1-51) does lead to (1-1), the simple Newtonian form.

It may be worthwhile to note that GM/Rc^2, the expression for a red-shift, is also identified with the ratio of the gravitational energy to the rest mass energy. When the former is small compared with the latter we expect the general relativistic correction to be small, also. It is to be shown later, quantitatively, that the last two correction terms in (1-51) are rather significant in neutron stars and that the use of Newtonian approximation (1-1) in place of (1-9) or (1-51) gives a serious deviation from the correct answers even for some of the lightest neutron stars.

CHAPTER II

COMPOSITION OF SURFACE LAYERS

II-1 GENERAL REMARKS

From the brief introductory discussion in the previous chapter we can see that the stellar composition enters the structure problems of neutron stars through the equation of state (1-5a'). The determination of relative abundances of components of the neutronic core (or hyperon core if the density is sufficiently high) is not too complicated, and that is done in the next chapter where the equation of state is the major topic. However, as is seen in what follows, a thorough treatment of the abundance distribution of the constituent elements near the surface is quite complicated, and I find it necessary to devote one whole chapter to that purpose. It is expected that the non-neutronic outer layers are very thin and in most of the previous work on neutron star models such regions were simply neglected. However, one of the aims of this research is to construct models which lead to as realistic results as possible, the composite equation of state of which includes the exact composition change in the outermost layers. Salpeter(12) has already pointed out the possibility of non-negligible effects of envelopes on some of the lightest neutron star models (by "lightest" the lowest densities allowed for a neutron star is meant).

In general stellar structure problems, there are various ways of determining the composition of stars. Reasonable theoretical estimates are possible through the theory of stellar evolution and nucleosynthesis. It is not the purpose of this thesis to go into any details of stellar evolution. However, it is worthwhile to point out that a sensible estimate of the composition of the surface layers of neutron stars is available through the study of the theories of some of the latest stages of stellar evolution (for instance, supernova explosions, white dwarfs, etc.) and with the help of nucleogenesis. Good review articles along these lines are found in such references as 9, 17, 28, 29, 30, 31, 32, 33, and many others.

According to the theory of nucleogenesis, the synthesis of elements is believed to start with hydrogen. The hydrogen burning, which transforms hydrogen to helium, and helium to the isotopes of carbon and oxygen, is responsible for the major part of the energy production in stars. Besides these, the s (meaning slow time scale neutron capture), α, and e (meaning equilibrium) processes, etc., are responsible for the synthesis of heavy elements in the iron group from light elements like C, O, Ne, which are first transformed to medium weight elements such as Mg, S, and Si. The general trend is that as a star becomes older its internal temperature and density is increased through nuclear energy generation and gravitational contraction.

With the increase in temperature the Coulomb barriers are overcome one by one, and more nuclear reactions of greater complexity involving heavier elements become possible. According to this theory, the main composition of older stars should be hydrogen while greater abundances of heavier elements should be expected in some of the newest stars and newest star clusters. The last statement is fully supported by observational facts. Neutron stars are thought to belong to the last stage of stellar evolution. Therefore, even though we may not know the exact path through which the star has reached this end point, we can at least assume that it has gone through the series of nuclear synthesis (which was briefly summarized above) to a certain extent, though we may not know how far it has proceeded and how high a maximum temperature it has reached in its life history before it has cooled to the last stage. The dynamic problem of neutron stars, like the exact mechanism of the formation of a neutron star, is outside the domain of the present research.

However, after having studied some of the theories of the latest stages of stellar evolution, especially of supernova explosions in references such as 9, 17, 29, and 32, I believe it to be quite possible that neutron stars are the end products of supernova explosions, and that the central temperature of the stellar configuration just before cooling to form a neutron star is as high as or even higher than several billion degrees. If the cooling takes place fast enough so as not to allow any appreciable change of composition (through any transformation processes), then we expect that the composition in its higher temperature stage is kept as the final composition even after cooling. This is a rather rough statement and more detailed explanations are given later. However, the point is that the neutrino energy loss which is responsible for a collapse of the core in a supernova explosion supplies an ideal mechanism for such a sufficiently quick cooling. Therefore, by investigating the configuration of matter around that temperature (the temperature where the freezing of the elements takes place), for any given density, it is possible to estimate the radial distribution of composition, if we know the radial distribution of density in a neutron star.

As is shown in more detail in the following sections, at temperatures exceeding a few billion degrees all nuclei are subjected to photodisintegration. That is, all manner of nuclear processes ((γ, α), (γ, P), (γ, n), (α, γ), (P, γ), (n, γ) and (P, n) reactions and others involving heavier nuclei) occur in great profusion. It is obviously hopeless to try to follow these reactions in detail, and in developing a theory we must resort to the method of statistical mechanics, that is, we can find the abundance distribution of nuclear species with the assumption that the whole configuration is in statistical equilibrium.

The generally known properties of the equilibrium configurations of nuclear matter in this temperature region (about a few billion degrees) are sketched below; if the density is less than about 10^7 gm/cm^3, the equilibrium configuration consists mainly of elements in the iron group which have the greatest average binding energy per nucleon when the temperature is less than about 5×10^9 °K. For higher temperatures a phase change to helium occurs under statistical equilibrium. For a higher density, the transition temperature to helium becomes somewhat higher and the equilibrium configuration for temperatures below the transition point shifts to the neutron-rich side of the heavy element valley of beta stability. The detailed investigation of those elements as a function of density at zero temperature as made independently by Salpeter(11) and Wheeler(8) are discussed in a later section and are re-investigated by the writer (II-3). The general trend is that as the density increases, the presence of more neutron-rich elements becomes energetically more favorable and finally a transition to a free neutron configuration takes place at a critical density.

As will be revealed in a later section, the density in a neutron star is almost constant in the interior until we come to the very edge of the star. Therefore, as we go outward near the surface, a sharp change in composition from an almost pure neutron configuration to various degrees of neutron-rich heavy elements with ionized electrons from layer to layer is expected, the final transition being to the iron group elements in the outermost layer.

In the following sections these points are investigated in detail, and some quantitative results are presented. However, before that there are several physical quantities to be introduced and calculated.

II-2. SEMI-EMPIRICAL MASS FORMULA AND THE NUCLEAR BINDING ENERGY

One of the most fundamental physical quantities appearing in the later calculations is the nuclear binding energy. For elements available in the laboratory it is best to use the experimental data. In most of the regions of temperature and density with which we are presently concerned, that is not the case. However, with the help of the semi-empirical mass formula originally introduced by Weiszacker and improved by various authors this difficulty has been overcome.

In simple form it can be expressed as

$$-Q = E = -a_1 A + a_2 A^{2/3} + a_3 Z^2/A^{1/3} + a_4 (N-Z)^2/A \qquad (2\text{-}1)$$

where Q is the nuclear binding energy, the first term on the right hand side is a volume term, representing the energy per particle in infinite nuclear matter, the second term gives a surface energy which takes care of the unsaturated "bonds" of those nucleons on the surface and is repulsive in effect, and the third is the Coulomb repulsive term which is just

$$\frac{1}{2}\iint \frac{\rho(\bar{r})\,\rho(\bar{r}')\,d\bar{r}\,d\bar{r}'}{|\bar{r}-\bar{r}'|} = \frac{3}{5}\,\frac{Z^2 e^2}{R} = \frac{3}{5}\,\frac{Z^2 e^2}{r_0 A^{1/3}} \qquad (2\text{-}2)$$

The last term is a symmetry volume energy, representing an additional energy required to express the tendency of nuclear matter toward equality of neutron and proton numbers. In equation (2-1) and in all discussions hereafter, "A" denotes the mass number, Z the atomic number or proton number, and N the neutron number. In the above, a_1, a_2, a_3 and a_4 are characteristic constants. Besides those appearing in (2-1), the addition of an extra term which expresses addional stability of nuclei with paired neutrons and protons, called a pairing energy, is required in a more complete treatment. In evaluating the Coulomb term in (2-2) the simple formula for a nuclear radius R

$$R = r_0 A^{1/3} \qquad (2\text{-}3)$$

was used (where $r_0 = 1.22 \times 10^{-13}$ cm), if the charge distribution is uniform. The semi-empirical mass formula is regarded as one of the most successful outcomes of the liquid drop model, but in this model some other important effects like shell effects are completely neglected.

For some of the problems we encounter this neglect is not justified. To take care of the fluctuations in nuclear masses related to shell structure, a number of efforts have been made, in most of which some analytical correction terms were suggested. Good review articles are found in references 34 and 35.

In my present calculation it was thought to be most appropriate to use the revised formula of Gameron,(36) which is valid for most of the regions of A except those corresponding to the lightest nuclei, where all the terms discussed above and more are included.

It is expressed in the form of mass excesses in Mev as

$$M-A = 8.367\,A - 0.783\,Z + E_v + E_s + E_c + E_{ex} + S(Z, N) + P(Z, N) \quad (2\text{-}4)$$

where the subscripts v, s, c, and ex denote the volume, surface, Coulomb and Coulomb-exchange energy respectively. The symmetry term is included both in the volume and surface terms. $S(Z, N)$ and $P(Z, N)$ are the empirical shell correction and pairing energies, whose numerical values for every N and Z are tabulated in reference 36. The analytic expressions of the first four terms are:

$$E_v = \alpha\ [\,1 - \frac{\beta}{\alpha}\frac{(A-2Z)^2}{A^2}\,]\ A \qquad (2\text{-}5a)$$

$$E_s = \gamma\ [\,1 - \frac{\phi}{\gamma}\frac{(A-2Z)^2}{A^2}\,]\ [\,1 - \frac{0.62025}{A^{2/3}}\,]^2\ A^{2/3} \qquad (2\text{-}5b)$$

$$E_c = 0.779 \frac{Z(Z-1)}{A^{1/3}} \left[1 - \frac{1.5849}{A^{2/3}} + \frac{1.2273}{A} + \frac{1.5772}{A^{4/3}}\right] \qquad (2\text{-}5c)$$

$$E_{ex} = -\,0.4323 \frac{Z^{4/3}}{A^{1/3}} \left[1 - \frac{0.57811}{A^{1/3}} - \frac{0.14518}{A^{2/3}} + \frac{0.49597}{A}\right] \qquad (2\text{-}5d)$$

The constants β and ϕ were determined from the position of the valley of beta stability and the constants α and γ were determined by a least-squares fit of the reference mass formula (the expression (2-4) without the shell and pairing terms) to experimentally measured atomic masses. The results are:

$\beta = 31.4506$ Mev, $\phi = 44.2355$ Mev, $\alpha = -17.0354$ Mev, $\gamma = 25.8357$ Mev.

In the expression for the surface effect E_s, the term with the coefficient ϕ/γ is a symmetry energy correction and the second bracket $\left[1 - \frac{0.62025}{A^{2/3}}\right]^2$ is due to the trapezoidal radial model used, where the boundary is considered to be diffuse and ill-defined. This is a more realistic model than those with sharply defined edges. That is:

$$R = 1.112\, A^{1/3} \left[1 - 0.62025/A^{2/3}\right] \times 10^{-13} \text{ cm} \qquad (2\text{-}6)$$

The exchange Coulomb energy arises from the correlation in the motion of the protons within the nucleus.

The results of Cameron's formula are discussed and compared with the work of others in reference 35, where the major cause of the rather large deviations in the region of lightest nuclei is attributed to an overestimation of the Coulomb exchange term for those nuclei. However, an inspection of this paper indicates that the fit is, in general, excellent in the range of $23 < A < 250$. The range of our major interest is safely within this limit.

The physical quantities of our particular concern, namely the nuclear binding energy Q, the neutron binding energy ϵ_n which is the energy in Mev required to remove one neutron from the nucleus (A, Z), the negatron decay energy ϵ^- which is the energy in Mev available for negative beta emission from the nucleus (A, Z) to the nucleus (A, Z +1), and the positron decay energy ϵ^+ which is the energy in Mev available for positron emission or electron capture from the nucleus (A, Z) to (A, Z−1), are obtained through the following relations derived from the definition of the respective quantity:

$$Q = Z M_p C^2 + N M_n C^2 - MC^2 = -[E_v + E_s + E_c + E_{ex} + S(Z,N) + P(Z,N)] \tag{2-7a}$$

$$\epsilon_n = Q(Z, N) - Q(Z, N - 1) \tag{2-7b}$$

$$\epsilon^- = Q(Z + 1, N - 1) - Q(Z, N) + 0.783 \tag{2-7c}$$

$$\epsilon^+ = Q(Z - 1), N + 1) - Q(Z, N) - 0.783 \tag{2-7d}$$

where $(M_n - M_p) C^2 = 0.783$ Mev was used. (2-7e)

Equations (2-5a) through (2-5d) with the known values of the constants are used in the evaluation of (2-7a). For $S(Z, N)$ and $R(Z, N)$ the numerical values listed in reference 36 were used. The quantities Q, ϵ_n, ϵ^- and ϵ^+ were computed in this manner for $1 \leq Z \leq 80$ and with each Z for $Z \leq N \leq 5Z$. The range of Z is extended up to 90 with the same range of N in the computation of Q. The results are stored in tabulated form.

The comparison of these results with experimental data (as in reference 37) shows an excellent agreement. For instance, for ${}_{32}Ge^{67}$, the experimental Q value from reference 37 is 578.190. Our result is $Q = 578.2255$, and the discrepancy is less than 0.1%. A similar check was made for 30 other elements chosen at random from the whole range, and as far as the experimental data offers values for comparison the agreement was found to be within 0.1% for all the elements with $Z \gtrsim 12$. For lighter elements with $Z \lesssim 8$, our results are not reliable.

The results of this section were used throughout the following computations whenever our range went beyond the region of experimentally determined masses.

II-3. EQUILIBRIUM CONFIGURATION FOR A COLD DENSE MATTER

a. General Discussion

It is a well-known fact of statistical mechanics that the most stable element (A_m, Z_m) in equilibrium is obtained by maximizing the total nuclear energy per nucleon with respect to A and Z. In the presence of electron degeneracy a slight modification enables us to use a similar argument.

Consider a nucleus (Z, A) and a nucleus (Z-1, A), and assume that the former is stable against a disintegration to the latter by the amount of energy ϵ_Z in the absence of electron degeneracy. Suppose an electron degeneracy with the amount of Fermi energy E_F enters. As soon as E_F becomes equal to or greater than ϵ_Z, (Z, A) will no longer be stable, the conversion to (Z-1, A) by the inverse beta process, $e^- + (Z, A) \rightarrow (Z-1, A) + \nu$, will occur, and the stability will be shifted to the latter element. In general, even Z and even A nuclei have larger value of ϵ_Z and if $E_F > \epsilon_Z$ two successive inverse beta decays will usually take place to (Z-2, A). If the Fermi energy E_F is larger than ϵ_{Z-2}, the beta decay energy of (Z-2, A), another set of inverse decays will follow, and so on. This will continue until the beta-decay energy between the nuclei gets larger than E_F. The larger the E_F the greater is the expected shift from the original valley of beta-stability.

Taking this into account, the quantity we are interested in is now the energy of the nucleus plus Z electrons relative to "A" free neutrons, which can be expressed as $(B - Z\,E'_F)$ where B is the total binding energy of the nucleus and E'_F is the Fermi energy of the electron gas minus the neutron-hydrogen rest-mass energy difference.

The most stable element is then obtained by maximizing the quantity

$$(B^*/A) \equiv (B/A) - (Z\,E'_F/A)\,.$$

b. Results of Others

Salpeter used this method to determine the composition of dense matter at zero temperature. His final results given in reference 11(b) are listed in Table 1a.

TABLE 1a

The Fermi energy and corresponding density for transitions under equilibrium conditions between various nuclei by E.E. Salpeter, taken from reference 11(b).

(Z,A)	(26,56)	(28,62)	(28,64)	(28,66)	(28,68)	(30,76)	(30,78)	(30,80)	(32,90)	(38,120)n
$\mu \equiv \frac{A}{Z}$	2.15	2.22	2.28	2.36	2.43	2.53	2.60	2.66	2.81	3.16
E_F (Mev)	0.6	2.5	3.9	6.1	7.0	8.5	9.5	14.8	20.6	24.0
log ρ (gm/cm^3)	7.15	8.63	9.15	9.69	9.87	10.13	10.28	10.84	11.28	11.53

Wheeler et al(8) used similar arguments to determine the composition in this range of density at zero temperature. Their results are summarized in Figure 1. Line (1) marks the ordinary valley of beta stability. The cross on this line is F_e^{56}. When $E_F = 0$, the equilibrium point is at F_e^{56}. As E_F is increased, the most stable element

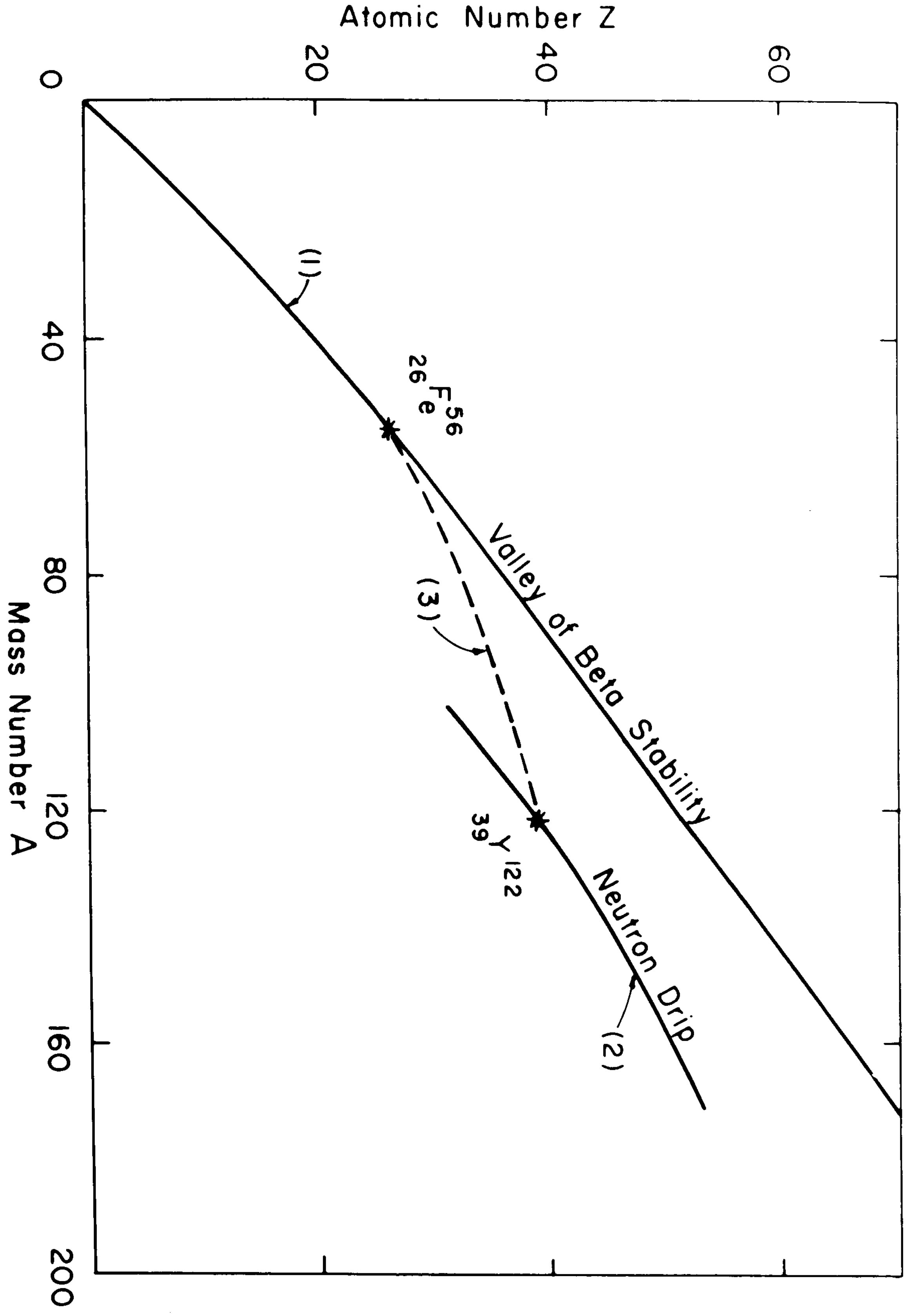
Atomic Number Z
0
20
40
60
Mass Number A
40
80
120
160
200
(1)
(2)
(3)
Valley of Beta Stability
Neutron Drip
$_{26}Fe^{56}$
$_{39}Y^{122}$

Figure 1

moves along the line (3) and finally at A = 122 and Z = 39, it meets the line (2), the neutron drip line, which represents the place where the neutron binding energy falls to zero. (2) is called the neutron drip line because as E_F, and hence the density, is increased beyond the intersection of (2) and (3), heavy nuclei are destroyed and neutrons drip off as we go along (2). (Note: Wheeler did not include shell terms.)

c. Results of this Research

In this research, it was thought to be worthwhile to reinvestigate the equilibrium configuration of a cold, dense matter in a more systematic way by the use of 7090 computer. First, the quantities A, B, and (B*/A) were calculated and listed as a function of Z and N in the ranges $11 \leqslant Z \leqslant 100$ and $1.5Z < N < 4Z$. This was repeated for $E_F = 0.17$, 5, 10, 15, 18, 20, 23, 25, and 30 Mev. The above values of N, Z, and E_F were selected so that our range of interest in the problem of neutron stars would be well covered. For an ionized gas of dense matter, the following conversion of E_F to density ρ is applicable to a first order approximation:

$$E_F = (3\pi^2)^{1/3}\,\hbar c\,(\rho N_o/\mu)^{1/3} \quad \text{(relativistic) or}$$

$$E_F = (3\pi^2)^{2/3}\,(\hbar^2/2m_e)\,(\rho N_o/\mu)^{2/3} \quad \text{(nonrelativistic)} \qquad (2\text{-}8)$$

where N_o is Avogadro's number and $\mu = A/Z$. A more accurate treatment (Section II-4) is made in the final calculation.

The maximization of (B^*/A) with respect to A and Z was made in the following manner. In the above table of (B^*/A) vs. Z, N, A, and B, the maximum value of (B^*/A) and the corresponding A were first chosen for each Z and denoted by $(B^*/A)_m$ and A_m, respectively. Next, the quantity $(B^*/A)_m$ selected in this manner was plotted vs. A_m in Figure 2. A particular value of Z is attached to each A_m through the first process. Then, the Z at the peak in the $(B^*/A)_m$ vs. A_m curve (Figure 2) gives the atomic number of the most stable element and was called Z_m. In this way the most stable element (A_m, Z_m) was selected for each value of E_F.

The result is summarized in Table 1 b, Table 2 and Figure 2. It certainly shows the shell effects and pairing effects and takes account of the individual fluctuations of the mass correctly. As E_F increases we see a flow of elements from one closed neutron shell to another. Up to $E_F = 18$ Mev, the $N = 50$ shell is the most stable. Beyond this point, the maximum point shifts to the $N = 82$ shell. At $E_F = 30$ Mev, the height of the elements near the $N = 126$ shell and that at the $N = 82$ shell are almost comparable, but the actual shift of the maximum element from the peak at the 82 shell to that at the 126 shell did not occur. The general trend of a steady increase of A_m and a steady

TABLE 1b

Most stable nuclei at different densities (different E_F), and their values (B^*/A) and (A_m/Z_m), for cold matter

E_F (Mev)	0.17	5	10	15	18	20	23	25	30
log ρ (gm/cm^3)	6.07	9.37	10.29	10.82	11.08	11.26	11.46	11.58	11.84
A_m	56	84	82	78	78	122	120	118	114
Z_m	26	34	32	28	28	40	38	36	32
N_m	30	50	50	50	50	82	82	82	82
maximum nucleus	F_e^{56}	S_e^{84}	G_e^{82}	N_i^{78}	N_i^{78}	Z_r^{122}	S_n^{120}	K_r^{118}	G_e^{114}
$\mu_m = \frac{A_m}{Z_m}$	2.15	2.48	2.56	2.78	2.78	3.05	3.16	3.28	3.56
(B^*/A) Mev/ptclc	8.797	6.631	4.650	2.787	1.703	1.027	0.060	-0.565	-2.041

TABLE 2

Some of the peak nuclei under equilibrium conditions at different Fermi energies E_F

E_F (Mev)	nucleus	Z	N	A	(B*/A) (Mev/ptcle)	E_F (Mev)	nucleus	Z	N	A	(B*/A) (Mev/ptcle)
5	$34S_e^{84}$	34	50	84	6.631	10	$32G_e^{82}$	32	50	82	4.6502
	K_r^{86}	36	50	86	6.621		Z_n^{80}	30	50	80	4.6446
	B_r^{85}	35	50	85	6.614		G_a^{81}	31	50	81	4.6339
	G_e^{80}	32	48	80	6.613		A_s^{83}	33	50	83	4.6163
	N_i^{66}	28	38	66	6.608						
	A_s^{83}	33	50	83	6.604						
	Z_n^{72}	30	42	72	6.602						
15	$_{28}N_i^{78}$	28	50	78	2.787	20	$40Z_r^{122}$	40	82	122	1.027
	C_u^{79}	29	50	79	2.773		M_o^{124}	42	82	124	1.020
	Z_n^{80}	30	50	80	2.770		N_b^{123}	41	82	123	1.018
	C_o^{77}	27	50	77	2.738		Y^{121}	39	82	121	1.013
25	K_r^{118}	36	82	118	-0.565	30	G_e^{114}	32	82	114	-2.041
	S_r^{120}	38	82	120	-0.574		S_e^{116}	34	82	116	-2.051
	Rb^{119}	37	82	119	-0.576		A_s^{115}	33	82	115	-2.054
	B_r^{117}	35	82	117	-0.584		G_a^{113}	31	82	113	-2.059
	S_e^{116}	34	82	116	-0.586		Z_n^{112}	30	82	112	-2.067
	Y^{121}	39	82	121	-0.599						
	A_s^{113}	33	80	113	-0.616		S_n^{178}	50	126	178	-2.073

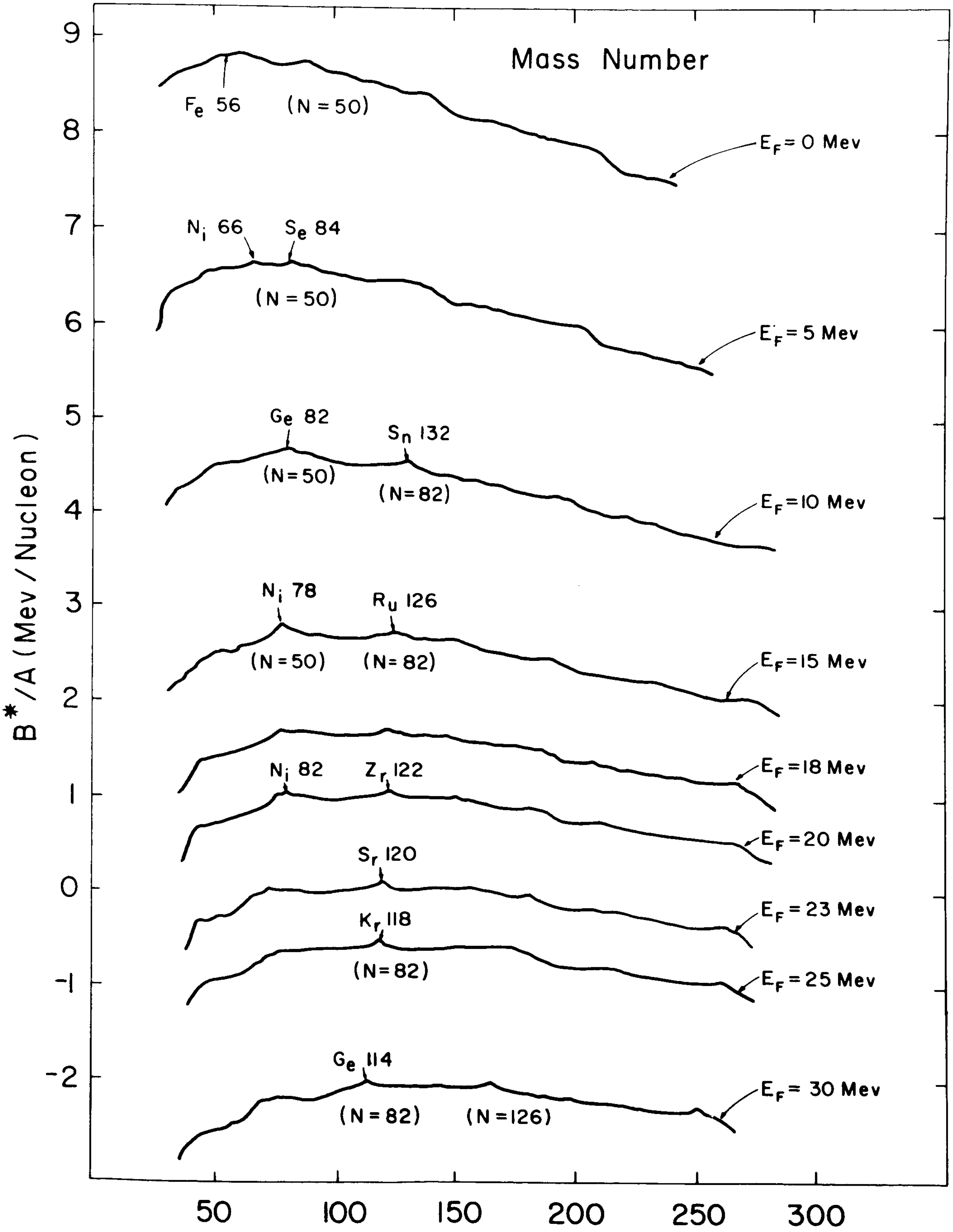
Mass Number
B*/A (Mev / Nucleon)
9
8
7
6
5
4
3
2
1
0
-1
-2
50
100
150
200
250
300
Fe 56
(N = 50)
E_F = 0 Mev
Ni 66
Se 84
(N = 50)
E_F = 5 Mev
Ge 82
Sn 132
(N=50)
(N=82)
E_F =10 Mev
Ni 78
Ru 126
(N=50)
(N=82)
E_F =15 Mev
E_F =18 Mev
Ni 82
Zr 122
E_F =20 Mev
Sr 120
E_F = 23 Mev
Kr 118
(N=82)
E_F = 25 Mev
Ge 114
(N=82)
(N=126)
E_F = 30 Mev

Figure 2

decrease of z_m (= Z_m/A_m in our notation) is observed in Figure 3 of reference 11 (a). When the shell effect enters this change is more nearly discrete. The sudden jump from one magic number to another is typical in my result. This effect is revealed in Salpeter's final result also (Table 1a), though the numbers attached to the various elements are somewhat different from mine. Salpeter estimated the accuracy of his result to be within 20%.(11(b)) Within this limit, the general agreement between Table 1a and Table 1b is satisfactory. Especially the agreement of the value $\mu \equiv (A_m/Z_m)$ between these two results is excellent. In both, it changes smoothly from 2.15 at Fe^{56} to 3.16 at Sr^{120}. The effective binding energy per nucleon (B^*/A) decreases smoothly as E_F is increased and becomes negative for $E_F > 23$ Mev, indicating that all heavy elements are unstable against disintegration to neutrons at these high densities.

The present method was used to determine the stability point as a function of density, but it is inadequate to find its temperature dependence. Also, the actual abundance curve (such as those shown in Figures 11 through 16) cannot be obtained in this way. To get these, we would have to depend on more elaborate abundance calculations including temperature effects (non-zero temperature treatment), and the rest of this chapter is devoted to that subject.

II-4 STATISTICAL EQUILIBRIUM ABUNDANCES

For statistical equilibrium to be maintained, the following conditions must be satisfied:

i) Energy must be statistically distributed among states of translation of each type of particle present.

ii) Statistical equilibrium requires that there be detailed balancing between reactions involving gamma ray emission and absorption, so that thermodynamic equilibrium will be maintained between matter and radiation.

iii) There must be suitable chain reactions connecting any pair of nuclei (A,Z) and (A',Z'), provided that these nuclei occur in appreciable abundance. As to the chain reactions, we can assume that only neutron, proton and α particle reaction are required to establish the chain between various nuclei.

iv) The beta process is important in maintaining the equilibrium between protons and neutrons (including bound nucleons as well as free ones). The importance of a particular beta reaction depends not only on the lifetime but also on the abundance of the nuclei involved.

We will note that satisfaction of the above conditions critically depends on the temperature with which we are dealing, and actually this sets the lower limit to the temperature at a few billion degrees.

Assuming that the above conditions are satisfied, the following equation of statistical equilibrium is derived in Appendix 1:

$$n(A,Z) = \omega(A,Z) \left(\frac{AMkT}{2\pi\hbar^2}\right)^{3/2} \left(\frac{2\pi\hbar^2}{MkT}\right)^{3A/2} \frac{n_n^{(A-Z)} n_p^{Z}}{2^A} \exp\left(Q(A,Z)/kT\right) \tag{2-9}$$

where $n(A,Z)$ = number density of the nucleus (A,Z)

n_n = " " " free neutrons

n_p = " " " free protons

$Q(A,Z)$ = binding energy (ground state) of the nucleus (A,Z)

$\omega(A,Z)$ = partition function of the nucleus (A,Z)

M = atomic mass unit

k = Boltzman's constant

$h = \hbar\, 2\pi$ = Plank's constant

T = temperature

A = mass number

Z = proton number.

It is convenient to re-express this as

$$n(A,Z) = f(A,Z,T) \left\{ n_n^{A} \left(\frac{n_p}{n_n}\right)^{Z} \right\}. \tag{2-10}$$

The term which depends on temperature but is independent of density is separated from the rest in the form $f(A,Z,T)$. Q in (2-9) was already calculated in Section II-2 and that can be used whenever experimental data is not available. $\omega(A,Z)$ is defined as

$$\omega(A,Z) = \sum_{\gamma} (2I_{\gamma} + 1) \exp(-E_{\gamma}/kT) \tag{2-11}$$

where I_{γ} is the spin of the γth level and E_{γ} is the energy of the γth level. Actual evaluation of $\omega(A,Z)$ is done in detail in a later section (II-9b). At the present stage it is sufficient just to note that the dependence of the abundance $n(A,Z)$ on $\omega(A,Z)$ is not large, and in order to make the present discussion easier we tentatively assume that $\omega(A,Z)$ is known. (For instance, if the excited states are neglected and the spin of the ground state is 1/2, $\omega(A,Z) = 2$.)

Assuming that Q and $\omega(A,Z)$ are known, the free parameters appearing in (2-9) are n_p, n_n and T. If densities and temperatures are given and if there is another relation which relates n_n and n_p to total density ρ, the abundance of any nucleus (A,Z) is determined uniquely for any given density and temperature.

The hitherto conventional method for providing another condition was to treat p, n, and e^- as the components of the chemical reaction $n \rightarrow p + e^-$ and to apply the statistical equilibrium relation to them. However, in the stellar interior where the neutrinos escape forever at a great rate as in our case, we cannot treat the above beta process as the chemical reaction, since the process is not reversible.

Under steady conditions, however, we can still say that the total number of electron emissions per unit time is equal to the total number of the inverse processes (negatron captures plus positron emissions) per unit time, and this furnishes us with the required condition. Denoting the electron emission by a subscript minus, the inverse processes by a subscript plus and expressing the rate per particle by $P(A,Z)$, and the number density by $n(A,Z)$, we can express the above steady state condition imposed on the beta processes as

$$\sum_i P_-(A_i, Z_i) n(A_i, Z_i) = \sum_k P_+(A_k, Z_k) n(A_k, Z_k) \tag{2-12}$$

The summation is taken over all the contributors to the beta reactions on each side.

In this research, the electron Fermi energy E_F was chosen as one of the free parameters instead of the density ρ. Therefore, the following procedure was adopted. Given E_F the corresponding electron number density n_e was first calculated through the relations

$$E_F = (3\pi^2)^{2/3} \frac{\hbar^2}{2m_e} n_e^{2/3} \quad \text{(non-relativistic)}$$

$$\text{or} \quad E_F = (3\pi^2)^{1/3} \hbar c \; n_e^{1/3} \quad \text{(relativistic)} \tag{2-13}$$

where $\hbar$ = Plank's constant $/2\pi$, c = velocity of light, and m_e = electron mass.

The conservation of charge requires that this n_e should be equal to the sum of all the positive ion number densities times Z:

$$n_e = \sum_j Z_j \, n(A_j , Z_j) \tag{2-14}$$

The summation is taken over all the ions j of interest with $A \geq 1$ and $Z \geq 1$. On the other hand, the conservation of mass requires that

$$\rho = \sum_k A_k \; n(A_k, Z_k) / N_o \tag{2-15}$$

where N_o is Avogadro's number, and the summation is taken over all the nuclei k of interest with $A \geq 1$ and $Z \geq 0$.

For a given E_F we know n_e through (2-13), therefore n_e in (2-14) can be assumed to be known for any given E_F. Thus we have three equations (2-10), (2-12) and (2-14) (namely, the statistical equilibrium abundance formula, the condition imposed on the beta processes under steady state, and the conservation of charge) for the three independent variables n_n, n_p, and T. In principle, solving the above three equations simultaneously solves our problem. Once the abundances n(A, Z) are known, the conservation of mass as expressed by the relation (2-15) will give us the corresponding density. This procedure was followed in this research.

One thing we have to note is that in using the beta process described above, (2-12), we must first know roughly which nuclei would contribute appreciably to the beta processes. The latter can be found if the rough abundance distribution is known beforehand. For that purpose a first approximate calculation of $n(A,Z)$, without the use of the reaction (2-12), is necessary, and it was made as follows.

II-5 THE ADJUSTMENT OF n_n AND n_p, AND THE ABUNDANCE CALCULATIONS, WITHOUT BETA PROCESSES

For ordinary terrestrial conditions where $E_F \simeq 0$, elements are beta-stable if both their electron and positron energies are negative. However, in such dense matter as we are dealing with where $E_F \gtrsim 5$ Mev, the valley of beta stability is shifted toward the neutron-rich side. Thus, the n_p and n_n were adjusted so that the maximum abundance would occur along the shifted valley of beta stability for each given Fermi energy. Combining (2-10), (2-13) and (2-14), we can relate the Fermi energy to the free neutron number density n_n and free proton number density n_p in the form

$$E_F = E_F(n_n, n_p) . \qquad (2\text{-}16)$$

The first input values of n_n and n_p for a given E_F were estimated by an approximate hand calculations based on the assumption that the nuclei involved were those giving the maximum at the peak for each of the selected values of E_F in Section II-3 and in the Figure 2. A program was constructed such that the computer adjusts n_n and n_p until the calculated Fermi energy through (2-16) agrees with the given Fermi energy within 0.1%. In this method, we adjust the combination $\left\{(n_n)^A \left(\frac{n_p}{n_n}\right)^Z\right\}$, but not n_n and n_p separately. It is quite possible, therefore, that the n(A,Z)'s calculated in this way do not give the maximum abundance in the valley of the beta stability. In that case, the input trial values of n_p and n_n were changed while keeping the product $\left\{n_n{}^A \left(\frac{n_p}{n_n}\right)^Z\right\}$ constant, and the calculations were repeated until the best fit to the center of the valley was obtained. This was done for $E_F = 0.17$, 5, 10, 15, 20, 23 and 25 Mev, and for T at 5 billion degrees.

Logarithms of n_n and n_p/n_n thus obtained are plotted against density in Figures 9 and 10 and shown as dotted curves. The number of free neutrons increases with increasing density while the ratio of the number of free protons to free neutrons decreases.

Values of n_n and n_p/n_n are then substituted into equation (2-9) to get the abundance n(A,Z) for all the nuclei (A,Z) of interest for each E_F. About 200 nuclei were selected for each E_F, which covered the whole of the peak regions in Figure 2 for cold matter.

The actual abundance curves thus obtained are not shown because they are similar to the final abundance curves obtained in a later section (II-9b), including beta reactions. However, the general behavior of how elements change with an increase of E_F is shown in Figure 3; also the first six nuclei, in the order of highest abundance are listed, together with the abundances, in Table 3, in the rows marked II-5 for each E_F. It is interesting to compare the peak nuclei listed in the first row with those obtained in Section II-3 listed in Table 1b. The agreement is perfect except at 5 Mev, where the peak nucleus is ${}_{28}\mathrm{Ni}^{66}_{38}$ in the present result while it is ${}_{34}\mathrm{Se}^{84}_{50}$ in Section II-3. This discrepancy is reasonable if we look at Figure 2. The peaks near Ni^{66} and Se^{84} are comparable in their heights in Figure 2. The former corresponds to the $Z = 28$ closed shell and the latter to the $N = 50$ shell. The general behavior of the stability point as a function of temperature is, as will be fully demonstrated later, a flow of elements down toward the lighter element side with an increase in temperature, if density is kept constant. The present result was obtained for $T = 5 \times 10^9$ °K but that in Section II-3 is for zero-temperature. As the temperature is raised from zero to 5 billion degrees the stability point apparently is shifted from $Z = 34$ to 28. The shifting of the peak position with the increase in temperature is more pronounced

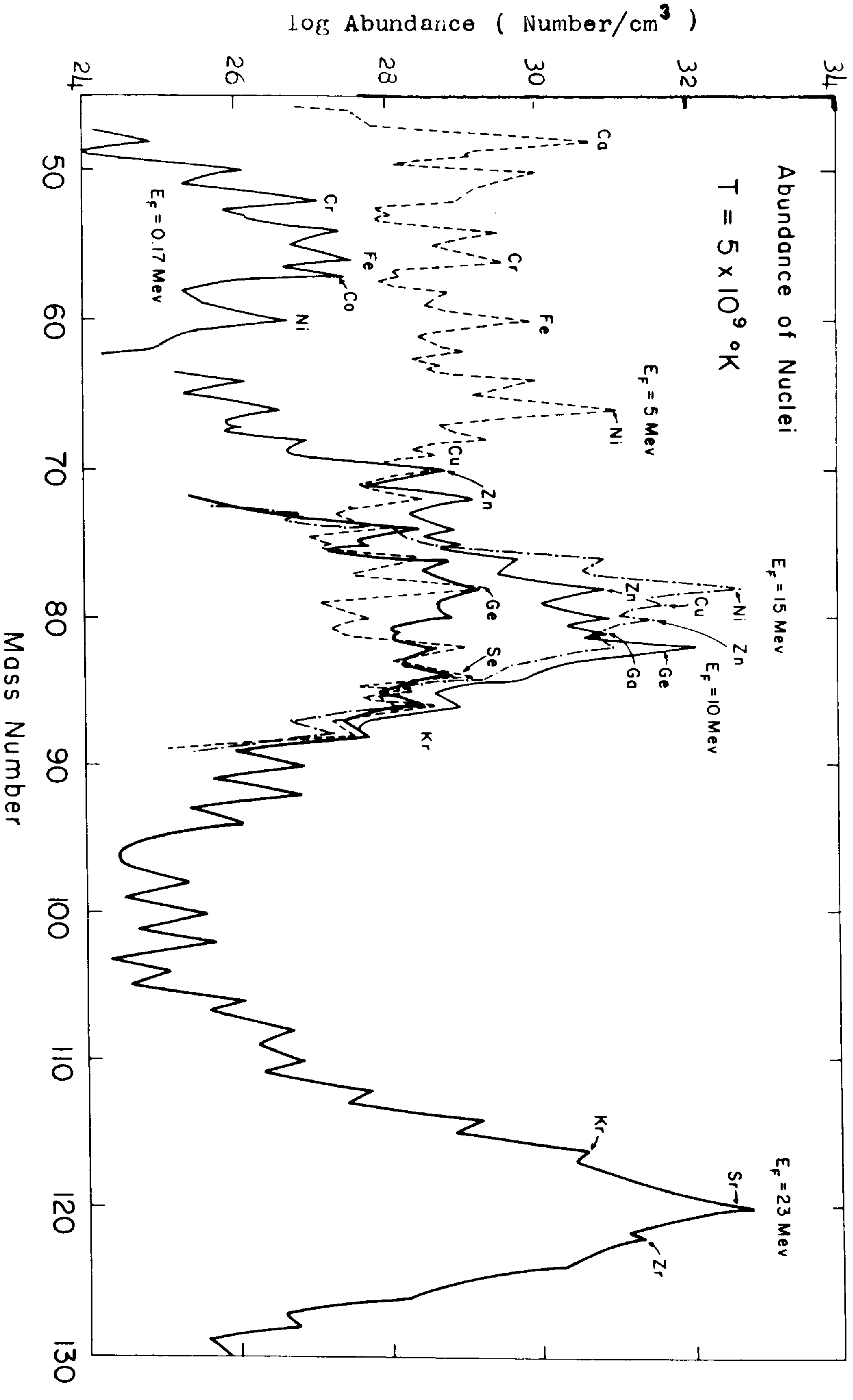
log Abundance (Number/cm^3)
24
26
28
30
32
34
Abundance of Nuclei
T = 5 x 10^9 °K
Mass Number
50
60
70
80
90
100
110
120
130
E_F = 0.17 Mev
E_F = 5 Mev
E_F = 10 Mev
E_F = 15 Mev
E_F = 23 Mev
Ca
Cr
Fe
Co
Ni
Cu
Zn
Ga
Ge
Se
Kr
Sr
Zr

Figure 3

TABLE 3

The first six nuclei in the order of highest abundance and their n(A,Z) at various Fermi energies and at T = 5 billion degrees

E_F(Mev)	0.17		5		10		15		20		23		Section
	nucleus	$\log n_A^Z$	nucleus	$\log n_A^Z$	nucleus	$\log n_A^Z$	nucleus	$\log n_A^Z$	nucleus	$\log n_A^Z$	nucleus	$\log n_A^Z$	
(1)	${}^{56}_{26}\mathrm{Fe}_{30}$	27.6	${}^{66}_{28}\mathrm{Ni}_{38}$	31.06	${}^{82}_{32}\mathrm{Ge}_{50}$	32.04	${}^{78}_{28}\mathrm{Ni}_{50}$	32.63	${}^{122}_{40}\mathrm{Zr}_{82}$	32.56	${}^{120}_{38}\mathrm{Sr}_{82}$	32.78	II-5
	${}^{56}_{26}\mathrm{Fe}$	27.72	${}^{66}_{28}\mathrm{Ni}$	30.90	${}^{82}_{32}\mathrm{Ge}$	32.10	${}^{80}_{30}\mathrm{Zn}$	32.38	${}^{80}_{28}\mathrm{Ni}_{52}$	32.71	${}^{120}_{38}\mathrm{Sr}$	32.78	II-9b
(2)	${}^{54}_{26}\mathrm{Fe}_{28}$	27.35	${}^{48}_{20}\mathrm{Ca}_{28}$	30.70	${}^{80}_{30}\mathrm{Zn}_{50}$	30.95	${}^{79}_{29}\mathrm{Cu}_{50}$	31.66	${}^{82}_{28}\mathrm{Ni}_{54}$	31.86	${}^{119}_{38}\mathrm{Sr}_{81}$	31.61	II-5
	${}^{52}_{24}\mathrm{Cr}$	27.37	${}^{64}_{28}\mathrm{Ni}$	30.51	${}^{78}_{30}\mathrm{Zn}_{50}$	30.58	${}^{78}_{28}\mathrm{Ni}$	32.22	${}^{82}_{28}\mathrm{Ni}$	32.26	${}^{122}\mathrm{Zr}$	32.22	II-9b
(3)	${}^{52}_{24}\mathrm{Cr}_{28}$	27.1	${}^{64}_{28}\mathrm{Ni}_{36}$	30.02	${}^{78}_{30}\mathrm{Zn}_{48}$	30.86	${}^{80}_{30}\mathrm{Zn}_{50}$	31.51	${}^{76}_{26}\mathrm{Fe}_{50}$	31.81	${}^{121}_{38}\mathrm{Sr}_{83}$	31.27	II-5
	${}^{54}_{26}\mathrm{Fe}$	26.78	${}^{48}_{20}\mathrm{Ca}$	30.31	${}^{81}_{31}\mathrm{Ga}$	30.40	${}^{79}_{29}\mathrm{Cu}$	31.91	${}^{76}_{26}\mathrm{Fe}$	32.24	${}^{119}_{38}\mathrm{Sr}$	31.85	II-9b
(4)	${}^{60}_{28}\mathrm{Ni}_{32}$	26.32	${}^{50}_{22}\mathrm{Ti}_{28}$	29.95	${}^{81}_{31}\mathrm{Ga}_{50}$	30.80	${}^{82}_{30}\mathrm{Zn}_{52}$	30.98	${}^{80}_{28}\mathrm{Ni}_{52}$	31.54	${}^{122}_{40}\mathrm{Zr}_{82}$	31.21	II-5
	${}^{60}_{28}\mathrm{Ni}$	26.72	${}^{54}\mathrm{Cr}$	30.26	${}^{80}_{32}\mathrm{Ge}$	30.28	${}^{82}\mathrm{Zn}$	31.15	${}^{81}_{28}\mathrm{Ni}$	32.06	${}^{121}_{39}\mathrm{Y}$	31.84	II-9b

TABLE 3 (cont'd)

E_F (Mev)	0.17		5		10		15		20		23		Section
	nucleus	$\log n_A^Z$	nucleus	$\log n_A^Z$	nucleus	$\log n_A^Z$	nucleus	$\log n_A^Z$	nucleus	$\log n_A^Z$	nucleus	$\log n_A^Z$	
(5)	${}_{24}\mathrm{Cr}_{26}^{50}$	26.11	${}_{26}\mathrm{Fe}^{60}$	29.92	${}_{32}\mathrm{Ge}_{51}^{83}$	30.25	${}_{28}\mathrm{Ni}_{48}^{76}$	30.81	${}_{40}\mathrm{Zr}_{81}^{121}$	31.35	${}_{39}\mathrm{Y}_{82}^{121}$	31.12	II-5
	${}_{27}\mathrm{Co}^{57}$	26.00	${}_{26}\mathrm{Fe}^{60}$	30.20	${}_{30}\mathrm{Zn}^{80}$	30.09	${}_{28}\mathrm{Ni}^{76}$	31.12	${}_{28}\mathrm{Ni}^{78}$	32.02	${}_{38}\mathrm{Sr}^{118}$	31.62	II-9b
(6)	${}_{25}\mathrm{Mn}_{28}^{53}$	26.06	${}_{24}\mathrm{Cr}_{32}^{56}$	29.58	${}_{30}\mathrm{Zn}_{49}^{79}$	29.78	${}_{30}\mathrm{Zn}_{51}^{81}$	30.61	${}_{42}\mathrm{Mo}_{82}^{124}$	31.32	${}_{37}\mathrm{Rb}_{82}^{119}$	30.92	II-5
	${}_{25}\mathrm{Mn}^{53}$	25.94	${}_{22}\mathrm{Ti}^{50}$	30.04	${}_{33}\mathrm{As}^{83}$	30.04	${}_{30}\mathrm{Zn}^{81}$	31.08	${}_{28}\mathrm{Ni}^{79}$	31.71	${}_{40}\mathrm{Zr}^{123}$	31.32	II-9b

when two adjacent peaks for different magic numbers are comparable. For instance, at $E_F = 20$ Mev, the peak nucleus is Zr^{122} at zero temperature, but as Figure 2 indicates the peaks near Zr and Ni are comparable in their heights and the more accurate calculation in Section II-9b reveals that the peak nucleus at 5 billion degrees (and 20 Mev) is Ni^{80} and not Zr^{122}, though the present calculation gives Zr^{122} as the peak nucleus even at 5 billion degrees (Table 3).

Similar calculations were tried at $E_F = 25$ and 30 Mev, but here, this method proved to be inapplicable. In this region, where neutrons are expected to dominate, it would probably be necessary to include the conditions imposed by beta reactions, which was omitted in the present method, but which is included in a more accurate method presented in Section II-9b.

Figure 3 demonstrates how the abundance curve changes in shape and how the peak position shifts in the Log n(A,Z)-A plane, with the increase of Fermi energy (that is, with the increase of density). The peak is near $A = 56$ and rather sharp when $E_F = 0.17$ Mev; it is very broad ranging from $A \sim 48$ to 88 when $E_F = 5$ Mev, but it is again well concentrated in a small range in A around 80 when $E_F = 10$ and 15 Mev. This corresponds to the $N = 50$ closed shell. With further increase in E_F, the abundance of nuclei at the $N = 82$ shell increases very quickly. At $E_F = 20$ Mev, the peak at the $N = 50$

shell and that at the N = 82 shell are comparable. When $E_F = 23$ Mev, the former (at the N = 50 shell) has already diminished to almost nothing and the latter (at the N = 82 shell) predominates, with Sn^{120} as the maximum nucleus.

In the simple approach in this section, other noticeable temperature effects were not prevalent, but the abundance curves plotted in this section were very useful when beta process contributors were selected in Section II-8. Further discussion will be deferred to Section II-9b, where the final abundance calculations were performed.

II-6 BETA REACTION RATES

The importance of the role played by beta processes in equilibrium abundances has already been emphasized. In dense matter such as expected near the surface of a neutron star a great deal of modification to terrestrial processes is necessary. The present section is devoted to that consideration. First, a brief review of the terrestrial processes is presented and then the modified formulae for the stellar rates will be derived.

a. Terrestrial Beta Processes

In an electron emission, a neutron in a nucleus is converted to a proton, and an electron and an antineutrino are emitted. The total energy change of the atom, E_{at}, or the energy available through this process, is shared by the electron and the neutrino. In a positron emission, a proton is converted to a neutron and a positron and a neutrino are emitted. The total energy change of the atom in this case is $E_{at} + 2mc^2$, where E_{at} now is the highest kinetic energy of the positron and mc^2 is the rest energy of the electron. The conversion of a proton in a nucleus to a neutron can take place by the capture of a bound electron of the atom instead of positron emission, especially when the energy change is less than $2mc^2$. (The most important of such processes is K capture where the electron in the innermost shell, the K shell, is captured.) These three are called beta reactions in general.

For the beta emission processes, the total energy is shared by the beta particle and the neutrino, and thus the energy of the beta particle is distributed continuously from the smallest possible value to the maximum energy, which is the total energy available for that process (neglecting neutrino mass). In these processes the beta particles and the neutrinos have to be treated relativistically. It is convenient to express energy by $W = (E/mc^2) + 1$ so that the energy will be distributed from 1 to $W_o = (E_o/mc^2) + 1$.

The transition probability depends on the phase space of the final state, the square of the transition matrix element $|M|^2$ and a term which takes into account the Coulomb forces exerted by the surrounding electron clouds on the emitted beta particle, denoted by F. The phase space of the final state is just the total number of possible neutrino states and of beta particle states and so is proportional to $P_e^2\, dP_e\, P_\nu^2\, dP_\nu$, where P is momentum and the subscripts e and ν denote electron and neutrino respectively. Noting that $P_\nu c = E_\nu = E_0 - E$, $\frac{P_e}{mc} = \sqrt{W^2 - 1}$, $W = E/mc^2 + 1$ (where E is β-particle energy), and that the final state phase space in the interval W to W + dW is proportional to

$$\sqrt{W^2 - 1}\, W\, (W_o - W)^2\, dW, \tag{2-17}$$

the probability P(W) of emission of a beta particle with energy W is

$$P(W)\, dW = g^2\, |M|^2\, F(Z,W) W (W^2-1)^{\frac{1}{2}} (W-W_o)^2 dW \tag{2-18}$$

where g depends only on the strength of the interaction.

The total transition rate is obtained by integrating (2-18), and can be expressed in the form

$$\lambda^{\pm} = \frac{\ln 2}{t^{\pm}} = g^2\, |M|^2\, f^{\pm}(Z,W_o) \tag{2-19}$$

where the Fermi function f was defined to be

$$f^{\pm}(Z,W_o) \equiv \int F^{\pm}(Z,W)\, (W^2-1)^{\frac{1}{2}} (W_o-W)^2 W\, dW \tag{2-20}$$

This applies to both positron emission (+ sign) and negatron emission (- sign). The difference in the expression for the two cases arises because the positron is accelerated through the Coulomb field of the surrounding electrons while the electron is decelerated. This difference leads to a different expression for F; thus we denote F for a positron by F^+ and that for an electron by F^-.

K capture is governed by the same nuclear matrix elements as beta decay; however, the transition probability for it depends on energy in a different way, due to the different phase volume and the electron eigenfunction. However, using an argument similar to that for the beta decays, we arrive at the same expression (2-19), provided the proper form is assigned to the Fermi function f. We denote this by f_K.

The function f generally depends only on the atomic number Z and the characteristic beta energy W_β (which is W_o in the beta emission processes and W_K, the atomic binding energy of the captured electron, in the capture process). This quantity combined with the half-life, (ft), called the comparative half-life, is extremely important. From the above equations, it is easy to show that $ft = \frac{\ln 2}{g^2|M|^2}$, and

$$\lambda = \frac{(\ln 2)f}{(ft)} \qquad (2\text{-}21)$$

That is, (ft) is a measure of the inverse square of the matrix element and the strength of the interaction. If the wave functions expressing the initial and final states are similar, the overlap is large and the matrix element is large, resulting in a small (ft) value. Since we use normalized wave functions, if the initial and final states are identical, the matrix element is 1 in an allowed transition. Since g is small, ft values are expected to be large. Thus, it is usual to use log ft.

We noted that the beta processes have to be treated relativistically. There are five types of expressions which are relativistically invariant, scalar, polar vector, tensor, axial vector and pseudoscalar interactions. These interactions give rise to different selection rules. The details which lead us to the selection rules are not shown here but the results are listed below:

Selection Rules

	Parity Change	Fermi	Gamow-Teller	log ft
Allowed	no	0	0, 1 $0 \not\rightarrow 0$	3 - 5
First forbidden	yes	0, 1 $0 \not\rightarrow 0$	0, 1, 2	6 - 8
Second forbidden	no	1, 2	2, 3 $0 \not\rightarrow 0$	9 - 11 .

This list proves useful later when the beta-process nuclei are selected for the abundance calculations. The Fermi selection rule corresponds to a scalar interaction where no spin flip occurs, while the Gamow-Teller rule includes the tensor interactions, where a spin flip can occur.

The distinction between the allowed and forbidden transitions will now be considered. The matrix element consists of the initial and the final wave functions which involve both the nuclear term and the electron-neutrino term. The electron-neutrino part can be approximated by plane waves. It turns out that the typical term, $\exp(-i\,\bar{P}\cdot\bar{r}/\hbar)$, of a plane wave for the electron-neutrino wave function is small compared with 1 so that this can be expanded in power series. In case the final and the initial nuclear states are not orthogonal and non-vanishing it is enough to include only the first term of the above expansion, which is 1. This case is called the allowed transition. If the matrix element in this case vanishes and if the inclusion of the second term of the expansion gives rise to a non-vanishing matrix element, the interaction is called first forbidden, and so on. The order of the forbidden transition is the number of the first term in this power series, starting with zero, which gives a non-vanishing matrix element.

From the above argument, the conclusion is that for any given degree of transition (allowed, first forbidden, etc.,) our problem boils down to the calculation of the Fermi function f, because once we know f the equation (2-21) gives us the transition rate λ. The analytic forms of f for beta emissions were obtained by Feenberg and Trigg,(38) and that for K capture by Major and Biedenharn.(39) Their results are quoted below. The Fermi function for positron emission f^+ and that for negatron emission f^- is given by $f^{\pm} = \langle R \rangle f_0^{\pm}$ where $\langle R \rangle$ is plotted as a function of W_0 in reference 33, and

$$f_0^{\pm} = U_1^{\pm} f_1 + U_2 f_2 + U_3 f_3$$

with $U_1^- = 2\pi\alpha Z / [1 - \exp(-2\pi\alpha Z)]$, where $\alpha \sim \frac{1}{137}$,

$$U_1^+ = -2\pi\alpha Z + U_1^-,$$

$$U_2 = -(U_1^-)^2 e^{-2\pi\alpha Z},$$

$$U_3 = -U_2 (2\pi\alpha Z - 3 + 2U_1^+), \qquad \text{(2-22a)}$$

and $f_1 = (W_0 - 1)^3 (W_0^2 + 3W_0 + 6)/30$,

$$f_2 = (W_0 - 1)^3 / 6,$$

$$f_3 = (W_0^2 - 1 - 2W_0 \ln W_0)/8.$$

The Fermi function for k capture f_k is

$$f_K \cong \tfrac{1}{2} \pi g_K^2 \; W_K^2 \qquad \text{(2-22b)}$$

where $\log_{10} g_K^2 = (7.9776-10) + 0.03256 Z - 10^{(0.48775-0.0380236Z)}$

where W_o is the maximum energy of the beta spectrum in mc^2 units including rest mass and W_K is the binding energy of k shell electrons in mc^2 units. The Fermi function for free electron capture in the absence of degeneracy f_c is given by(40)

$$f_c = 6 \times 10^{-3} \rho \, f_K / Z^2 \qquad \text{(2-22c)}$$

b. Beta Transition Rates in a Dense Stellar Interior

The temperature range we are interested in is above a billion degrees. At such a high temperature most of the atomic electrons in a stellar interior are ionized. In our density range of 10^6 gm/cm^3 < ρ < 10^{12} gm/cm^3, those electrons can be regarded as constituting a degenerate

Fermi gas. Therefore, we are now dealing with the beta stability of various kinds of nuclei in the Fermi sea of an electron gas.

Under such a circumstance the phase space available for electrons is reduced, which decreases the electron emission rate considerably because of the Pauli exclusion principle. The positron emission is hardly affected, except through a negligibly small electron screening effect. Due to the lack of the presence of bound electrons, the capture of orbital electrons is negligible, too. Therefore, the major process inverse to the electron emission is now not positron emission nor bound electron capture but the capture of continuum electrons. Therefore, our concentration will be focused on the derivation of the transition rates of the electron emission and continuum electron capture in the presence of electron degeneracy.

(i) Capture rates of continuum electrons –

In Section II-6a we saw that all the rates (electron emission, positron emission and electron capture) end up with the expression (2-21), provided a suitable meaning is attached to the Fermi function f. The essential difference imposed by degeneracy is due to the effect of the number density of the surrounding electrons on the rate of capture, which exist because of the fact that the rate of this reaction is proportional to the probability that a continuum electron is present at the nucleus where it is captured, which in turn is proportional to electron density. This effect is correctly taken care of by an additional factor $\{1 + \exp[(W-\mu)/\tau]\}^{-1}$ known as "the Fermi distribution function," in the expression for the transition probability. Then, following the same procedure as in Section II-6a, we get

$$\lambda = \int_{\text{over all energy}} g^2 \,|\,M\,|^2\, F(Z,W)(W^2-1)^{\frac{1}{2}} W_\nu^2 W dW \,\{1 + \exp[(W-\mu)/\tau]\}^{-1}$$

where $\tau \equiv kT/mc^2$, μ = chemical potential/mc^2, and W_ν = neutrino energy/mc^2. Thus, if we define the Fermi function for continuum electron capture by

$$f_c = \int_{W_o}^{\infty} (W^2-1)^{\frac{1}{2}}\, W W_\nu^2 F(Z,W)\, \{1 + \exp[(W-\mu)/\tau]\}^{-1} dW, \qquad (2\text{-}23)$$

we get the same expression for the rate as (2-21). That is,

$$\lambda = \ell n\, 2/t = (\ell n\, 2) f_c/(ft) \qquad (2\text{-}24)$$

This is a powerful expression, since ft depends on $|\,M\,|^2$ only, which is fixed for a given set of initial and final states, independent of the mode of transition. As the Fermi energy E_F of the surrounding electrons increases, the terrestrially stable elements and even the terrestrial electron emitter will become unstable against continuum electron capture when E_F exceeds the electron decay energy. Thus the element which decays by electron emission terrestrially, as well as those which decay by positron emission and bound electron capture terrestrially, can now decay by capture of continuum electrons. However, whatever the terrestrial origin may be, the nuclear species we are dealing with before and after the transition does not change. Therefore, by having information on the properties of the nuclei before and after the corresponding terrestrial transition (the values of W_β, Z, spin change, and parity change), which enables us to estimate the ft value, we can calculate the stellar rate of transition by equations (2-23) and (2-24). In the capture process of continuum electrons,

$$e_c^- + (A,Z) \rightarrow (A,Z-1) + \nu, \qquad (2\text{-}25)$$

the neutrino energy $W_\nu = W_0 + W$, and f_c reduces to

$$f_c = \int_{W_0}^{\infty} (W^2-1)^{\frac{1}{2}} W (W_0 + W)^2 F (1 + \exp[(W-\mu)/\tau])^{-1} dW . \qquad (2\text{-}23')$$

A more rigorous derivation may be found in reference 41.

(ii) Electron emission rate in a dense plasma –

The effect of the exclusion principle in a dense plasma on the β^- decay probability occurs due to the fact that the number of final states per unit energy interval $P(W)$ is reduced because of the electron phase space already occupied, which is a function of the Fermi-Dirac distribution function $\{1 + \exp[(W-\mu)/\tau]\}^{-1}$. The number of electron momentum states between P_e and $P_e + dP_e$ already occupied is

$$\propto \left(\frac{4\pi^2 P_e^2 \, dP_e}{\hbar^3}\right)\left(\frac{1}{1+\exp[(W-\mu)/\tau]}\right)$$

which has to be subtracted from the whole electron momentum space.

Therefore, the modified expression for P(W) dW is now

$$P(W)\,dW = g^2 |M|^2 F(Z,W)\, W (W^2-1)^{1/2} (W-W_0)^2 \times \left[1 - \frac{1}{1+\exp[(W-\mu)/\tau]}\right] dW \tag{2-26}$$

and substituting this into the expression for the total transition rate, we obtain

$$\lambda = \frac{\ln 2}{(f_s^- t)} \, f_s^- \tag{2-27a}$$

with

$$f_s^- = \int_1^{W_0} F (W_0-W)^2 \sqrt{W^2-1}\; W \times \left\{1 - [1+\exp((W-\mu)/\tau)]^{-1}\right\} dW \tag{2-27b}$$

or

$$f_s^- = f^0 \left(1 - \frac{\Delta}{f^0}\right) \tag{2-27c}$$

where for convenience the following notation was used:

$$f^0 \equiv \int_1^{W_0} F (W_0-W)^2 \sqrt{W^2-1}\; W \, dW = \text{terrestrial Fermi-function} \tag{2-28}$$

$$\Delta \equiv \int_1^{W_0} F (W_0-W)^2 \sqrt{W^2-1}\; W \{1+\exp[(W-\mu)/\tau]\}^{-1} dW \tag{2-29}$$

μ = chemical potential/mc^2

The above applies to electron emission. We note that when $f^0 \leqq \Delta$ no transition occurs. A more rigorous derivation may be found in reference 41.

(iii) Modified Fermi function for the degeneracy limit -

W_o in (2-23') is the energy available through the transition of the nucleus (A,Z) to (A,Z-1). Therefore if $W_o \geq -1$, this process is exoergic, that is, even with no electron energy it will take place. Such processes correspond to the elements which exhibit terrestrial positron emission or bound electron capture. In this case, the lower limit of integration in (2-23) is 1. If $W_o < -1$, the capture process is endoergic, that is, the electron energy must be greater than W_o for capture to take place and the lower limit of integration is W_o.

In the degenerate limit, the exponential term in the Fermi-Dirac distribution function is much less than 1 and $\Big[1 + \exp\Big((W - \mu)/\tau\Big)\Big] \cong 1$. Therefore, (2-23') reduces to the integration

$$f_{cp} = \int_{\text{or } \left\{\begin{matrix} W_o & \text{endoergic} \\ 1 & \text{exoergic} \end{matrix}\right.}^{W_F} W \sqrt{W^2 - 1}\ (W + W_o)^2\, F dW$$

(where $W_F = E_F/mc^2 + 1$)

where now the Coulomb factor F can be simplified by approximation

$F = 2\pi\alpha Z \quad \text{if} \quad 2\pi\alpha Z > 1$

given in reference 38.

$F = 1 \quad \text{if} \quad 2\pi\alpha Z < 1$

For the electron emission, if we set $\Big\{(1 + \exp\big[(W-\mu)/\tau)\big]\Big\} = 1$, then $f^o = \Delta$, which corresponds to no transition. Therefore, the second term in (2-26) was expanded and only terms up to the second term were retained. Then, exp $[(W-\mu/\tau)]$ becomes the leading term. The same approximation for the Coulomb factor was applied to the electron emission formula. The results are summarized below:

(A) $2\pi\alpha Z > 1$ $(Z > 23)$

(1) Capture of free e^-

$$f_{CD} = \frac{2\pi\alpha Z}{5}\left[W_F^5 + \frac{3}{2}W_0W_F^4 + \frac{5}{3}W_0^2W_F^3 - \left(1 + \frac{5}{2}W_0 + \frac{5}{3}W_0\right)\right] \quad (W_0 > -1) \quad \text{or}$$

$$f_{CD} = \frac{2\pi\alpha Z}{5}\left[(W_F - |W_0|)^5 + \frac{1}{2}|W_0|(W_F - |W_0|)^4 + \frac{1}{3}|W_0|^2(W_F - |W_0|)^3\right] \quad (W_0 < -1) \tag{2-30}$$

(2) e^- emission

$f_D^- = f^0\left(1 - \frac{\Delta}{f^0}\right)$ with

$$\Delta/f^0 = D_1(W_F, W_0)/D_1(W_0, W_0) \text{ where } D_1 \text{ was defined by} \tag{2-31}$$

$$D_1(x, y) = x^5 - \frac{5}{2}yx^4 + \frac{5}{3}y^2x^3 - \left(1 - \frac{5}{2}y + \frac{5}{3}y^2\right)$$

(B) $2\pi\alpha Z < 1$ $(Z < 23)$

(1) e^- capture

$$f_{CD} = \frac{P_F^5}{5} + \frac{P_F^3}{3}(1 + W_0^2) + \frac{W_0}{4}\left[2P_FW_F^3 - P_FW_F - \ln(P_F + W_F)\right] \text{ -----(if } W_0 > -1) \text{ or} \tag{2-32}$$

$$f_{CD} = \frac{1}{5}\left[(W_F - |W_0|)^5 + \frac{|W_0|}{2}(W_F - |W_0|)^4 + \frac{1}{3}|W_0|^2(W_F - |W_0|)^3\right] \text{ ----(if } W_0 < -1)$$

(2) e^- emission

$$f_p^- = f^0 \left(1 - \frac{\Delta}{f^0}\right)$$

$$\frac{\Delta}{f^0} = D_2(P_F, W_0)/D_2(P_0, W_0) \quad \text{with} \tag{2-33}$$

$$D_2(x, y) = x^5/5 + (y^2+1)x^3/3 - \frac{y}{4}\left\{2x(1+x^2)^{3/2} - x(x^2+1)^{1/2} - x \ln\left[x + (1+x^2)^{1/2}\right]\right\}$$

where $\frac{P_F}{mc} = (W_F^2 - 1)^{\frac{1}{2}}$, $\alpha \sim 1/137$,

f^0 = terrestrial e^- emission Fermi function.

c. Discussion of the Results

The modified Fermi functions f_{cp} for continuum capture and f_p^- for the electron emission were calculated by the use of formulae derived above, for

E_F(Mev)	0	5	10	15	20		23
Z	26	28	32	28	28	40	38

The corresponding atomic number Z was selected from the result of Section II-5, namely, the element of maximum abundance as found there was used. Two values Z = 28 and 40 were used for E_F = 20 Mev because there were two peaks of comparable height at this Fermi energy. The abundance distribution for $E_F \gtrsim$ 25 Mev could not be calculated by the simple method of Section II-5, but the general behavior indicated that already at 25 Mev the free neutrons would dominate. Therefore, we expect the elements contributing to beta processes to be some of the lightest neutron rich elements. He^7 is already unstable against neutron emission and so Helium of maximum neutron number is He^6. H^4 is unstable against neutron emission and thus the most probable contributor to the beta process from hydrogen isotopes seems to be H^3. We expect also that some heavy elements near the peak in the zero temperature abundance distribution which are stable against neutron emission will be present. Such elements were already obtained in Section II-3, namely Z = 36 for 25 Mev and Z = 32 for 30 Mev. Therefore, for those highest two values of E_F, the following Z's were selected.

E_F (Mev)	25	30
Z	0, 1, 2, 36	0, 1, 2, 32

The Fermi functions f for all cases were calculated as a function of W_o for the selected families of values of Z and E_F as shown above. Besides these, f for zero Fermi energy was calculated by the use of equations presented in (2-22a) through (2-22c). In evaluating f^o appearing in the expression for stellar electron emission rate, the f values in (2-22a) were used. In the derivation of the capture rate in (2-30) and (2-32), the approximation was made separately for the cases $W_o > -1$ and $W_o < -1$.

In Figure 4, the result for $E_F = 20$ Mev and $Z = 20$ is shown, where f was plotted as a function of absolute value of $W_0 = (E_0/mc^2) + 1$. The portions of the curve denoted by (1) and (3) were obtained by the first of the equations (2-30)

which is exactly valid for exoergic capture but breaks down for endoergic capture with the threshold energy appreciably greater than the rest mass. The portion marked (2) was obtained from the second of the equations (2-30)

Both approximations deviate appreciably in the intermediate region $25 \lesssim |W_0| \lesssim 38$. Therefore, in this region the two curves were smoothly interpolated by hand. The graph shows that when the threshold energy exceeds the Fermi energy, the element in question disintegrates by negatron emission, while when $W_0 < W_F$, electron capture takes place. The regions (2) and (1) correspond to the case in which the element under the terrestrial condition (zero electron Fermi energy) disintegrates by electron emission but becomes unstable against continuum electron capture in the electron gas of Fermi energy 20 Mev. The region marked (3) corresponds to the electron capture whose terrestrial counter-part disintegrates either by positron emission or by bound electron capture.

The over-all effect of density on electron capture is shown in Figure 5 and that on electron emission in Figure 6, in each of which the corresponding modified Fermi function f was plotted against the absolute

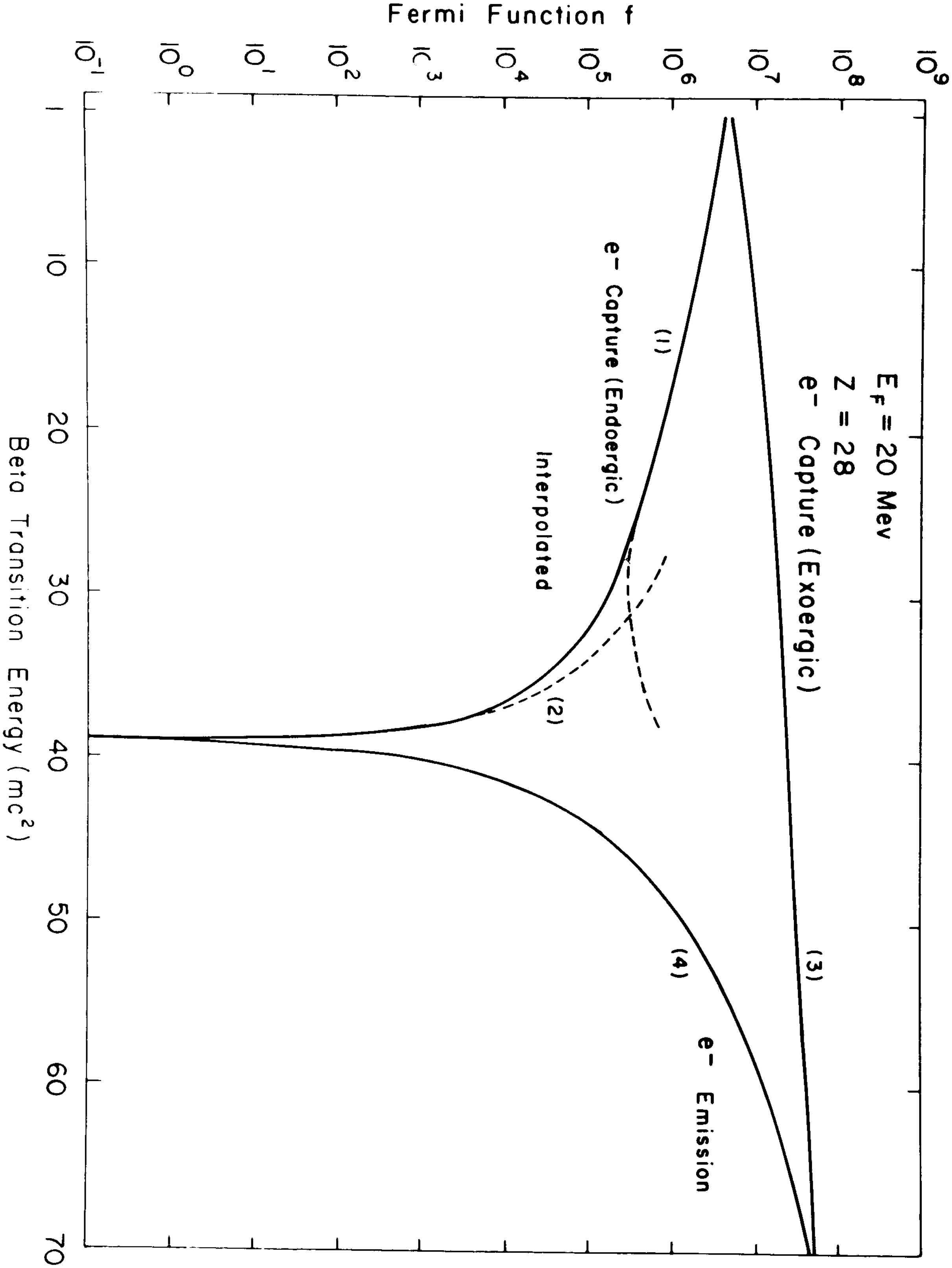
Fermi Function f
10^{-1}
10^{0}
10^{1}
10^{2}
10^{3}
10^{4}
10^{5}
10^{6}
10^{7}
10^{8}
10^{9}
E_F = 20 Mev
Z = 28
e^- Capture (Exoergic)
(3)
e^- Capture (Endoergic)
(1)
Interpolated
(2)
(4)
e^- Emission
1
10
20
30
40
50
60
70
Beta Transition Energy (mc^2)

Figure 4

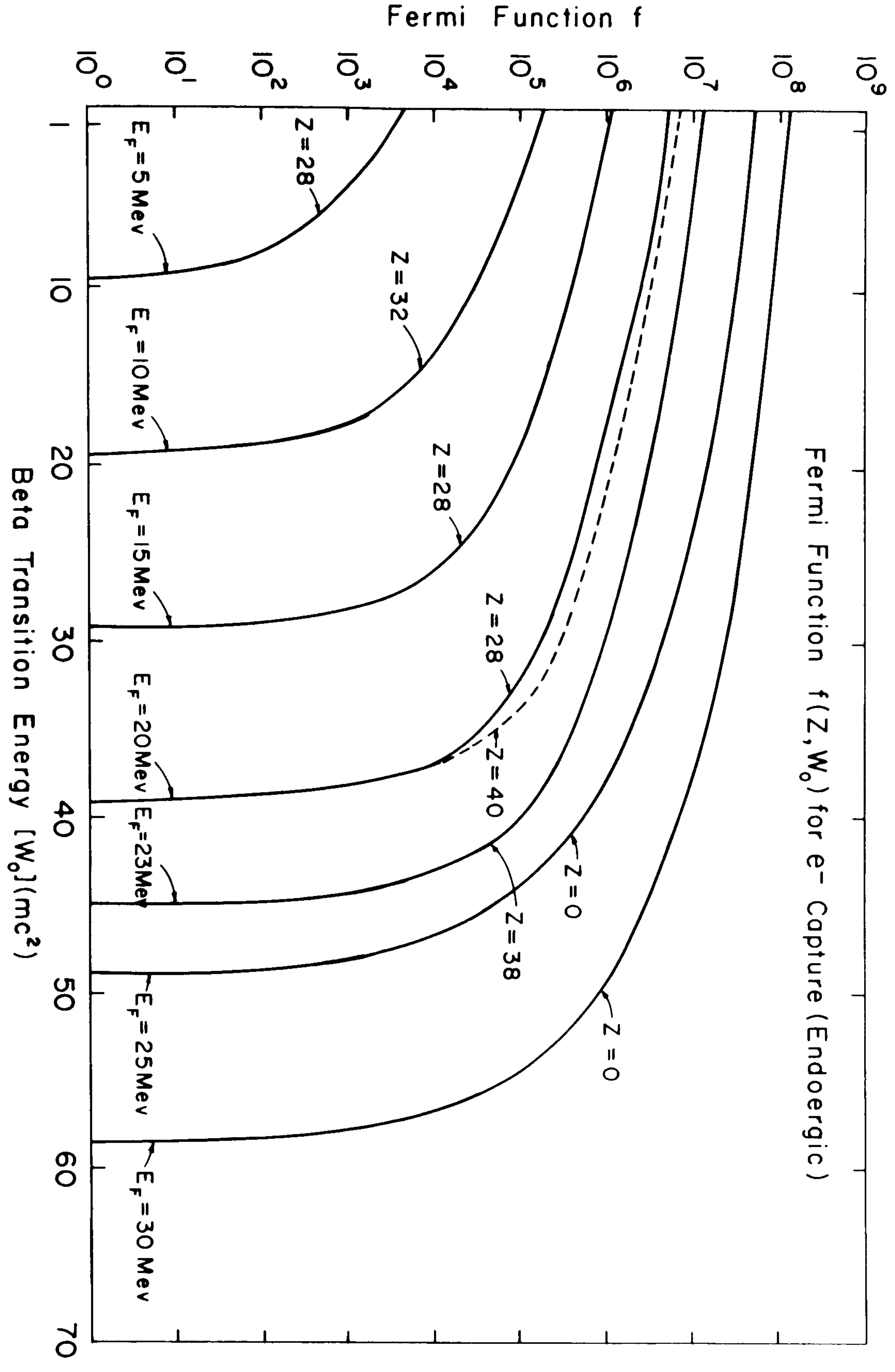
Fermi Function f(Z,W$_0$) for e⁻ Capture (Endoergic)
Fermi Function f
10^0
10^1
10^2
10^3
10^4
10^5
10^6
10^7
10^8
10^9
1
10
20
30
40
50
60
70
Beta Transition Energy [W$_0$](mc^2)
Z = 28
E$_F$ = 5 Mev
Z = 32
E$_F$ = 10 Mev
Z = 28
E$_F$ = 15 Mev
Z = 28
Z = 40
E$_F$ = 20 Mev
E$_F$ = 23 Mev
Z = 0
Z = 38
Z = 0
E$_F$ = 25 Mev
E$_F$ = 30 Mev

Figure 5

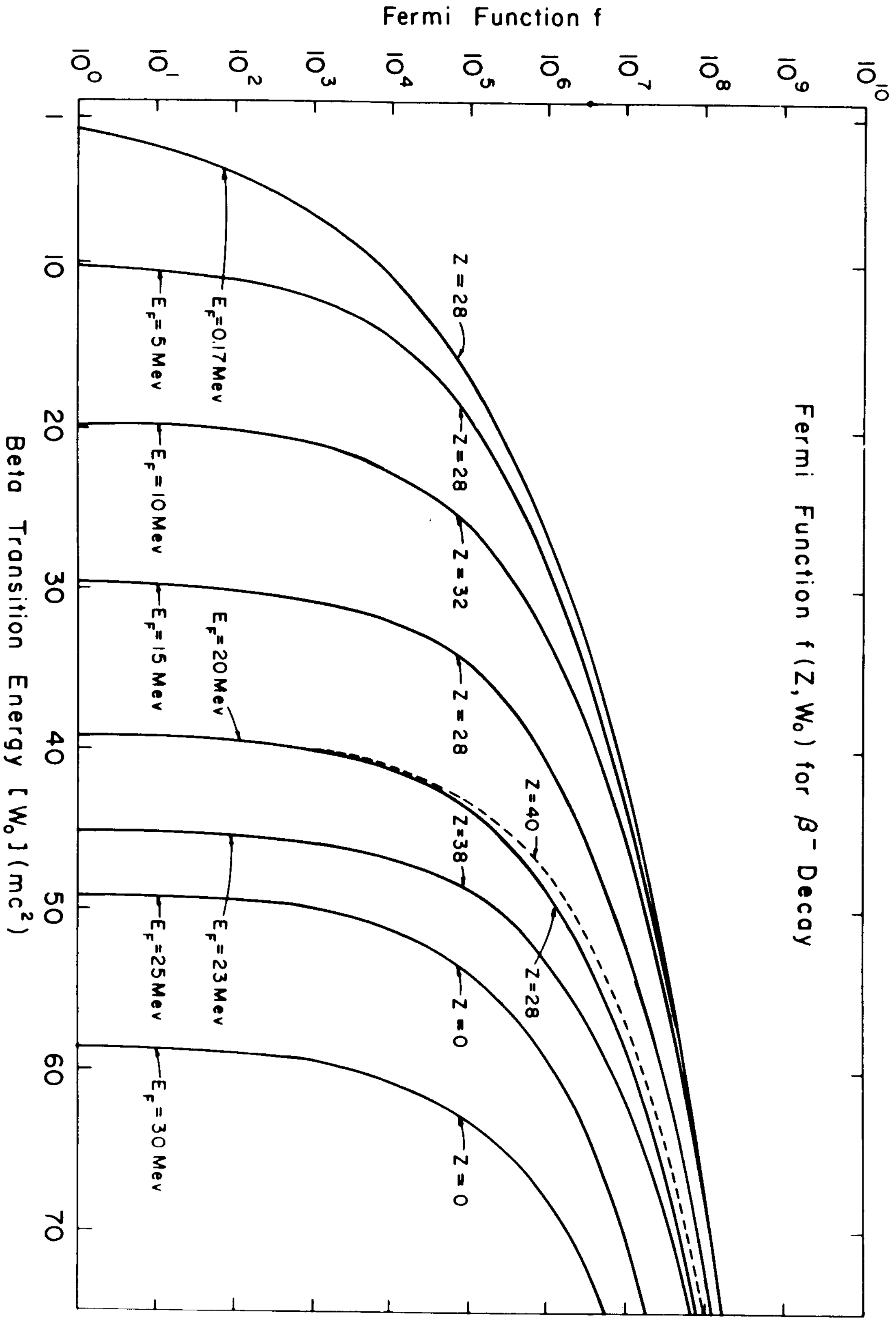
Fermi Function f
10^0
10^1
10^2
10^3
10^4
10^5
10^6
10^7
10^8
10^9
10^{10}
Fermi Function f(Z, W_0) for β^- Decay
Beta Transition Energy [W_0] (mc^2)
1
10
20
30
40
50
60
70
Z = 28
E_F=0.17 Mev
E_F = 5 Mev
Z = 28
E_F = 10 Mev
Z = 32
E_F = 15 Mev
Z = 28
E_F = 20 Mev
Z = 40
Z = 38
Z = 28
E_F = 23 Mev
E_F = 25 Mev
Z = 0
E_F = 30 Mev
Z = 0

Figure 6

value of the threshold energy of the beta transition of the corresponding mode (including rest mass) in units of mc^2, for a family of E_F values. For $E_F = 20$, the effect of Z on the Fermi function is also shown. Clearly, the e^- emission rate is greatly decreased with the increase of E_F, and hence of density, while the e^- capture rate increases rapidly with rise in E_F. For the same E_F, the rate is shown to be somewhat less for smaller values of Z.

II-7 PHOTO-BETA RATES

The temperatures being considered here are high enough for the contribution of the nuclear excited states to the beta process to be important. Since most of the excitations are due to photons, such beta reactions involving the excited levels are called "photo-beta processes."(40) The over-all rate including the excited states can be expressed as

$$P_\beta = \sum_i a_i \lambda_i = \sum_i a_i \frac{\ln 2}{(ft)_i} f_i \qquad (2\text{-}34)$$

where

$$a_i = \frac{(2J_i + 1)}{\omega(T)} \exp(-E_i/kT) \qquad (2\text{-}35)$$

is the fractional population of the excited state i. The notation used is

$$\omega(T) = \sum_j (2J_j + 1)\ \exp.(-E_j/kT) = \text{Partition function} \qquad (2\text{-}35a)$$

J_i = the spin of the energy state i

E_i = the energy of the state i

T = temperature

To get the total number of beta processes per unit time required for the abundance calculation as described in Section II-4, the above expression has to be multiplied by the abundance of the nucleus in question, and summed over all the nuclei which will contribute appreciably to the total rate, as seen in the equation (2-12). If the ground state is already undergoing a fast transition, the contribution of the excited states will enter only as a perturbation, but if some decay from the excited states is allowed, while decay from the ground state is forbidden in a higher degree, the rate of transition will be greatly accelerated by the inclusion of the excited states for a sufficiently high temperature.

II-8 SELECTION OF BETA-REACTION NUCLEI

In the final abundance calculation we must include the condition imposed on beta processes (2-12)

$$\sum_i P_-(A_i, Z_i)\, n(A_i, Z_i) = \sum_k P_+(A_k, Z_k)\, n(A_k, Z_k) \qquad (2\text{-}12)$$

where the $P_{\pm}$'s are evaluated through equations (2-34) and (2-35). The summation in each side of (2-12) is over all the nuclei contributing appreciably to electron emission and its inverse process. Each side of the equation depends on the abundance of each nucleus; thus, the first criterion for determining the contributor is that its abundance $n(A,Z)$ is large enough. This is known from the work in Section II-3 and II-5. In the first sorting process, the following method was adopted, in the abundance curves obtained in II-5 (Figure 3) if the peak was broad and flat, as in the $E_F = 5$ Mev case, the nuclei with abundance $n(A_i, Z_i) \gtrsim 10^{-4} n(A_m, Z_m)$ were included, while if it was as sharp as in the case of $E_F = 10$ and 15 Mev, an abundance even as low as $n(A_i, Z_i) \cong 10^{-6} n(A_m, Z_m)$ was included where $n(A_m, Z_m)$ is the maximum abundance at the peak. The nuclei with lower abundances than the above limits were not included at all, except in unusual cases.

The nuclei selected in this manner are further restricted by selection rules discussed in Section II-6, through the ft value in the denominator in (2-34). Rough values of ft can be determined through the assignment of spin and parity of a parent and the daughter nucleus for each beta reaction concerned. It is hopeless to do so individually for all the excited states and for that purpose a statistical approach was used as explained later, but for the ground states and the first few excited states such assignment is possible by the help of (i) the shell model, and (ii) empirical data such as given in reference 42.

(i) The shell model -

Here I am not going to discuss the shell model itself (since there are a number of excellent review articles, like reference 43, 44, etc., but merely to list some of the rules deduced from the shell model which were used in my selection of the nuclei.

(a) The ground states of all nuclei with an even number of protons Z and neutrons N have spin $J = 0$ and even parity, 0^+.

(b) In a nucleus, if Z is odd and N is even, the ground state properties are determined by the protons alone and similarly for the opposite case, i.e., for N odd and Z even, the neutrons determine the properties of the nucleus.

(c) In a nucleus of odd A, the nucleons of odd number couple their spins in such a way that the total spin is that of the last unpaired one.

The above rules plus the level diagram of the shell model such as Figure IV 3 of reference 43 are sufficient for determining most of the spin-parity values of the ground states and the lowest excited states of odd A nuclei. For N or Z higher than 50 the exact configuration predicted by the shell model and verified by experiment differs for N odd nuclei and Z odd nuclei but all such cases are covered in the Table VI-1 in reference 43, which I used for the selection of most of the odd A nuclei.

For even A nuclei, the following rules were employed:

(d) For even-even nuclei, the ground states have $J = 0^+$ with almost no exceptions.

(e) For the first excited states of even-even nuclei one-third of the cases have $J = 2^+$, for another third in lighter nuclei, the assignment is $J = 4^+$.

(f) The states of even spin, in general, have even parity and of odd spin, odd parity, for even-even nuclei. The level order most generally followed is $0^+, 2^+, 4^+, 6^+$.

(g) For odd-odd nuclei, Nordheim's weak rule states, if both the odd proton and the odd neutron are in levels in which the intrinsic spin s and the orbital angular momentum ℓ are parallel, that is, if $j_n = \ell_n + \frac{1}{2}$ and $j_p = \ell_p + \frac{1}{2}$, or both are anti-parallel, $j_n = \ell_n - \frac{1}{2}$ and $j_p = \ell_p - \frac{1}{2}$, j_n and j_p tend to add, although not to the highest possible value. Nordheim's strong rule states: if one kind of nucleon is in a level where ℓ and s are anti-parallel, while the other kind is in a level with parallel ℓ and s, that is if $j_n = \ell_n + \frac{1}{2}$ and $j_p = \ell_p - \frac{1}{2}$, or $j_n = \ell_n - \frac{1}{2}$ and $j_p = \ell_p + \frac{1}{2}$, the total angular momentum $J = | j_n - j_p |$.

(h) For odd-odd nuclei, one proton of j and one neutron-hole of j in the same level couple to give a total angular momentum $J = 2j - 1$, that is 1 unit less than the maximum addition.

These rules in general are more applicable for heavier elements because of the dominance of j-j coupling, and from our previous results, the elements we are most interested in for $E_F \lesssim 23$ Mev are heavier than iron. There are other regularities discussed in references 43 and 44 and all were used to the fullest extent.

In this way, for all the nuclei sorted by the first procedure and their corresponding daughter nuclei in both electron emission and its inverse process, that is, for (A,Z), (A,Z + 1) and (A, Z-1), spin and parity were assigned. Whenever empirical data were available (up to some neutron-rich nuclei at 5 Mev), the empirical results were used. If the spin and parity change between the parent and the daughter corresponds to a transition forbidden by a degree higher than the third (log ft > 20), such a transition was discarded without exception. After studying a number of empirical data, the selection rules discussed roughly in Section II-6 were further subdivided into the following empirical criteria:

Degree of transition	Allowed		1st Forbidden					2nd		3rd		4th
Spin change ΔJ	0	1	0	1	1	1	2	2	3	3	4	4, 5
Parity change $\Delta \pi$	no	no	yes	yes	yes	yes	yes	no	no	yes	yes	no
log ft	3~5	4~6	6.5~7	6.5~7	7~7.5	8.5~9	8~9	10	12	15	20	average 23
Comment				$p \rightleftarrows d$	$d \rightleftarrows f \rightleftarrows g$	$h \rightleftarrows g$				average 17		

p, d, f, g, h correspond to orbital angular momentum $\ell = 1, 2, 3, 4, 5$.

Generally, an nth forbidden transition has $\Delta J = n, n + 1$ and $\Delta \pi = (-1)^n$.

The third forbidden transition was not discarded only when the abundance of the nuclei involved was unusually high and when the spin assignment was not too accurate because of Nordheim's weak rule on odd-odd nuclei. For instance, in the transition (80, 31) to (80,30) for $E_F = 15$ Mev, the shell model predicts spin-parity assignment of p 3/2 for odd Z of 31 and g9/2 for odd N of 49, and according to Nordheim's weak rule the maximum spin of the parent is 6 and parity is - . The ground state of the daughter is 0^+, and the transition to the ground state was discarded. However, the first excited state of the daughter can be 2^+, and the parent spin could be a value less than 6, and in that case this transition to the first excited state can very likely be a 2nd or 3rd forbidden transition. In such a case, the third transition was not necessarily discarded, especially if the abundance was large. Whenever there was an ambiguity in the assignment (due to lack of information on excited states, uncertainty due to Nordheim's weak rule for odd-odd nuclei, etc.), the highest possible value was assigned to log ft so that the ambiguous nucleus will not overrule the nuclei whose assignments are clearer (like most of the ground states of odd A nuclei).

For the nuclei which survived the two sorting processes just described, log ft was predicted through the spin-parity assignment for the parent and the daughter nuclei, beta decay energy was obtained from the table made in Section II-2, and from that, log f was calculated using the equations in Section II-6, and $P_{\pm}$ was calculated by equations (2-34) and (2-35); then, these values together with the logarithms of product $P_{\pm}n(A,Z)$ were tabulated. The last entry, $P_{\pm}\, n(A,Z)$ is a measure of the importance of the element (A, Z). Therefore, all the nuclei whose $P_{\pm}\, n(A,Z)$ turned out to be less than 10^{-8} times the maximum were discarded. In this way about 15 to 20 nuclei for the beta process and about the same number for the inverse process were left as the final candidates. This was repeated for each value of Fermi energy E_F. The result for $E_F = 10$ Mev is shown in Tables 4a and 4b.

The comparison of the assignments made through the shell model with the experimental data shows almost perfect agreement for ground states of odd A nuclei. In the assignment of the lowest few excited states of all nuclei and the ground states of even A nuclei (especially of odd-odd nuclei), where the uncertainty of prediction through the shell model is expected to be large, much effort was concentrated on the deduction from empirical data so that the final assignment of these values (some of which are listed in Tables 4a and 4b) would not be too far from reality.

For instance, let us focus our attention on the element (79, 29) in Table 4a. p3/2- for the ground state of the parent is clear from the shell model. The spin and parity of the daughter (79,30) are determined

TABLE 4a

β^- decay nuclei at $E_F = 10$ Mev. Notations: (i) $*i$ denotes the ith excited state, (ii) "?" means the assignment is ambiguous due to Nordheim's weak rule, etc., (iii) "1st" means the first forbidden process, "a" means the allowed transition, etc., (iv) the symbol such as "2^-" in the 5th column means the transition involves spin change of 2 and parity change, while the symbol such as "1^+" means spin change of 1 and no parity change, etc., (v) E_β is the beta transition energy in Mev, (vi) $P_{\pm}$ n(A,Z) in the last column gives the measure of the importance of the element (A,Z) as the contributor to beta process.

	Parent		spin and Parity assignment		degree of forbiddenness	log ft	E_β	log f	log n(A, Z)	log $\left(\frac{n(A,Z)P}{\ln 2}\right)$
	A	Z	Parent	daughter						
	73	28	$\frac{7}{2}^{+}$?	$P3/2^-$	2^- 1st	8.5	10.34	2.23	27.8	21.5
	75	28	$g9/2^+$	$(f\frac{5}{2}^-)^{*2}$	2^- 1st	9	10.95	3.33	27.1	21.43
	77	29	$P3/2^-$	$(7/2^+)^{*1}$	2^- 1st	9	10.28	2.2	28.8	22.0
	77	29	$P3/2^-$	$(\frac{1}{2}^-)^{*2}$	1^+ a	6	10.24	1.9	28.8	24.7
	79	29	$P3/2^-$	$(\frac{1}{2}^-)^{*1}$	1^+ a	6	10.5	2.8	27.8	24.6
Max →	81	30	$d5/2^+$	$P3/2^-$	1^- 1st	6.5	12.90	4.9	28.06	26.46
	82	31	4^- or $3^-_?$	$(2^+)^{*1}$	$2^-_?$ 1st	9	12.00	4.3	28.45	23.75
	83	31	$P3/2^-$	$d5/2^+$	1^- 1st	6.5	13.00	4.92	27.35	26.17
	85	32	$d5/2^+$	$P3/2^-$	1^- 1st	6.5	10.96	3.6	27.52	24.62
	84	33	4^- or $3^-_?$	$(2^+)^*_?$	$1^-_?$ 1st	8.5	10.2	0.2	28.3	20.0
	85	33	$P3/2^-$	$d5/2^+$	1^- 1st	6.5	10.15	1.7	28.38	23.58
	86	33	4^- or $3^-_?$	$(2^+)^{*1}_?$	$1^-_?$ 1st	8.5	11.5	4	26.7	21.7
	87	33	$P3/2^-$	$d5/2^+$	1^- 1st	6.5	12.10	4.44	25.9	23.04
	89	34	$d5/2^+$	$P3/2^-$	1^- 1st	6.5	10.52	2.9	25.2	21.6

TABLE 4b

e^- capture nuclei at $E_F = 10$ Mev, with the same notation as that introduced in Table 4a.

Parent		Spin and Parity assignment		degree of for-biddenness	log ft	E_0 (Mev)	log f	log n(A,Z)	$\log\left(\frac{n(A,Z)P_+}{\ln 2}\right)$
A	Z	Parent	Daughter						
75	30	$7/2^{+}_{?}$	$(5/2^-)^{*2}$	$1^{-}_{?}$ 1st	7.5	9.7	1.5	27.44	21.44
77	31	$P3/2^-$	$(7/2^+)^{*1}$	2^- 1st	8.5	8.47	3.38	27.28	22.16
77	31	$P3/2^-$	$(1/2^-)^{*2}$	1^+ a	6	8.67	3.25	27.28	24.53
79	31	$P3/2^-$	$(1/2^-)^{*1}$	1^+ a	6	9.43	-3	29.54	20.54
80	31	6^- or $5^{-}_{?}$	$(2^+)^{*1}$	2^- 1st	8.5	10.07	0	29.06	20.56
79	32	$g9/2^+$	$(9/2^+)^{*1}_{?}$	0^+ a	8	8.4	3.4	26.8	22.2
81	32	$g9/2^+$	$P3/2^-$	3^- 3rd	15	9.09	2.8	29.71	17.51
81	33	$P3/2^-$	$(1/2^-)^{*1}$	1^+ a	6	7	3.9	26.2	24.1
→ 83	33	$P3/2^-$	$d\,5/2^+$	1^- 1st	6.5	9.44	2.2	29.54	25.24
84	33	4^- or 2^-	$(2^+)^{*1}$	$2^{-}_{?}$ 1st	9	9.726	2.3	28.3	21.6
83	34	$g9/2^+$	$(9/2^+)^{*1}_{?}$	1^+ a	7	7	3.9	25.8	22.7
85	35	$P3/2^-$	$g5/2^+$	1^- 1st	7	6.74	4.04	25.14	22.18
87	35	$P3/2^-$	$d5/2^+$	1^- 1st	6.5	8.28	3.42	25.28	22.2
88	35	4^- or $3^{-}_{?}$	$(2^+)^{*1}$	2^- 1st	8.5	8.8	3	25.32	20.32

by the unpaired last neutron, the 49th one. For neutron numbers from 39 to 49, the last neutron has the assignment p1/2 or g9/2, and its levels are expected to be spaced close together. Therefore, if the ground state is g9/2, it is very likely that the first excited state is 1/2 – . For N = 49, the assignment given in Table VI-1 in reference 43 through the shell model is g9/2, therefore, we expect p1/2 for the first excited state. This prediction was checked in the following way: all odd A nuclei with N = 49 listed in reference 42 were picked up. These are $_{42}Mo^{91}$, $_{40}Zr^{89}$, $_{38}Sr^{87}$, $_{36}Kr^{85}$ and $_{34}Se^{83}$. All of them have spin-parity of 9/2 +for the ground state and of 1/2 – for the first excited state without exception. Therefore, assignment of 1/2 – to the first excited state of the daughter of this transition, (79, 30), is quite justifiable.

To predict the spacing between the lowest excited state and the ground state, general deduction from empirical data was again used. The spacing is generally large at closed shells, sometimes of the order of a few Mev, and it goes down to the order of a few hundred kev in the intermediate region. Most of the elements concerned in this research are near magic numbers, due to the fact that the abundance peaks concentrate at magic numbers, most of them at 28,50 and 32. Our cases were solved, therefore, by investigating the general behavior of the level spacing of the first few excited states mostly in these regions. Some of the empirical properties deduced are:

N	50	50	48	52	54
Z	28	30	30	30	30
(Mev) E_1	2	1.8	1	1	0.8

all in the 2 +state, where E_1 is the 1st excited level above the ground state in Mev.

In effect, we can summarize what was done to select the beta nuclei as follows: nuclei whose abundance is too small were simply discarded; some of the lowest excited states were included only in case the ground state spin and parity assignment prohibited the beta process in too high a degree to give any appreciable contribution to the total rate and when the spin and parity assignment to some of the low excited states predicted a much less forbidden beta process with a fair amount of certainty. If both the ground and the low excited states showed too high a degree of forbiddenness or whenever the spin and parity assignment were too ambiguous, such nucleus was simply discarded.

I believe the treatment of the problem in the way described above is more extensive than necessary, because, actually, only a few key nuclei govern the final beta process. If we do not include higher excited states in balancing both sides of the equation (2-12) imposed on beta transitions, we should, perhaps, include more than ten elements on each side, but when we include all the excited states as was done in the final abundance calculations (II-9b), it was found, after investigation, that it is only the maximum nucleus and its daughter nucleus in both directions of decay, thus a total of four nuclei, which really govern the total process. Out of about 30 nuclei selected here for each E_F, therefore, only about 4 remained in the final calculation. However, because of the importance of those key nuclei, I believe it is worthwhile to start from about 50 nuclei and apply careful sorting procedures as was done here.

II-9 EQUILIBRIUM ABUNDANCE CALCULATIONS

a. A Sample Calculation

A sample calculation was made including all the nuclei just selected in the previous section, II-8, but without the inclusion of excited states higher than those considered there, at $E_F = 15$ Mev and $T = 5 \times 10^{9}$ °K. The computer was instructed to continue computation until n_p and n_n were adjusted such that the total number of electrons emitted per unit time was equal to that of the electrons captured per unit time to within 0.1%. The result is

$$n_n = 10^{31.725}, \text{ and } n_p = n_n \times 10^{-13.584}$$

while the same quantities obtained in section II-5 without the beta condition are $n_n = 10^{32 \pm 1}$, and $n_p = n_n \times 10^{-14 \pm 1}$.

The general agreement is good.

b. Final Abundance Calculations

(i) Nuclear Level Structure - The procedure to be followed for the final abundance calculations is outlined in Section II-4. The formulae presented in that section together with photo-beta equations (2-34) and (2-35) with the Fermi function f obtained in Section II-6 provide us with all the necessary relations. In the final calculations, the summation over all the excited nuclear levels has to be carried out. Up till now $\omega(A,Z)$ which appears in (2-9) was set equal to 2. However, now this approximation is dropped and the exact form of $\omega(A,Z)$ in (2-11) is computed, carrying out the summation over all the excited states. There are two other places in which the summation over excited nuclear levels becomes necessary; one is in the partition function (2-35a) in photo-beta processes and the other is the summation $\sum_i \lambda_i a_i$ appearing in the equation (2-34) which represents the total photo-beta rate per nucleus. If the states involved are just the first few and all the spin-parity assignments have been given for each state as in the case of Section II-9a there is no problem.

When a sufficiently large number of levels and high values of level densities are involved, a conventional statistical approach is adequate. That is, we can just replace the sum by integration over the quantity of interest times level density. Excited energy levels of about 8 Mev are rather well known through neutron resonances. In this and higher regions the level spacing is sufficiently small and conventional level density formulae are valid. In the simplest form this can be expressed as

$$\rho(u) = C \exp\left[2\sqrt{au}\right] \tag{2-36}$$

where $\rho(u)$ is the level density and u is the energy of the excited level, and a and C are constants. Some rough estimates of a and C are given in reference 44, p. 372. Quite a few improvements have been made on this original form, and now very complicated expressions designed to make best fits to the experimental results are available.(45) Unfortunately, however, such formulae are not much help in the present problem, because the contribution to the photo-beta reaction is expected to be greatest from the excited levels around 3 to 6 Mev in the temperature range in which we are presently interested.(29) This statement is further confirmed by the results of actual calculations carried out in this research.

The conventional level density formulae do not give good results for excited levels in the region 3-6 Mev. For some of the terrestrial elements, the level structure of nuclei is rather well known. Ericson pointed out that if the logarithm of the total number of nuclear levels below a given excitation energy N versus that energy u is plotted, a good straight-line relation is obtained. Levels of S^{33}, Fe^{53}, Fe^{55}, Fe^{57} and M_n^{56} are plotted in this manner in reference 46; level structure thus shown in graphical form is distinct up to an excitation energy of about 6, 4.5, 4, 3.5 and 2.5 Mev for S^{33}, Fe^{58}, Fe^{55}, Fe^{57} and Mn^{56} respectively.

From the experimental data compiled in reference 42, similar graphs were plotted for other elements also. A typical example is shown in Figure 7. The staircase in Figure 7 clusters closely about the straight line. This line can be extrapolated to 6 or 7 Mev where conventional level density formulae start to become applicable. With the help of plots like Figure 7, our present difficulty in the summation of excited states is overcome. Namely, from the way such a figure is plotted, it is clear that the following relation applies:

$$N = \exp\left[a(u - u_0)\right] \tag{2-37}$$

where N is the total number of states up to the excitation energy u, and "a" and u_0 are constants which are determined by the slope and the intercept of the straight line drawn along the staircase, respectively. Because "a" and u_0 are known through this graphical method, we are now provided with a means of direct summation over all the excited states up to about 6 to 8 Mev. In the present research this method was adopted up to 10 Mev (that is, the straight line extrapolation was extended to 10 Mev) and the levels were terminated there. The result revealed that this method is justified up to T =5 billion degrees (the contribution from higher excited states can be neglected if the temperature is not too high), but a serious deviation was noted at 10 billion degrees.

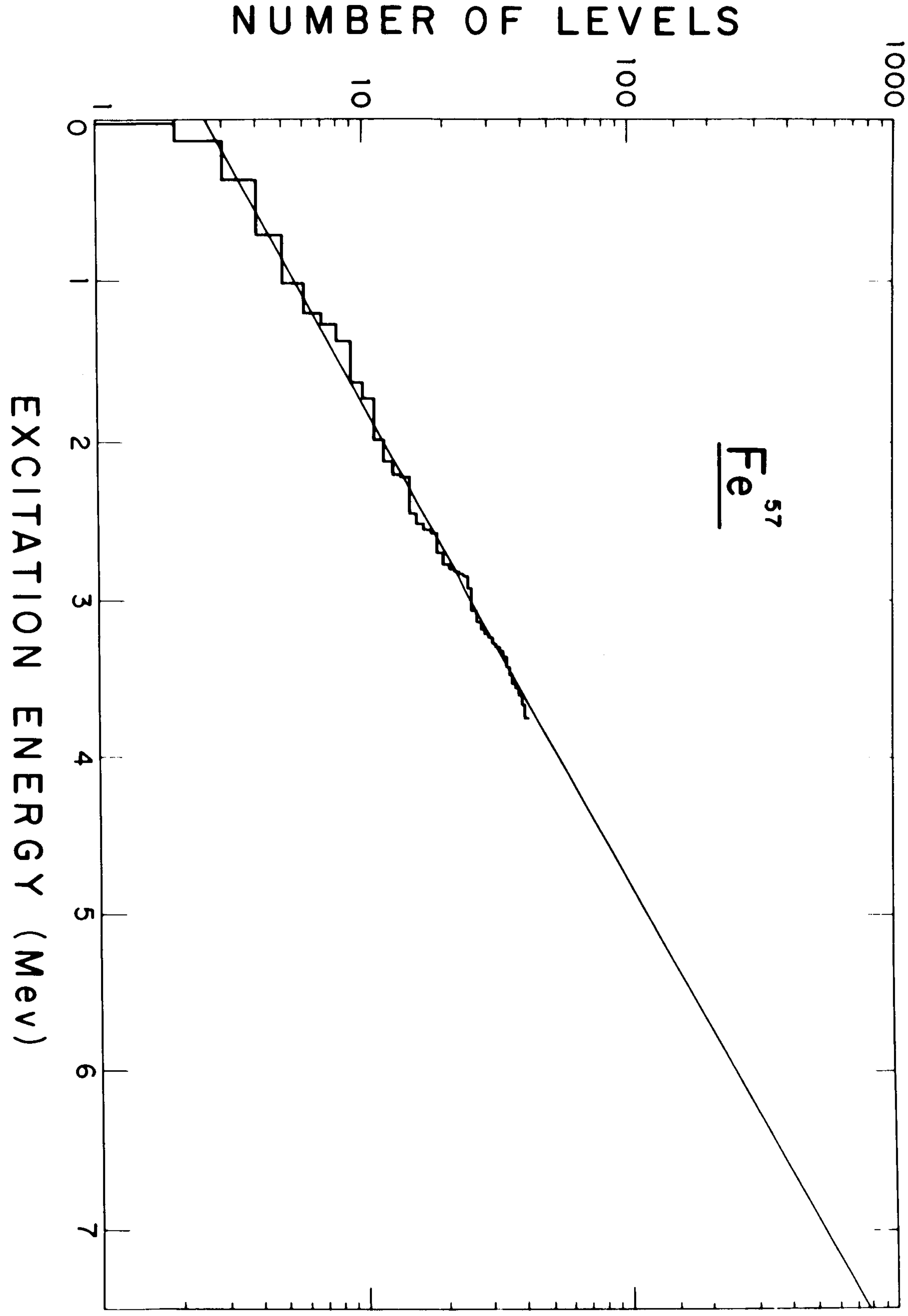
NUMBER OF LEVELS
1
10
100
1000
0
1
2
3
4
5
6
7
EXCITATION ENERGY (Mev)
Fe^{57}

Figure 7

Questions may arise as to how this method can be applied to nuclei whose level structures are not known experimentally, as is the case with most of the neutron rich nuclei we have to deal with. This problem has been overcome as follows. Recently more systematic investigations along this line were made by Cameron et al,(47) in which sufficiently large amounts of empirical data were accumulated. From these data were determined empirical values of a and u_o which appear in (2-37). Their results were:

$$\begin{aligned} a &= 0.020\,A \quad (\text{Mev}^{-1}) \text{ for odd-odd nuclei} \\ a &= 0.016\,A \quad (\text{Mev}^{-1}) \text{ for all except odd-odd nuclei.} \end{aligned} \qquad (2\text{-}38a)$$

No such clear-cut expression is possible for u_o because the intercept spreads out all over a large domain rather randomly, but the over-all average is taken to be

$$\bar{u}_o \sim -0.5 \text{ Mev} \qquad (2\text{-}38b)$$

This value of u_o is adequate when too high an accuracy is not required. For instance, (2-38b) along with (2-38a) was used in evaluating $\omega(A,Z)$ in (2-9) and (2-11), because the number of nuclei involved is tremendous (about 400 nuclei) and because a high degree of accuracy is not required in this case.

A more detailed treatment is desirable in the final calculation of photo-beta rates because only four nuclei are involved for a given density. The empirical values of "a" given in (2-38a) are, however, more or less universal and they are thought to be more reliable than those determined through an individual approach, because, for neutron-rich nuclei, for whose properties there is no direct experimental data, no direct individual approach is possible. To evaluate u_o, the author made use of the fact that many of the nuclear properties are determined by the unpaired nucleons, the last nucleon in the partially filled shell, and, therefore, it is possible to deduce a rough empirical estimate of the level structure by investigating the level structure of terrestrially existing nuclei whose empirical data are available and whose odd nucleon number is the same as that of the neutron-rich nucleus being considered. Even though this is a rather indirect approach, it turned out that u_o obtained in this manner seemed much more reliable than that in (2-38b).

In the procedure followed, graphs like Figure 7 were first plotted for all the nuclei available in experimental data such as reference 42, of the same number of N or Z as the neutron-rich nucleus of interest. For instance, in determining u_o of the beta-decay key nucleus $_{28}Ni^{79}$ at 15 Mev in Table 5 (P.112), a staircase, like that in Figure 7, was plotted for all the elements with N = 51 and also with Z = 28, which were found in empirical data. Such plots were also made for many other nuclei both inside of and outside of the regions near magic numbers in order to see the general effect of closed shells. Then, a straight line was drawn with the slope "a" obtained from (2-38a) through the lower portions of the staircase, and finally the intercept u_o was read off for each nucleus appearing in Table 5, and for four more nuclei which govern the beta process at $E_F = 25$ Mev which are introduced in Section II-9b (iii).

(ii) Spin and Parity Distribution - The statistical weight $(2\,J_i + 1)$ and $(ft)_i$ for the excited state i appearing in the expression for the photo-beta rate and the abundance formula are evaluated through the use of spin and parity distribution functions.

The spin distribution is predicted theoretically to be(45,46)

$$\begin{aligned}\rho(J) &= \rho(0)\left[\exp(-J^2/2C\tau) - \exp(-(J+1)^2/2C\tau)\right] \\ &\simeq \rho(0)(2J+1)\exp\left[-(J+\tfrac{1}{2})^2/2C\tau\right]\end{aligned} \qquad (2\text{-}39)$$

where $\rho\,(J)$ is the density of levels with spin J, $\rho\,(0)$ is the density of levels with zero spin, τ is the nuclear temperature and C is a constant. Some authors use a symbol σ instead of $2C\tau$ of the above which are related to each other by

$$\sigma = \sqrt{C\tau} \qquad (2\text{-}40)$$

σ is a parameter which characterizes the distribution function and is a slowly varying function of the energy of the excited states u through τ. The first problem we have to face in using equation (2-39) is that of selecting the value of $2C\tau$ (or σ) to be employed.

This parameter for light nuclei (e.g. Al^{28}) is investigated by Hibdon.(43) Hibdon evaluated the constant C for a nuclear radius

$R = 1.4A^{1/3} \times 10^{-13}$ cm to be

$$C = \left[B^2A^{5/3}/55\right] \text{ Mev}^{-1} \tag{2-41}$$

where A is the mass number and B is a constant which when set equal to 0.55 gives the best fit to the observed level densities. He concluded that $2C\tau = 6$ (corresponding to $\tau = 2.1$ Mev) gives the best fit to the observational results for Al^{28}.

Huizenga investigated the effects of different assignments of δ on the isomeric cross section ratios in the region of heavier nuclei of A from about 80 to 200.(49)

Reference 49(a)				Reference 49(b)
Br^{81}	Se^{82}	Zr^{90}	In^{115}	Au^{197}
$\delta \sim 5$	$2 < \delta < 3$	$\delta \sim 5$	$5 < \delta < \infty$	$3 < \delta < 5$

When $\delta = 2$, $2C\tau = 8$; $\delta = 3$ corresponds to $2C\tau = 18$; $\delta = 5$ to $2C\tau = 50$; $\delta = 10$ to $2C\tau = 200$. Generally, a small change of δ corresponds to a large change in $2C\tau$. In the present research, the following approach was adopted. Nuclear temperature τ is defined as the inverse of the derivative of entropy S with respect to the excited state energy U, while entropy is the logarithm of nuclear level density $\rho(U)$,

$$\tau = \left[\frac{\partial S}{\partial U}\right]^{-1} = \left[\frac{\partial \ln \rho(U)}{\partial U}\right]^{-1} \tag{2-42}$$

It may be argued that it is rather meaningless to carry out detailed calculations of nuclear temperatures as a function of U since it is a very slowly varying function and especially because in the intermediate energy range of about 3 Mev which we encounter in the photo-beta processes such a statistical approach may not be well justified. However, just to satisfy my own curiosity τ was calculated through equation (2-42) using the simplest expression of nuclear level density given in (2-36) which was taken from reference 44, and the numerical values of constants given on p. 372 of the same reference were used, as they were thought to be adequate when we are making order-of-magnitude estimates. Equation (2-41) with B (= 0.55) given by Hibdon was used to evaluate C. In this way $2C\tau$ was calculated. Some of the results are listed below.

U	$2C\tau$		
(Mev)	at A = 67	at A = 83	at A = 121
1.3	9.8	10	13.4
2	12.3	12.4	16.4
2.5	13.6	13.7	18.2
3	14.9	15.1	20
4.1	17.4	17.6	23.4
6.1	21.2	21.5	28.4
8.1	24.5	24.8	32.8
10	27.1	27.5	36.4

One of the most general conclusions from Huizenga's work is that δ is about 2 to 5 for heavier elements. This agrees with my results shown above, because they indicate that for A about 60-120, δ is about 2 to 4 when U is between 1 and 10 Mev. Hibdon's best fit ($2C\tau = 6$) corresponds to $\delta = 1.73$. His investigation was done for neutron resonances which involve excited levels at about 8 Mev. The comparison of his value with the values listed above (P. 105) may give an impression that the latter are rather high in value. However, we note that $2C\tau$ is an increasing function of mass number A, through (2-41), and we expect higher numerical values of $2C\tau$ for heavier elements. It may be worthwhile to emphasize at this point that what we are concerned about is the general behavior of δ (the parameter characterizing the spin distribution) and not its exact numerical value, and we can conclude from the above comparisons that the method outlined previously is satisfactory as a means of evaluating the spin distribution function in our present problem.

Having settled the parameter δ (or $2C\tau$) in equation (2-39) for the spin distribution, we next discuss how this formula is to be applied to our problem.

For this purpose it is useful to see the general behavior of the spin distribution given by (2-39). For different discrete values of J, p (J) was first computed for a typical value of $\delta = 3$. It turned out that

J	0	1	2	3	4	5	6	7
p (J)	0.07	0.18	0.23	0.207	0.149	0.090	0.045	0.019

That is, it is meaningless to include $J > 10$. Therefore, the statistical weight factor $(2J_i + 1)$ of the ith level was computed by taking the average through the relation

$$\langle \overline{2J+1} \rangle = \sum_{J_\ell=0}^{10} (2J_\ell+1)\,\rho(J_\ell) \Big/ \sum_{J_\ell=0}^{10} \rho(J_\ell) \quad \text{or}$$
$$\langle \overline{J} \rangle = \sum_{J_\ell=0}^{10} J_\ell\, \rho(J_\ell) \Big/ \sum_{J_\ell=0}^{10} \rho(J_\ell) \qquad (2\text{-}43)$$

The general result is that for lower excited states around a few Mev, the average spin $< \bar{J} >$ is about 2 to 3, while for excited levels as high as about 10 Mev, $< \bar{J} >$ goes up to about 4 to 5. For heavier elements higher spins were obtained at the same energy. For instance, for $A = 67$, $< \bar{J} > = 2.3$ and 4.1 for $U = 1.3$ and 10 Mev respectively; for $A = 83$, $< \bar{J} > = 2.65$ and 4.2 for $U = 2$ and 10 Mev respectively; and for $A = 121$, $< \bar{J} > = 2.8$ and 4.9 for $U = 1.4$ and 10 Mev respectively. For all the values of A illustrated above, the average spin is about 3 at an energy of 3 Mev. The region of spin of about 2 to 3,5 seems to give greatest contribution to the photo-beta rates at $T = 5$ billion degrees.

This result agrees with the general behavior in the work of Hibdon and Huizenga. In reference 49(a), the distribution of spin is plotted (p.1307) against J. Maximum J comes at about 2.5 for $\sigma = 3$, while 4.6 is the approximate value for $\sigma = 5$. My results quoted above were computed at $\sigma = 3$. In Hibdon's paper (reference 48, p. 191) the maximum is at around $J = 1.2$. For lighter nuclei higher spins are very unlikely to occur because the possible angular momentum for small Z or N is restricted to small values as is clear from the shell model. On the other hand, when Z or N approaches or exceeds 50, a spin as high as 3.5 to 4.5 is possible through the g7/2 and g9/2 levels. This argument applies to ground states. Generally, higher spins are expected to be possible for excited states than for ground states. Therefore, our values of average spin of 2 to 5 for A in the region from about 60 to 120 and excited energy levels from a few Mev to about 10 Mev are perfectly reasonable. We note, from reference 49, δ of 3 to 5 is expected in our case, which corresponds to a maximum spin of 2.5 to 4.6.

Having settled the problem of evaluation of the statistical weights (2J + 1), it now remains to show how the comparative half life (ft) appearing in the formula for the photo-beta rate is to be estimated. As was noted in Section II-7, the effect of the excited states on the beta-rate comes as a perturbation to the rate of transitions between ground states. It is, therefore, sufficient to include only allowed transitions for excited states. Consequently, log ft was set equal to 5.5 for all the transitions between excited states. The question then arises as to which of all possible transitions between all possible pairs of excited levels of the parent nucleus and those of the daughter nucleus are allowed transitions. That is, each component of the photo-beta rate of excited states $(a_i \lambda_i)$ in (2-34) with ft set equal to $10^{5.5}$ must be multiplied by the probability of its being an allowed transition, before the summation is carried out, supposing that every possible pair of excited levels of the parent and the daughter nuclei were included in the summation.

The transitions between ground states and the lowest few excited levels up to about 1 to 2 Mev were determined by the method outlined in Section II-8. The summation over the lowest states and that over the rest of the excited states were carried out independently and both were summed together at the end. It was necessary to follow this order because, while the former was settled already by the method of Section II-8, the latter has to be treated by the method to be outlined in this section.

The probability of the occurance of an allowed transition among all possible transitions between all possible pairs of excited states of the parent and the daughter nuclei was predicted in the following manner: Let us consider a transition between the ith state of a parent nucleus (A, Z) and the jth state of its daughter nucleus (A', Z'). The selection rule for an allowed transition requires that for an allowed transition the spin change be 0 or 1 with no parity change. That is, for any given spin J_i of the ith state of the parent, the spin J_j of the jth state of the daughter can be only equal to J_i or $J_i \pm 1$ for $J_i \geq 1$ and equal to J_i or $J_i + 1$ for $J_i = 0$. The probability of the spin of the ith state of the parent to be a particular value J_i is $\rho(J_i) / \sum_{J_\ell = 0}^{10} \rho(J_\ell)$, that of the jth state of the daughter nucleus to be a particular value J_j is similarly $\rho(J_j) / \sum_{J_\ell = 0}^{10} \rho(J_\ell)$. J is supposed to take any discrete value between 0 and 10. Therefore, for each J_i from 0 to 10 of the parent, the probabilities of the spin to be actually J_i is multiplied by the sum of the probabilit that the spin of the daughter be any one of the $J_i \pm 1$ and J_i, that is, the sum of the probabilities of these three cases (or of the two cases, $J_{\underset{d}{j}} = J_i$ and $J_{\underset{d}{j}} = J_i + 1$, when $J_i = 0$). Then, all such quantities evaluated for J_i form 0 up to 10 are added together. According to Ericson (p. 449 reference 46), positive and negative parities are almost equally probable. Then, for either parity of the ith state of the parent, the probability for the parity of the $\underset{d}{j}$th state of the daughter to be the same as that of the parent is 1/2. This is multiplied by the probability of satisfying the spin selection rule just outlined. Multiplying this last quanity (the probability for a particular transition to satisfy both spin and parity selection rules for an allowed transition) by the photo-beta rate of this transition $(a_i \lambda_i)$ and carrying out the summation over all such terms for all possible pairs between the excited states of the parent and those of the daughter, the total photo-beta rate per nucleus of a particular nucleus (A, Z) is found.

It turns out, according to this method, that there is generally about one chance in four that this transition is an allowed transition in lower excited states of a few Mev, while there is only about one chance out of 5 to 6 for higher excitation levels of about 6 to 8 Mev. This is as expected because for lower states a smaller variety of spin values is possible (average J is smaller) and therefore there is a greater chance for the parent and the daughter to have similar spin values while a greater range of spin becomes available with the increase of excited levels and the chance for coincidence $(J_d = J_i \pm 1, 0)$ becomes less.

(iii) Discussion of the Results - The final calculation was carried out in the range of densities and temperatures corresponding to

$T_9 = 2, 3, 4, 5, 10$; $T_9 = T(^\circ K)/10^9$

$E_F = 0.17, 5, 10, 15, 20, 23, 25, 30$ Mev.

After a careful re-examination of the nuclei for beta transitions selected in Section II-8, four nuclei for each E_F listed in Table 5 turned out to be the most important and these were chosen as the key nuclei to govern the photo-beta condition. In Table 5, $\omega(T)$, $P_\pm$, and the expected total rate $\beta_\pm \equiv P_\pm\, n(A,Z)$, using the $n(A,Z)$ from Section II-5, are tabulated for each nucleus.

The information obtained about the properties of the ground state and the first excited states in Section II-8 were used in the summation over the low energy region, and the summation over the region of higher excited levels was carried out in the manner just described in sub-section II-9b(i).

Equations(2-22a), (2-22b), and (2-30) through (2-33) were used to obtain f as a function of W_0 , the energy difference before and after

TABLE 5 - The key nuclei for photo-beta reactions, their photo-beta reaction rates $P_{\pm}$ (+ for e^- capture and - for e^- emission), partition functions $\omega(T)$, and rough estimates of $P_{\pm}\, n(A,Z)$, where $n(A,Z)$ were taken from Section II-5, and $P_{\pm} = \sum_i [\ln 2(2J_i + 1) f_i e^{-U_i/kT}/(ft)_i] / \omega(T)$, $\omega(T) = \sum_k (2J_k+1) e^{-U_k/kT}$ in cgs units, at different electron Fermi energies.

E_F		Key Nucleus	$\omega(T)$	Log $P_{\pm}$ (number/sec-nucleus)			Log $\beta^{\pm}$ ($cm^{-3}\,sec^{-1}$), where $\beta^{\pm} \equiv P_{\pm} n(A,Z)$		
(Mev)		T	5×10^{9} °K	5×10^{9} °K	3×10^{9} °K	2×10^{9} °K	5×10^{9} °K	3×10^{9} °K	2×10^{9} °K
5	k +	$_{29}Cu^{67}$	5.905	-2.929	-3.42	-3.56	25.39	24.90	24.76
	c +	$_{28}Ni^{65}$	7.877	-4.127	-6.25	-7.80	25.02	22.90	21.35
	e -	$_{27}Co^{65}$	9.681	-2.053	-2.89	-2.95	25.71	24.87	24.81
	n -	$_{28}Ni^{67}$	4.645	-2.293	-3.81	-4.60	26.20	24.70	23.9
10	k +	$_{33}As^{83}$	6.734	-1.615	-4.16	-4.32	27.92	25.38	25.22
	c +	$_{31}Ga^{81}$	5.698	-3.001	-8.16	-13.0	27.0	22.64	17.80
	e -	$_{30}Zn^{81}$	6.733	+0.160	-1.70	-1.76	28.66	26.80	26.74
	n -	$_{32}Ge^{83}$	7.079	-1.634	-5.16	-6.92	28.62	25.09	23.33
15	k +	$_{31}Ga^{81}$	5.547	-0.465	-2.86	-3.02	27.60	25.21	25.04
	c +	$_{29}Cu^{79}$	4.738	-2.766	-6.60	-9.76	28.87	25.04	21.88
	e -	$_{28}Ni^{79}$	6.593	-0.640	-2.89	-2.90	29.94	27.69	27.68
	n -	$_{30}Zn^{81}$	7.395	-2.551	-6.80	-10.4	28.05	23.80	20.20
20	k +	$_{41}Nb^{121}$	16.604	+3.761	-1.6	-3.42	32.63	27.27	25.45
	c +	$_{41}Nb^{123}$	14.685	+1.606	-4.1	-8.1	32.67	26.96	22.96
	e -	$_{40}Zr^{123}$	13.076	+3.888	-1.6	-2.9	34.76	29.27	27.97
	n -	$_{40}Zr^{121}$	11.710	+1.810	-3.5	-7.52	33.08	27.77	23.75
23	k +	$_{40}Zr^{121}$	10.053	2.226	-2.5	-2.67	31.53	26.80	26.63
	c +	$_{38}Sr^{119}$	7.774	1.208	-4.3	-8.13	32.82	27.31	23.5
	n -	$_{37}Rb^{119}$	6.490	3.446	-2.0	-2.66	34.35	28.90	27.24
	e -	$_{39}Y^{121}$	5.143	3.502	-1.8	-2.66	34.65	29.32	28.46

the transition. The comparative half life, ft, and the statistical weights, $\omega(T)$, were taken care of in the manner just described in Section II-9b(ii).

The rate per nucleus for each element, $P_{\pm}$, for each Fermi energy E_F as a function of temperature was calculated through (2-34) and (2-35), and plotted. The results are tabulated in Table 5. The typical curves for four nuclei at $E_F = 0.17$, 15 and 23 Mev are shown in Figure 8. The curves for other values of E_F are not shown in Figure 8 to avoid over-crowding.

The rate per nucleus times the abundance $\beta_{\pm} \equiv P_{\pm}\, n(A,Z)$ is a measure of the importance of the nucleus (A, Z) in the photo-beta summation in (2-12). In Table 5, the nucleus marked by k is the maximum nucleus (the leading term in the summation) for the capture process; that marked by e is the maximum for the electron emission process; that marked by c is the minor element in capture and is at the same time the daughter of the electron emission of the nucleus marked e; and finally the nucleus marked n is the minor element for electron emission and at the same time the daughter of the leading capture process of nucleus marked k. There are a number of captures and emissions between nuclei marked by k and n and between those marked by c and e, but k is expected to be stronger than c, while e is expected to be stronger than n. This argument applies especially to ground states.

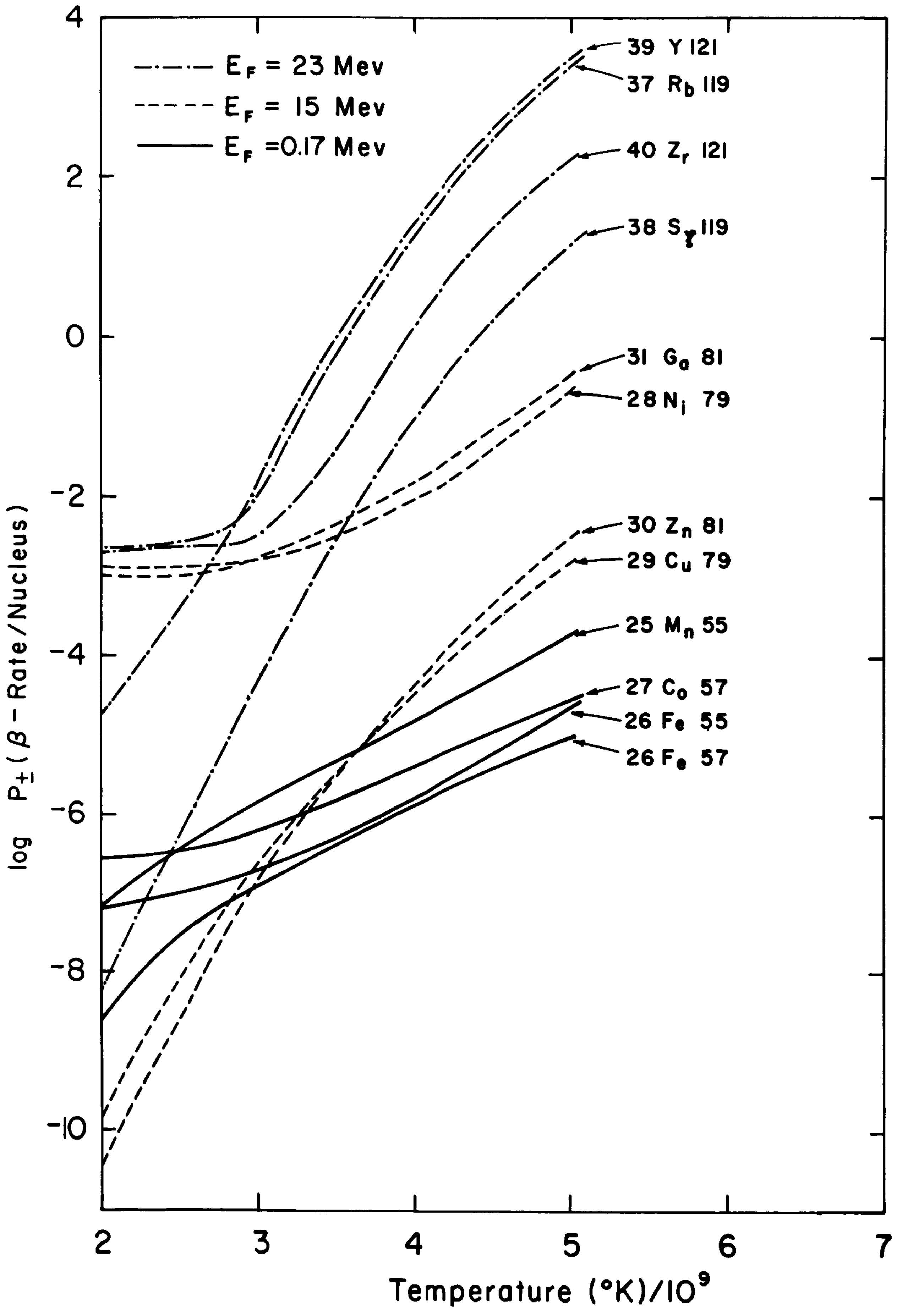

E_F = 23 Mev
E_F = 15 Mev
E_F =0.17 Mev
39 Y 121
37 Rb 119
40 Zr 121
38 Sr 119
31 Ga 81
28 Ni 79
30 Zn 81
29 Cu 79
25 Mn 55
27 Co 57
26 Fe 55
26 Fe 57
4
2
0
-2
-4
-6
-8
-10
2
3
4
5
6
7
log P± (β - Rate/Nucleus)
Temperature (°K)/10^9

Figure 8

Let us focus our attention on the last three columns of Table 5, where the measure of importance of individual nuclei $\beta_{\pm}$ is displayed. The exact number listed should not be taken too seriously, because the abundance n(A,Z) obtained in Section II-5 (which is not the final abundance but only the first order approximation) was used in this computation. In the final equilibrium calculation, the sum of contributions from capture nuclei k and c must be exactly equal to the sum of those from emission nuclei e and n, but this is not necessarily so in Table 5. For instance, for $E_F = 10$ Mev, the $\sum_i \beta^-_i$ is higher than $\sum_j \beta^+_j$, and therefore the n_n and n_p obtained in Section II-5 must be re-adjusted so that the total abundance of emission nuclei Z_n^{81} and G_e^{83} will be somewhat reduced while those of capture nuclei As^{83} and G_e^{81} will be somewhat increased, until both sides of the equation (2-12) become equal. In effect, this makes the equilibrium point be shifted to the less neutron rich side than in II-5. As is displayed in Table 3, this shift is negligibly small at 10 Mev (we still have Ge^{82} as the top nucleus, and the general features of the curve are not changed). This shift to the less neutron rich side is visible at 20 Mev and 5 billion degrees, where the top nucleus in the final calculation stays at Ni^{80} (the N = 50 shell) and does not switch over to Zr^{122} at the N = 82 shell, but in the previous calculation in Section II-5 the top nucleus was Zr^{122}. It may be noted, however, that both in Section II-5 and here the peak at the N = 50 magic number and the 82 magic number are comparable at 20 Mev, and that a slight change in equilibrium condition can change the maximum point from one peak to another. As will be shown later, the peak does go up to Zr^{122} at 2 billion degrees, where the cold matter approximation applies better.

It is expected that at low enough temperatures where the contribution to photo-beta rates by higher excited states becomes negligible, the nature of the ground and the lowest excited states are more obvious. From our results, that evidently happens at 2 billion degrees, because at this temperature the behavior is just as expected from the properties of these lowest states. Namely, in all cases at 2 billion degrees, the major nuclei marked by k and e have larger values of total rate $\beta_{\pm}$ than those of the minor nuclei c and n expected from the properties of the lowest states, while this is not true if the temperature is increased to 5 billion degrees. For instance, at 5 Mev, the total rate of the minor nucleus Ni^{67} is larger than that of the major nucleus Co^{65} for the emission process, and similar switching from major to minor and minor to major nuclei happens at 23 Mev, too. This is because of the fact that the criteria for the major and minor nuclei were originally made through the selection rules applied to the particular properties of the ground and lowest excited states only, while as temperature increases, the contribution from higher excited states becomes more and more important and is independent of the spin and parity of the lowest states. The general effect is to make individual nuclei more indistinguishable. This deviation of the behavior from that expected from the cold matter approximation is larger for higher temperatures.

Once we knew $P_{\pm}$ for each key nucleus involved, our problem was solved uniquely by following the procedure described in Section II-4, by the use of the equations (2-9) through (2-15). $P_{\pm}$ for all key nuclei of the photo-beta processes were stored as a function of Fermi energy and temperature as the input to the IBM 7094 computer so that equations (2-10) and (2-12) supply one function relating n_n and n_p. Another relation is furnished by (2-14) and (2-13a) or (2-13b) for any given E_F and temperature. The two unknowns n_n and n_p are determined uniquely by these two relations. The actual procedure followed was to first make a guess of n_n and n_p from the previous results of Section II-5, substitute these values into both sides of (2-12) and (2-14), and then calculate each side of each equation separately including all the nuclei of interest, about 400 in the final abundance calculation through (2-14) for the whole range of density, and all the key nuclei for beta reactions in (2-12), and then compare each side of the equation with the other. This was done both for equation (2-12) and (2-14) simultaneously, and was repeated until the final re-adjustment of n_n and n_p made the right-hand side and the left-hand side agree to within 0.1%. When this condition was fulfilled for a given E_F and T, the program was repeated with a different set of values of E_F and T, until the whole ranges of E_F and T listed at the beginning were covered. The corresponding density was calculated simultaneously through equation (2-15), the summation being taken over all of the 400 nuclei.

The final values of the free neutron number density n_n and the ratio of free proton number density to neutron number density n_p/n_n in logarithmic scale as a function of density for a family of temperatures are plotted in Figures 9 and 10. The dashed curves correspond to the results of Section II-5, at $T = 5 \times 10^9$ °K. The agreement is satisfactory, noting the rough approximation adopted in Section II-5. The temperature effect is striking. Both quantities n_n and n_p/n_n increase rapidly with temperature. With the increase of density, n_n increases but n_p/n_n decreases. These graphs show that, at a density of about 3×10^{11} gm/cm^3 and above, neutrons are dominant and the proton number is negligible. As the density goes below $\rho_c \sim 3 \times 10^{11}$ gm/cm^3, the free neutron number drops more steeply at lower temperatures. For instance, at $T = 2 \times 10^9$ °K and $\rho \sim 10^{11}$ gm/cm^3, slightly below the critical density ρ_c, the neutron number density is 10^{-10} times the value at $\rho_c \sim 3 \times 10^{11}$ gm/cm^3, and, therefore, we can regard 2 billion degrees as a freezing point. That is, at $T = 2 \times 10^9$ °K, there exists a distinct transition of equilibrium configurations from heavy nuclei to neutrons at around 3×10^{11} gm/cm^3, and the cold matter approximation of Section II-3 is perfectly

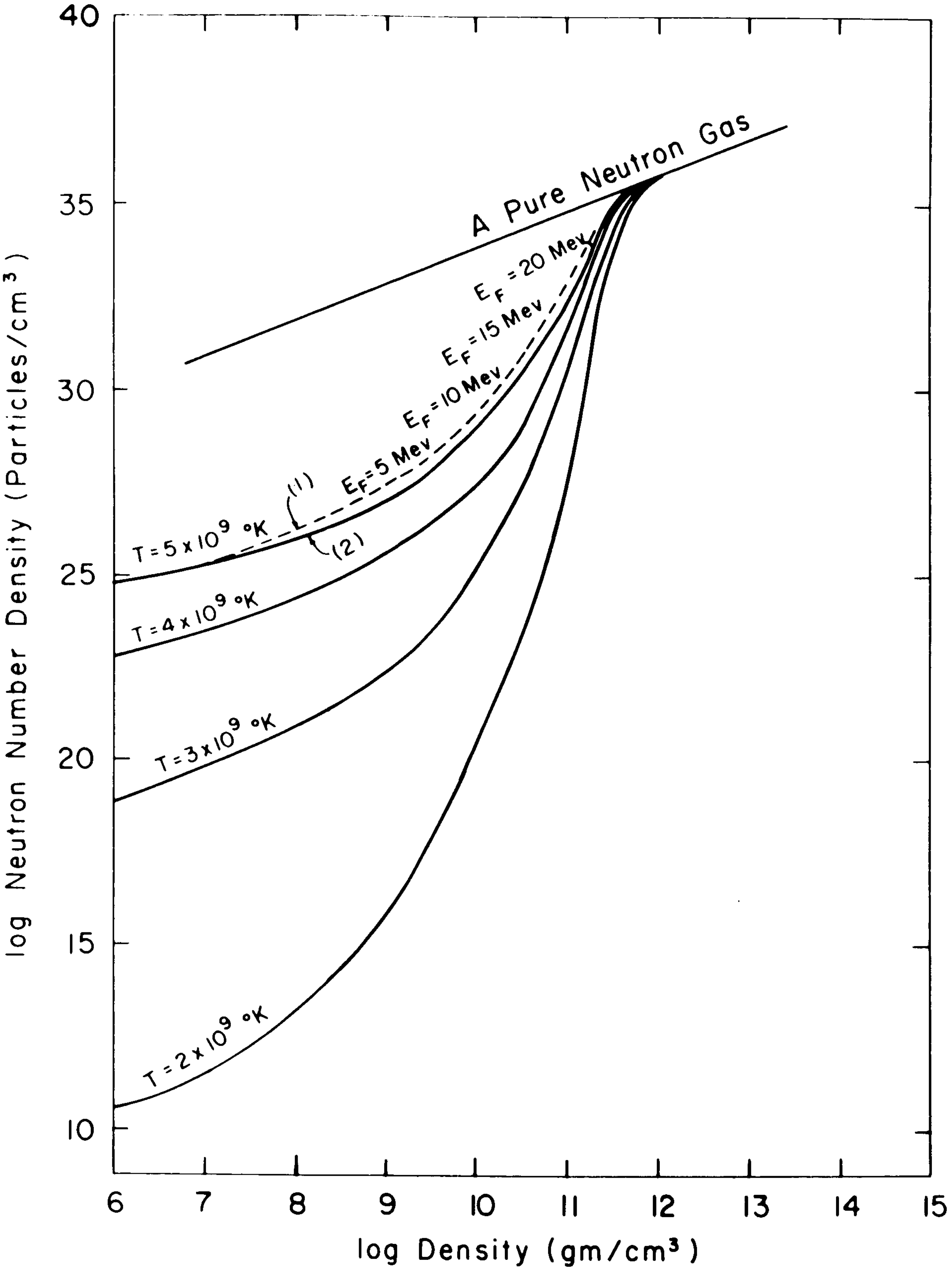
A Pure Neutron Gas
E_F = 20 Mev
E_F = 15 Mev
E_F = 10 Mev
E_F = 5 Mev
(1)
(2)
T = 5 x 10^9 °K
T = 4 x 10^9 °K
T = 3 x 10^9 °K
T = 2 x 10^9 °K
log Neutron Number Density (Particles/cm³)
40
35
30
25
20
15
10
log Density (gm/cm³)
6
7
8
9
10
11
12
13
14
15

Figure 9

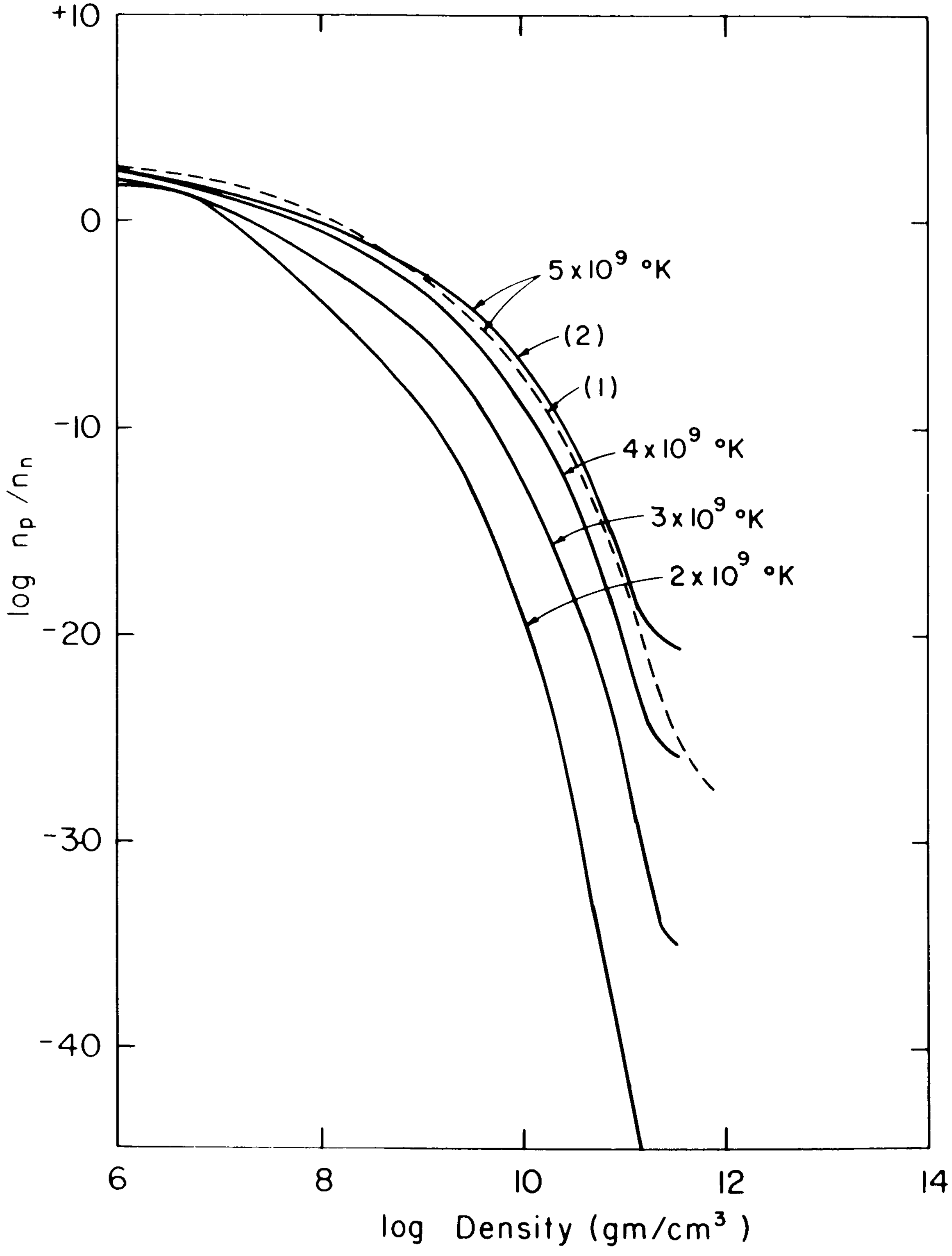
+10
0
-10
-20
-30
-40
log n_p/n_n
6
8
10
12
14
log Density (gm/cm³)
5 x 10⁹ °K
(2)
(1)
4 x 10⁹ °K
3 x 10⁹ °K
2 x 10⁹ °K

Figure 10

valid. The straight line near the top of Figure 9 corresponds to a pure neutron configuration.

The final results obtained in this section are displayed in Figures 11 through 16 at E_F = 0.17, 5, 10, 15, 20 and 23 Mev, respectively, at a temperature of 5 billion degrees.

The first 6 nuclei from the maximum in the descending order and their abundances are tabulated in Table 3 for both the first results (II-5) and the final results (II-9b). A slight shift from the zero-temperature point toward lighter elements and a lesser degree of shift toward the less neutron-rich side (smaller value of molecular weight $\mu \sim A/Z$) at higher temperatures are expected and such effects are generally noticeable in Table 3, especially at $E_F = 20$ Mev, as has already been discussed, where the two peaks at Ni^{80} and Z_{η}^{122} are comparable. However, in all other cases a slight change in shape of the peak in these two results was not noticeable in the abundance curves, and consequently, to avoid repetition, the first abundance curves plotted in Section II-5 are not shown here. The change in abundances of nuclei with increase of density as discussed in Section II-5 and displayed in Figure 3 applies exactly in our final result. This can be easily checked by comparing each abundance curve displayed in Figures 11 through 16 of this section with each corresponding curve displayed in Figure 3 of Section II-5. The only noticeable difference between these two results comes at 20 Mev, where the peak at Z_{η}^{122} is

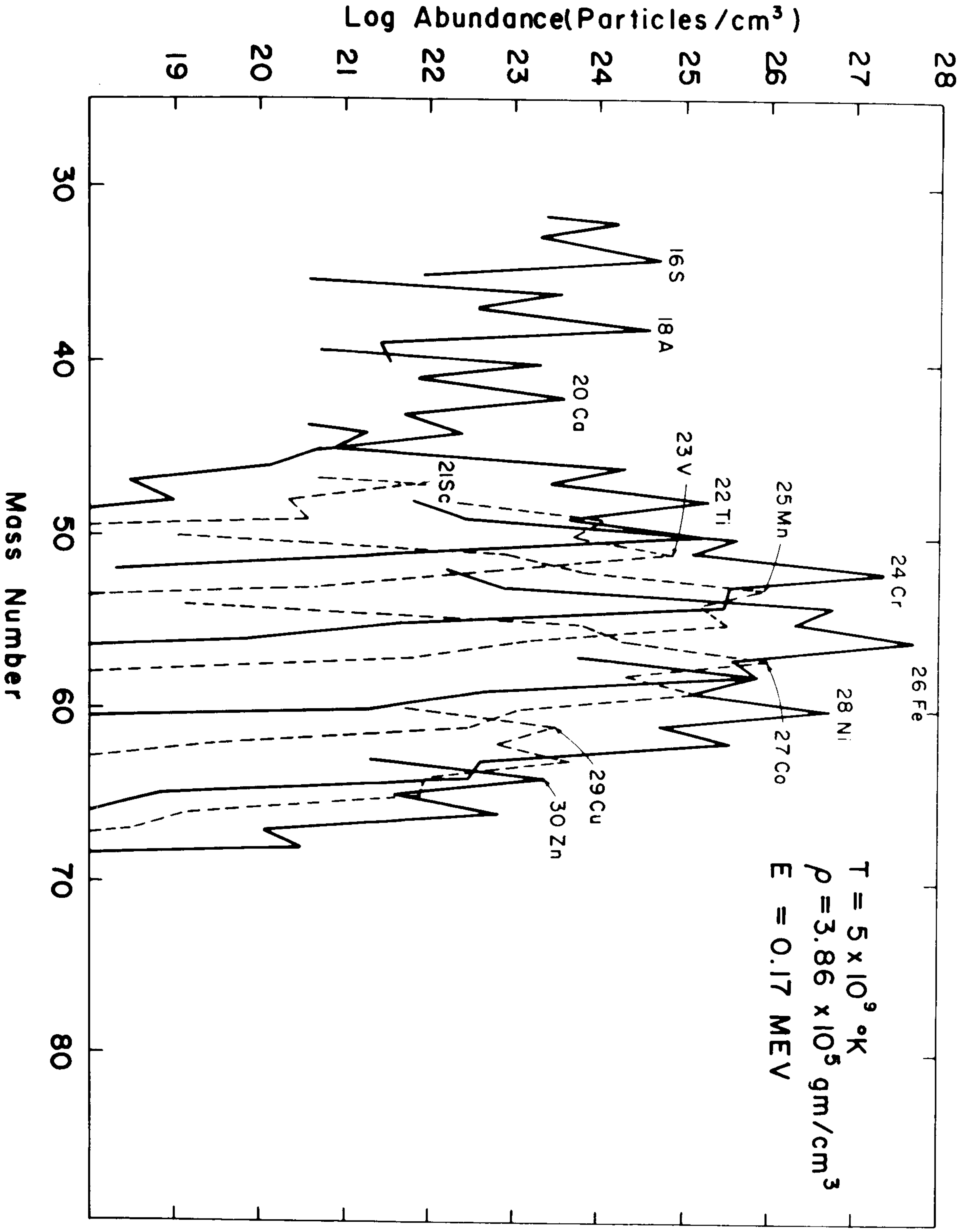
Log Abundance(Particles/cm³)
19
20
21
22
23
24
25
26
27
28
Mass Number
30
40
50
60
70
80
16S
18A
20Ca
21Sc
22Ti
23V
24Cr
25Mn
26Fe
27Co
28Ni
29Cu
30Zn
T = 5 x 10⁹ °K
ρ = 3.86 x 10⁵ gm/cm³
E = 0.17 MEV

Figure 11

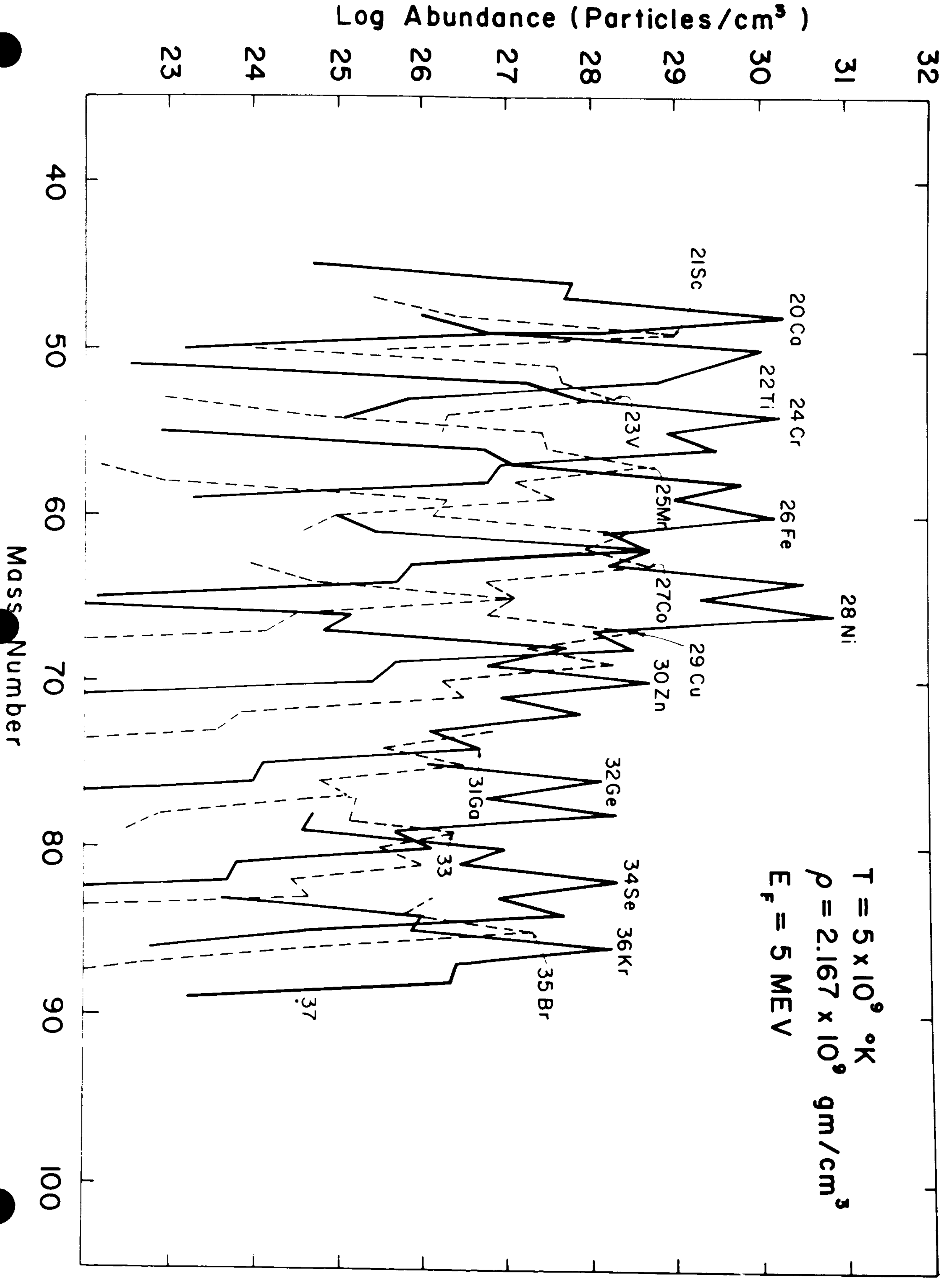
Log Abundance (Particles/cm³)
23
24
25
26
27
28
29
30
31
32
Mass Number
40
50
60
70
80
90
100
T = 5x10⁹ °K
ρ = 2.167 x 10⁹ gm/cm³
E_F = 5 MEV
20Ca
21Sc
22Ti
23V
24Cr
25Mn
26Fe
27Co
28Ni
29Cu
30Zn
31Ga
32Ge
33
34Se
35Br
36Kr
37

Figure 12

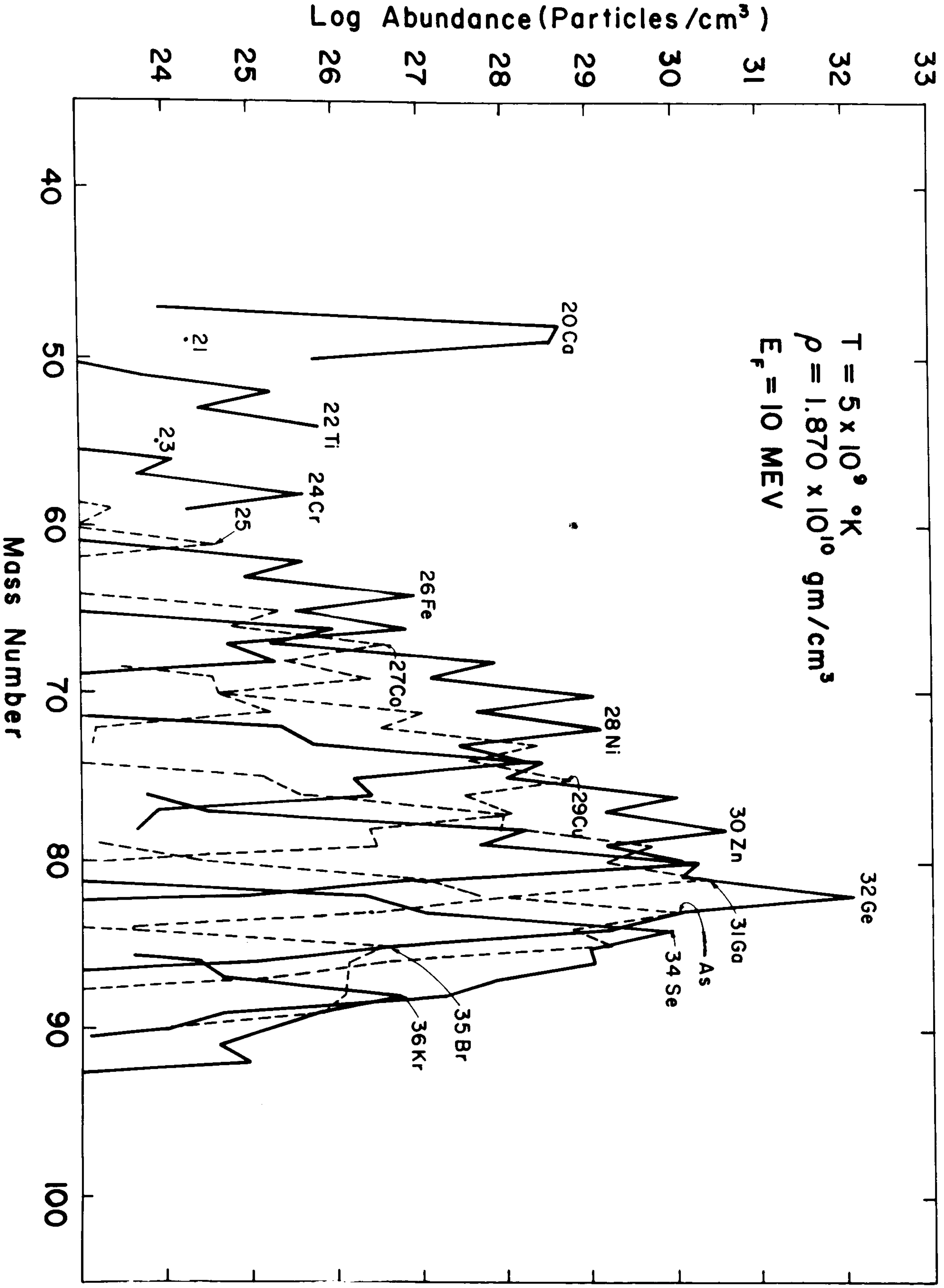
Log Abundance (Particles/cm³)
24
25
26
27
28
29
30
31
32
33
T = 5 x 10⁹ °K
ρ = 1.870 x 10¹⁰ gm/cm³
E_F = 10 MEV
20Ca
21
22Ti
23
24Cr
25
26Fe
27Co
28Ni
29Cu
30Zn
31Ga
32Ge
As
34Se
35Br
36Kr
40
50
60
70
80
90
100
Mass Number

Figure 13

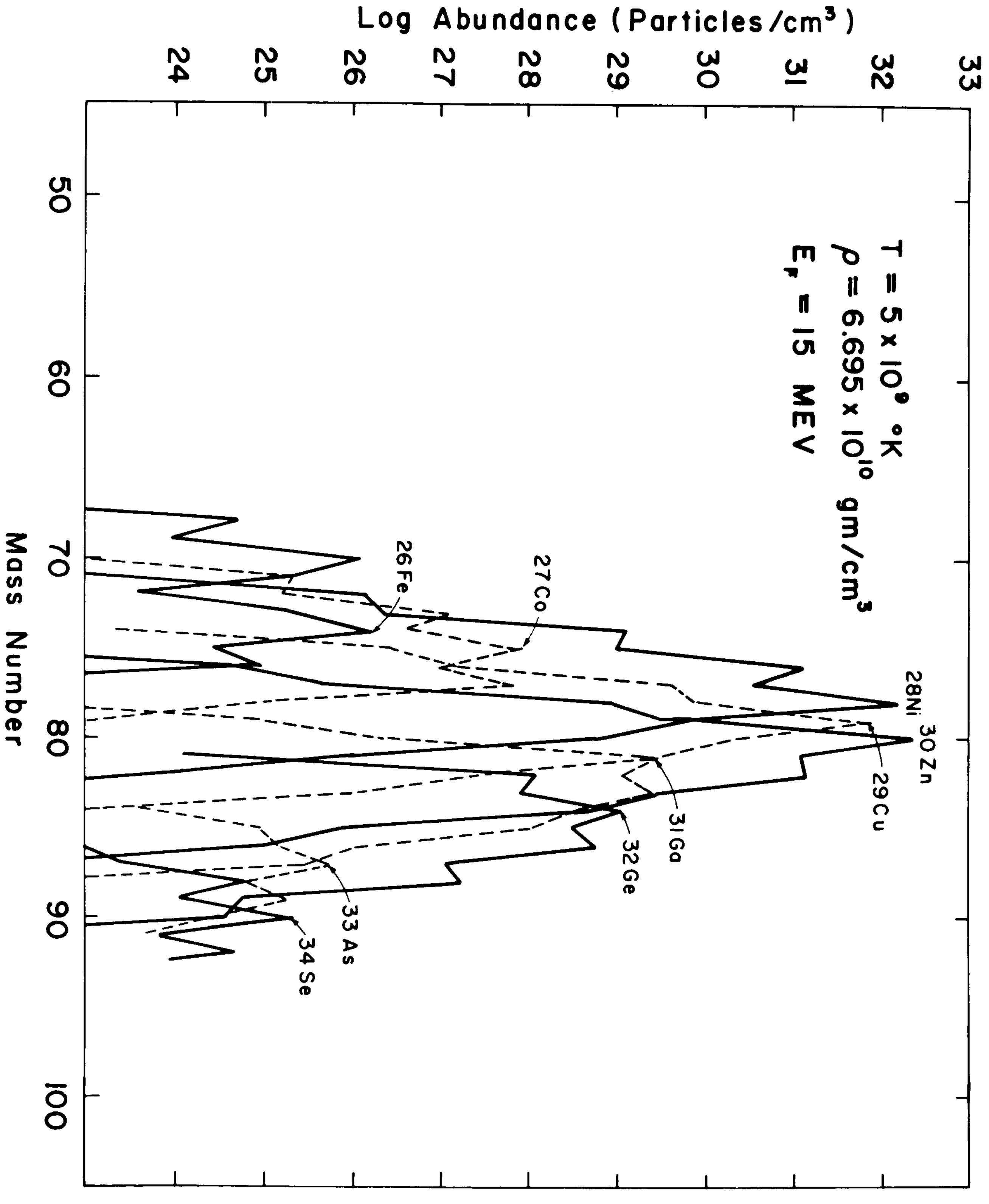

Log Abundance (Particles/cm³)
24
25
26
27
28
29
30
31
32
33
Mass Number
50
60
70
80
90
100
T = 5 x 10⁹ °K
ρ = 6.695 x 10¹⁰ gm/cm³
E_F = 15 MEV
26 Fe
27 Co
28 Ni
29 Cu
30 Zn
31 Ga
32 Ge
33 As
34 Se

Figure 14

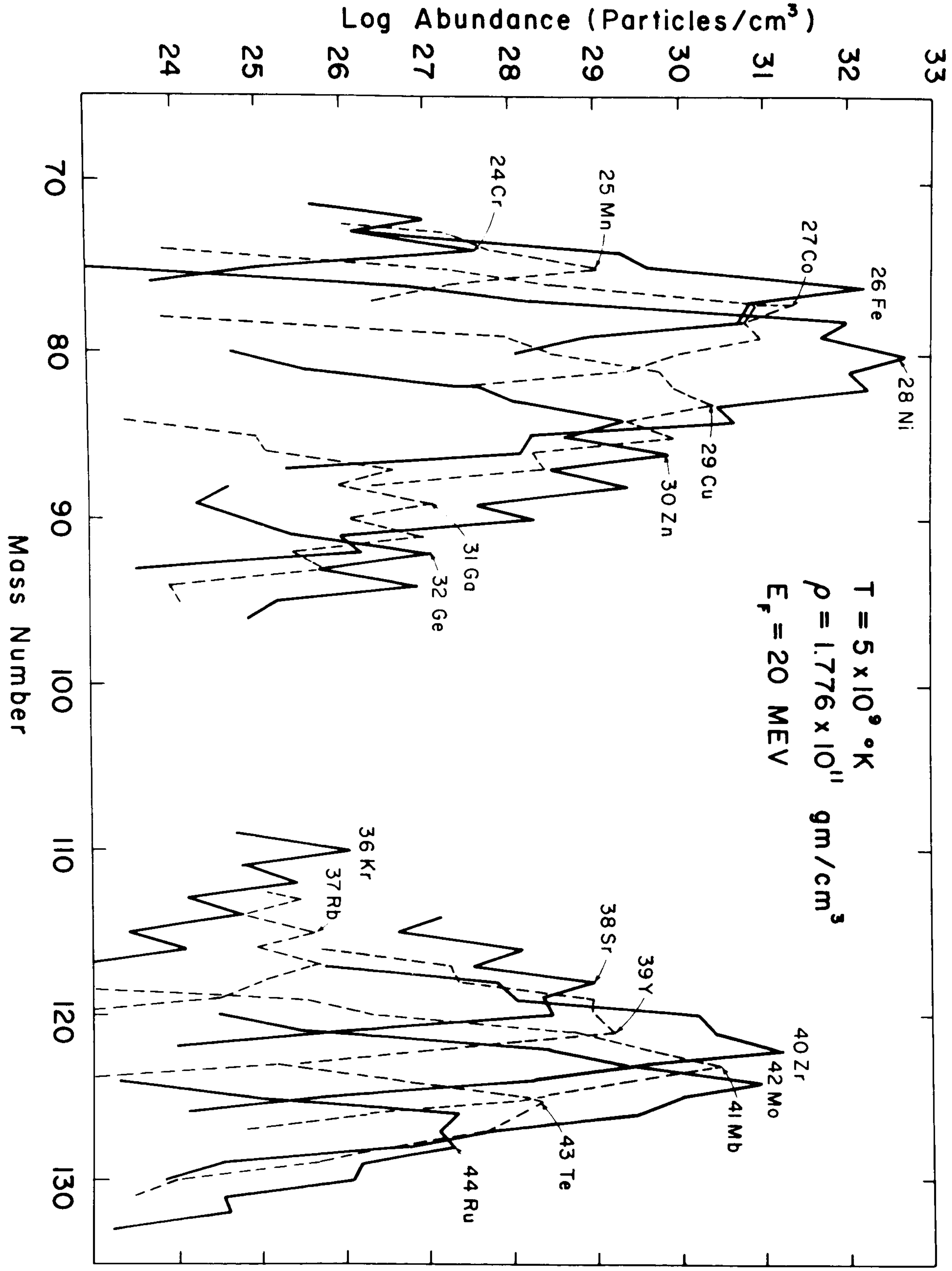
Log Abundance (Particles/cm³)
24
25
26
27
28
29
30
31
32
33
70
80
90
100
110
120
130
Mass Number
T = 5 x 10⁹ °K
ρ = 1.776 x 10¹¹ gm/cm³
E_F = 20 MEV
24 Cr
25 Mn
27 Co
26 Fe
28 Ni
29 Cu
30 Zn
31 Ga
32 Ge
36 Kr
37 Rb
38 Sr
39 Y
40 Zr
42 Mo
41 Mb
43 Te
44 Ru

Figure 15

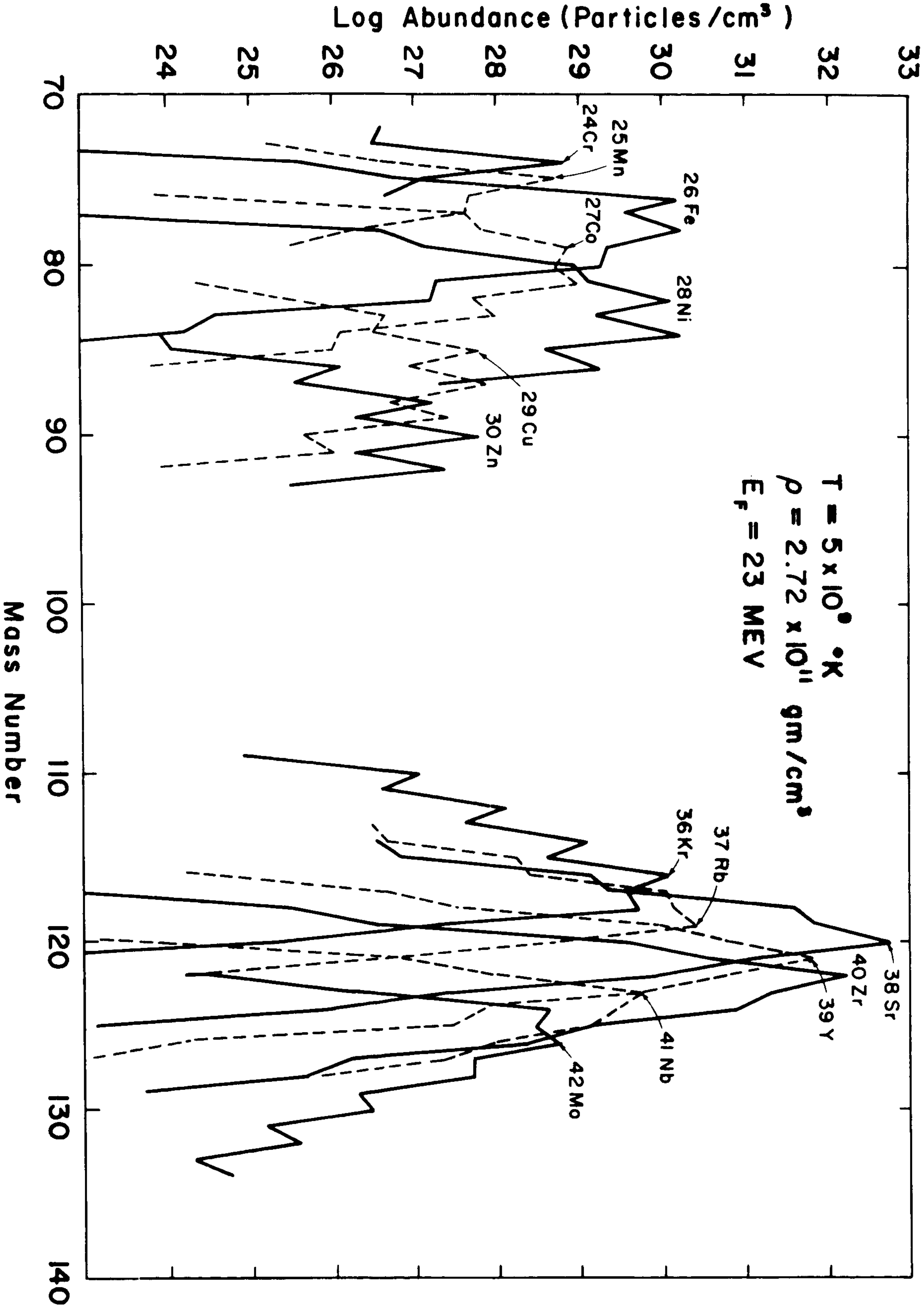
Log Abundance (Particles/cm³)
24
25
26
27
28
29
30
31
32
33
Mass Number
70
80
90
100
110
120
130
140
T = 5 x 10⁹ °K
ρ = 2.72 x 10¹¹ gm/cm³
E_F = 23 MEV
24Cr
25Mn
26Fe
27Co
28Ni
29Cu
30Zn
36Kr
37Rb
38Sr
39Y
40Zr
41Nb
42Mo

Figure 16

higher than that at Ni^{80} in the previous results (Section II-5), while it is reversed in the final results in this section (Figure 15). A slight increase of humps at lighter isotopes of the same elements is noticed, too. For instance, a careful comparison shows that the Ni^{64} hump in Figure 12 is higher than that in Figure 3, which is the expected effect of temperature.

A striking change in shape of the abundance curve is noticed if we compare the results at $T = 5 \times 10^9$ °K and those at 2×10^9 °K. For this purpose the abundance curves at these temperatures at $E_F = 10$ Mev are plotted together in Figure 17. The maximum nucleus is the same, that is, Ge^{82}. The difference is that, at the lower temperature (2×10^9 °K), the peak is sharply concentrated around Ge^{82} and that the contribution of all elements other than a few isotopes of Ge, Zn, Se and Ni is negligible, with the abundance less than 10^{-10} times the maximum, while other elements around the peak become more important with the increase of temperature. This is why for a very cold body it is justified to use the method in Section II-3 as a first order approximation, where only the top nucleus was included. When the temperature becomes as high as 5×10^9 °K, this is no longer justified, because in Section II-3 we used the approximation $\rho = A_m\, n(A_m, Z_m)/N_o$ (where A_m and Z_m is the mass number and atomic number of the top element and N_o is the Avogadro's number) but at sufficiently high temperatures this approximation breaks down and

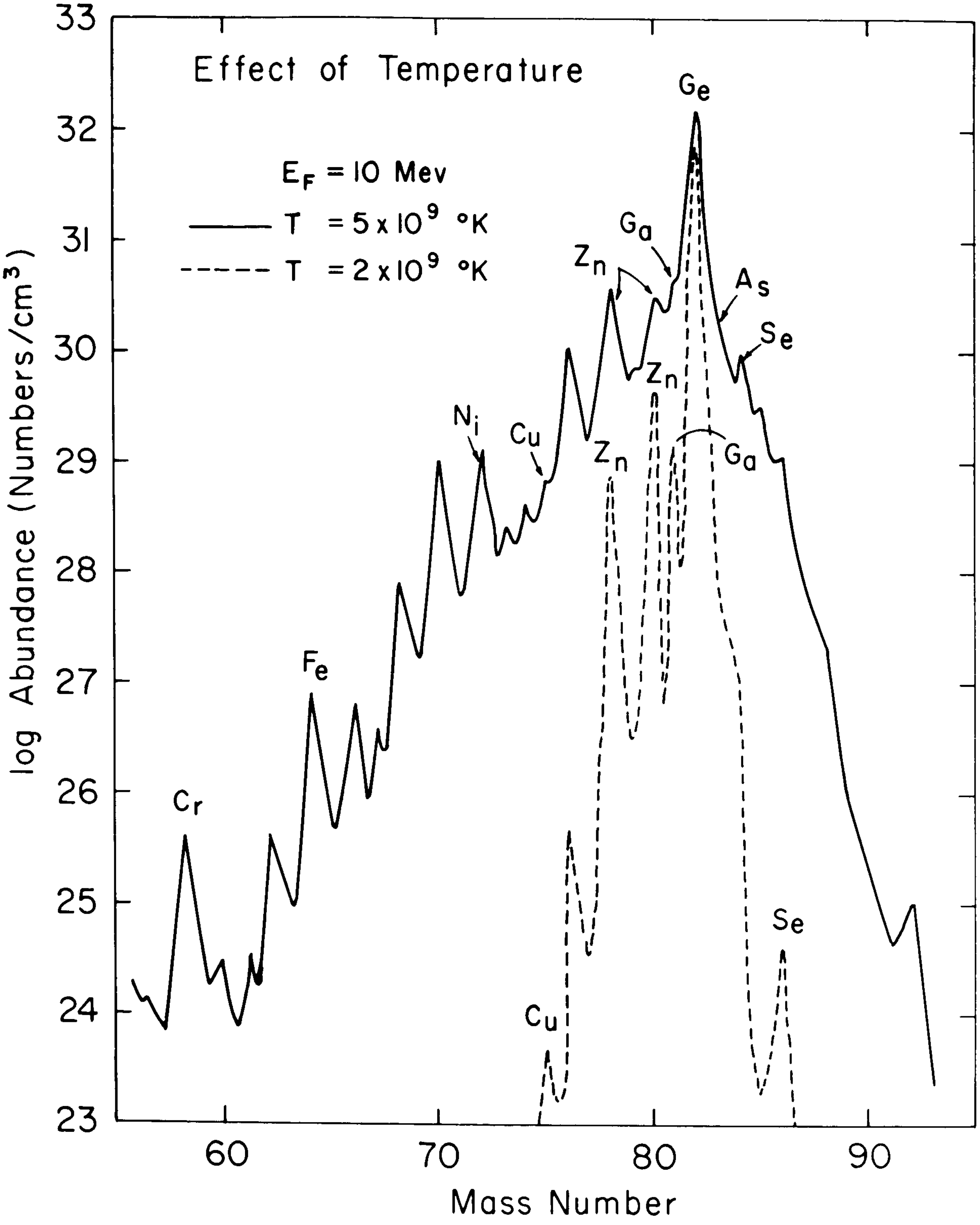
Effect of Temperature
E_F = 10 Mev
T = 5 x 10⁹ °K
T = 2 x 10⁹ °K
log Abundance (Numbers/cm³)
Mass Number
33
32
31
30
29
28
27
26
25
24
23
60
70
80
90
Cr
Fe
Ni
Cu
Zn
Ga
Ge
As
Se
Zn
Zn
Ga
Cu
Se

Figure 17

an exact summation of $\rho = \sum_i A_i\, n(A_i, Z_i)/N_o$ must be carried out over all the nuclei of appreciable abundance, as was done in this section. As can be noticed in Figure 17, the increase of abundance with the increase of temperature is more significant on the ligher side of the peak.

As temperature is increased above 5 billion degrees up to a point where a sudden transition to the neutron phase takes place, the behavior nearly remains constant. At this point, a transition from the peak at the heavier element group to the peak at the lighter element group takes place very quickly and all elements are converted to pure neutrons within a very narrow temperature range. The exact temperature at which this transition to the neutron configuration takes place is very sensitive to density. For a density higher than $\sim 10^{12}$ gm/cm^3, we have a neutronic configuration even at zero temperature; for slightly lower density, the transition temperature is expected to be slightly higher than 5 billion degrees. For the much lower density of about $10^7 \sim 10^{10}$ gm/cm^3, the transition temperature is near but somewhat lower than 10 billion degrees. For a density lower than $\sim 10^7$ gm/cm^3, transitions, first to helium at around $5 \sim 6$ billion degrees, and then to neutrons at about 10 billion degrees, are expected from our investigation. At $T = 10^{10}$ °K, the equilibrium point is shifted to neutrons at all densities considered (0 Mev $< E_F <$ 30 Mev).

The nuclear abundances at $T = 2 \times 10^9$ °K are depicted in Fig. 18. The general behavior is the same as at $T = 5 \times 10^9$ °K (Figure 3). Let us

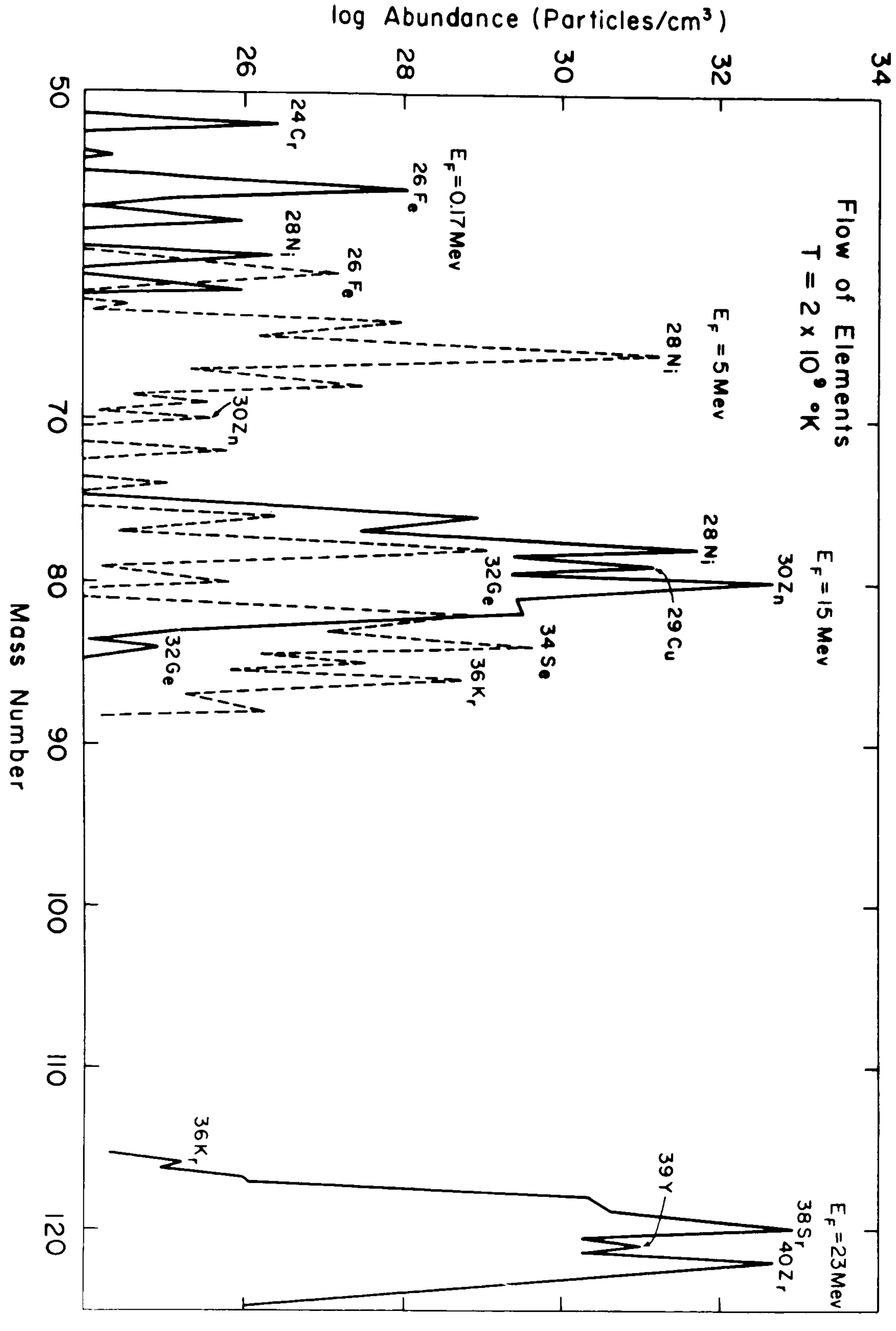
Flow of Elements
T = 2 x 10⁹ °K
log Abundance (Particles/cm³)
26
28
30
32
34
Mass Number
50
70
80
90
100
110
120
E_F=0.17Mev
24 Cr
26 Fe
28 Ni
26 Fe
E_F = 5 Mev
28 Ni
30 Zn
E_F = 15 Mev
28 Ni
30 Zn
29 Cu
32 Ge
34 Se
36 Kr
32 Ge
E_F =23Mev
38 Sr
40 Zr
39 Y
36 Kr

Figure 18

examine the $E_F = 5$ Mev curve. At $T = 5 \times 10^9$ °K (Figure 12), the abundances of other nuclei (than the top nucleus) is so great that the peak is almost flat, in the broad range from A = 20 to almost 90, and it involves various kinds of isotopes of the various elements. Nuclear reactions in each direction through complicated networks connecting great numbers of nuclei, at this temperature, are sufficiently rapid which allows the existence of unstable elements with noticeable abundance. When the temperature is decreased to 2×10^9 °K, the curve is seen to have changed in that sharp peaks now appear at Ni^{66} and near Se^{84} (dashed curve in Figure 18). It is interesting to compare this curve with Figure 2 for a cold body. In Figure 2, the two peaks at Ni^{66} and Se^{84} are almost comparable, though the latter enjoyes the maximum position. In the final calculation at $T = 5 \times 10^9$ °K, the former peak at Ni^{66} is much more pronounced, but the curve at 2×10^9 °K shows that the latter seems to gain a more important position. However, we do not know whether a further decrease of temperature will allow the actual switching over of the maximum from Ni^{66} to Se^{84}. The equilibrium conditions discussed in the beginning of Section II-4 break down at around 2 billion degrees and it is meaningless to carry out calculations for lower temperature. Both the approach for cold matter and that employed in this section are subject to various kinds of uncertainties (which arise, for instance, from the way in which the photo-beta reactions were treated and their key nuclei were selected, etc.), and the most legitimate treatment will be that we do not determine the maximum nucleus either at Ni^{66} nor at Se^{84} but simply regard that either one could be the candidate with a small estimated error. This is no difficulty at all in our case, because in our composition calculation of the surface layers of neutron stars, all the nuclei near the peak (not only the maximum) are included in the summation, and, therefore, it does not matter much which is the actual maximum.

I wish to emphasize the positive side, namely, that the abundance distribution obtained in two entirely different approaches leads to a striking agreement, which is clear from comparing the results of this section with those in Section II-3.

Similar calculations were carried out at 3 and 4 billion degrees also. At 4 billion degrees no interesting change from 5 billion degrees is observed. The abundance curves display almost similar shapes at the same positions. At 3 billion degrees the numerical values of the various quantities are almost halfway between the case of 5 billion and 2 billion degrees. The abundance curves are also intermediate in their shapes, while the peaks remain at the same positions. At 20 Mev, the maximum stays at Ni down to 3 billion degrees. The transition from the peak near Ni to the peak near Zr for lower temperatures, therefore, has occured between 3 and 2 billion degrees.

I should now like to describe how the high density region was treated. In Section II-5, it was noted that the simple technique of adjustment used in that section failed for $E_F = 25$ Mev. This indicates that matter consists mostly of neutrons in this density region, as expected. It was pointed out in Section II-6c that under such circumstances (where neutrons predominate), some of the lightest neutron-rich elements like H^3 and He^6 may be abundant. If the temperature is sufficiently high, it is possible that the heavy elements around the peak regions in Figure 2 (cold matter approximation) may coexist in equilibrium with neutrons and some of the lightest elements, even if such elements are unstable against the emission of neutrons and beta particles. Therefore, an additional investigation was made in this high density region, namely, at $E_F = 20$, 23, 25, and 30 Mev. After a careful investigation of beta processes in the region of the lightest particles, it was concluded that the following induced capture processes are most important:

$H_e{}^6 + e^- \rightarrow H^6 \rightarrow H^3 + 3n$ if $E_\beta = 21.54$ Mev is exceeded

$H_e{}^4 + e^- \rightarrow H^3 + n$ if $E_\beta = 20.6$ Mev is exceeded

$H^3 + e^- \rightarrow 3n$ if $E_\beta = 9.29$ Mev is exceeded.

These endoergic reactions do occur if the Fermi energy of an electron exceeds E_β. At $E_F = 20$ Mev, only the last reaction is energetically possible, while for 23 and 25 Mev, all of them are energetically possible.

All of the above reactions are first forbidden transitions and therefore log ft was set equal to 6.5. The curves like those in Figures 4, 5, and 6 were used to determine f. The f values thus obtained and $P_+ = \left[\ln 2/(ft)\right] f$ for each case are listed below:

E_F	log f			log P+		
(Mev)	H^3	H_e^4	H_e^6	H^3	H_e^4	H_e^6
20	5.7			-0.96		
23	6.4	4.3	3.1	-0.26	-2.36	-3.56
25	7.2	5.7	5.28	+0.54	-0.96	-1.38
30	7.7	6.8	6.62	+1.04	+0.14	-0.04

At $E_F = 25$ Mev, the following remained as the final key nuclei for beta processes in the heavy element region: ${}_{37}Rb^{117}$, ${}_{39}Y^{121}$, ${}_{33}As^{113}$, and ${}_{35}Br^{117}$. In the summations which appear in the abundance formula and the related formulae, all the nuclei in the peak regions of the $E_F = 25$ Mev and 30 Mev curves in Figure 2 were added to the nuclei previously selected for $E_F \lesssim 23$ Mev, and the computations were repeated including the beta processes of the lightest elements.

The results are (i) the additional beta processes in the lightest element regions are not important enough to give any appreciable change in the final result at $E_F \lesssim 23$ Mev, because the abundance of H^3, He^4, and He^6 (which, with the exception of neutrons, are expected to predominate in this region), as given in Table 6, are not sufficiently great at these densities; and (ii) at $E_F \gtrsim 25$ Mev, however, the total matter density for a given E_F is greatly increased as the result of inclusion of these beta processes.

The final numerical results are summarized in Table 6. For Fermi energies of 0.17, 5, 10, 15, 20, 23, and 25 Mev at $T = 5 \times 10^9$ °K and 2×10^9 °K, the following quantities are tabulated: the density ρ, the nucleus (A_m, Z_m) of maximum abundance, its abundance $n(A_m, Z_m)$, the neutron number density n_n, the proton number density n_p, the He^4, H^3, and He^6 abundances n_α, n_t, and n_{He^6} respectively, the electron number density n_e, the total positive ion number density n_{ion}, the electron molecular weight μ_e, and the corresponding quantity for positive ions μ_{ion}. $n(A,Z)$ is defined by (2-9), ρ by (2-15), n_e by (2-14), (2-13a) and (2-13b), while the last three quantities in the table are defined by

$$
\begin{aligned}
n_{ion} &= \sum_i n(A_i, Z_i) \\
\mu_e &= \Big[\sum_k A_k n(A_k, Z_k)\Big] \Big/ \Big[\sum_i Z_i n(A_i, Z_i)\Big] \qquad (2\text{-}44) \\
\mu_{ion} &= \Big[\sum_k A_k n(A_k, Z_k)\Big] \Big/ \Big[\sum_i n(A_i, Z_i)\Big]
\end{aligned}
$$

where k sums over all nuclei for $A \geq 1$, and $Z \geq 0$, and i sums over all nuclei for $A \geq 1$ and $Z \geq 1$.

At $T = 5 \times 10^9$ °K and $E_F = 0.17$ Mev, the number density of helium exceeds that of Fe^{56}, the maximum heavy element, and there was, therefore, some trouble in the adjustment, and the numbers in the first row in Tabel 6 are estimated to be in error to about 10%. The partial densities of helium and iron at this point are nearly equal, and it is expected that with a slight increase in temperature, we will get an almost pure helium configuration.

TABLE 6. Final equilibrium abundance calculations. Density ρ, the mass number and atomic number A_m and Z_m of the element of maximum abundance and its number density $n(A_m, Z_m)$, neutron, proton, He^4, H^3, He^6, electron, and total positive ion number density n_n, n_p, n_α, n_t, n_{He^6}, n_e, and n_{ion}, and electron and positive ion molecular weight μ_e and μ_{ion}, respectively, are listed at seven different values of electron Fermi energy E_F in Mev, at $T = 5 \times 10^9$ °K and 2×10^9 °K, respectively. ρ is in gm/cm^3 and all number densities are expressed in particles/cm^3.

T	E_F (Mev)	log ρ	A_m	Z_m	log $n(A_m, Z_m)$	log n_n	log n_p	log n_α	log n_t	log n_{He^6}	n_e	n_{ion}	μ_e	μ_{ion}
$T = 5 \times 10^9$ °K	0.17	3.86×10^5	4	2	27.02	25.00	26.76	28.61			1.01×10^{29}		2.08	
	5	2.17×10^9	66	28	31.00	28.21	23.48	27.12	19.31	15.22	5.50×10^{32}	2.15×10^{31}	2.375	60.75
	10	1.87×10^{10}	82	32	32.09	29.82	21.11	25.62	20.17	16.94	4.40×10^{33}	1.38×10^{32}	2.563	81.75
	15	6.70×10^{10}	78	28	32.20	31.76	17.97	23.19	20.89	18.38	1.48×10^{34}	5.09×10^{32}	2.720	79.29
	20	1.78×10^{11}	80	28	32.77	33.67	14.56	20.20	21.31	19.22	3.59×10^{34}	1.29×10^{33}	2.985	83.14
	23	2.72×10^{11}	80	28	32.30	33.93	14.07	19.76	21.35	19.30	5.35×10^{34}	1.86×10^{33}	3.06	88.3
	25	8.18×10^{11}	118	36	32.95	35.43	10.94	16.79			6.88×10^{34}	1.87×10^{33}	7.158	263.22
$T = 2 \times 10^9$ °K	0.17	3.64×10^5	56	26	27.51	11.70	12.6	17.27	-10.4	-25.00	1.01×10^{29}	3.89×10^{27}	2.16	56.36
	5	2.15×10^9	66	28	31.27	17.11	6.1	14.59	-6.32	-16.86	5.49×10^{32}	1.94×10^{31}	2.362	66.76
	10	1.87×10^{10}	82	32	32.14	22.25	-2	9.44	-3.76	-11.73	4.40×10^{33}	1.37×10^{32}	2.563	81.99
	15	6.31×10^{10}	80	30	32.65	26.10	-8	4.51	-2.37	-8.96	1.42×10^{34}	4.77×10^{32}	2.677	79.81
	20	1.70×10^{11}	80	28	33.02	30.89	-17	-2.96	-1.33	-6.86	3.60×10^{34}	1.28×10^{33}	2.848	79.85
	23	2.79×10^{11}	120	38	32.86	33.21	-21	-7.36	-1.35	-6.90	5.35×10^{34}	1.38×10^{33}	3.138	122.10
	25	6.81×10^{11}	118	36	32.95	35.28	-26	-12.12	-1.67	-7.55	6.87×10^{34}	1.86×10^{33}	5.970	221.08

The helium abundance, however, drops to practically nothing by the time the temperature has dropped to 2 billion degrees, as the first row in the $T = 2 \times 10^9$ °K box in Table 6 indicates.

This table also shows that n_n increases and n_p decreases steadily with increasing density, but that the proton number is negligible throughout and its importance is restricted to the fact that it is one of the key parameters for the solution of the problem together with n_n and T. As to the tritium and He^6, their number densities are negligible in general but their participation in the beta process causes an effect of some importance at 25 Mev.

At 5 billion degrees, He^4 is never important for $E_F > 5$ Mev, the neutrons are negligible up to $\rho \sim 10^{10}$ gm/cm^3, and at $E_F = 23$ Mev, the neutron number exceeds the number of nuclei of maximum abundance Ni^{80} but its partial density is still less than that of Ni^{28}.

At $E_F = 25$ Mev, neutrons predominate. This is also demonstrated by the value of μ_e and μ_{ion} at this point. For a pure neutron configuration μ_e as defined in (2-44) is infinite. The sudden increase of μ_e at 25 Mev as observed in this table can be, therefore, taken as the indication that the phase transition to neutron configuration has taken place by the time the Fermi energy has risen to 25 Mev. The consideration of the behavior of the gas for densities higher than this is deferred to the next chapter. There is no point in carrying out the calculation of this section (for the heavy element configuration) at $E_F \geqslant 30$ Mev, because the deviation due to neutrons is so significant already at 25 Mev.

At $T = 2 \times 10^9$ °K, all light particles except neutrons are negligible. The general behavior of the neutron number density is similar to the case for 5 billion degrees, except that n_n drops far more sharply with decreasing density at 2 billion degrees than at 5 billion degrees. Some interesting differences between these two temperature regions are noted in Table 6. At $E_F = 0.17$ Mev, the most abundant nucleus shifts from Fe^{56} at $T = 2 \times 10^9$ °K to He^4 at $T = 5 \times 10^9$ °K, a slight shift from Zn^{80} to Ni^{78} occurs at 15 Mev, and there is also a rather significant shift at 23 Mev.

In the definitions of (2-44), the summation over i is carried out over all nuclei except neutrons, while that over k is carried over all nuclei including neutrons. If the neutron number is negligible, $\mu_e \sim (\overline{A/Z})$ and $\mu_{ion} \sim \bar{A}$. That is, these are a measure of the average value of the quantities A/Z and A, respectively, in the absence of neutrons. A comparison of μ_{ion} and A_m is therefore interesting. The behavior is just as expected. Up to about 5 Mev, the effect of helium ($A = 4$) keeps μ_{ion} smaller than the A_m of heavy nuclei. At $E_F = 10$ and 15 Mev, μ_{ion} and A_m almost coincide. As the Fermi energy is further increased, μ_{ion} becomes larger than A_m. This is because in the definition of μ_{ion} in (2-44), the summation in the numerator includes neutrons, while that in the denominator does not. As a consequence of this, μ_{ion}

becomes greater than a straight average of the quantity A when neutrons predominate. The deviation is enormous especially at $E_F = 25$ Mev, where μ_{ion} is more than twice as large as the A_m of the peak nucleus. This is another powerful indication that transition to the neutron phase has occured before this point is reached, somewhere between $E_F = 23$ and 25 Mev.

The results shown in Table 6, except the first row, are estimated to be reliable to within 5%.

II-10 DETERMINATION OF SURFACE COMPOSITION

Having calculated the actual abundance as a function of temperature as well as of density we are now ready to complete the discussion started in Section II-1. We can assume that the formation of a hot neutron star was completed at a very high temperature (say, about 10 billion degrees), and then picture it as a hot, somewhat extended body, which is cooling rapidly, mainly because of the tremendous rate of energy loss by neutrinos. (A quantitative description of neutrino cooling is deferred to Chapter V.) The neutrino loss rate becomes unimportant at a little below a billion degrees; however, we noted that freezing occurs before that. Statistical equilibrium breaks down at around two billion degrees (Section II-4) on the average, which means that the precise freezing point depends on the individual processes along the individual networks, depending on the abundance of the nuclei involved and the rates of the processes. However, it is expected that all such processes break down below about 2 billion degrees. This expectation is consistent with the results just obtained in the previous section (II-9b).

For temperatures below the freezing point, slow nuclear processes and ordinary beta processes may, if given enough time, change the composition slightly from the statistical equilibrium value. However, the neutrino cooling rate is still quite fast even below the freezing point and remains so until the temperature drops to about several hundred million degrees, and we can therefore assume that not enough time is allowed for those slow processes to take place. We are particularly interested in neutron stars with an internal temperature in the approximate range 10^8 to 3×10^9 °K. This is because at higher temperatures such stars cool so rapidly that they escape any means of direct detection while at lower temperatures they are too faint to be observed. Therefore, if we hope to detect the star, its temperature must be restricted to the range stated above. The information from x-ray measurements is perfectly consistent with this expectation (Chapter V).

The above argument leads us to the conclusion that the statistical equilibrium configuration near the freezing point is to be regarded as the surface composition of our neutron star. A possible deviation from this conclusion may come about due to diffusion processes (V-4d). When the scale heights near the surface are sufficiently small, such an effect may cause some appreciable change in the result, as seen in Chapter V.

It is, however, encouraging to note that the composition enters the equation of state, and hence the stellar structure problem, in the form of the molecular weight μ_e or μ_{ion} or electron number density n_e and these quantities are rather insensitive to temperature according to the results shown in Table 6. (The values at 25 Mev are excluded because this energy corresponds to the neutronic phase, outside the range of the present investigation.) A large drop in the value of μ_e at $E_F = 0.17$ Mev and $T = 5 \times 10^9$ °K, as compared with the value at $T = 2 \times 10^9$ °K, is due to the iron-helium conversion. That is, the maximum element at 5×10^9 °K is helium with $\mu_e = 2$, while the maximum element at 2×10^9 °K is iron whose μ_e value is 2.15. μ_e at the two extreme temperatures 2 and 5 billion degrees practically coincide at $E_F = 5$ and 10 Mev. It is more reasonable to attribute the discrepancy of about 3% between μ_e at 5 and 2 billion degrees, at $E_F = 15$ to 23 Mev, to the uncertainties inherent in the method employed, rather than to a temperature effect.

The conclusion is that in the actual construction of a final composite equation of state to be used in our models, the most reasonable procedure will be to take, at each given density, the average of n_e(or μ_e) at 2 billion degrees and that at 5 billion degrees, noting that the difference between the two is extremely small.

CHAPTER III

EQUATION OF STATE

I. INTRODUCTION

It was emphasized in the first chapter that the equation of state is one of the decisive factors in stellar structure problems. There it was expressed in a symbolic form as:

$$P = P(\rho, T, C) \qquad (3\text{-}1)$$

which expresses pressure as a function of density ρ, temperature T, and C which represents the composition. The exact form of (3-1), of course, depends on the particular problem we are to deal with. For instance, if the total pressure supporting the gravitational force inside a star comes from an ideal gas of particles of number density n, it is just

$$P = n\,k\,T \qquad (3\text{-}2)$$

where k is Boltzman's constant. In general, the number density is related to matter density in a simple way. For example, if a star consists of ionized nuclei (A,Z) and completely ionized electrons, and if the partial pressure of nuclei (A,Z) is negligible compared with the electron pressure,

$$\begin{aligned} &n = \rho/\mu H \text{ where } \mu = A/Z, \text{ and } H \text{ is the mass of a proton,} \\ &\text{and } P = k\rho T/(\mu H). \end{aligned} \qquad (3\text{-}3)$$

If matter consists of a completely degenerate gas of particles of number density n, then

$$P = K_1 n^{5/3} \qquad (3\text{-}4a)$$

in the non-relativistic case and

$$P = K_2 \, n^{4/3} \tag{3-4b}$$

in the relativistic case. K_1 and K_2 are constants.

The above examples apply when there are no interaction forces between particles. When the interaction between particles enters, the equation of state can take quite a complicated form. A more general form of the equation of state which applies to the whole degenerate region including both extreme limits (non-relativistic and relativistic) is particularly useful in this research and will be derived in Section III-3. The equation of state for a real gas (meaning "with interaction forces") is investigated in Section III-4. The density appearing in the general relativistic equations is not the common matter density but a total energy density and special care must be taken to recognize this point. There is also an upper limit to the pressure according to the theory of relativity (Section II-5). These aspects will be discussed in later sections. The composite equation of state which is to be used in this research is constructed in Section III-6. Before that, however, we should note that, the better the model we try for, the more it is necessary to deal with a complex structure of various mixtures (not homogeneous matter). For instance, in a simplest approximation we may use just a pure neutron configuration for neutron star models. However, if we analyze the situation more carefully, we find neutron matter to be generally contaminated with various other particles. Therefore, it will be advantageous to concern ourselves with the equation of state for mixtures. In the most general form,

$$P = \Sigma \, P_i(n_i \, , \, T), \tag{3-5}$$

$$n(\rho) = \Sigma \, n_i$$

That is, the total pressure P is the sum of partial pressures P_i of each component i giving an appreciable contribution to the pressure, while the partial pressure of a component P_i is related to the total density of matter ρ (or n) through the partial density of the component n_i. To evaluate the last expression, namely the relation between the partial density of each component and the total density, the relative concentration of each component must be known. Before going into the main discussion of the equation of state, I think it best, for the sake of convenience, to settle this problem of composition first.

III-2 EQUILIBRIUM CONFIGURATION OF MATTER AT HIGH DENSITIES

a. General Discussion

In the previous chapter the equilibrium abundances were investigated up to a density of about 10^{12} gm/cm^3. We noted that the matter consists mainly of iron group elements (ordinary terrestrial elements) up to a density of about 10^7 gm/cm^3; as the density is increased the equilibrium configuration shifts from these ordinary elements to the more neutron-rich nuclei (namely, the nuclei with larger values of A and smaller values of Z/A). The shift is greater the higher the density, and finally when the density reaches about 3×10^{11} gm/cm^3, transformation to neutrons begins. It is interesting to see what happens after that. As the density is further increased eventually all the heavy nuclei will dissolve into free neutrons by means of electron capture, and a pure neutron configuration is expected to result. However, the last statement is not exactly correct because neutrons are unstable against decay to protons and electrons by 0.782 Mev, the neutron-hydrogen mass difference. Therefore, the neutron gas has to be contaminated with protons and electrons, and the minimum partial density of the proton-electron gas must be 10^7 gm/cm^3. In degenerate cold matter, we can assume that all the particles are in the lowest states. That is, the total energy is just the sum of the rest masses of all bosons and the sum of the Fermi energies including the rest masses of all fermions present. For a neutron-proton-electron system the stability is acquired when the neutron Fermi energy plus 0.782 Mev becomes equal to the sum of the electron Fermi energies and the proton Fermi energies, because each fermion occupies cells of phase independently. If the neutron Fermi energy exceeds the amount required by the above equality, two neutrons at the top of the Fermi sea, on colliding, could each be transformed into a proton and an electron. This process will continue until the equilibrium condition is achieved. With the further increase in the total density of matter, the partial densities of neutrons, protons and electrons increase, and when the Fermi energy of the electrons reaches the rest mass of the muon, 106 Mev, neutrons can be transformed into protons and negative muons through the reaction

$$n \rightarrow P + \mu^- + \bar{\nu} \qquad (3\text{-}6)$$

where $\bar{\nu}$ represents an antineutrino. With a further increase of energy, various kinds of hyperons are created, one by one. The appearance of a new particle occurs whenever the Fermi energies (including the rest mass) of the initial and the final particles become equal to the threshold energy for the creation of that particular particle. The situation is analogous to the concept of communicating channels in nuclear physics where a channel for a certain nuclear reaction becomes open when the incident particle acquires an energy greater than or equal to the threshold energy of the reaction. What was said above about the reaction $n \to P + e^- + \bar{\nu}$ regarding the way the equilibrium condition is reached applies also to the reactions involving mesons and hyperons. Some of the hyperon production reactions are:

$$\begin{gathered} 2n \to P + \Sigma^-, \quad 2n \to 2\Lambda^0, \quad 2n \to P + \Xi^-, \\ 2P \to 2\Sigma^+, \quad 2\Lambda^0 \to 2\Sigma^0, \quad 2\Lambda^0 \to 2\Xi^0, \\ n + \Lambda^0 \to P + \Xi^- \end{gathered} \tag{3-7}$$

We note immediately that in these reactions strangeness is not conserved. The time scales of processes like (3-7) are on the order of 10^{-9} sec, which is long compared to nuclear time scales but extremely short from the astronomical point of view. Even though faster reactions exist, these are fast enough to maintain equilibrium. Consequently we can safely assume that thermodynamic equilibrium is maintained throughout.

The density at which the hyperon transformations take place is in the range from 10^{15} to 10^{17} gm/cm^3, far above nuclear density, and as will soon be quantitatively shown, all the constituent baryons (nucleons and hyperons) and leptons (excluding neutrinos which escape from the star as soon as they are created) are highly degenerate soon after creation at the threshold energy. Even when the temperature is as high as 5 billion degrees (the typical temperature used in calculations in Chapter II), the degeneracy is so high that the cold matter approximation is fully justified. (For instance at $T = 5 \times 10^9$ °K and $\rho = 10^{15}$gm/cm^3, the ratio of neutron Fermi energy to kT is about 400.) Therefore, in the preceding and the following discussion of the equilibrium concentration of components at total densities of order of or higher than nuclear density ($\rho \gtrsim 10^{13}$ gm/cm^3), we can assume that all the constituent particles are in their lowest energy states. To make the discussion most general, the configuration in which all possible baryons, mesons, and leptons are in equilibrium in the density range $10^{15}-10^{17}$ gm/cm^3 is treated in the next section, and the results derived there are applied later to more restricted cases. For reasons to become clear shortly (upper limit to the pressure – Section III-5), it follows that higher density values than this are of no interest to us. It should be added that π^- mesons do exist at some of the highest densities in our range.

b. Abundances of Various Components in a Highly Degenerate Baryon Gas

Let us consider an assembly of all kinds of sub-atomic particles, the criteria for the existence and absence of the respective particles, and their relative abundance at a given total density at zero temperature, in a density region of a few orders of magnitude higher than nuclear density.

Some years ago we had a rather tidy list of 30 so-called "elementary" particles. Today 60 or 70 more are added to our list. The first problem we face in this section is to determine which of this profusion of particles survive as the authentic components of our baryon gas in our range of interest. First of all, positrons, photons, neutrinos, positive muons, positive pions and K mesons are all absent at zero temperatures because nothing prevents their decay and annihilation. On the other hand, stability is established between hyperons, nucleons, negative muons and electrons; that is, due to the complete degeneracy of baryons and electrons at zero temperature and the Pauli exclusion principle, the decay products of those particles find no unoccupied place in phase space. The stability of pions is established through the high degeneracy of muons at very high densities. Even though it seems hopeless to take into account all the newly discovered particles properly, the situation is not so bad. First we note that most of the new particles are isobars of familiar nucleons and hyperons in the original 30, and they are in higher states (i.e. heavier) than the originals. As a matter of fact, the final models show that most of the newly discovered particles are in states too high to enter our picture. This is because their effect becomes appreciable only for $p \gtrsim 7 \times 10^{16}$ gm/cm^3, while the present method breaks down before that, due to the relativistic limit on pressure.

Let us consider the lowest states of baryons, N $(939, \frac{1}{2}^+)$, Λ $(1115, \frac{1}{2}^+)$, Σ $(1193, \frac{1}{2}^+)$, and Ξ $(1318, \frac{1}{2})$. Among all other sub-atomic particles, only the isobars of nucleons in the first excited states, denoted by n* and p*, possess masses lower than or comparable with those of the lowest state hyperons listed above. The ground state baryons plus n* and p* turned out to be sufficient in the present problem. Besides these, some leptons and mesons may also enter. In conclusion, it has been decided that the inclusion of the following 13 particles is sufficient for the investigation of our baryon gas below a density of about $10^{17.5}$ gm/cm^3:

$$e^-, \mu^-, p, p^*, n, n^*, \Lambda, \Sigma^0, \Sigma^+, \Sigma^-, \Xi^-, \Xi^0, \pi^- \qquad (3\text{-}8)$$

Most other sub-atomic particles simply do not exist in our degenerate baryon gas due to the fact that their stability is set up by weak interactions and there is nothing to prevent their decay and annihilation as with positrons, positive muons, etc., which have already been mentioned. Some others are absent due to the higher threshold density required for their appearance, as is also the case for most of the excited baryons.

Our problem is now reduced to the actual determination of relative concentration of the 13 sub-atomic particles listed above, in (3-8). (In the above discussion, the words "elementary particles" were avoided, and instead they were called "sub-atomic" particles because some authors feel the former is not a suitable expression.)

Due to the assumption of zero temperature, we first note that

(i) the energy of the system is minimum at equilibrium. - Besides the requirement of minimum energy and conservation of energy, we also note that the total baryon number must be conserved in all processes responsible for the establishment of the equilibrium, and also that the star as a whole, as well as each of its local macroscopic regions, must be electrically neutral; namely,

(ii) conservation of baryon number, and

(iii) conservation of electric charge.

These three requirements are sufficient to determine the abundance of the individual components uniquely as a function of total density. Mathematically, these are written as

$$\epsilon = \frac{c}{2\pi^2\hbar^3}\sum_k a_k \int_0^{P_k} P^2 (M_k^2 c^2 + P^2)^{1/2} dP + n_\pi m_\pi c^2 \qquad (3\text{-}9)$$

where the subscript k denotes $e^-, \mu^-, p, p^*, n, n^*, \Lambda, \Sigma^{0,+,-}$ and $\Xi^{0,-}$

$$\sum_\ell n_\ell = \text{const} \equiv n \tag{3-10}$$

where ℓ denotes a sum over all baryons, and

$$\sum_+ n_+ Z_+ = \sum_- n_- Z_- \tag{3-11}$$

where the integration in the first is from zero to the Fermi momentum, the top of the Fermi sea in momentum space; and ϵ is the total energy density, M the mass, c the velocity of light, p the momentum, n the total baryon number density, n_π the pion number density, m_π the pion mass, $a_k = 2I_k + 1$ is the statistical weight and h is Plank's constant. $n_\pm$ are the positively and negatively charged particle number densities and Z is the charge. An important relation between number density and Fermi momentum is

$$P_k = \left(\frac{6\pi^2}{a_k}\right)^{1/3} \hbar\, n_k^{1/3} \tag{3-12}$$

which is applicable for all fermions. Applying this relation to all fermions, the last two equations reduce to

$$\frac{1}{2}\sum_\ell a_\ell P_\ell^3 = \text{const} \quad \text{and} \tag{3-10'}$$

$$P_p^3 + 2P_{p^*}^3 + P_{\Sigma^+}^3 - P_{e^-}^3 - P_{\Sigma^-}^3 - P_{\Xi^-}^3 - P_{\mu^-}^3 - 3\pi^2\hbar^3 n_\pi = 0 \tag{3-11'}$$

The constant on the right-hand side of (3-10') depends on the total baryon number density. (Conservation of lepton number is not included in the fundamental conditions because neutrinos escape from the star, and the number of leptons in a given volume is not fully specified but is determined by the total baryon number under thermodynamic equilibrium.)

Now our problem boils down to the determination of the minimum of equation (3-9) together with the supplementary conditions (3-10') and (3-11'). Such minimum value problems are well known in classical mechanics. By setting equal to zero the quantity Φ with respect to each P_k, the minimum state of the system is achieved, where Φ is defined as

$$\begin{aligned}\Phi = {} & \frac{C}{2\pi^2\hbar^3}\sum_k a_k\int_0^{P_k} P^2(M_k^2C^2+P^2)^{1/2}\,dP + n_\pi m_\pi C^2 \\ & + \alpha(P_p^3 + 2P_{p*}^3 + P_{\Sigma^+}^3 - P_{\Sigma^-}^3 - P_{e^-}^3 - P_{\mu^-}^3 - 3\pi^2\hbar^3 n_\pi - P_{\Xi^-}) \\ & + \beta(P_n^3 + 2P_{n*}^3 + P_\Lambda^3 + P_{\Sigma^0}^3 + P_p^3 + 2P_{p*}^3 + P_{\Sigma^+}^3 + P_{\Sigma^-}^3 + P_{\Xi^-}^3 + P_{\Xi^0}^3)\end{aligned} \quad (3\text{-}13)$$

The arbitrary constants α and β are eliminated through the differential equations

$$\frac{\partial\Phi}{\partial P_k} = 0 \quad (3\text{-}14)$$

where the subscript k runs through all particles appearing in the original three equations, e, μ, P, P^*, n, n^*, Λ, Σ^0, Σ^+, Σ^-, Ξ^- and Ξ^0. The results are:

(a) for positively charged baryons $k = P$, P^* and Σ^+,

$$(M_k^2c^2 + P_k^2)^{1/2} = (M_n^2c^2 + P_n^2)^{1/2} - (m_e^2c^2 + P_e^2)^{1/2} \quad (3\text{-}15a)$$

(b) for negatively charged baryons $k = \Sigma^-$ and Ξ^-,

$$(M_k^2c^2 + P_k^2)^{1/2} = (M_n^2c^2 + P_n^2)^{1/2} + (m_e^2c^2 + P_e^2)^{1/2} \quad (3\text{-}15b)$$

(c) for neutral baryons $k = n^*$, Λ^0, Σ^0, and Ξ^0,

$$(M_k^2c^2 + P_k^2)^{1/2} = (M_n^2c^2 + P_n^2)^{1/2} \quad (3\text{-}15c)$$

(d) as the relation between leptons and mesons,

$$(m_\mu^2 c^2 + P_\mu^2)^{1/2} = (m_e^2 c^2 + P_e^2)^{1/2} = m_\pi c \qquad (3\text{-}15d)$$

At lower densities all particles whose threshold densities are higher than the actual density are absent and, therefore, their number density is simply zero. For such particles j, the equation $n_j = 0$ replaces one of the equations in (3-15a)-(3-15d). The relative concentration of each component present is determined uniquely by solving equations (3-10'), (3-11') and (3-15a) through (3-15d) simultaneously. As we go from lower to higher densities we meet the phase transition from phase of lower densities (fewer particles) to that of higher densities (a larger number of particles). This problem of concentration as a function of total density is investigated quantitatively in the next sub-section.

c. Number Densities at Different Phases

(i) Proton-electron Phase - This corresponds to the region of the partial density of the electron-proton gas below ~ 10^7 gm/cm^3, where the sum of proton and electron threshold energies is less than neutron rest mass, and the transformation such as $n \rightarrow P + e^- + \bar{\nu}$ eliminates the existence of neutrons and all other particles except protons and electrons. In this case, our equations reduce simply to

$$n_e = n_p = \rho/H \qquad (3\text{-}16)$$

where ρ is the total matter density and H is the proton mass. The first equality relation is just (3-11). The condition (3-10) was used to obtain the last equality relation.

(ii) Neutron Phase - This corresponds to the range $10^{12} \lesssim \rho \lesssim 8 \times 10^{14}$ gm/cm^3 where the sum of the proton and electron threshold energies is larger than the neutron rest mass but where the electron threshold energy is lower than the muon rest mass. In this case equations (3-10'), (3-11'), and (3-14) reduce to

$$n_e = n_p = n_0 \chi^{-3} \left\{ \left[1 + \alpha \chi / \pi + \chi^2 (n_n / n_0)^{2/3} \right]^{1/2} - 1 \right\}^3 \quad (3\text{-}17)$$

with $\alpha = (M_n - M_p)/m_e = 1.564;\ \chi = 2\pi m_e / M_p;$

$$(3\text{-}18)$$

and $n_0 = 8\,(m_e c/\hbar)^3 = 8/\lambda\!\!\!^{-}{}_e^3,$

$$n_n + n_p = n \ \text{(total baryon number density)} \simeq \rho / H. \quad (3\text{-}19)$$

$\lambda\!\!\!^{-}{}_e$ is the compton wave length. Once the neutron number density n_n is specified, the concentration of protons n_p, that of electrons n_e, the total baryon number density n, and the total matter density ρ are found from above.

(iii) Nucleon-muon-electron Phase - We noted in Section III-2a that when the electron Fermi energy reaches about 106 Mev, negative mu-mesons are created through reaction (3-6). For densities higher than this but below the threshold density of the first hyperon appearance, neutrons, protons, negative muons and electrons exist in equilibrium. The equilibrium abundance of each of the constituent particles is calculated from

$$\begin{aligned} (M_p^2 c^2 + P_p^2)^{1/2} &= (M_n^2 c^2 + P_n^2)^{1/2} - (P_e^2 + m_e^2 c^2)^{1/2} \\ (m_\mu^2 c^2 + P_\mu^2)^{1/2} &= (P_e^2 + m_e^2 c^2)^{1/2} \qquad (3\text{-}20) \\ P_e^3 + P_\mu^3 &= P_p^3 \end{aligned}$$

which are deduced from (3-11'), (3-15a) and (3-15d).

To a first approximation, $(P_e^2 + m_e^2 c^2)^{\frac{1}{2}} \sim P_e$ since electrons are already highly relativistic (relativistic parameter $x = P_F/m_e c \sim 6$ near $\rho \sim 10^{15}$ gm/cm^3), and the second of the above equations leads us to

$$n_\mu = n_e\left[1 - (A_\mu/n_e)^{2/3}\right]^{3/2} \tag{3-21}$$

where $A_\mu = (3\pi^2 \lambda_\mu^3)^{-1}$, and $\lambda_\mu = \hbar/m_\mu c$, the muon compton wave length. In this region the muon numbers are still sufficiently small (for instance at $\rho \sim 10^{15}$ gm/cm^3, $\log n_\mu \sim 36.4$, while $\log n_n \cong 38.8$, $\log n_p \sim \log n_e \cong 37.1$) and the number densities of protons and electrons are found in terms of neutron number densities from (3-17). Then equations (3-17), (3-19) and (3-21) completely determine n_p, n_e, n_μ, n, and ρ as a function of n_n.

It may be noted in (3-21) that when $n_e < A_\mu$ no muons exist and therefore A_μ is the threshold electron number density for creation of μ^--mesons. This corresponds to a total matter density of about 8×10^{14} gm/cm^3.

(iv) Hyperon Phase - In the range of density from about 10^{15} gm/cm^3 to 10^{17} gm/cm^3, the hyperons listed in (3-8) begin to appear and rapidly increase in number with an increase in density. In this phase all equations in (3-15a) - (3-15d) are valid except those where pion terms are present. These equations together with the condition of conservation of electric charge and baryon density lead us to

$$\begin{gathered} \mathcal{E}_{Y^0} = \mathcal{E}_n, \quad \mathcal{E}_{Y^+} = \mathcal{E}_n - \mathcal{E}_e, \quad \mathcal{E}_{Y^-} = \mathcal{E}_n + \mathcal{E}_e \\ \mathcal{E}_e = \mathcal{E}_\mu, \quad \sum n_{Y^+} = \sum n_{Y^-} + n_e + n_\mu \end{gathered} \tag{3-22}$$

as the equilibrium equations. Here, $\mathcal{E}_k \equiv (M_k^2 c^2 + P_k^2)^{\frac{1}{2}}$, n is the number density and the subscripts Y^+, Y^-, Y^0 denote positive, negative, and neutral baryons respectively. The equations (3-22) are further simplified to

$$(a)\quad n_k = \frac{1}{2} a_k n_k \left[1 - (A_k^0/n_n)^{2/3}\right]^{3/2} \quad \text{for } k = \Lambda, \Sigma^0, \Xi^0, n^*,$$

$$(b)\quad n_k = \frac{1}{2} a_k n_p \left[1 - \left(\frac{A_k^+}{n_p}\right)^{2/3}\right]^{3/2} \quad \text{for } k = \Sigma^+ \text{ and } p^*,$$

$$(c)\quad n_{\Xi^-} = \frac{1}{2} a_k n_{\Sigma^-} \left[1 - (A_{\Xi^-}/n_{\Sigma^-})^{2/3}\right]^{3/2} \tag{3-23}$$

where
$$A_k^0 = \frac{1}{3\pi^2 \bar{\lambda}_k^3}\left[1 - (M_n/M_k)^2\right]^{3/2},$$

$$A_k^+ = (3\pi^2 \bar{\lambda}_k^3)^{-1}\left[1 - (M_p/M_k)^2\right]^{3/2},$$

$$A_{\Xi^-} = (3\pi^2 \bar{\lambda}_{\Xi^-}^3)^{-1}\left[1 - (M_{\Sigma^-}/M_{\Xi^-})^2\right]^{3/2},$$

$$\bar{\lambda}_k = \hbar/(M_k c)$$

$a_k = 2I_k + 1$ is the statistical weight and I_k is the spin of the particle k. $I_k = 3/2$ for nucleon isobars n^* and p^* and their $a_k = 4$, but for all other particles in this phase $a = 2$.

An argument similar to that for the muon phase implies that the A_k^0 are the threshold neutron number densities, the A_k^+ are the threshold proton number densities and A_{Ξ^-} are the threshold Σ^- hyperon number densities for the creation of the particle k (or of Ξ^- in the last case).

In (3-23) the numbers of positively charged particles have been expressed in terms of proton numbers, that of the negatively charged particles Ξ^- in terms of Σ^-, and neutral particles in terms of neutron numbers. To obtain all the abundances in terms of neutron number densities, n_e, n_p and n_{Σ^-} must be related to n_n. Such relations have been provided by those equations of (3-22) which were not used in the derivation of (3-23). This problem has been solved graphically and the results are plotted in Figures 19 and 20: in the former, electron and proton number densities, and in the latter, on an enlarged scale the number densities of e^-, p, π^- and Σ^- have been plotted against neutron number densities, in which the whole range of the hyperon phase has been covered. Equations (3-21), (3-23), plus Figures 19 and 20 provide means for determining the abundances of all the constituent particles once the neutron number density n_n is specified. Then equation (3-10) gives us the total baryon number density and the relation

$$\rho = \sum_k M_k n_k , \qquad (3\text{-}24)$$

the total matter density. Later it will become clear that it is most convenient to chose n_n as a free parameter instead of ρ, in this region.

The abundance of the various particles in the hyperon phase has been calculated in the manner described above and is shown in Figure 21. For $\rho \lesssim 10^{15}$ gm/cm^3 the total baryon and neutron numbers practically coincide; for $\rho \gtrsim 3 \times 10^{15}$ gm/cm^3 the rapid rise in the number of other baryons depresses the neutron numbers considerably from the curve of total baryon numbers. By the time the density increases to about 5×10^{16} gm/cm^3 the concentrations of all the baryons are about 10^{39} — 10^{40} cm^{-3} and they are all of the same order of magnitude. The electron and μ^- number densities exhibit a sudden dip a little above $\rho = 10^{15}$ gm/cm^3, where the Σ^- hyperon appears. n_μ and n_e become constant at around $\rho = 10^{17}$

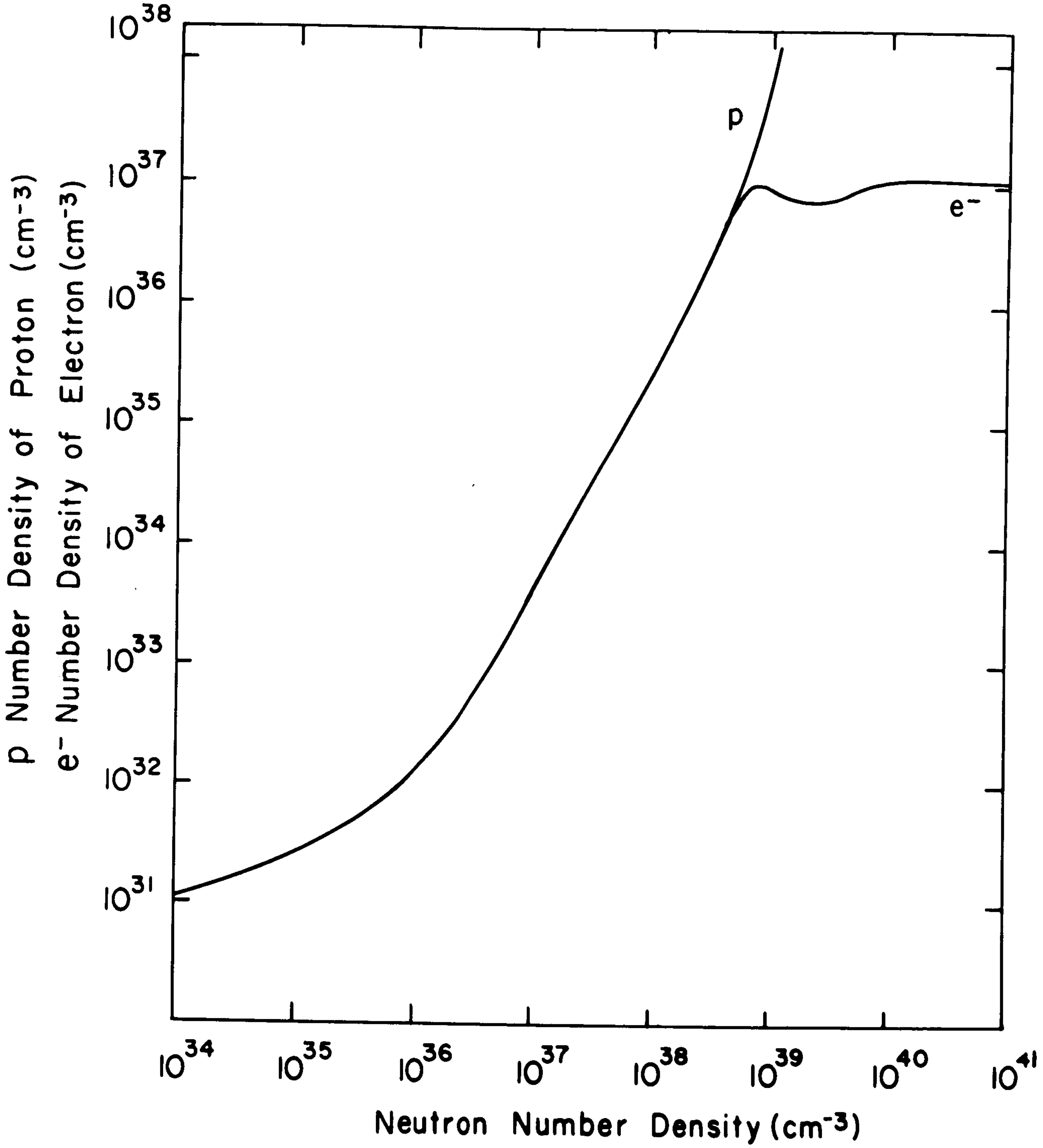
p Number Density of Proton (cm-3)
e⁻ Number Density of Electron (cm-3)
10^38
10^37
10^36
10^35
10^34
10^33
10^32
10^31
p
e⁻
10^34
10^35
10^36
10^37
10^38
10^39
10^40
10^41
Neutron Number Density (cm-3)

Figure 19

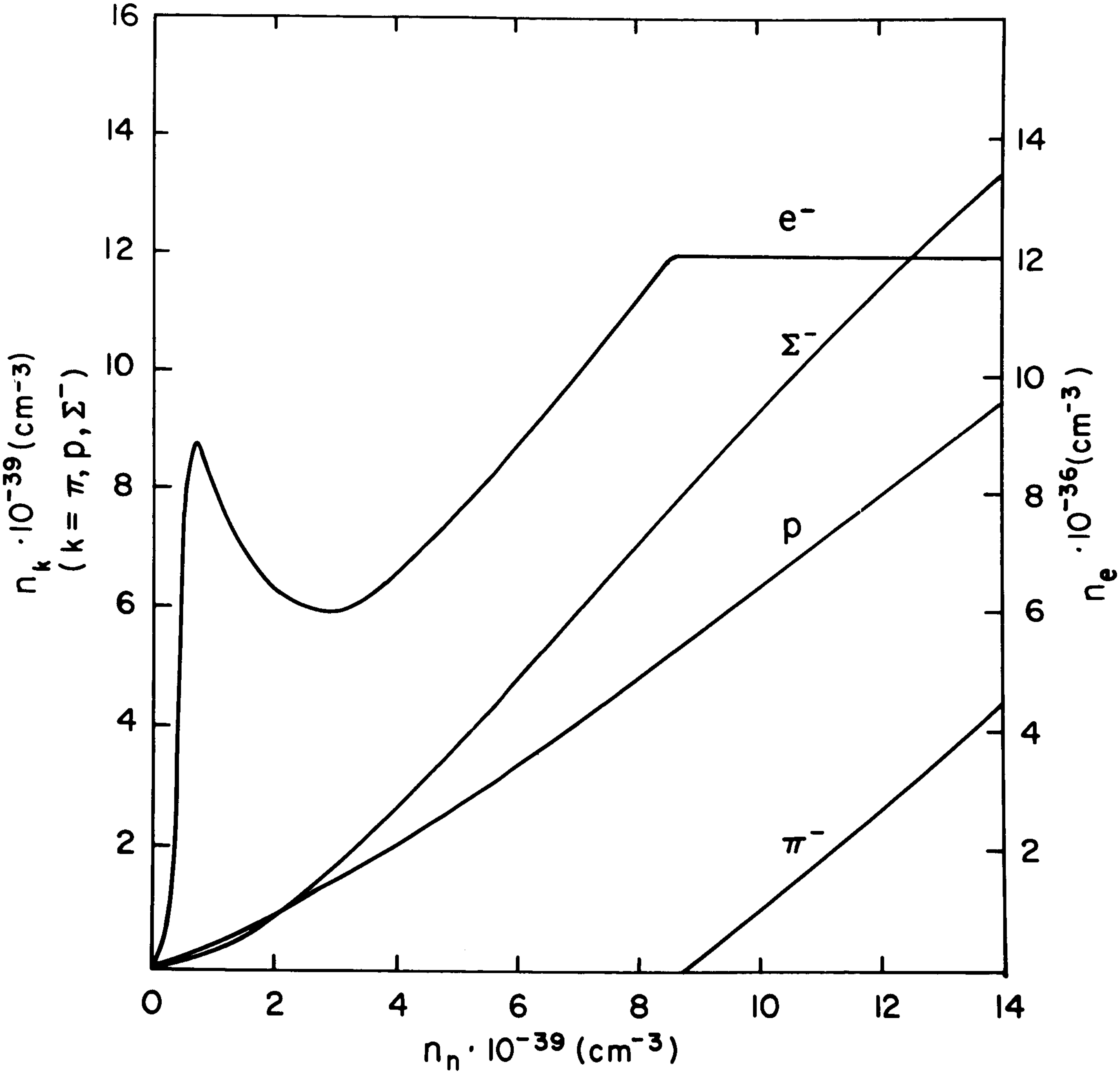
16
14
12
10
8
6
4
2
0
2
4
6
8
10
12
14
14
12
10
8
6
4
2
$n_k \cdot 10^{-39} (cm^{-3})$
$(k = \pi, p, \Sigma^-)$
$n_e \cdot 10^{-36} (cm^{-3})$
$n_n \cdot 10^{-39} (cm^{-3})$
e^-
Σ^-
p
π^-

Figure 20

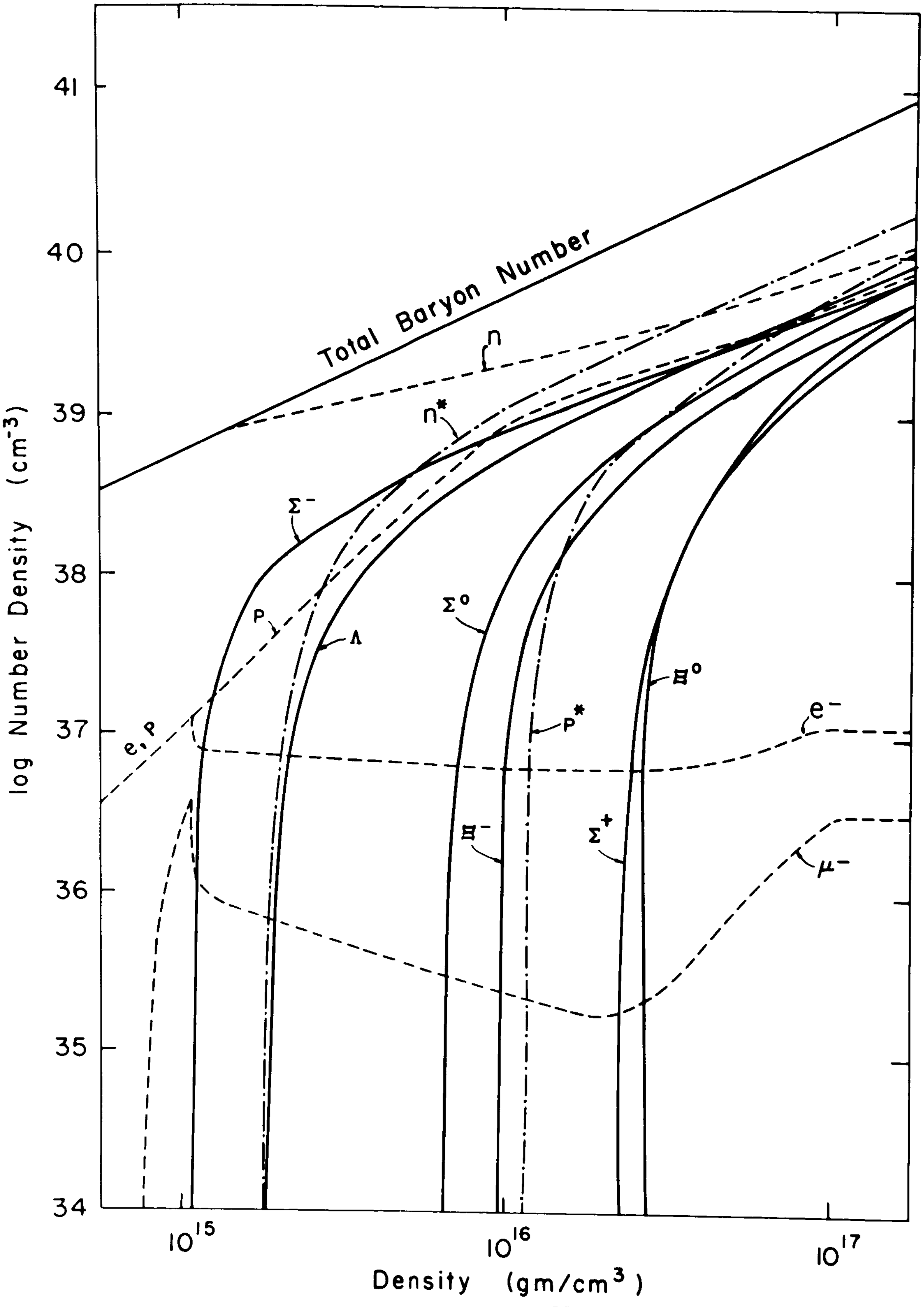
Total Baryon Number
n
n*
Σ⁻
p
Λ
Σ⁰
Ξ⁰
p*
e⁻
e, p
Ξ⁻
Σ⁺
μ⁻
41
40
39
38
37
36
35
34
log Number Density (cm⁻³)
10¹⁵
10¹⁶
10¹⁷
Density (gm/cm³)

Figure 21

gm/cm^3 due to the appearance of π^- mesons, as will be discussed in the next sub-section. The hyperon threshold density ρ_o (the density where a particular hyperon of question appears), total baryon number density n, and the neutron number density at each threshold point n_n are listed in the table below. The particles are arranged in the order of appearance with an increase of density. t_n is a relativistic parameter defined as $t_n = 4 \sinh^{-1} (P_F{}^n/M_n c)$ where $P_F{}^n$ is the Fermi momentum of neutrons which is related to neutron number density as $P_F{}^n = (3\pi^2)^{\frac{1}{3}} \hbar \, n_n{}^{1/3}$ in a relativistic case. M_n is the proton mass.

	μ^-	Σ^-	Λ	n*	Σ^o	Ξ^-	P*	Σ^+	Ξ^o	π^-
log ρ_o	14.39	15.05	15.28	15.23	15.84	16.01	16.10	16.38	16.45	17.21
log n	38.67	38.83	39.05	39.05	39.50	39.75	39.83	40.09	40.18	40.9
log n_n	38.67	38.82	38.98	38.98	39.27	39.34	39.37	39.46	39.57	40.04
t_n	1.93	2.15	2.41	2.41	2.856	2.98	3.09	3.42	3.50	4.37

It may be worthwhile to note that the order in which the particles appear is not in the order of increasing masses. For instance, Σ^- is much heavier than Λ^o, but Σ^- begins to appear at lower densities than Λ^o. The reason is that the Σ^- hyperons have to neutralize the positive charge of the protons whose concentration increases with increasing n_n (as seen in Figure 21), and starting from a certain point, the production of Σ^- is energetically more economical than that of one new proton and two new electrons. The same argument also accounts for the appearance of Ξ^- hyperons earlier than Σ^+ hyperons which are much lighter.

The results are also summarized in Table 7 where the total baryon number density $n = \Sigma n_k$, the number density n_k and the relativistic parameter t_k of each particle k are tabulated for seven typical density values in the hyperon phase (in the range of 10^{15} gm/cm$^3 \lesssim \rho \lesssim 10^{17}$ gm/cm^3). These equations were evaluated for each of the different particles by successively letting k equal n, p, e, Σ, etc., in the previous equations. This table also shows the way various sub-atomic particles come into existence in succession with an increase in density. We note that t_e of electrons is much higher than that of other particles. This is because electrons are already extremely relativistic in this region. The table shows also that all the heavy particles approach the relativistic region (note that $P_F \simeq Mc$ when t is around 3 to 4) when the density reaches about 10^{17} gm/cm^3.

(v) Pion Phase - When the total matter density exceeds 1.4×10^{17} gm/cm^3, it becomes more economical energetically if electrons or μ^- are converted to π^-. This corresponds to the case where the threshold energy of the electrons and negative muons exceeds the rest mass of the negative pions. In this case all the equations in (3-15a) through (3-15d) are valid. After this point is reached the number densities of electrons and μ^--mesons stay constant with a further increase in total density at

$$n_e = 1.2 \times 10^{37} \text{ cm}^{-3} \cong (3\pi^2 \lambda\!\!\!^{-}_{\pi}{}^3)^{-1}$$
$$n_\mu = 3.36 \times 10^{36} \text{ cm}^{-3} = \frac{c^3}{3\pi^2} (m_\pi{}^2 - m_\mu{}^2)^{3/2} / \hbar^3 \qquad (3\text{-}25)$$

This is because all the excess electrons and μ^- above the threshold value are converted to π^- in a higher density region. The π^- number density increases

TABLE 7. Properties of sub-atomic particles in the critical region of $10^{15} \lesssim \rho \lesssim 10^{17}$ gm/cm^3. Σn_k, n_k, t_k and ρ are the total baryon number density, the number density, the relativistic parameter of kth particle, and the total matter density, respectively, in c.g.s. units.

log ρ		15.05	15.30	15.60	15.90	16.07	16.36	17.02
log (Σn_k)		38.83	39.07	39.35	39.64	39.80	40.09	40.74
Log n_k	n	38.82	38.99	39.13	39.27	39.35	39.51	39.92
	P	36.95	37.66	38.22	38.78	38.99	39.23	39.71
	e	36.90	36.86	36.83	36.80	36.79	36.78	37.06
	μ	35.98	35.81	35.63	35.42	35.32	35.29	36.48
	Σ^-	36.67	38.12	38.53	38.82	38.97	39.20	39.71
	Λ	-	36.48	38.11	38.61	38.82	39.13	39.74
	n^*	-	36.78	38.41	38.91	39.12	39.43	40.04
	Σ^0	-	-	-	37.38	38.19	38.81	39.64
	Ξ^-	-	-	-	-	37.59	38.58	39.50
	P^*	-	-	-	-	-	38.78	39.75
	Σ^+	-	-	-	-	-	-	39.29
	Ξ^0	-	-	-	-	-	-	39.39
$t_k = 4 \sinh^{-1} (P_F^k/M_k c)$	n	2.16	2.44	2.68	2.94	3.096	3.42	4.36
	P	0.54	0.92	1.40	2.11	2.432	2.86	3.86
	e	24.66	24.54	24.45	24.36	24.32	24.31	25.16
	μ	2.17	1.92	1.70	1.45	1.35	1.32	3.04
	Σ^-	0.341	1.04	1.42	1.78	1.986	2.38	3.52
	Λ	-	0.32	1.09	1.58	1.834	2.29	3.44
	n^*	-	0.32	1.09	1.58	1.834	2.29	3.44
	Σ^0	-	-	-	0.59	1.084	1.72	3.05
	Ξ^-	-	-	-	-	0.622	1.32	2.54
	P^*	-	-	-	-	-	1.43	2.84
	Σ^+	-	-	-	-	-	-	2.41
	Ξ^0	-	-	-	-	-	-	2.35

so rapidly with the increase of total energy after the threshold point, that it soon becomes of the order of densities of the other members of the mixtures.

d. Summary

The above results show that the critical density at which hyperons appear is about three times as high as the normal nuclear density.

The general results for the whole region are shown in Figure 22. In order to avoid over-crowding the hyperons in this graph have been grouped together in a stripe. The rise of the numbers of these elements is so rapid (almost vertical lines) right after the thresholds have been crossed that the effect of non-degeneracy can be safely neglected in the later calculations. The neutron Fermi energy is about 510 Mev when $n_n \sim 6 \times 10^{38}$ cm^{-3}. All through the region of the hyperon phase, the electron number densities are roughly two to three orders of magnitude lower and the μ^- meson number densities are about three to four orders of magnitude lower than the neutron number densities.

Similar work is found in reference 13. The general agreement is satisfactory, although there are minor small discrepancies in some of the numerical results.

III-3 EQUATION OF STATE FOR A DEGENERATE IDEAL GAS

We note that all the particles appearing in the density regions below about 10^{17} gm/cm^3 are fermions. Even at higher densities the appearance of any bosons except negative pions would be very unlikely unless the total densities

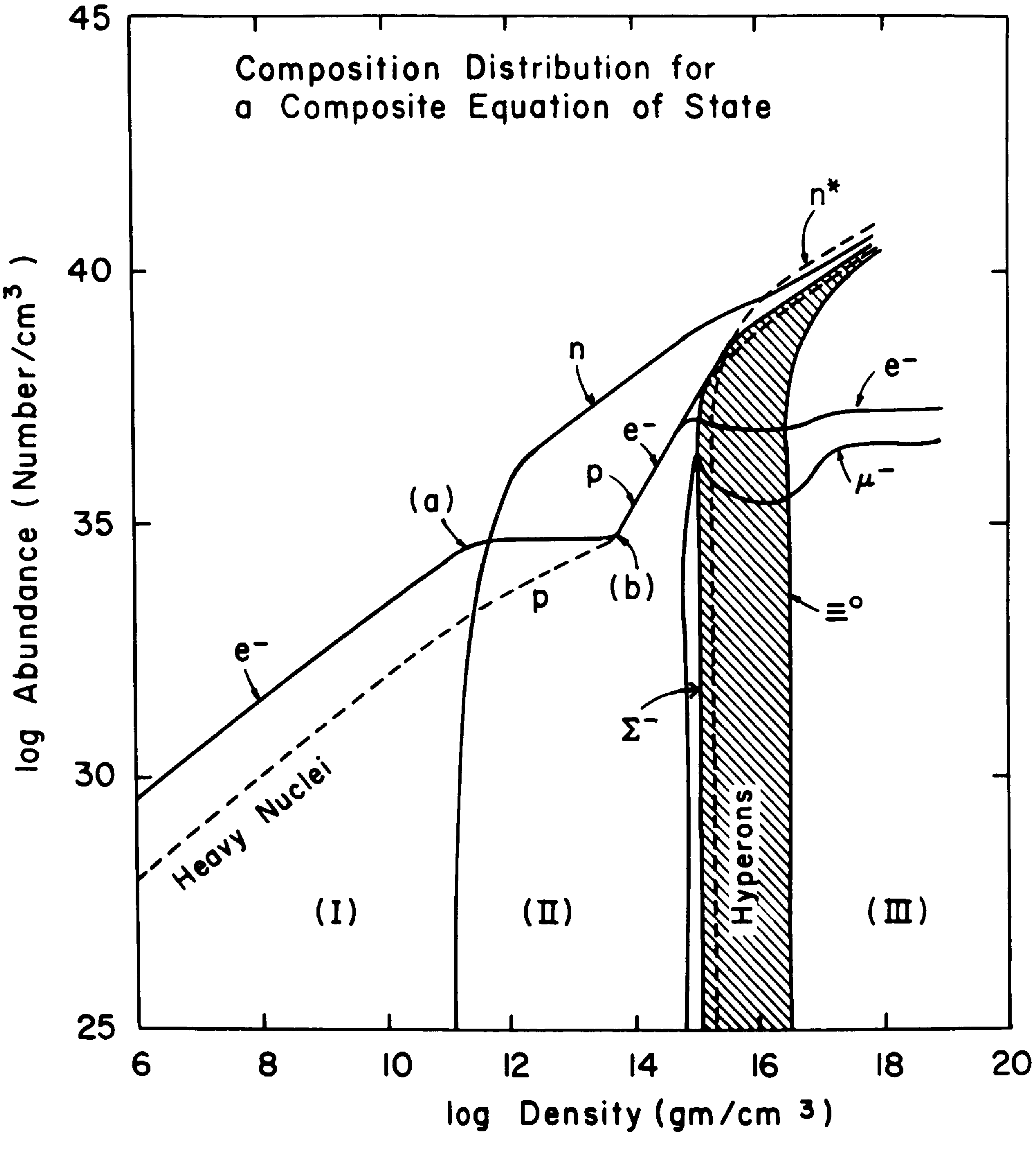

Composition Distribution for a Composite Equation of State
log Abundance (Number/cm^3)
log Density (gm/cm^3)
45
40
35
30
25
6
8
10
12
14
16
18
20
n*
n
e⁻
e⁻
e⁻
p
p
(a)
(b)
μ⁻
Ξ°
Σ⁻
Heavy Nuclei
Hyperons
(I)
(II)
(III)

Figure 22

were to rise to unrealistically high values. Realizability in nature of even the pion phase is rather questionable. In our problem of neutron stars the upper limit set on possible values of pressure gives the upper limit of the density range in which the equation of state of hyperon gases is properly applicable. As is demonstrated later, this limit is reached below the threshold for the appearance of pions.

In the density and temperature regions of interest ($10^{12} < \rho < 10^{17}$ gm/cm^3, $T < 5 \times 10^9$ °K) all particles present in the mixtures are in a highly degenerate state. Therefore, the most general expression of the equation of state for a degenerate gas of any fermions which apply to both the non-relativistic and relativistic regions is extremely desirable. First, in this section, such an equation for an ideal gas (that is, without interaction forces) will be derived. In the next section, the complete expressions with interaction forces will be considered.

Number density n, kinetic energy density $\mathcal{E}_{KE}$ and pressure P for fermions are expressed as(7):

$$n = \int_0^\infty \frac{Z}{V}(E)\,dE \Big/ \left[\exp(\alpha + E/\tau) + 1\right]$$

$$\mathcal{E}_{KE} = \int_0^\infty \frac{E}{V} Z(E)\,dE \Big/ \left[\exp(\alpha + E/\tau) + 1\right] \qquad (3\text{-}26)$$

$$\text{and } P = \frac{\tau}{V} \int_0^\infty \log\left\{1 + \exp\left[-(\alpha + E/\tau)\right]\right\} Z(E)\,dE$$

$$\text{where } E = (P^2c^2 + m^2c^4)^{1/2} - mc^2 \qquad (3\text{-}27)$$

and $Z(E)\,dE$ = the number of quantum states between E and E + dE.

Generally, it is more convenient to express this in momentum space as

$Z(P)\,dP = \dfrac{8\pi V}{h^3} P^2\,dP$ = number of quantum states with momentum between P and P + dP.

E is the energy, P the momentum, m the mass of the particle, $\alpha = \mu/kT$ and $\tau = kT$, where μ is the chemical potential. In complete degeneracy, $1 + \exp(\alpha + E/\tau) = 1$ and all the states are filled up to Fermi energy E_F and terminated there. In that case the above equations reduce to

$$n = \frac{8\pi m^3 c^3}{\hbar^3} \int_0^{\theta^0} \sinh^2\theta \cosh\theta \, d\theta$$

$$\mathcal{E}_{KE} = \frac{8\pi m^4 c^5}{\hbar^3} \int_0^{\theta^0} \sinh\theta \cosh\theta (\cosh\theta - 1) \, d\theta \tag{3-28}$$

$$P = \frac{8\pi m^4 c^5}{3\hbar^3} \int_0^{\theta^0} \sinh^4\theta \, d\theta$$

with $\sinh\theta \equiv P/mc$, $\sinh\theta^0 \equiv P_F/mc$ where P_F is the Fermi threshold momentum, $E = mc^2(\cosh\theta - 1)$. (3-29)

After the integrations are carried out, they are expressed in parametric form as:

$$n = \frac{8\pi m^3 c^3}{3\hbar^3} \sinh^3\frac{t}{4} \tag{3-30a}$$

ε is the energy density including rest mass

$$\mathcal{E} = (\sinh t - t) K \tag{3-30b}$$

$$P = \left(\sinh t - 8\sinh\frac{t}{2} + 3t\right)\frac{K}{3} \tag{3-30c}$$

where $K = m^4 c^5/(32\pi^2 \hbar^3)$ is a constant. (3-31)

The new parameter t is defined as

$$t = 4\theta_0 = 4\sinh^{-1}(P_F/mc) \tag{3-32}$$

The last five equations are extremely important in our problems and will be referred to frequently.

I think it worthwhile to explain how the above equations are applied to equations of state which are to be used in evaluating ordinary hydrostatic equations (without general relativity) as well as to those corresponding to the general relativistic equations.

In the former (without general relativity), the densities appearing in the stellar structure equations are ordinary matter densities. For a pure neutron gas, the density ρ is just number density n times neutron mass M_n, and (3-30a) plus this relation gives us the expression for ρ in terms of t:

$$\rho = \frac{8\pi M_n^3 c^3}{3 \hbar^3} \left(\sinh^3 \frac{t}{4}\right) M_n \tag{3-33}$$

This plus (3-30c) then represent the parametric form of the equation of state for a pure neutron gas without general relativity.

If we are dealing with a gas consisting of non-degenerate nuclei (A,Z) and completely ionized highly degenerate electrons, then the number density of electrons and total matter density are related to each other through the first equation in (3-3) and using the notation used in (3-3), the density can be expressed in parametric form through (3-30a) as

$$\rho = \mu H \frac{8\pi m_e^3 c^3}{3 \hbar^3} \sinh^3 \frac{t}{4} \tag{3-34}$$

This plus (3-30c) give us the equation of state for a degenerate electron gas. We note that the parametric expression of the equation of state for a degenerate electron gas is identified with the equation of state used by

Chandrasekhar for white dwarfs (p. 415) of reference 7 if the parameter t here and x there are related to each other through

$$t = 4 \sinh^{-1} x \tag{3-35}$$

$$\text{or} \qquad x = P_F / mc \tag{3-36}$$

An equation of state in the form of (3-30c) plus (3-34) is valid in the outer layers of neutron stars of sufficiently low density where electron pressure is dominant and where the general relativistic effect is unimportant.

In the greater part of neutron cores or hyperon cores, as we noted in Chapter I, the general relativistic expression of the structure equations (1-8) and (1-9) must be used. In these equations, the equations of state appear in a form containing $\mathcal{E}(P)$ (energy density) instead of $\rho(P)$ (matter density). In this case, equations (3-30b) and (3-30c) constitute a parametric form of the equation of state for an ideal gas.

In this research the last form of the equation of state (3-30b) and (3-30c) for the partial energy density and the partial pressure of all the constituent particles in mixtures is used, for electrons as well as for other heavier particles, because in the low density limit, (3-30b) in all cases reduces to (3-34) for electrons and to (3-33) for baryons.

III-4 EQUATIONS OF STATE FOR A DEGENERATE REAL GAS

a. General Discussion

The equations derived in the previous section are valid if interaction between particles is negligible. For instance, from the work in reference 11(b), we conclude that all the correction terms to the equation of state of a Fermi gas of non-interacting electrons are negligible in the density range of interest in this research ($\rho \gtrsim 10^9$ gm/cm^3) and the formulae derived in the previous section is perfectly valid for electrons.

The situation is quite different for baryons. This is because the normal nuclear densities are around 3×10^{14} gm/cm^3, while the densities we encounter in typical neutron star problems are about 10^{14} to 10^{16} gm/cm^3. As the density of a neutron gas increases above about 10^{12} gm/cm^3 the attractive nucleon-nucleon interaction potential begins to become effective and depresses the total energy and pressure below the values of ideal Fermi gases. It is well known that the nuclear potential in effect becomes strongly repulsive in the extremely high density limit to prevent collapse (for $\rho > 10^{15}$ gm/cm^3). The exact details of the behavior of nuclear potentials in this range (higher than nuclear densities) are not yet well known. However, various models of nuclear potentials in different density regions have recently been constructed by different authors.(11b), (51), (52),(53) Some of these models which are particularly interesting in the problem of neutron stars are discussed in the next sub-sections b to f.

Before that, a brief outline of how the equation of state is to be modified in the presence of such interaction forces will be considered. In general, if the internal energy is expressed by U and the matter density by ρ, the corresponding pressure is obtained by taking the derivative of U with respect to ρ and by/ multiplying it by ρ/V where V is the total volume of the system and the whole expression is evaluated at zero temperature, namely,

$$P = \left(\frac{\rho}{V} \frac{\partial U}{\partial \rho} \right)_{T=0} \tag{3-37}$$

In the derivation of parametric forms of the equation of state in the previous section, the energy term consists of kinetic energy and rest mass energy, and the pressure is that due to the kinetic energy. Therefore, the equation of state for a real gas is obtained by adding the additional pressure due to the interaction potential expressed by equation (3-37) to the pressure due to kinetic energy expressed by (3-30c), while the interaction potential energy density is simply added to (3-30b) to obtain the total energy density. Then, the two equations for P and ϵ represent a parametric form of the equation of state for a degenerate real gas. In this case, U in (3-37) stands for the interaction potential.

At the present stage, the behavior of nuclear forces at high particle speeds is not well known. These forces may be dependent not only on mutual distances but on particle velocities and spins as well, or they may involve tensor foces. A serious problem seems to be that many theories which appear to work so successfully in low energy regions fail very badly in high energy regions, although some successful attempts have been made recently, such as a work by Serber(53). Regarding the interaction forces between hyperons, the situation is even worse. As has been stated in reference 54, "the difficulty to explain even the most predominant features of high-energy collisions remains as great as sixteen years ago." Faced with this fact one may feel that the problem must be abandoned until further progress is made in the fundamental theory.

However, it is still thought worthwhile to try to construct models as realistically as possible. The results of this research seem to indicate that such an effort has not been in vain.

Qualitatively, we expect that with an increase of density, the interaction potential first decreases, reaching a minimum when the distance between particles is of the order of the pion compton wave length, and then, for $\rho \gtrsim 10^{15}$ gm/cm^3, it begins to increase rapidly. The introduction of repulsive forces between baryons at close range leads to increased pressure which increases the mass of the configuration. Therefore, the maximum mass limit is expected to be larger if proper interaction forces are taken into account.

Since the nucleon-nucleon potential is more easily investigated than the more general problem of interactions between baryons, and since it appears that the interactions between hyperons are the same strong interactions which bring the nuclear forces within a nucleus into play, potentials which are constructed to fit nucleon-nucleon experimental data are used in this research as the average potential fields which apply to all baryons.

b. Skyrme Equation of State(9,10)

A simple three-body effective nuclear potential has been constructed by Skyrme which represents quite well many features of the more complicated many body approach. In this model, the total energy density including rest energy is expressed as

$$\epsilon = c^2 \rho + 7.98 \times 10^9 \rho^{5/3} + 9.79 \times 10^{-6} \rho^{8/3} - 1.381 \times 10^5 \rho^2 , \quad (3\text{-}38a)$$

where ρ is the ordinary matter density in gm/cm^3 and $\mathcal{E}$ is expressed in ergs/cm^3.

The internal energy (without rest mass) of the system of N nucleons in a volume $(N/6.025) \times 10^{23}\,\rho$ is then given by

$$U = [7.98 \times 10^{9}\,\rho^{2/3} + 9.79 \times 10^{-6}\,\rho^{5/3} - 1.381 \times 10^{5}\,\rho]\; N \times 10^{23}/6.025 \qquad (3\text{-}38b)$$

From (3-37) and (3-38b) the pressure is

$$P = 5.32 \times 10^{9}\,\rho^{5/3} + 1.632 \times 10^{-5}\,\rho^{8/3} - 1.381 \times 10^{5}\,\rho^{2}. \qquad (3\text{-}38c)$$

P is in dynes/cm^2. The first term represents the kinetic energy contribution of the neutrons and the other two terms represent the most important contributors to Skyrme's mean effective potential.

The above derivations are based on the non-relativistic approximation. Equations (3-38a) plus (3-38c) then represent the parametric form of the equation of state for a real degenerate neutron gas in a non-relativistic region. The relativistic Skyrme equation of state is obtained by a simple modification. It is summarized below

$$\mathcal{E}(t) = K(\sinh t - t + 23.9\,\sinh^{8}\frac{t}{4} - 10.1\,\sinh^{6}\frac{t}{4})$$

$$P(t) = K[(\sinh t - 8\sinh\frac{t}{2} + 3t)/3 + 39.9\,\sinh^{8}\frac{t}{4} - 10.1\,\sinh^{6}\frac{t}{4}] \qquad (3\text{-}39)$$

where $K = m^{4}c^{5}/32\pi^{2}\hbar^{3}$

$$\frac{t}{4} = \sinh^{-1}(P_F/m_c);\; P_F = (3\pi^{2})^{1/3}\,\hbar\, n^{1/3}$$

c. Saakyan's Equation of State for a Real Baryon Gas(14)

Because of the scant knowledge we have of the physics of this problem, Ambartsumyan and Saakyan suggested(14) a somewhat arbitrary simple form of potential

$$V(n) = 3.2 \times 10^{-83} n^2 - 6.4 \times 10^{-5} \tag{3-40}$$

and assumed that each baryon experiences this same potential, where n is the total baryon number density. The formula is chosen so that at $n > 10^{40}$ cm^{-3}, V(n) exceeds the kinetic energy of the particles including the rest energy, and at lower densities it coincides with the depth of the potential well of ordinary nuclear matter. This potential form is constructed to provide a qualitative fit to the available data. Their composite equation of state is:

$$\mathcal{E} = \mathcal{E}_0 + nV(n) ; \quad P = P_0 + n^2 \frac{\partial V}{\partial n} \tag{3-41}$$

where

$$\begin{aligned} \mathcal{E}_0 &= K_n \sum_k \frac{a_k}{2} \left(\frac{M_k}{M_n}\right)^4 (\sinh t_k - t_k) \\ &\quad + n_\pi m_\pi c^2 \\ P_0 &= K_n \sum_k \frac{a_k}{2} \left(\frac{M_k}{M_n}\right)^4 (\sinh t_k - 8 \sinh \frac{t_k}{2} + 3 t_k)/3 \end{aligned} \tag{3-42}$$

where $K_n = M_n^4 c^5 / (32 \pi^2 \hbar^3)$

The extra factor $[a_k (Mk/M_n)^4/2]$ is the result of expressing the constant K_k of particle k in terms of K_n of neutrons. k runs over all fermions present except neutrons. M_n = neutron mass, and M_k = mass of particle k.

d. Salpeter's Equation of State(11b)

Salpeter investigated the possible forms of the equation of state for a real neutron gas through a semi-empirical approach.(11b) Instead of density ρ, a parameter r_o defined by $R = r_o A^{1/3}$ is used, where R is the radius of a nucleus of mass number A. r_o is expressed in fermis (10^{-13} cm) and in the case of neutron gases is related to ordinary matter density ρ through

$$\rho = 3.96\ r_o^{-3} \times 10^{14}\ \mathrm{gm/cm^3} \qquad (3\text{-}43)$$

He found the energy per particle in a low density region in analytical form by using the ordinary phase shift approximation and the effective range theory, and concluded that there is no bound state in this region.

In an intermediate range around normal nuclear density, the total energy per nucleon E is first expressed as a function of r_o, z (= Z/A), and three constants which are evaluated by fitting them against experimental information on "ordinary" complex nuclei. For this purpose a simple form of semi-empirical mass formula is used:

$$-E(z, A) = a_1 - a_2 (1-2z)^2 + a_3 A^{-1/3} + a_4 Z^2 A^{2/3} \qquad (3\text{-}44)$$

where a_1, a_2, a_3, and a_4 are constants for binding, symmetry, surface and Coulomb energy terms respectively. Because of the uncertainty in the symmetry energy coefficient a_2, four possible values of a_2 are used. The analytical expression for energy per particle for $a_2 = 29$ Mev for ordinary nuclear matter ($x \cong \frac{1}{2}$) and for the pure neutron configuration (z = 0) are

$$E(r_o, z=\tfrac{1}{2}) = r_o^{-2}[-0.763 + 1.065\ r_o^{-1} + 0.382\ r_o^{-2} + 0.459\ r_o^{-3} - 1.712\ r_o^{1.21}]\ 29.0\ \mathrm{Mev}$$

$$\text{and}\ E(r_o, z=0) = r_o^{-2}[0.157 + 0.710\ r_o^{-1} + 0.321\ r_o^{-2} + 0.697\ r_o^{-3} - 1.368\ r_o^{-1.21}]\ 29.0\ \mathrm{Mev} \qquad (3\text{-}45)$$

Pressure is then obtained from

$$P(r_o) = -(4\pi\ r_o^2)^{-1}\ d\,E(r_o)/d\,r_o \qquad (3\text{-}46)$$

For the lowest value of a_2(22 Mev) the neutrons are bound. For $a_2 = 26$ Mev, the energy never becomes negative but there is a local minimum near $r_o = 2$ fermis. For the rest of the models ($a_2 = 29$ and 34 Mev) the neutron matter is not bound.

The model of $a_2 = 34$ Mev has the highest values of pressure and Salpeter concluded that this case is the most probable.

In the high density region he assumed a static repulsive core of radius 0.45 fermis and applied the "cell-method" to treat this region. According to this method, the potential energy becomes infinite for $r_o = 0.25$ fermis.

e. Equation of State of Wheeler, Harrison and Wakano(8,60)

Their equation of state is plotted in Figure 10-1 of reference 60. At the lowest density limit, the matter consists of solid Fe^{56} of density 7.8 gm/cm^3; therefore its compressibility is very small, and the P/ρ vs. ρ curve is almost vertical until the iron atoms are pressure ionized. Then follows the region of atomic physics. The equation of state corresponding to this region was obtained by correcting the Fermi-Thomas atom model for pressure effects according to the theory of Feynman, Metropolis and Teller. When the pressure ionization is completed pressure increases first as $\rho^{5/3}$, and then, for $\rho \approx 10^7$ gm/cm^3, as $\rho^{4/3}$. The equation of state in this region has been constructed by Chandrasekhar (Chapter IV-2a). In the region $10^7 < \rho < 10^{11}$ gm/cm^3 electrons are captured and the stable nuclei shift from iron to Y^{122} in the manner described in Chapter II-3b. For $\rho \gtrsim 10^{12}$ gm/cm^3 the main composition is neutrons. Wheeler et al did not make a detailed analysis of the complexity encountered after the nuclear density has been reached. They used two different approaches in the high density regions: (1) the simple equation of state of an ideal Fermi gas with 1/9 electrons and protons and 8/9 neutrons, and (2) the hard core approximation, that is, it was assumed that nucleons act upon each other with a hard core effective potential at a distance of about 0.5 fermis.

f. Levinger-Simmons Equation of State

One of the most interesting quantitative works on the neutron-neutron potential in the intermediate density range (near the normal nuclear density) has been published by Levinger and Simmons.(52) Since their work covers the most important region of density for typical neutron star models, the potentials suggested by them are extensively used in this research. In the following their potentials will be introduced first and then equations of state will be constructed using these same potentials.

Instead of using matter density directly, the Fermi wave number k_f is used as the parameter representing density. k_f is related to Fermi momentum through $p_f = \hbar k_f$. At this point, it will be convenient to give relations between different parameters used by different authors to express density. According to the definition $R \equiv r_o A^{1/3}$, for neutrons $A = 1$ and r_o is the radius of the average volume occupied by one neutron. Let us denote this volume by v, and the number density of neutrons by n. Noting that Fermi momentum is related to number density by $P_f = \hbar k_f = (3\pi^2)^{1/3} \hbar n^{1/3}$, the relations between neutron number density n, the average separation r_o and the Fermi wave number k_f are

$$n = \frac{1}{v} = \left[\frac{4}{3}\pi r_0^3\right]^{-1} = \frac{k_f^3}{3\pi^2} \tag{3-47}$$

This leads us to a simple relation

$$k_f = 1.912 / r_o \tag{3-48}$$

On applying the relation $\rho = M_n n$ further, we obtain (3-43) as a relation between ρ and r_o. From (3-43) and (3-48) the relation between ρ and k_f is

$$\rho = 5.64 \times 10^{13} k_f^3 \qquad (3\text{-}49)$$

where k_f is expressed in f^{-1}. (f means fermis, 10^{-13} cm.)

These relations are extremely useful when the results of the work of different authors are compared.

In the Levinger-Simmons potentials the following assumptions are made; the neutron-neutron potential is well-behaved and velocity dependent, charge independence is valid, perturbation theory is applicable and the second-order energy in the perturbation expansion is negligible in the intermediate density region. The last statement is verified in the aforementioned reference. By the assumption of charge independence the result for the neutron-neutron potential can be fitted to the experimentally determined ones for proton-proton phase shifts. This was done by Levinger and Simmons but they neglected to correct for Coulomb effects. The density region in which $0.5 < k_f < 2f^{-1}$ has been covered. Two different velocity-dependent potentials have been adjusted to fit the observed nucleon-nucleon ^1S and ^1D phase shifts. Velocity dependence is assumed for two reasons: (1) it is necessary to fit the observed ^1S phase shifts and (2) it prevents the collapse which is familiar in the nuclear matter problem.

Three potential forms are used, with characteristics as described above. They are conveniently called v_α, v_β, and v_γ, defined as

(i) $\hat{V}_\alpha = -V_0 J_1(r) - (\lambda/M)\bar{P}\cdot J_2 \bar{P}$ where $\bar{P} = -i\hbar\nabla$ and

$$J_1(r) = J_2(r) = \begin{cases} 1, & (r<b) \\ 1/2, & (r=b) \\ 0; & (r>b) \end{cases} \qquad \begin{array}{l} V_0 = 16.9 \text{ Mev} \\ \lambda = -0.21 \\ b = 2.4 \text{ f} \end{array} \tag{3-50}$$

(ii) $\hat{V}_\beta = -V_0 J_1(r) - (\hbar^2\lambda/Mc)\delta(r-c) - (\lambda/M)\bar{P}\cdot J_2(r)\bar{P}$

$$V_0 J_1(r) = \begin{cases} 51 \text{ Mev}, & (r<b) \\ -\text{OPEP}, & (r>b) \end{cases} \qquad J_2(r) = \begin{cases} 1, & (r<c) \\ 1/2, & (r=c) \\ 0, & (r>c) \end{cases} \tag{3-51}$$

OPEP $= -10.83 \exp(-0.708\, r)/0.708\, r$ Mev, $b = 1.6$ f, $c = 0.5$ f, $\lambda = -1.64$

(iii) $\hat{V}_\gamma = -V_0 J_1(r) + (1/M)[P^2 w(r) + w(r) P^2]$

$$V_0 J_1(r) = [1 + 2w(r)]\left\{112 \exp(-1.4r) - \frac{\hbar^2}{M}\frac{[w'(r)]^2}{[1+2w(r)]^2}\right\} \tag{3-52}$$

$$w(r) = 5 \exp(-3.6\, r)$$

v_α fits the accepted low-energy parameters and gives ^1S phase shifts in rough agreement with experimental data but gives much too small values for ^1D phase shifts. For $k_f b > 2$, the region of most interest to us, the ^1D phase shifts start to become important. Because of this, the potential v_α is not used in this research although it is the simplest in form of all three in that it has the shape of a simple square well.

v_β has four adjustable parameters V_0, b, c, and λ, and gives a satisfactory fit to the ^1S and ^1D phase shifts from 20 to 340 Mev. OPEP is the one pion exchange potential which becomes effective for $r > 1.6$ f.

v_γ gives a good fit to ^1S phase shifts and a fair fit to ^1D phase shifts. This potential also gives a good fit at low energies with effective range = 2.65 f and scattering length = − 23.6 f. The units used in (3-50) through (3-52) are: energies in Mev and lengths in fermis f. The three given above are examples of non-local potentials, expanded in powers of p, retaining terms only up to p^2, and adjusted to the two-body experimental data up to 340 Mev (lab system). A rough guess as to the potential in (triplet) odd states is made such that the static terms are weakly attractive in the odd states and the velocity-dependent terms are the same in all states. The tensor and spin-orbit forces are not included.

The first order energies are calculated in the following manner: The total energy through first order E is

$$E = \langle \Phi \mid \hat{H}_o \mid \Phi \rangle + \langle \Phi \mid \hat{v} \mid \Phi \rangle \tag{3-53}$$

where H_o is the kinetic term, treated as the unperturbed Hamiltonian, and $\hat{v}$ is the perturbation given in equations (3-50) through (3-52). Levinger and Simmons used the non-relativistic expression for the kinetic energy term $\hat{H}_o = P^2/2m$ and obtained $\langle \Phi \mid H_o \mid \Phi \rangle = (\frac{3}{5})\, N \,\frac{\hbar^2 k_f^2}{2M}$ where N is total number of particles.

The perturbation term is expressed as a combination of four terms v_o, v_e, ω_o, and ω_e, representing the ordinary static, the exchange static, the ordinary velocity-dependent, and the exchange velocity-dependent terms, respectively. The preceding quantities are determined by the following formulae:

$$\langle \Phi(r) | -V_0 J_1(r) | \Phi(r) \rangle = -(4\pi V_0/\Omega) \int J_1(r)\, r^2 dr \quad \text{for } v_o,$$

$$\langle \Phi(r) | -V_0 J_1(r) | \Phi(-r) \rangle = -(4\pi V_0/\Omega) \int J_1(r)\,(\sin 2kr/2kr)\, r^2 dr \quad \text{for } v_e, \tag{3-54}$$

$$\langle \Phi(r) | (-\lambda/M)\bar{P} \cdot J_2(r) \bar{P} | \Phi(r) \rangle = \left(\frac{4\pi \hbar^2 \lambda}{M\Omega}\right) k^2 \int J_2(r)\, r^2 dr \;(-1)$$

for ω_o of v_α and v_β. ω_o of v_γ is obtained by the same integral if the term $-\lambda J_2(r)$ is replaced by $2\omega(r)$. ω_e is determined by a similar integral in which $\Phi(r)$ in the last expression is replaced by $\Phi(-r)$. In the above, $\Omega = vN = \frac{4}{3}\pi r_o^3 N$. For a Serber force, there are 1/8th of N^2 pairs interacting in even (spin-singlet) states. The four potential terms for a Serber force are then

$$v_o = -(V_0/6\pi)\, k_f^3 \int J_1(r)\, r^2 dr \qquad \text{for } v_\alpha, v_\beta, v_\gamma$$

$$v_e = -(V_0/2\pi) \int J_1(r)\, f_1(2k_f r)\, dr/r \qquad \text{for } v_\alpha, v_\beta, v_\gamma$$

$$\text{where } f_1(y) = -(12/y^2)\sin y + (3/y - 12/y^3)\cos y + 3/y + 12\, y^2$$

$$\omega_o = -(\lambda/20\pi)(\hbar^2/M)\, k_f^5 \int J_2(r)\, r^2 dr \qquad \text{for } \hat{v}_\alpha, \hat{v}_\beta \tag{3-55}$$

$$\omega_e = (\hbar^2\lambda/8\pi M) \int J_2(r)\, f_3(2k_f r)\, dr/r^3 \qquad \text{for } v_\alpha, v_\beta$$

$$\text{where } \quad f_3(y) = (-30 + 360/y^2)\sin y$$

$$+ (3y - 144/y + 360/y^3)\cos y - (36/y + 360/y^3)$$

ω_o and ω_e for a potential $\hat{v}_\gamma$ are obtained by replacing $-\lambda J_2(r)$ in the last two expressions above by $2\omega(r)$.

The ordinary integral of the static term v_o and the ordinary integral of the velocity-dependent term ω_o are evaluated from the first and the third equations above for the each of the three potentials $\hat{v}_\alpha, \hat{v}_\beta, \hat{v}_\gamma$. They are given below.

	Potential v_α	Potential v_β	Potential v_γ
Static v_o (Mev)	$-4.12\, k_f^3$	$-3.02\, k_f^3$	$-4.02\, k_f^3$
v-dep. V_o (Mev)	$0.64\, k_f^5$	$0.045\, k_f^5$	$0.28\, k_f^5$

(3-56)

(k_f in f^{-1})

No such simple expressions are available for exchange integral terms. However, analytical forms are deduced for the exchange integral of the static term v_e of the potential v_α and v_β in the form:

$$v_e = -(v_o/2\pi)\, f_2(2k_f b) \qquad \text{where} \tag{3-57}$$

$$f_2(y) \equiv 4\cos y/y^3 + 4\sin y/y^3 + \cos y/y + \mathrm{Si}(y)^* - 3/y - 4/y^3$$

Similarly, the exchange integrals of the velocity dependent term of $\hat{v}_\alpha$ and $\hat{v}_\beta$ are expressed analytically as

---

*See reference 55

$$\omega_e = (\hbar^{2}\lambda k_f^2/2\pi M) f_4(2k_f c) \tag{3-58a}$$
$$f_4(y) = 72/y^5 + 12/y^3 - 72\cos y/y^5 - 72\sin y/y^4 + 24\cos y/y^3 + 3\sin y/y^2$$

and similarly for v_γ as

$$\omega_e = (3\beta^2\gamma\hbar^2/4\pi M) f_5(2k_f/\beta) \tag{3-58b}$$
$$f_5(y) = \frac{1}{4}y - \tan^{-1}y + \left(\frac{1}{y}\right)\left[(1+\tfrac{1}{2}y^{-2})\ln(1+y^2) - \tfrac{1}{2}\right]$$

The above results show that all four terms v_o ω_o, v_e, and ω_e are functions of k_f only but for v_e and ω_e the dependence on k_f is not simple at all. In reference 52 numerical values of v_e and ω_e for three potential models v_α, v_β and v_γ for different values of k_f in their range are tabulated (Table IV of reference 52). To take care of different exchange mixtures each term of v_o, ω_o, v_e and ω_e is multiplied by an appropriate coefficient. These are defined by

$c_1 = 1 + 3(V-/V+) = 1.3$ where $\frac{V-}{V+} = 0.1$ is the ratio of static forces in odd and even states,

$c_2 = 1 + 3(\lambda-/\lambda+) = 4$ where $\lambda-/\lambda+ = 1$,

$c_1' = 1 - 3(V-/V+) = 0.7$ where $V-/V+ = 0.1$, and (3-59)

$c_2' = 1 - 3\lambda-/\lambda+ = -2$ where $\lambda-/\lambda+ = 1$ for v_o, ω_o, v_e and ω_e respectively.

The energy per nucleon in the final form is then

$$\boxed{\begin{aligned}\mathcal{E} = \frac{E}{N} &= \frac{3}{5}(\hbar^2 k_f^2/2M) + c_1 v_o + c_2\omega_o + c_1' v_e + c_2'\omega_e \\ &= 12.5\,k_f^2 - \alpha k_f^3 + \beta k_f^5 + c_1' v_e(k_f) + c_2'\omega_e(k_f)\end{aligned}} \tag{3-60}$$

where α and β are constants to be determined from c_1 and c_2 given above and v_o and ω_o given in (3-56).

The first term, the kinetic energy term, is proportional to k_f^2 (non-relativistic);

the second term, the ordinary integral of the static term, is proportional to k_f^3; the third term, the ordinary integral of the velocity-dependent term, is proportional to k_f^5; while the last two terms are more complicated. As the table in (3-56) shows the static term v_o is negative, representing the attractive force, while the velocity dependent term w_o is positive, and represents a repulsive force for large k_f, namely, for high density.

For very small k_f, the kinetic energy is dominant and all the rest, coming from a nucleon-nucleon interaction, are negligible. With an increase of k_f, at first the second term depresses the energy due to the attractive force but gradually, with a further increase of k_f, the third term takes dominance over the second and energy goes above the value for a non-interacting Fermi gas. The exchange terms are equal in magnitude to the corresponding ordinary integrals at low density, that is, $v_e \approx v_o$ and $\omega_e \approx \omega_o$; but become negligible at higher densities, that is, $| v_e | \ll | v_o |$ and $| \omega_e | \ll | \omega_o |$ as $k_f \rightarrow \infty$.

v_α, v_β and v_γ as a function of k_f are tabulated in Table V of reference 52. They agree with each other up to $k_f \approx 1\ f^{-1}$, but v_α deviates from the rest sharply for higher values of k_f. The general agreement between v_β and v_γ is good for $k_f < 2$. This shows that the shape independence is no longer valid in the higher density regions. This is reasonable because $k = 2$ corresponds to a density of about 4×10^{14} gm/cm^3, which is somewhat higher than normal nuclear densities ($\sim 3 \times 10^{14}$ gm/cm^3). That is, we are within nuclear force range and the exact shape of the potential should give a large effect.

Because of the poor fit of v_α in the density region of interest, v_α is discarded, and v_β, v_γ and a combination of v_β and v_γ are used in this research. From the above results (3-60), (3-56) and (3-57) through (3-58b), with the help of Table IV of reference 52, $\epsilon \equiv E/N$, the energy per particle, is computed. Energy density $\mathcal{E}$ is then obtained through the relation

$$\mathcal{E} = \epsilon\, n \text{ (where } \epsilon = \frac{E}{N}) \qquad (3\text{-}61)$$

n is the number per unit volume. The equation (3-37) for pressure is modified in this case as

$$P = n^2 \frac{\partial \epsilon}{\partial n} \qquad (3\text{-}62)$$

It is desirable that the kinetic energy be expressed in a more general form which applies to both relativistic and non-relativistic cases. Then the first term of (3-60) is replaced by the more complete expressions given in the previous section (III-3). The final expression of the equation of state for the Levinger-Simmons potential is then represented by

$$\mathcal{E} = K\,(\sinh t - t) + n(-\alpha k_f^3 + \beta k_f^5 + 0.7\, V_e - 2 w_e)\,C \text{ (ergs/cm}^3) \qquad (3\text{-}63)$$

$$P = \frac{1}{3}\left[K(\sinh t - 8 \sinh \frac{t}{2} + 3t) + n(-3\alpha k_f^3 + 5\beta k_f^5)\,C\right] + P_{ex} \text{ (dynes/cm}^2)$$

where $P_{ex} = n^2 C\left[0.7 \frac{\partial V_e}{\partial n} - 2\frac{\partial w_e}{\partial n}\right]$

$$K = m^4 c^5/(3\pi^2 \hbar^3) = 5.117 \times 10^{35} \left(\frac{m}{m_n}\right)^4 \text{ (dynes/cm}^2)$$

where m is the mass of the particle in question and m_n is the neutron mass.

C is a conversion factor from Mev to cgs units

$C = 1.6021 \times 10^{-6}$ ergs./Mev

$\alpha = 1.3\, a_1$, $\beta = 4\, a_2$ where

$a_1 = 3.02$, $a_2 = 0.045$ for v_β in Mev,

$a_1 = 4.02$, $a_2 = 0.28$ for v_γ in Mev. (3-63′)

k_f and t are related through $k_f = \frac{mc}{\hbar}\sinh\frac{t}{4}$, and n and k_f through (3-47). From the above information, pressure and energy densities can be expressed as a function of the parameter t alone and they constitute a complete expression of the Levinger-Simmons equation of state which is used in this research.

It is extremely time-consuming to calculate $v_e, \omega_e, \partial v_e/\partial n$ and $\partial \omega_e/\partial n$ analytically through the use of equations (3-57) and (3-58). In this research, instead, a graphical method has been used. Namely, v_e and ω_e tabulated in reference 52 have been plotted against k_f as shown in Figure 23 and the slopes have been measured. The table listing a set of discrete values of v_e, ω_e, $\frac{\partial v_e}{\partial n}$ and $\frac{\partial \omega_e}{\partial n}$ thus obtained graphically has been used as a basis for interpolation in the region where $k_f \leq 2$ and for extrapolation for the region $k_f > 2$. That extrapolation in this way for higher density regions is justified can be seen by noting that the exchange terms v_e and ω_e are negligible compared with the ordinary terms v_o and ω_o for $k_f \gtrsim 2$.

g. Results

The results are shown in Figure 24, where the total energy per nucleon (including both kinetic and potential energies) is plotted against density. The curves marked v_β and v_γ correspond to the equation of state with the two different kinds of potential used in this section. In addition, the equations of state of Skyrme, Salpeter and of non-interacting particles (kinetic term only) are shown for the purpose of comparison. Even the highest pressure (a_2 = 34 Mev in Section III-4d) in Salpeter's models is considerably lower than that of all the

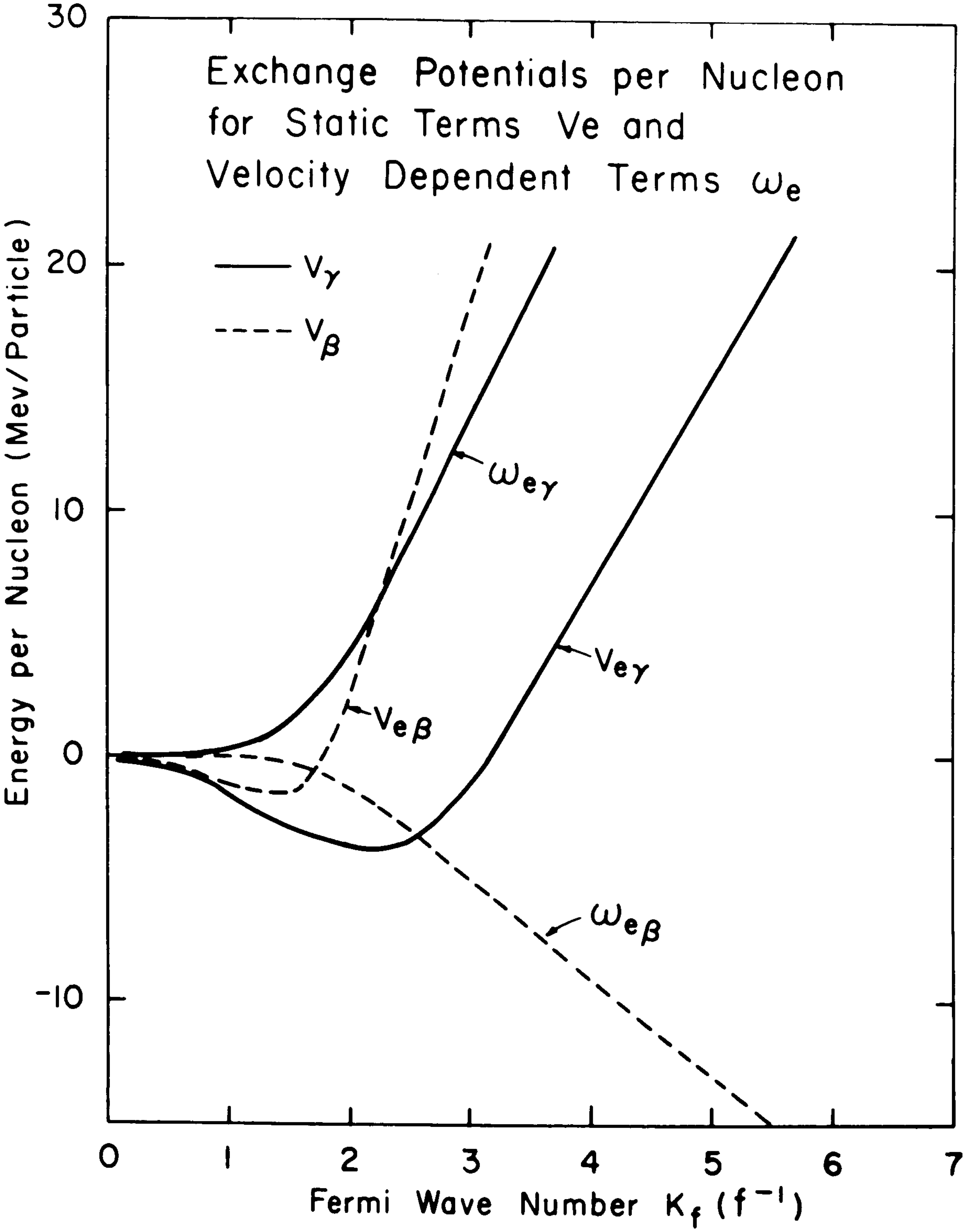
Exchange Potentials per Nucleon for Static Terms Ve and Velocity Dependent Terms ω_e
V_γ
V_β
$\omega_{e\gamma}$
$V_{e\gamma}$
$V_{e\beta}$
$\omega_{e\beta}$
Energy per Nucleon (Mev/Particle)
30
20
10
0
-10
0
1
2
3
4
5
6
7
Fermi Wave Number K_f (f^{-1})

Figure 23

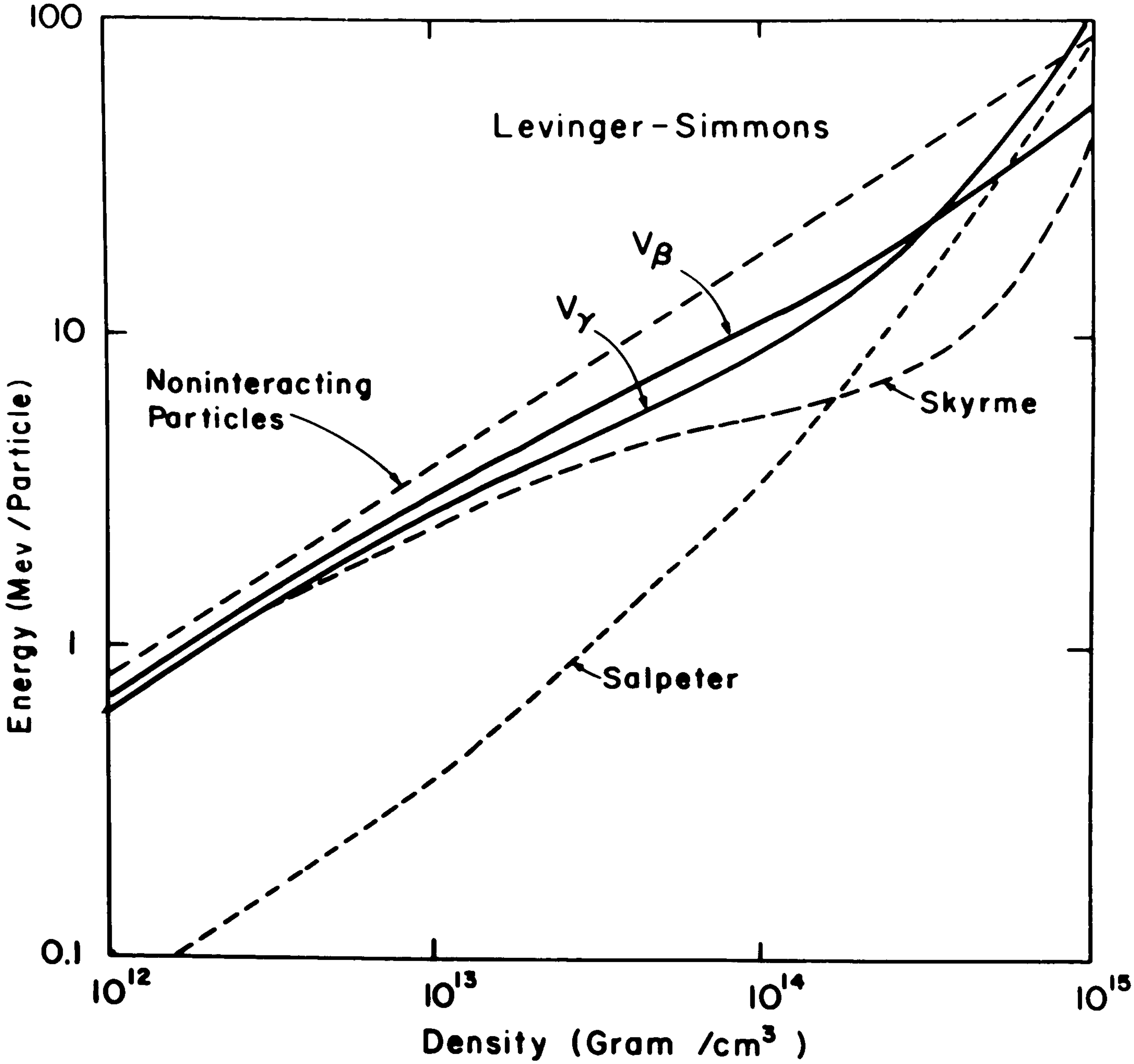
Levinger-Simmons
Vβ
Vγ
Noninteracting Particles
Skyrme
Salpeter
Energy (Mev /Particle)
Density (Gram /cm³)
100
10
1
0.1
10¹²
10¹³
10¹⁴
10¹⁵

Figure 24

other models but this is not surprising as can be seen by noting the large uncertainties inherent in the semi-empirical approach used in Section III-4d.

Among the two potentials V_β and V_γ of Levinger and Simmons, the difference is small in the region of attractive forces but V_γ has a much stronger repulsive effect in the higher density region. This is due mainly to the larger value of the coefficient of the repulsive term, β or a_2 in (3-63') for V_γ as compared with those of v_β. With no nuclear forces all curves would coincide with the line marked "non-interacting particles." The over-all effect of the nuclear potential in most of the region shown in Figure 24 is attractive, but the graph indicates that near $\rho \sim 10^{15}$ gm/cm^3 repulsive terms are already becoming dominant over the rest.

III-5 RELATIVISTIC LIMITATIONS ON THE EQUATION OF STATE

To explain the behavior in high density regions, it has been more or less customary to use the approximation of an incompressible fluid, that is, a hard core repulsive potential which goes to infinity abruptly at a hard core distance (varying from about 0.2 to 0.5 fermis depending on models). Matter becomes incompressible and the pressure can become infinite at a finite density in such models.

In reality, the nucleon core is not ideally rigid and the infinitely large repulsive force acting at a fixed distance may have to be replaced by a more realistic model of the interaction, such as the repulsive terms of the interaction potentials presented in the last section.

However, it is also known that the theory of relativity prohibits the pressure from going to infinity at a finite density. The generally accepted limitation to the pressure imposed by the relativistic principles has been

$$P \leq \frac{\varepsilon}{3} \qquad (3\text{-}64)$$

where P is the pressure and ε the energy density. The inequality sign corresponds to a system of free non-interacting particles with non-vanishing rest masses and the equality sign applies only to electromagnetic fields.

Using the notation of reference 56, the derivation of (3-64) by Landau and Lifshitz is summarized below:

The energy-momentum tensor for an assembly of non-interacting particles has been shown to take the form (p. 89 of reference 56)

$$T_{ik} = \mu c \frac{dx_i}{ds}\frac{dx_k}{dt}$$ where

$$\mu = \sum_A m_A \delta(\bar{r} - \bar{r}_A)$$ is the mass density.

In particular the diagonal space components are reduced to

$$T_{ii} = -\sum_A m_A c^2 \delta(\bar{r} - \bar{r}_A)\left(1 - v_A^2/c^2\right)^{1/2} \leq 0$$

That is, T_{ii} becomes negative for non-vanishing masses and a particle velocity v_A less than the velocity of light. When $m_A = 0$ or $v_A = c$, which corresponds to photons, T_{ii} is zero. There is no real solution for $T_{ii} > 0$. The space components of the energy-momentum tensor of a macroscopic body have been shown (p. 93 of reference 56) to be

$$T_{ii} = -\varepsilon + 3P.$$

Combining this with the above inequality relation, we obtain (3-64). That is, the pressure should never exceed 1/3 of the energy density for non-interacting particles of finite masses and the pressure is equal to 1/3 $\mathcal{E}$ for photons. We immediately notice that above derivation does not prove that the same limitation should apply to interacting particles also. Zel 'dovich(57) proposed that relation (3-64) may be violated in the case of strongly interacting particles, and that a more rigid limitation which should apply to any system is

$$P \lesssim \mathcal{E} \tag{3-65}$$

This absolute limit is set by the fact that "the speed of sound must not exceed the speed of light." The speed of sound is given by(58)

$$D^2 = c^2 \, \partial P / \partial \mathcal{E} \tag{3-66}$$

where D is the speed of sound, c that of light, and P and $\mathcal{E}$ are pressure and energy density as before. If (3-64) is valid, then $D \lesssim c/\sqrt{3}$, but if $P \lesssim \mathcal{E}$, (3-66) leads us to $D < \mathcal{E}$. Since no velocity should exceed the velocity of light according to the theory of relativity, the limitation $P \lesssim \mathcal{E}$ should be an absolute one.

The possibility of the violation of the condition (3-64) arises, for instance, for the case of a fermion field interacting with a boson field. In general, the Lagrangian which describes the fields in interaction is the sum of the free field term and the interaction term. If a spinor field ψ interacts with the scalar boson field ϕ through a direct coupling term, the total Lagrangian(59) is given by:

$$\mathcal{L} = \mathcal{L}_n + \mathcal{L}_m + \mathcal{L}_I$$

where

$$\mathcal{L}_n = -\frac{1}{2}\bar{\psi}(-i\not\nabla + m)\psi - \frac{1}{2}\left(i\frac{\partial\bar{\psi}}{\partial x^{\mu}}\gamma^{\mu} + m\bar{\psi}\right)\psi$$

$$\mathcal{L}_m = -\frac{1}{2}\left(\mu^2\phi^2 - \phi_{\mu}\phi^{\mu}\right)$$

$$\mathcal{L}_I = -G\bar{\psi}\Gamma\psi\phi$$

Γ is an operator which can have any of the following forms:

$$\Gamma = I,\ \gamma_\mu,\ i\gamma_\mu\gamma_\nu,\ i\gamma_5\gamma_\mu,\ \gamma_5$$

G is the coupling constant for direct coupling, μ is the inverse compton wave length $mc/\hbar$ and m is the mass of the particle associated with the field.

The variation of $\mathcal{L}$ with respect to the boson field ϕ leads us to the field equation for ϕ,

$$(\Box + \mu^2)\,\phi = -\,G\bar{\psi}\,\Gamma\psi \tag{3-67}$$

Then, $\bar{\psi}\,\Gamma\,\psi$ acts as a source term for the boson field ϕ, just as the current acts as a source for an electromagnetic field in Maxwell's equations. If the source term is independent of time, there exists solutions of (3-67) which are independent of time in which case $\Box = -\nabla^2$. In particular, for a point charge at rest at the origin the source term on the left is just of a delta function type and we are led to a simple solution of a Yukawa potential type

$$\phi = g\,e^{-\mu r}/r \tag{3-68}$$

where g is a constant corresponding to the interaction charge. Such a potential may represent the interaction of the fermion current with a vector meson field and may well explain the repulsion between baryons in the ultrahigh density regions.

The force between two charges under the potential (3-68) is

$$|F_{12}| = -g\frac{d\Phi}{dr_{12}} = -g^2\frac{d}{dr_{12}}\left(e^{-\mu r_{12}}/r_{12}\right) \tag{3-69}$$

the corresponding interaction energy per each pair is then

$$g\Phi = g^2 e^{-\mu r_{12}}/r_{12} \tag{3-70}$$

If we note that an interaction potential of the above form applies to every pair of particles, we find that the energy per particle is

$$E = M + \frac{1}{2}\int n g \phi \, dV = M + 2\pi g^2 n/\mu^2 \qquad (3\text{-}71)$$

where M is the mass of a particle, n the average number density and g is its charge, $\mu = mc/\hbar$ as before. In the above, c has been set equal to 1. The energy density and pressure are then

$$\mathcal{E} = n E = Mn + 2\pi g^2 n^2/\mu^2 \qquad (3\text{-}72a)$$

$$P = \frac{\partial E}{\partial n} n^2 = 2\pi g^2 n^2/\mu^2 \qquad (3\text{-}72b)$$

From these two equations it is clear that for a finite number density n, $P < \mathcal{E}$ while as $n \to \infty$, $P \to \mathcal{E}$, but it never happens that $P > \mathcal{E}$.

It has been demonstrated above that for baryons under repulsive forces of the type (3-69), which may occur at ultrahigh density, the main pressure comes from the repulsion among baryons through a field of vector mesons and the pressure due to Fermi energies is of no importance as the density goes to infinity.

Generally, the energy density has a power-law dependence on n of the form $\mathcal{E} = a\, n^{\nu}$ where ν is some number and a is a constant. The energy per particle is then $E = a\, n^{\nu-1}$, and the pressure is

$$P = \frac{dE}{dn} n^2 = (\nu - 1)\, a n^{\nu} = (\nu - 1)\, \mathcal{E} .$$

The asymptotic behavior $P = \frac{\mathcal{E}}{3}$ corresponds to $\nu = 4/3$, while $P = \mathcal{E}$ corresponds to $\nu = 2$. In this case, $P = \mathcal{E} = a\, n^2$ which is consistent with (3-72a) and (3-72b) as $n \to \infty$.

From (3-47), $n \propto k_f^3$, and from (3-63), $\mathcal{E} \to a\, n^{8/3}$ and $P \to \frac{5}{3}\, a\, n^{8/3}$ as n goes to infinity (where a is a constant). This means that for the Levinger-

Simmons equation of state, $P \rightarrow \frac{5}{3} \mathcal{E}$ and $D \rightarrow \sqrt{\frac{5}{3}}\, c$, and the speed of sound does exceed the speed of light. Equations (3-38a) and (3-38c) reveal that $P \propto \rho^{8/3}$ and $P > \mathcal{E}$ at $\rho = \infty$ for the Skyrme equation of state. It has been pointed out by Zel'dovich that the asymptotic equations (3-72a) and (3-72b) start to become valid just about at the point where Salpeter's "cell-method" (Section III-4d) starts to become applicable. The conclusion is that all the proper models of the equation of state for a real gas (with repulsive terms) eventually exceed or approach the limit $P = \mathcal{E}$. As soon as this point has been reached, the equation of state must be switched over to the absolute limit of $P = \mathcal{E}$. After that, the question of which baryons, and how many kinds of baryons, are to be included in the mixture has no effect on the equation of state, because in this limit the pressure depends only on the total baryon number density n, and not on the properties of the individual components.

The Levinger-Simmons equation of state (which has been used in this research) reaches this limiting point at around $\rho \sim 10^{16} \sim 10^{16.5}$ gm/cm^3, and that is why the inclusion of higher excited isobars of subatomic particles is not necessary (Section III-2) in this research. This is far below the threshold for the appearance of pions and because of this the pion phase has not been included in the final composite equation of state which is constructed in the next section.

It was noted earlier that the repulsive forces acting at close range may lead to a considerable increase in the possible maximum limit on the total stellar mass (Section III-4a) over that for the case where the equation of state of non-interacting particles has been used. Due to the upper limit set on pressure by relativity as discussed here, this increase in the total mass of stars and the point of the maximum mass may be considerably limited. This problem is further investigated after the neutron star models have actually been constructed.

III-6 COMPOSITE EQUATION OF STATE

The final equation of state for mixtures has been constructed as follows: It has been noted that the interaction forces are negligible for leptons, and the equation of state for an ideal gas has been used to obtain the partial pressures and partial energy densities of electrons and muons (equations (3-30b) and (3-30c)). It has been assumed that all baryons present are under the same potential field of the type v_β or v_γ , the Levinger-Simmons potential, which is a function of total baryon density. Therefore, k_f appearing in equation (3-63) corresponds to the total baryon number density. The actual formulae used are summarized below:

$$\mathcal{E}_{L,S} = K_n \sum_j \frac{1}{2} a_j \left(\frac{m_j}{m_n}\right)^4 (\sinh t_j - t_j) + [V(n)]n \qquad (3\text{-}73)$$

$$P_{L,S} = \frac{K_n}{3} \sum_j \frac{a_j}{2} \left(\frac{m_j}{m_n}\right)^4 \left(\sinh t_j - 3\sinh \frac{t_j}{4} + 3t_j\right) + n^2 \frac{\partial V(n)}{\partial n} \qquad (3\text{-}74)$$

where the summation is over all particles (both leptons and baryons) present. We have noted that the appearance and the abundance of each particle is a function of the total baryon number density n. Therefore with an increase in n, more particles are included in the first terms of the above summations. $a_j/2$ is the ratio of statistical weight of the jth particle to the neutron.

$$K_n = m_n^4 c^5 / (32\pi^2 \hbar^3) = 5.117 \times 10^{35} \text{ dynes/cm}^3$$

$a_j = (2I_j + 1)$, I_j is the spin, and m_n is the neutron mass.

t_j is related to the number density of jth particle through

$$n_j = \frac{8\pi m_j^3 c^3}{3\hbar^3} \sinh^3 \frac{t_j}{4} \tag{3-75}$$

The potential terms are

$$V(n) = (-\alpha k_f^3 + \beta k_f^5 + 0.7 V_e - 2 w_e) C \quad (\text{ergs/cm}^3)$$

$$n^2 \frac{\partial V(n)}{\partial n} = \Big[\frac{n}{3}(-3\alpha k_f^3 + 5\beta k_f^5) + n^2 (0.7 \frac{\partial V_e}{\partial n} - 2 \frac{\partial w_e}{\partial n})\Big] C \quad (\text{dynes/cm}^2) \tag{3-76}$$

where $k_f = (3\pi^2 n)^{1/3}$

$n = \sum_\ell n_\ell$ summed over all baryons ℓ which are present. (3-77)

$C = 1.602 \times 10^{-6}$ ergs/Mev.

α and β are constants given in (3-63'). $v_e, \omega_e, \frac{\partial V_e}{\partial n}, \frac{\partial \omega_e}{\partial n}$ have been determined by the method outlined in the last part of Section III-4f.

First the relativistic parameter t_n of the neutrons has been chosen as a free parameter. Then n_n is found from (3-75). The abundances n_j of all the particles j which are present in different phases have been already calculated in terms of n_n in Section III-2. With the help of (3-75) each n_j can then be converted to t_j . These values are substituted in (3-73) and (3-74) for all particles present to obtain the first terms of energy density and pressure. On substituting the partial number densities of all baryons n_ℓ into (3-77) above, the total baryon number density n is found. Then the potential terms of energy density and pressure are determined through the above equations (3-76).

The total matter densities are found from the equation

$$\rho_m = \sum_j m_j n_j \tag{3-78}$$

In this way the composite equation of state is expressed in terms of a parameter t_n for neutrons which is related to neutron Fermi momentum P_F through $t_n = 4 \sinh^{-1} \left(\frac{P_F}{m_n c} \right)$ and to the neutron number density through (3-30a).

In the higher density region where abundances are calculated by the method of Section III-2, the number densities of all elements are expressed in terms of neutron number density and the above form of the equation of state with t_n as a free parameter is perfectly valid. However, in the much lower density region of heavy ions and electrons of Chapter II, abundances are expressed in terms of matter density ρ. At zero-temperature no neutrons are present for densities below about 3×10^{11} gm/cm^3 and the parameter t_n itself loses its meaning.

Furthermore, the problem still remains regarding the intermediate region. To explain the situtation, number densities of different elements are plotted as a function of matter density in Figure 22. In this graph let us focus our attention on the electron number density curve marked e^-. The part for density below about 3×10^{11} gm/cm^3 was obtained from Table 6, the results of Chapter II. Let us call this region (I). The part for $\rho > 8 \times 10^{13}$ gm/cm^3 was obtained by the method described in Section III-2. Let us call this region (III). The intermediate region where 8×10^{13} gm/cm$^3 > \rho > 3 \times 10^{11}$ gm/cm^3 will be called (II). The border between region (I) and (II) is marked by (a), and that between (II) and (III) by (b). In region (I), we noted that electrons are captured by heavy nuclei when density increases. The nuclei containing too many neutrons will eventually become unstable and disintegrate into free neutrons. At a density slightly higher than (a), the elements near the peak at $E_F \approx$ 23 Mev, such as $_{38}\mathrm{Sr}^{120}$, will coexist with free neutrons. By the time we come to the border (b), all the heavy nuclei are expected to disappear leaving only neutrons, protons and electrons in equilibrium. The exact behavior of the transition of elements from the group of heavy nuclei, electrons and neutrons at (a) into the pure neutron-proton-electron configuration at (b) is quite complicated but the principles which govern the condition of equilibrium are the same in regions (I), (II) and (III), namely, the conservation of total energy, charge, and total baryon number including both the bound and the continium states. Also we note that a discontinuous change of ion numbers is not allowed. This means that a sudden change of heavy elements of ($Z \simeq 38$) to protons ($Z = 1$) at a fixed density does not occur in reality. It is most reasonable to assume rather that the charge Z changes from around 38 to 1 from (a) to (b) (in the density range from 3×10^{11} gm/cm^3 to 3×10^{13} gm/cm^3) in a smooth way. In this case the ionic charge Z is expressed in the following way:

$$Z = 1 + 37x \quad \text{where} \quad x \equiv (\rho_2 - \rho)/(\rho_2 - \rho_1)$$

where ρ_1 and ρ_2 are the matter densities at (a) $\rho_1 = 3 \times 10^{11}$ gm/cm^3 and (b) $\rho_2 = 8 \times 10^{13}$ gm/cm^3, respectively.

Actually, electron number density increases slightly as we go from (a) to (b) with an increase of neutron number density, but an order of magnitude analysis reveals this rise is quite small and not appreciable in Figure 22. This indicates that the greater part of the extra density as we go from (a) to (b) takes the form of neutron partial density. Figure 22 also indicates that there is a rise in the total ion number density as the ionic charge changes from about 38 at (a) to 1 at (b).

At zero temperature region (I) is an ion-electron phase with no neutrons. With a finite temperature a sharp rise in neutron number densities near (a) occurs (from Chapter II); the lower the temperature, the sharper the rise. In region (II), positive ions (heavy nuclei and protons), electrons and neutrons are present where the relative concentrations change rapidly from (a) to (b). Up to this point, it has been most convenient to express everything in terms of matter density ρ, because the abundances n_n, n_e, etc., have been expressed in terms of ρ in this region. t_n and t_e are found from n_n and n_e through (3-75) and they have been substituted into the equation of state (3-73) - (3-74). For $\rho > 8 \times 10^{13}$ gm/cm^3, everything has been expressed in terms of n_n and t_n has been chosen as the free parameter. Special care has been taken so that all the physical quantities are continuous at (b) where the free parameter is changed from ρ to t_n. It has been shown that the pressure obtained in this way (Levinger-Simmons potential) eventually crosses the line $P = \mathcal{E}$. Immediately, on crossing this line, the equation of state is switched from (3-73) - (3-74) to the asymptotic equation of state. Both of the asymptotic expressions $P = \mathcal{E}$ and $P = \frac{1}{3}\mathcal{E}$ have been used, because there is no guarantee that $P > \frac{1}{3}\mathcal{E}$ is actually realized physically, even though it has been shown in Section III-5 that this is possible.

The solid line in Figure 25 represents the final composite equation of state. The nearly straight line in the lower density region corresponds to the electron-heavy ion configuration. Even though it is not apparent from the graph this line is found to be slightly bent downward if we examine it more carefully, which is due to the decrease of Z/A with the increase in density in this region. The big dip at around $10^{12} \sim 10^{15}$ gm/cm^3 is due to the attractive potential; in high density regions it is seen to be switched over to the asymptotic equation $P = \mathcal{E}$.

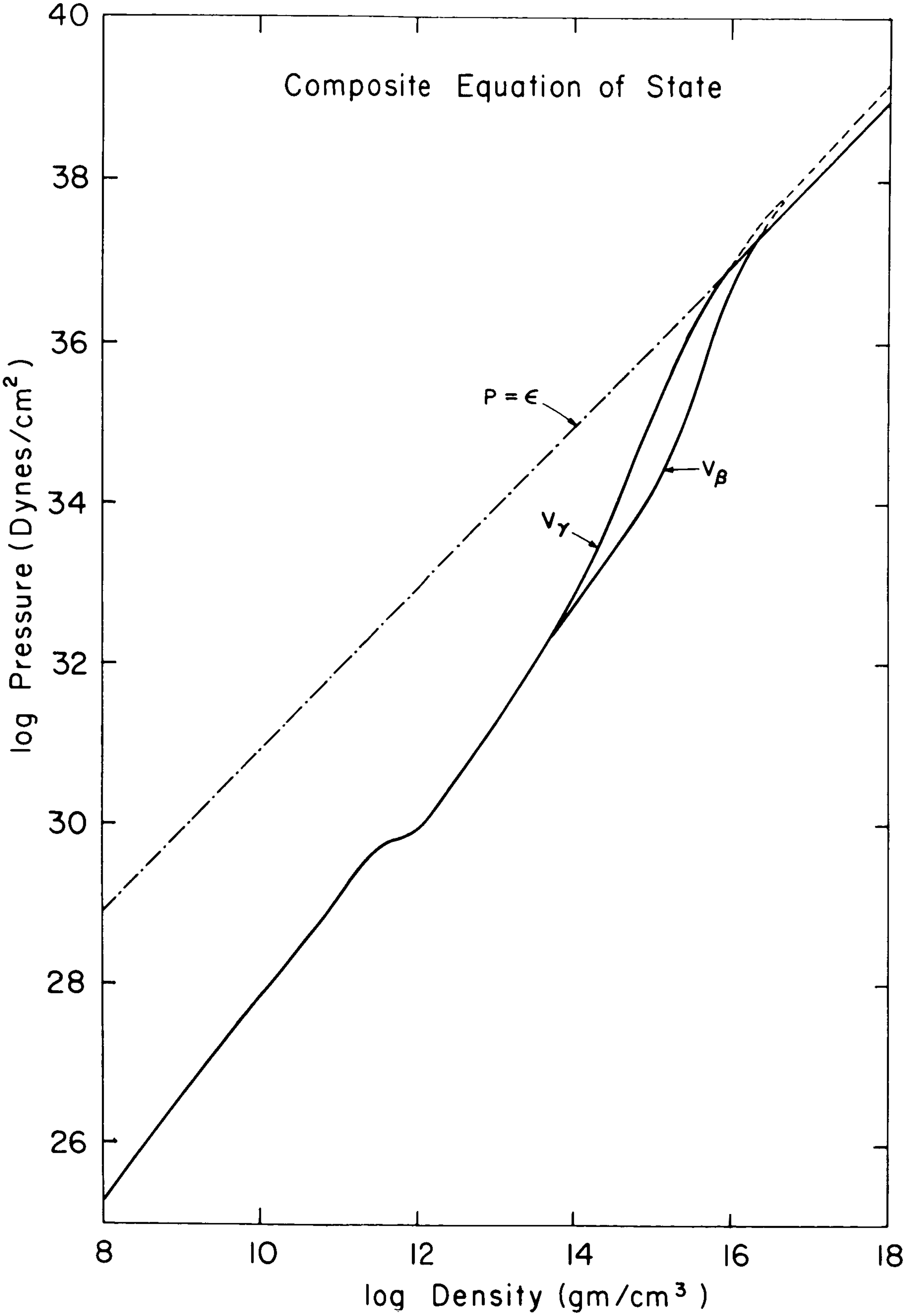
Composite Equation of State
log Pressure (Dynes/cm^2)
log Density (gm/cm^3)
40
38
36
34
32
30
28
26
8
10
12
14
16
18
$P = \epsilon$
V_γ
V_β

Figure 25

CHAPTER IV

MODELS OF COLD NEUTRON STARS

IV-1 GENERAL REMARKS

The problem of the internal structure of neutron stars is fundamentally related to the properties of dense matter. The discussion in the previous two chapters reveals that dense matter has properties which differ markedly from those of ordinary matter. From the study of the equilibrium composition in terms of densities considered in these chapters, we recognize that the problem of the structure of degenerate stars can be worked out in two phases. In one phase the density of the star is relatively low, being around 10^6 gm/cm^3. In this case the crushing force of gravity is counteracted by the pressure of degenerate electrons. A star in this category, that is, one for which the equilibrium configuration is in the electron-nuclear phase, is generally known as a white dwarf. Because the Fermi pressure of the electrons is not sufficient to balance the gravitational force in such a star when the mass is greater than a certain critical limit (about 1.4 $M_{\odot}$), the theory indicated the conclusion that beyond the mass limit the star would be crushed to a point.(7) However, before this limit is reached, it is now known that through the inverse beta processes, electrons are captured by the nucleus and the equilibrium state gradually shifts from the electron-nuclear phase to the neutron-phase in the manner detailed in the last two chapters. It has been shown that a stellar configuration whose central density lies in the range from $10^{8.5}$ gm/cm^3 to $10^{13.5}$ gm/cm^3 (the transition region from the electron-nuclear to the neutron phase) is unstable(8) but another stable stellar configuration is reached when the central density becomes equal to or greater than about 10^{14} gm/cm^3. Here, neutrons are the primary component in the equilibrium composition of the star and, consequently, it is generally known as a neutron star. When the central density $\rho^c \gtrsim 10^9$ gm/cm^3, the electron pressure is no longer sufficient to counteract the enormous pressure due to gravity which increases rapidly with increasing density, but with a further increase of density, the number of free neutrons increases, and when the neutron number density reaches about 2.6×10^{38} cm^{-3}, the partial pressure of degenerate neutrons becomes sufficient to counteract gravity. This corresponds to a total matter density near normal nuclear density (about 3×10^{14} gm/cm^3), where the Fermi level of the neutrons is about 60 Mev. In this region neutrons constitute a non-relativistic degenerate gas. When the central density rises further, another crushing point is reached where even nuclear matter is crushed. At the first crushing point (known as Chandrasekhar's mass limit), the pressure of degenerate electrons is overcome by gravitational forces. At the second crushing point (known as the Oppenheimer-Volkoff mass limit), gravitational force has overcome even the pressure of degenerate nuclear matter.

The title of this thesis is "Neutron Star Models," but because of the interesting behavior of degenerate stars in general, densities ranging from the white dwarf regions to the neutron star regions have been covered in this research, although of course the main emphasis has been placed on higher density regions. For the purpose of comparison, I think it convenient to first introduce the models of other physicists. (In the following, the notation ρ or ρ_m is used for matter density, and $\mathcal{E}$ for energy density, unless otherwise stated. The symbol $M_\odot$ or $\odot$ denotes the mass of the sun = 1.935×10^{33} gms.)

IV-2 PREVIOUS WORK

a. Models of White Dwarfs

An extensive investigation of the general problems related to white dwarfs is found in reference 31. Theoretical models of white dwarfs have been constructed by Chandrasekhar.(7) From equations (3-28) and (3-29) we get

$$P = A f(x) \; ; \qquad \rho = n \mu_e H = B x^3$$

$$f(x) = x\,(2x^2 - 3)(x^2 + 1)^{1/2} + 3 \sinh^{-1} x \text{ , where} \qquad (4\text{-}1)$$

$$A = \pi m^4 c^5/(3h^3) = 6.01 \times 10^{22}, \; B = 8\pi m^3 c^3 \mu_e H/(3h^3) = 9.82 \times 10^5 \mu_e$$

with the same notation as used in Chapter III, and $x = p_F/mc$. These equations, which are identical with (3-30c) and (3-34) if the relation between t and x is as given in (3-35), are used as the equation of state in Chandrasekhar's models. The Newtonian equations (1-1) and (1-2) were then integrated, with the usual boundary conditions.

The relation between the central density and the mass of his models is shown in Figure 26, where μ_e is set equal to 2. As the density goes to infinity, mass approaches a critical value of $1.44\,M_\odot$. Rudkjöbing(62) pointed out that Chandrasekhar's maximum mass is too large due to the neglect of a relativistic "spin-orbit" effect coming from the strong radial electric field in white dwarfs. When this modification is taken into account, the limiting mass reduces to about $1.2\,M_\odot$. Rudkjöbing's result is plotted in Figure 26 together with those for other

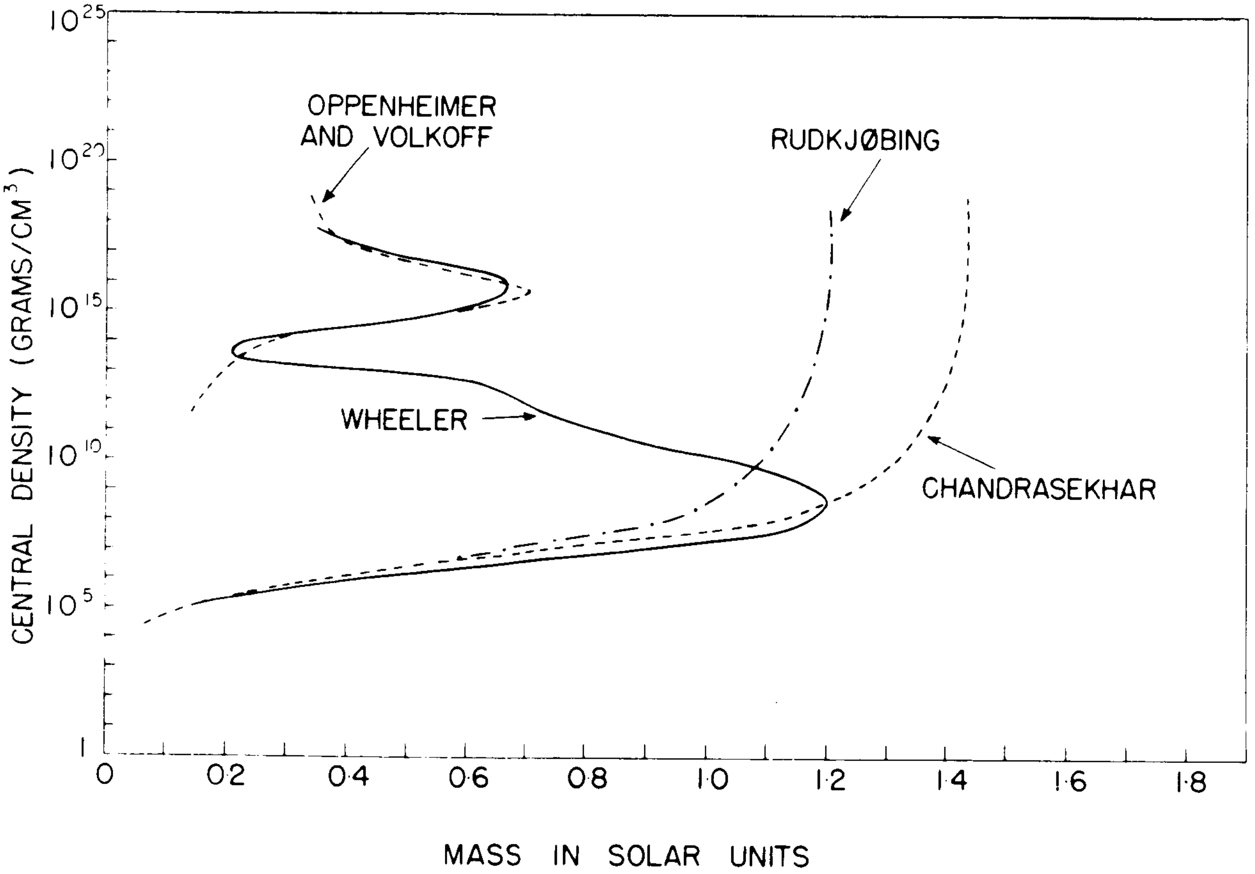
10^{25}
10^{20}
10^{15}
10^{10}
10^{5}
1
CENTRAL DENSITY (GRAMS/CM^3)
0
0·2
0·4
0·6
0·8
1·0
1·2
1·4
1·6
1·8
MASS IN SOLAR UNITS
OPPENHEIMER AND VOLKOFF
RUDKJØBING
WHEELER
CHANDRASEKHAR

Figure 26

models. His conclusions have been criticized by Salpeter (reference 11(b)). The mass-radius relation of Chandrasekhar's models is shown as a dashed curve in the upper portion of Figure 27. All of the white dwarfs observed lie along the curves in the lower portion of Figure 26, with mass ranging from about 0.2 to 1.2 $M_\odot$. The typical radii of such stars range from about several thousand kilometers to ten thousand kilometers, as Figure 27 indicates.

b. Original Work by Landau(1)

By applying the equilibrium condition to bodies of large mass and by using Newtonian mechanics, Landau in 1932 reached the following conclusions. The minimum mass a stable degenerate star can have is about 0.001 $M_\odot$, the maximum mass for a mixture of electrons and nuclei is roughly 1.5$M_\odot$, and that of a pure neutron configuration is about 6$M_\odot$. His estimate of the minimum mass was based on the requirement that the sum of the gravitational and kinetic energies per particle of core should be lower than the energy per particle in stable nuclei. The particular case of oxygen was used in his derivation. Minimum mass of stable neutron stars was estimated to be about 0.2$M_\odot$(63). His estimate of the maximum mass of an electron-nuclear configuration (white dwarfs) is excellent, but his maximum mass of about 6$M_\odot$ for neutron stars is too large. This is mainly because the Newtonian theory of gravitation that he used in his analysis is not justified for neutron stars, although it is perfectly valid for white dwarfs.

c. Limiting Mass by Oppenheimer and Serber(3)

Apparently stimulated by Landau's proposals, an improvement was applied to

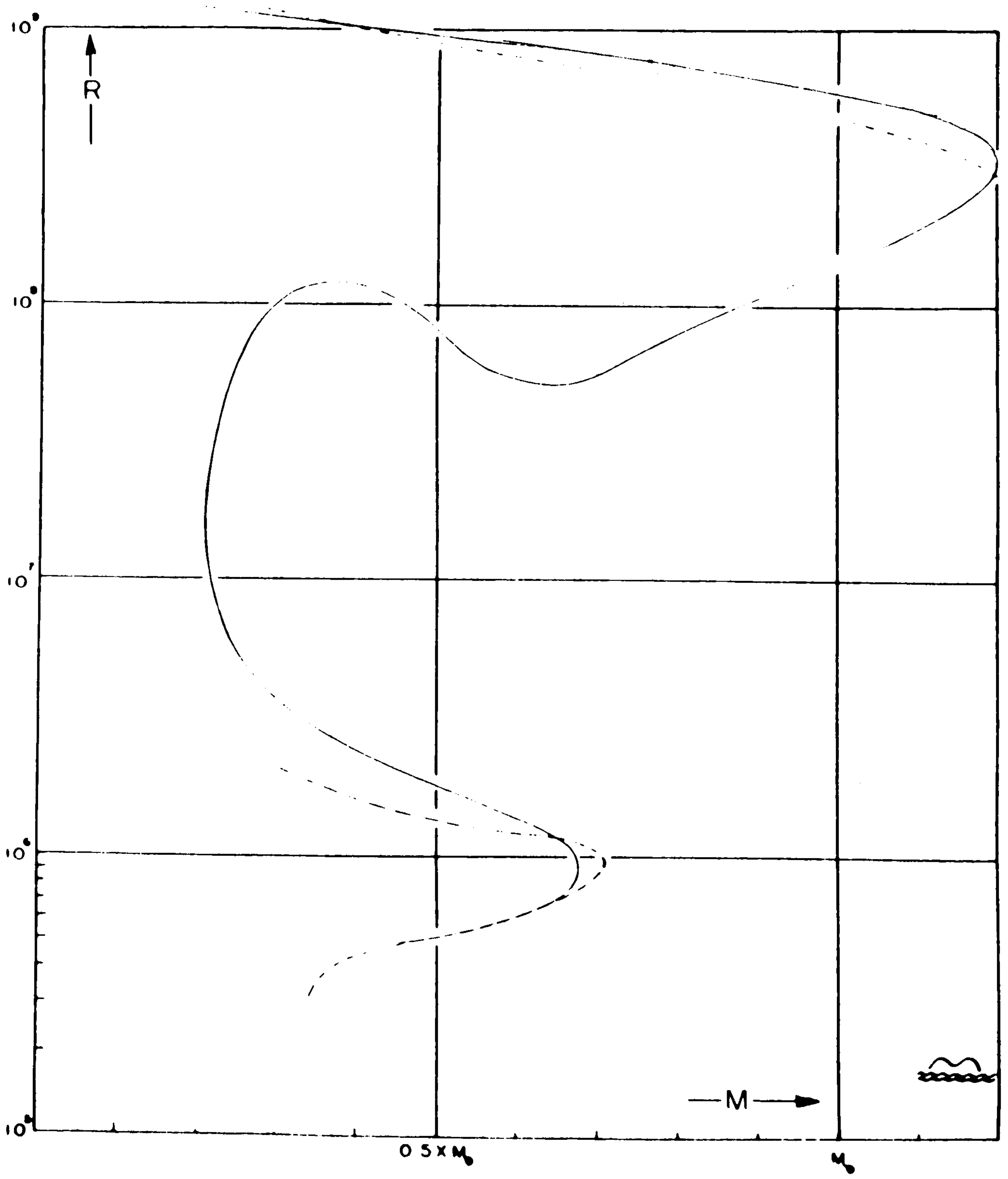

Figure 27

the estimates of minimum mass of stable stellar neutron cores by Oppenheimer and Serber (1958). They adopted a requirement that the neutron's free energy in the core be less than that in the nucleus in order that the core be stable with respect to the most firmly bound nuclei — which led them to about $1/6M_{\odot}$ as the minimum mass. They also noted that in the region where a neutron configuration can exist, nuclear forces should not be neglected, and they assumed the forces between neutrons to be of the spin-exchange saturating type. This reduced the minimum mass for core stability to $0.1M_{\odot}$.

d. Models of Neutron Cores by Oppenheimer and Volkoff(4)

In 1939, Oppenheimer and Volkoff made an important step forward from Landau's original work, by constructing structure equations of general relativity and by using the equation of state of an ideal Fermi gas of neutrons. If the functions $\mathcal{E}$ (P) in (1-8) and (1-9) are eliminated through the equation of state expressed in the forms (3-30b) and (3-30c), the two hydrostatic equations are expressed in terms of the parameter t only. In this form, the hydrostatic equations were integrated from $U = 0$ and $t = t^c$ at $r = 0$ to $r = R$ where $t = 0$ and $U = M$. R determines the boundary of the matter distribution and the radius as seen by a distant observer. M determines the observable or gravitational mass. The system of units as introduced in Chapter I was adopted.

The central density-mass relation of their models is shown by the upper dashed curve in Figure 26 and their mass-radius relation is given by the dashed curve in the lower portion of Figure 27. Their result may be summarized as follows:

the mass increases with increasing t^c until a maximum is reached at about $t^c = 3$, after which the mass drops until a value of about $1/3M_\odot$ is reached at $t^c = \infty$. No static solution exists at all for $M > 3/4 M_\odot$, two solutions exist for $(3/4) M_\odot > M > 1/3M_\odot$, and one solution exists for $M < 1/3M_\odot$, but if its mass is less than about $0.1M_\odot$ a neutron core is no longer stable against disintegration into nuclei and electrons. At the point of maximum mass which comes at about $0.7M_\odot$, the radius is about 10 kilometers and the central density is about 10^{16} gm/cm^3. (See Figures 26 and 27.)

They approached the stability problems using the theory of polytropes, and concluded that among the two solutions in the range $3/4 \geqslant M \geqslant 1/3M_\odot$, the less dense models are stable, while the more condensed ones are unstable. The radius of their stable models is about 10 to 20 km, the central densities lying between about 10^{12} and 10^{16} gm/cm^3. They posed the interesting question of what happens on bodies exceeding the critical mass $3/4M_\odot$. If repulsive nuclear forces are taken into account the same authors estimated qualitatively that the maximum mass may reach about $1M_\odot$. This result was obtained by applying the relativistic limitation $P = 1/3\, \mathcal{E}$.

e. Models of Degenerate Stars by Wheeler, Harrison and Wakano(8, 60)

Applying their composite equation of state introduced in Section III-4e, equations (1-8) and (1-9) were integrated with the boundary condition at the center $U(0) = 0$ and $\mathcal{E}(0) = \mathcal{E}^c$. The radius of the star was taken as the distance from the center to the point where $P = 0$. Their results are summarized in Figures

26 and 27 (solid curves). Up to a central density 10^7 gm/cm, the agreement between the Chandrasekhar, Wheeler and Rudkjöbing models is quite satisfactory, but Wheeler's models deviate more and more from the models of Chandrasekhar and Rudkjöbing for $\rho^c > 10^8$ gm/cm^3. This is because the inverse beta process is included in Wheeler's equation of state which prevents the electron number density from increasing indefinitely with an increase in central density. That is, electrons are lost through the capture process and the electron pressure does not rise sufficiently with the increase of matter density. A turning point occurs at around $1.2M_\odot$. In the region of central density from about 10^8 gm/cm^3 to $10^{13.5}$ gm/cm^3, equilibrium mass decreases with an increase of central density. For a reason to be explained later, this range occurs in an unstable region while in the lower portion of the curve up to about $1.2M_\odot$, stars are stable. When the central density has reached the order of magnitude of normal nuclear density, neutron pressure is sufficiently large to again give stable configurations. Wheeler's models for $\rho^c \gtrsim 10^{14}$ gm/cm^3 are essentially the same as the previous models of Oppenheimer and Volkoff.

f. Cameron's Models of Neutron Stars(9)

In the previous models of neutron stars, nucleon-nucleon interactions were entirely neglected, although Oppenheimer and Volkoff gave a brief discussion on the importance and possible effects of such nuclear forces. Cameron took the important first step of constructing neutron star models in which these interaction forces were taken into account quantitatively. The Skyrme equation of state, introduced in Section III-4b, was used for that purpose. Not only observable mass, but also proper mass and gravitational binding in mass units was obtained by integrating equations (1-45) and (1-46) and the usual relativistic hydrostatic equations (1-8) and (1-9), simultaneously. The radius was defined as the distance from the center to the point where the density has decreased to 10^8 gm/cm^3, which corresponds to the point where the scale height (that is, the distance over which the pressure falls by a factor e) is about 20 meters in the lightest models and about 1 cm in the densest models. Nineteen models were constructed in this manner. To see the effect of the short range strong repulsive forces encountered at high densities, a hard core model was also constructed whose parameters were fitted to experimental data on high energy proton-proton interactions. The potential goes to infinity at a hard core distance of 0.4 fermis. In this model, the gas abruptly becomes incompressible at a density of 3.7×10^{16} gm/cm^3, and obeys equation (3-38c) at lower densities.

The results are presented in Table 1, Figures 3 and 4 in reference 9. The density profiles of his models are shown in Figure 28. Except for some of the densest models, the density distribution inside a neutron star is practically constant until we come to the very edge, then it drops abruptly, almost vertically down to zero. This behavior more than justifies the fact that the integration was terminated at $\rho = 10^8$ gm/cm^3. In the higher density regions the equation of the density profile was given in analytic form as $\rho = 8 \times 10^{19}/r^{3/4}$ for ρ up to $\rho = \rho^c$, that is, until the uppermost curve in Figure 28 meets the horizontal line $\rho = \rho^c$. The radius in the stable region is almost constant, ranging from about 7 to 9 kilometers.

Cameron confined the range of validity of his models to within the region of central density less than or equal to about 10^{15} gm/cm^3. The reason is that a

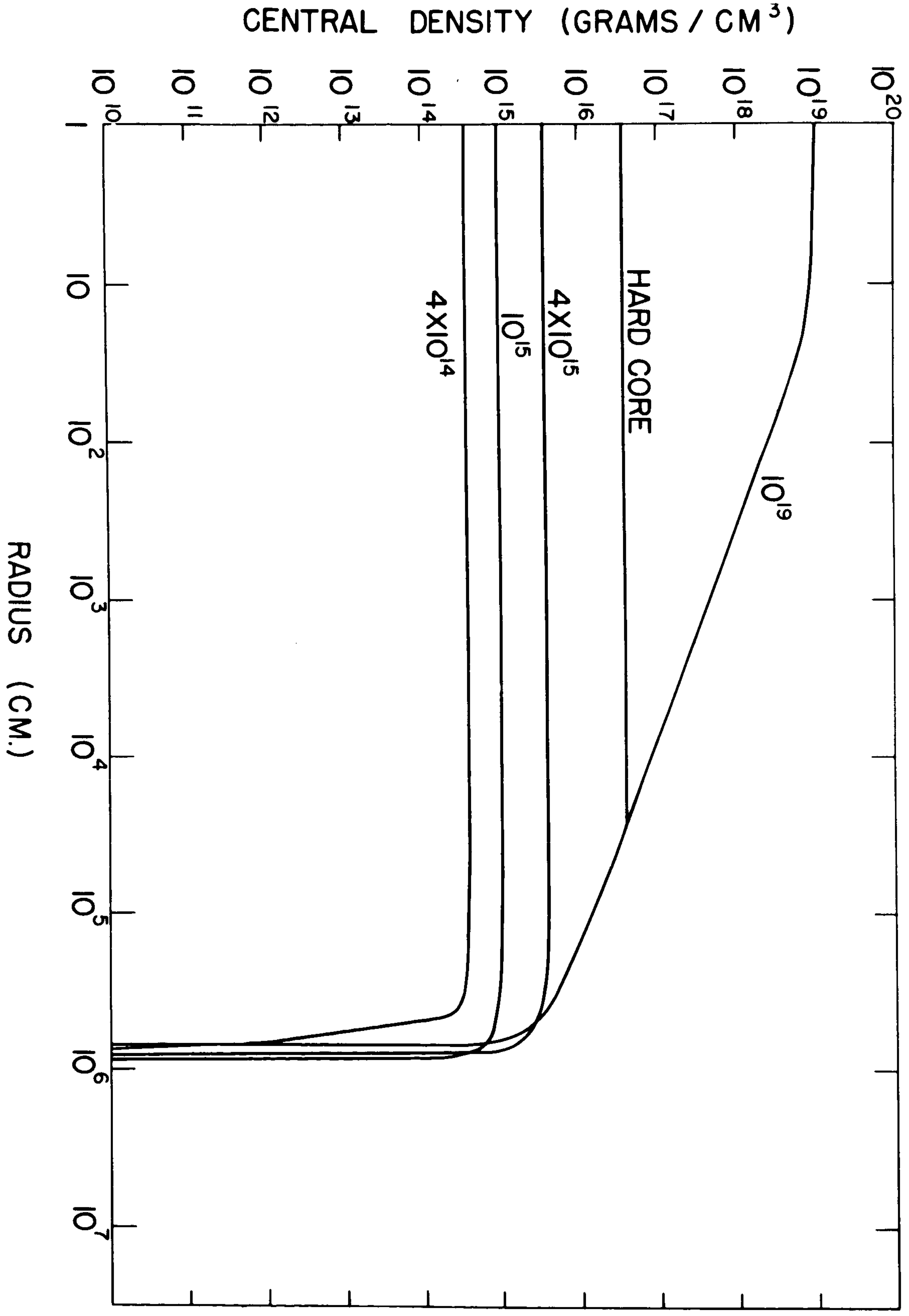
CENTRAL DENSITY (GRAMS / CM^3)
10^{10}
10^{11}
10^{12}
10^{13}
10^{14}
10^{15}
10^{16}
10^{17}
10^{18}
10^{19}
10^{20}
RADIUS (CM.)
1
10
10^2
10^3
10^4
10^5
10^6
10^7
4×10^{14}
10^{15}
4×10^{15}
HARD CORE
10^{19}

Figure 28

considerable amount of uncertainty is inherent in the higher density regions because for $\rho > 10^{15}$ gm/cm^3: (1) four-body and higher terms in the nuclear potentials may become significant and would tend to make the pressure-density curve even steeper, and (2) on the other hand the hyperons present for $\rho > 10^{15}$ gm/cm^3 will first depress the Fermi level of the neutrons far below the value expected for a pure neutron gas which he was considering in this work.

On applying this criterion to his models, some of which are listed in Table 8, we conclude that they must certainly be reliable up to about 1 solar mass. At $\rho^c = 10^{15}$ gm/cm^3, the exact value of the observable mass is $0.74M_\odot$ and the radius is 8.75 km. At the slightly higher central density of 1.5×10^{15} gm/cm^3, the mass has increased to $1.36M_\odot$ (almost twice as large as the Oppenheimer-Volkoff mass limit of $0.7M_\odot$), and the radius is 9.26 km (about the same as the radius of Oppenheimer-Volkoff star of $0.7M_\odot$). This is a significant result to which it is worth calling attention. The maximum observable mass comes at about 2 solar masses, with a radius of 8.2 kilometers. Noting that here the central density of the star is already 4×10^{15} gm/cm^3 where the equation of state is unreliable, Cameron comments in his paper that his figure for the maximum mass should not be taken too literally.

The most important outcome of Cameron's work was that it gave the first quantitative indication of the possibility that the observable mass of stable neutron stars might be considerably larger than $0.7M_\odot$, earlier maximum mass limit on such an object. It might in fact be even larger than the mass limit set on white dwarfs (about 1.2 to $1.4M_\odot$).

TABLE 8. Original neutron star models by Cameron (Skyrme type) in medium and low density regions, where ρ^c is the central matter density, P^c is the central pressure, R is the stellar radius, and M, M_P, and M_B are the gravitational mass, proper mass, and binding energy in mass units.

ρ^c (gm/cm^3)	P^c(dynes/cm^2)	R(km)	$M/M_\odot$	$M_P/M_\odot$	$M_B/M_\odot$
1×10^{13}	1.164×10^{31}	27.94	0.04424	0.04434	0.00009819
3×10^{13}	4.398×10^{31}	23.26	0.04754	0.04768	0.0001456
1×10^{14}	1.163×10^{32}	21.41	0.04426	0.04441	0.0001483
2×10^{14}	3.474×10^{32}	20.49	0.03608	0.03622	0.0001209
3×10^{14}	1.306×10^{33}	10.40	0.03278	0.03300	0.0002134
4×10^{14}	3.632×10^{33}	7.409	0.07062	0.07157	0.0009427
6×10^{14}	1.479×10^{34}	7.533	0.2295	0.2375	0.005349
8×10^{14}	3.830×10^{34}	8.232	0.4701	0.5008	0.03075
1×10^{15}	7.830×10^{34}	8.752	0.7459	0.8212	0.07554
1.5×10^{15}	2.750×10^{35}	9.262	1.357	1.626	0.2695

The minimum mass of stable neutron stars was also estimated. It was pointed out that in models with smaller densities, the gravitational binding in mass units is much less than 1% of the proper mass and that such models are energetically unstable against transformation into iron white dwarfs. Using an argument more or less similar to the one which led Oppenheimer and Serber to their value of about 0.1 $M_\odot$ for the lower mass limit (IV-2c), in Cameron's models the minimum mass for stability was estimated to be 0.05 $M_\odot$.

Another contribution of Cameron's paper is the useful discussion on hot neutron star models. A possible mechanism for the formation of neutron stars is discussed here and several interesting problems which had not been touched upon in previous papers on this subject were posed. One, for example, concerning the effect of hot atmospheres and of cooling on the detectability of neutron stars prompted me to undertake the present research.

g. Models for Zero-temperature Stars by Hamada and Salpeter(12)

Using the equation of state constructed in reference 11(b), Salpeter and Hamada investigated the properties of degenerate stars. The Newtonian equations of hydrostatic equilibrium were integrated from the center to the point where $P = 0$. To see the effect of composition, a set of models with different elements and another set with an equilibrium composition of cold matter as introduced in Section II-3b were constructed. As in Wheeler's models, the mass of Salpeter's models reaches a maximum at a certain point as central density is increased, and with a further increase in ρ^c, the mass decreases, due to the electron captures in the equation of state used.

At this maximum point, $M/M_\odot = 1.4$, 1.36, 1.34, 1.17, and 1.11, and $\log \rho^c = 9.78$, 9.5, 9.28, 8.16, and 9.1, for a chemical composition of C^{12}, Mg^{24}, Si^{28}, S^{32}, and Fe^{56}, respectively. The radius of a star at this point is from 2 to 4 times $10^{-3}\ R_\odot$, (where $R_\odot = 6.951 \times 10^5$ km, the solar radius), depending on the composition. For the equilibrium composition, the maximum mass is $1.015 \odot$, the radius is $3.5 \times 10^{-3} R_\odot$ and the central density is around 10^9 gm/cm^3. Near the critical mass, the equilibrium composition appears to give the smallest mass as compared with other compositions.

Neutron star models were constructed with the Skyrme-Cameron equation of state (3-38c). In the outer layers of a star in which $\rho < 3.4 \times 10^{11}$ gm/cm^3, the equilibrium composition was used. An interesting outcome is that some of the lightest neutron star models ($10^{13} < \rho^c < 4 \times 10^{14}$ gm/cm^3) have large envelopes of heavy nuclei and electrons. For instance, when $\rho^c = 3.3 \times 10^{14}$ gm/cm^3, $R = 4.06 \times 10^{-3}\ R_\odot$, $M = 0.82\ M_\odot$, the mass contained in the neutron core is only about 5% of the total mass, and the radius of the core is only about 0.3% of the radius of the star (with its envelopes included). The most extended envelope ($R = 8.8 \times 10^{-3}\ R_\odot$) is obtained when $\rho^c = 3.42 \times 10^{14}$ gm/cm^3; both mass and radius fall rapidly with an increase of central density beyond this value. The mass reaches a minimum value of $0.05 M_\odot$ at $\rho^c = 3.5 \times 10^{14}$ and then increases fairly rapidly. When $\rho^c = 10^{15}$ gm/cm^3, then $M \sim 1 M_\odot$. The effect of the envelope on the radius is negligible for $\rho^c \gtrsim 5 \times 10^{14}$ gm/cm^3 and that on the mass is negligible for $\rho^c \gtrsim 3.5 \times 10^{14}$ gm/cm^3. Noting that the effects of general relativity are completely neglected, Salpeter comments that the tremendous effect of the envelope near $\rho^c \sim 3.4 \times 10^{14}$ gm/cm^3 indicated in the above discussion may be unrealistic. These results will be compared with my results later in this paper.

h. Superdense Stars of Ambartsumyan and Saakyan(14,15,16)

(i) Work in Reference 14 – Ambartsumian and Saakyan constructed a series of superdense stellar models for: (a) an ideal Fermi gas of an assembly of baryons in equilibrium, and (b) a real gas of the same composition in which interaction forces are taken into account. For (a), the equation of state with the interaction terms $nV(n)$ and $n^2(\partial V/\partial n)$ in (3-41) set equal to zero was used, and for (b), these interaction terms were included although the second term in (3-40) was neglected. The equilibrium concentrations of various elements as obtained in reference 13 (similar to the revised values of abundances obtained in this research, in Section III-2) were used. t_n, the "relativistic parameter" of neutrons, was used as a parameter of integration, and the integration of equations (1-8) and (1-9) was carried out from the center to the point where $t_n = 0$. The mass-central density relations (dashed curves) and the radius-central density relations (solid curves) for their models of an ideal gas (marked (1)) and a real gas (marked (2)) are shown in Figure 29. The central density is represented by the expression $\tan^{-1} t_n(0)$. The maximum mass for an ideal baryon gas is about $0.64 M_\odot$, somewhat lower than the Oppenheimer-Volkoff value of $0.7M_\odot$; that for a real baryon gas is about $1.0M_\odot$. The corresponding radius at each maximum mass is, for an ideal gas about 11 km, and for a real gas about 6 km. At maximum mass, the central energy density of the star is about 2.4×10^{15} gm/cm^3 for an ideal gas and about 10^{16} gm/cm^3 for a real

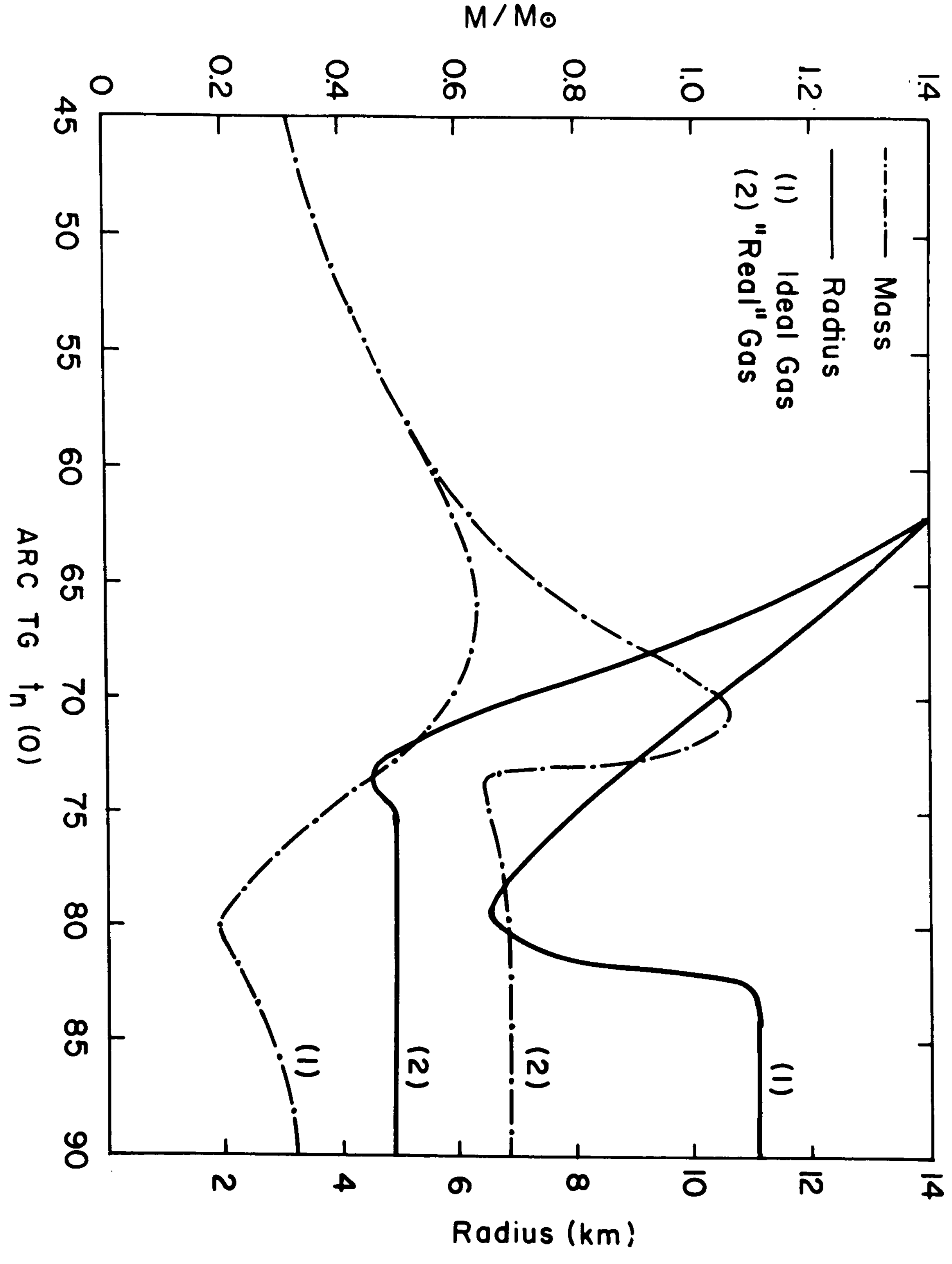
M/M⊙
0
0.2
0.4
0.6
0.8
1.0
1.2
1.4
Mass
Radius
(1) Ideal Gas
(2) "Real" Gas
45
50
55
60
65
70
75
80
85
90
ARC TG t_n (0)
(1)
(2)
(2)
(1)
2
4
6
8
10
12
14
Radius (km)

Figure 29

gas. After passing the maximum, the mass drops with a further rise in central density, reaching a minimum of about $0.2M_\odot$ for an ideal gas and about $0.64M_\odot$ for a real gas before increasing slightly. Similar minima occur for radii, also. In the high density limit, these models develop a central singularity. The asymptotic values of radius and mass are about 11 km and $0.32M_\odot$ for an ideal gas and about 5 km and $0.7M_\odot$ for a real gas. A model of an incompressible fluid was also constructed. For $\mathcal{E}^c \lesssim 10^{15}$ gm/cm^3 the entire stellar body consists of neutrons, while for $\mathcal{E}^c > 10^{15}$ gm/cm^3 a hyperon core is developed at the center and rapidly grows to almost 1/3 of the total stellar size. For $t_n{}^c > 3$ (or $\mathcal{E}^c > 1.1 \times 10^{16}$ gm/cm^3) the bulk of the star's mass is in the hyperon core, and the effect of the outer envelopes of neutrons (and of electrons and protons in envelopes further out) is not important.

(ii) Work in Reference 15 - To complete their discussion on the internal structure of superdense stars started in reference 14, Ambartsumian and Saakyan calculated the following physical quantities of the same models for (a) an ideal baryon gas, and for (b) the real baryon gas constructed as in reference 14: (1) the actual stellar radius R_o (or the proper radius) defined by (1-43), (2) the total baryon number of the star, N, defined by (1-44), and (3) two kinds of gravitational packing fraction a_1 and a_2 defined as follows:

$$a_1 = \Delta M_1/N m_H, \text{ where } \Delta M_1 = N m_H - M \qquad (4\text{-}2)$$

$$a_2 = \Delta M_2/M, \text{ where } \Delta M_2 = M_o - M,\ M_o = 4\pi \int_0^R \sqrt{-g_{rr}(r)}\, r^2\, \mathcal{E}(r)dr \qquad (4.3)$$

where $c = 1$, m_H is the proton mass, M is the gravitational mass of the star U(R),

ΔM is the binding energy in mass units (or gravitational mass defect), and M_o is the total energy density integrated over the whole proper volume. Besides these quantities, the radial distribution of parameter $t_n^{(r)}$ (corresponding to density distribution), the mass U(r), the time metric $g_{oo}(r)$, and the radial component of the metric $g_{rr}(r)$ were calculated for an ideal baryon gas. Some of the results in references 14 and 15 are shown in Table 9. Near the surface, g_{rr} is about 1 to 1.3 and g_{oo} ranges from 0.7 to 1 for models with t_n^c from 1 to ∞ (that is, for ρ^c from 10^{14} gm/cm^3 to ∞). g_{oo} vanishes at the center and shows a singularity at $t_n^c = \infty$. Gravitational mass is plotted against total baryon number in Figure 5 of reference 15. For $N > 6.5 \times 10^{56}$, there are two or three solutions of the structure equations (i.e. two or three values of gravitational mass M) for one value of N, for N up to 13.5×10^{56}. For a larger number of baryons there exists no solution. At the maximum point, there is one value of mass (the maximum mass) where $t_n^c \sim 2.9$ (or $\mathcal{E}^c \sim 10^{16}$ gm/cm^3). The definition of ΔM_1 above corresponds to our M_b (the gravitational binding) defined in Section I-4c. Our definition differs somewhat from their definition. ΔM_2 from the definition appears to express the difference between the actual macroscopic mass of the star and the mass observed by a distant observer.

(iii) Work in Reference 16 - Saakyan pointed out that the expression for energy density $\rho = mn$ used in reference 9 is an oversimplified one, and repeated the calculation using the relativistic expression for Skyrme's equation of state (3-39). The conclusion is that the result of reference 9 and that of reference 16 coincide for $\mathcal{E}^c < 10^{15}$ gm/cm^3 and $M < 1 M_\odot$, but for higher densities the two

TABLE 9. Models of Ambartsumyan and Saakyan, where t_n^c is the relativistic parameter of neutrons at the center, ε^c is the central energy density, R_o is the proper radius, M is the observable mass, N is the total baryon number, and a_1 and a_2 are two kinds of packing fraction as defined as (4-2) and (4-3).

	t_n^c	ε^c(gm/cm^3)	Radius R_o (km)		$M/M_\odot$		N 10^{-56}	a_1	a_2
			Star	Hyperon Core	Star	Hyperon Core			
IDEAL GAS	1.0	1.00×10^{14}	21.1	-	0.306	-	4.03	0.100	0.0180
	1.8	6.60×10^{14}	15.2	-	0.557	-	7.23	0.085	0.0552
	3.0	1.09×10^{16}	10.4	3.49	0.519	0.237	6.56	0.060	0.104
	4.0	8.29×10^{16}	9.12	2.79	0.329	0.209	4.01	0.024	0.129
	5.0	3.45×10^{17}	7.48	2.13	0.228	0.161	2.48	-0.091	0.159
	6.0	1.15×10^{18}	8.24	1.83	0.177	0.125	1.96	-0.073	0.198
	∞	∞	11.1	2.31	0.324	0.112	3.70	-0.038	0.109
REAL GAS	2.4	2.36×10^{15}	11.2	4.9	0.860	0.353	11.0	0.071	0.145
	3.0	1.67×10^{16}	6.97	5.68	1.028	0.966	12.7	0.023	0.450
	3.2	5.75×10^{16}	6.31	5.33	0.847	0.817	9.8	-0.027	+0.472
	3.4	1.38×10^{17}	6.56	5.00	0.673	0.650	6.55	-0.22	+0.546
	4.0	1.61×10^{18}	7.15	5.29	0.670	0.615	6.83	-0.16	0.552
	7.0	2.88×10^{22}	7.21	5.32	0.686	0.631	7.00	-0.16	0.545
	∞	∞	7.19	5.30	0.691	0.643	7.03	-0.16	0.548

deviate from each other appreciably. The maximum mass occurs at about the same central density, but its value is reduced from about $2M_\odot$ to $1.7M_\odot$.

IV-3 MODELS CONSTRUCTED IN THIS RESEARCH

a. General Remarks

From the previous discussions we see that a general procedure for obtaining models of dense stars consists of a step by step integration of the equations of hydrostatic equilibrium (1-1) and (1-2), or (1-8) and (1-9), and related differential equations such as (1-45) and (1-46), and using a suitable expression of the equation of state and the proper boundary conditions at the center and on the surface. In this research various forms of the equation of state are used; that for (1) an ideal gas, (2) a real gas with Skyrme interaction, and (3) a pure neutron gas or a complicated configuration of mixtures with a Levinger-Simmons type interaction — V_β, V_γ or a combination of the two, $V_{\beta\gamma}$. In the following the models constructed in this research are presented in the order of increasing complexity, starting with the simplest case — an ideal Fermi gas of neutrons. Finally, six models are selected from these as basic models to be used extensively in Chapter V. The results will be discussed and compared with the models of others.

A brief inspection of the differential equations of Chapter I shows that they cannot be solved analytically. There are various methods for the numerical solution of such differential equations. In this research, the Adams predictor-corrector method(64) was used for all the numerical integrations performed. Besides this, another technical problem is that an interpolation of a high order of accuracy is required in the various kinds of numerical work (for instance, this problem was already faced in Section III-4f in evaluating the Levinger-Simmons potentials of the exchange type v_e and ω_e and their derivatives). To meet this requirement the polynomial interpolation method$^{(64)}$ has been adopted throughout this research. A special interpolation subroutine using the polynomial method and an integration subroutine using the Adams method of high accuracy constructed by Mr. B. Sackaroff at the computer department of the Goddard Institute for Space Studies became available. These subroutines are used in conjunction with the main programs and other subroutines I constructed, whenever necessary. The numerical errors, inherent in any numerical analysis, should, therefore, be considerably eliminated.

b. Models With an Ideal Fermi Gas of Neutrons

The model construction in this research started with this simplest kind for various reasons: (1) to double check previous results with the 7094 computer, (2) to orient myself to the work and to make sure that the main Fortran program and subroutines I constructed worked properly by comparing my results with those of others, and, most importantly, (3) to calculate other interesting physical quantities such as the gravitational binding and its behavior as a function of central density, something which had not been done before.

Equations (1-8) and (1-9) as well as other differential equations of interest such as (1-45) and (1-46) have been integrated with the equation of state (3-30b) and (3-30c), from the center (where $u(0) = 0$, and $t_n(0) = t_n{}^c$) to the point $r = R$ where the density drops to 10^8 gm/cm^3. The general shape of the density profiles of these models are similar to those obtained earlier by Cameron and shown in Figure 28, which indicates that this surface boundary condition is perfectly legitimate for neutron stars whose central density and mean density are both above about 10^{14} gm/cm^3.

The results are shown in Figures 30, 31, and in Table 10. In Figure 30, the dashed curve represents the gravitational mass (which is actually seen by a distant observer)as a function of the central energy density. The maximum mass is approximately $M \sim 0.72_{\odot}$ where $\mathcal{E}^c \sim 4 \times 10^{15}$ gm/cm^3, as expected. A comparison of Figure 30 with Figure 26 shows that this is in perfect agreement with the previous work. In previous work, models with central energy density $\mathcal{E}^c$ up to about 10^{17} gm/cm^3 have been constructed by the usual methods and then one more model with $\mathcal{E}^c = \infty$ was constructed by using an analytic approximation. That is, there was a gap between the model with $\mathcal{E}^c \sim 10^{17}$ gm/cm^3 and the one with the central singularity ($\mathcal{E}^c = \infty$). It is interesting to explore the behavior of superdense stars in these ultrahigh density regions. In the present research, the integration was carried out for a sequence of models (which included those with central energy density $\mathcal{E}^c$ as high as $10^{22} \sim 10^{23}$ gm/cm^3) until no fluctuation from a straight vertical line (in the $\mathcal{E}^c - M$ plane) was observed in a plot like that shown in Figure 30. The straight vertical line is a sign that we are already in a singular region, and that the mass, radius and other properties of models lying on this vertical line are those possessed by the extreme model with $\mathcal{E}^c = \infty$. Figure 30 shows the outcome of such an investigation. Instead of going straight from the point $\mathcal{E}^c \sim 10^{17}$ gm/cm^3 to $\mathcal{E}^c = \infty$, both the gravitational mass track and the proper mass track in

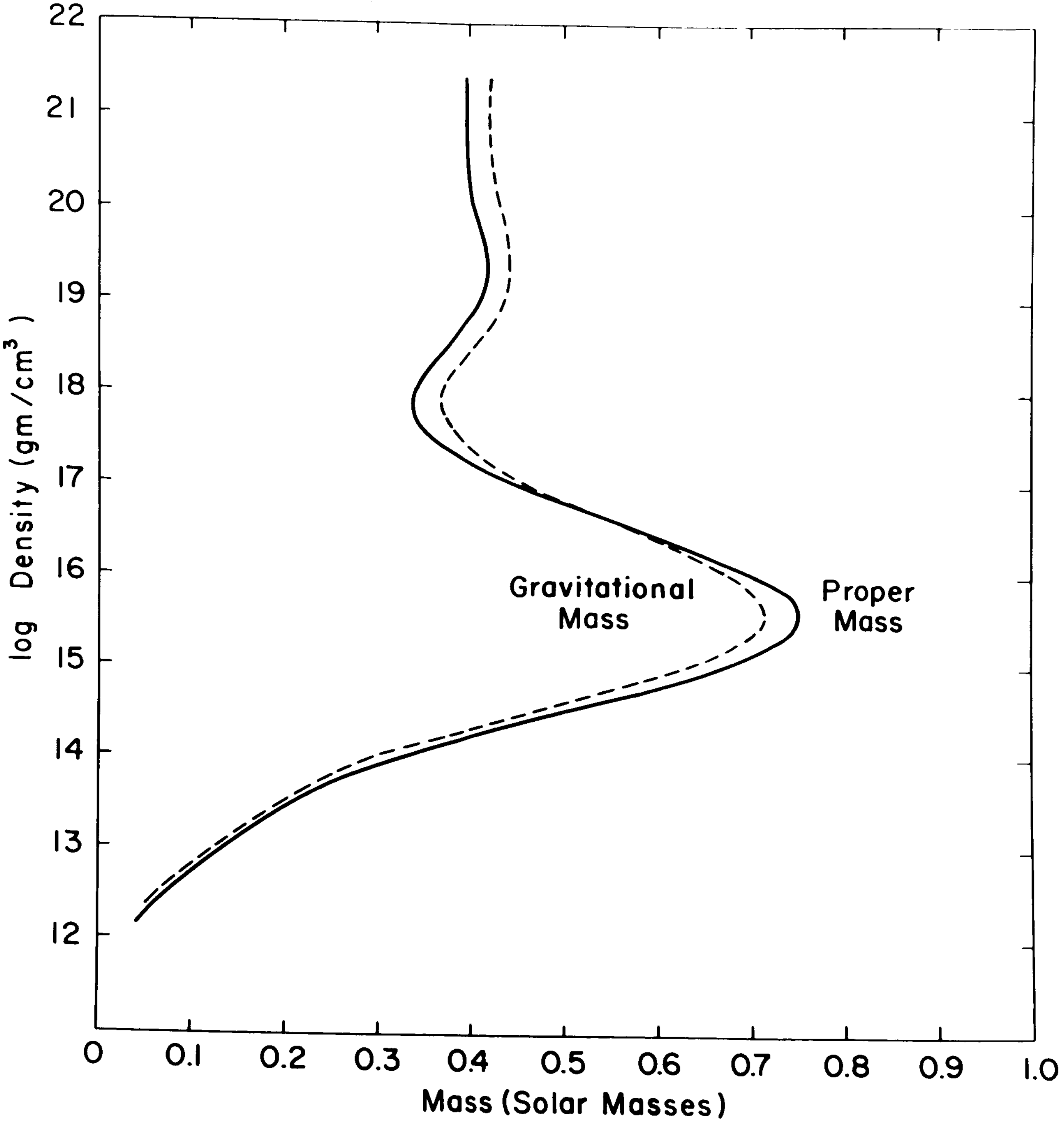
log Density (gm/cm^3)
22
21
20
19
18
17
16
15
14
13
12
0
0.1
0.2
0.3
0.4
0.5
0.6
0.7
0.8
0.9
1.0
Mass (Solar Masses)
Gravitational Mass
Proper Mass

Figure 30

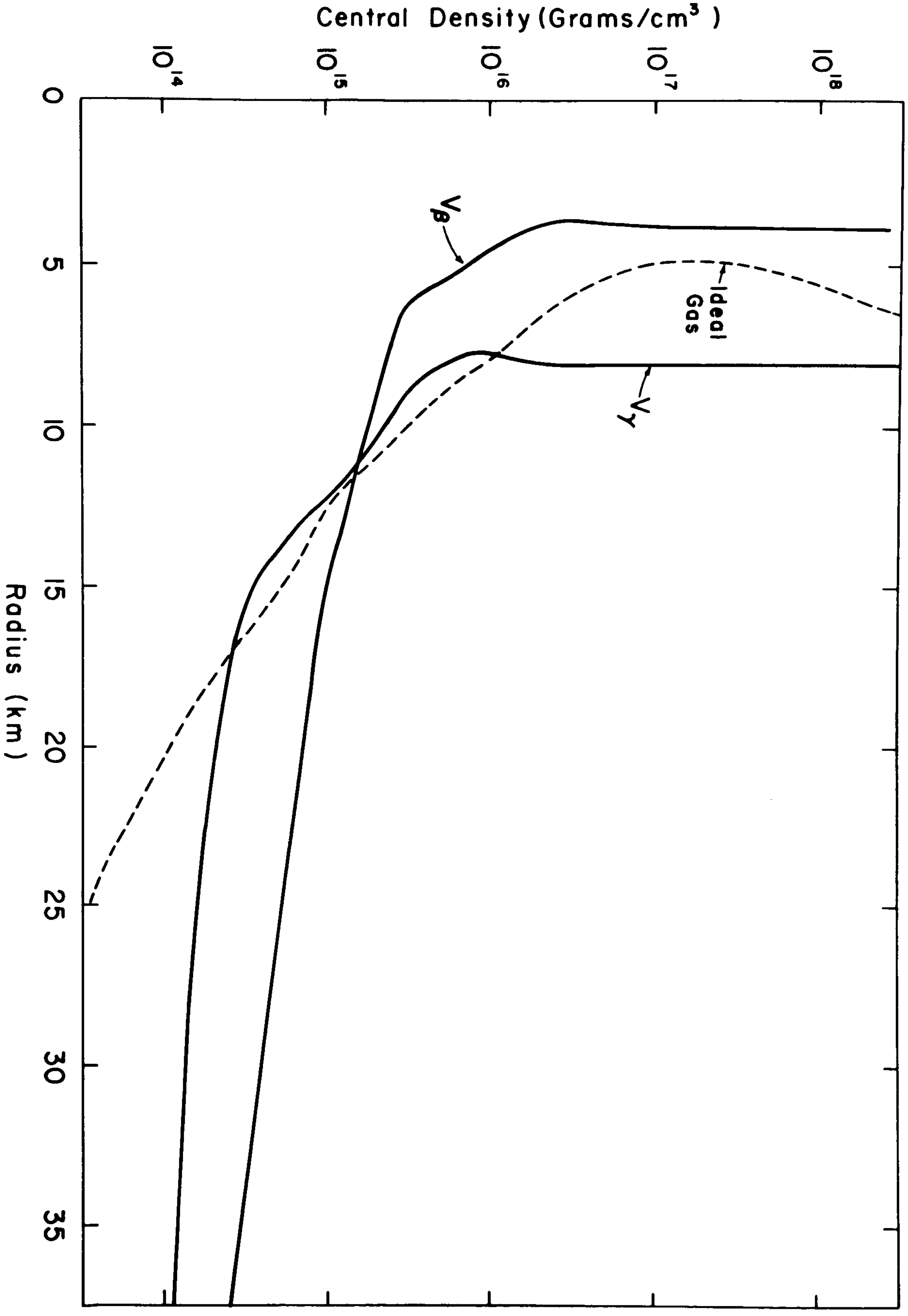
Central Density (Grams/cm³)
10^{14}
10^{15}
10^{16}
10^{17}
10^{18}
Radius (km)
0
5
10
15
20
25
30
35
V_β
Ideal Gas
V_γ

Figure 31

TABLE 10. Neutron star models with an ideal gas (α is the ratio of the binding energy in mass units to proper mass, $g_{44}(R)$ is the time metric, $g_{rr}(R)$ is the radial component of metric at R, $\wp(R)$ is the red shift, and other symbols are those introduced in Tables 8 and 9.)

$\log_{10}\mathcal{E}^c$ (cgs)	$\log_{10} P^c$ (cgs)	R(km)	$M/M_\odot$	$M_P/M_\odot$	$M_B/M_\odot$	$\alpha \equiv \frac{M_b}{M_P}$	$g_{44}(R)$	$-g_{rr}(R)$	$\wp(R)$	t_n^c
12.411	30.415	39.16	0.05436	0.05813	0.00327	0.0562	0.996	1.035	0.0021	0.3
13.7000	32.522	23.54	0.2251	0.2321	0.0070	0.0301	0.972	1.029	0.014	0.8
14.813	34.346	14.19	0.5643	0.5911	0.0263	0.0453	0.883	1.130	0.0584	1.8
15.497	35.365	9.870	0.7057	0.7418	0.0359	0.0684	0.790	1.265	0.105	2.8
16.024	36.112	7.326	0.6753	0.7019	0.0266	0.0376	0.728	1.372	0.136	3.8
16.503	36.729	5.815	0.5759	0.5863	0.0104	0.0177	0.708	1.564	0.146	4.8
17.047	37.377	4.976	0.4559	0.4432	-0.0127	-0.0287	0.730	1.370	0.135	6.0
17.489	37.872	5.004	0.3885	0.3604	-0.0281	-0.0780	0.772	1.296	0.114	7.0
17.93	38.35	5.640	0.3664	0.3358	-0.0306	-0.0914	0.808	1.238	0.096	8.0
18.36	38.80	6.358	0.3889	0.3616	-0.0273	-0.0784	0.820	1.220	0.090	9.0

the $\mathcal{E}^c$ - M plane experience one minimum-mass-hump (at around log $\mathcal{E}^c \sim 17.7$) and one maximum-mass-hump (at around log $\mathcal{E}^c \sim 19.4$) before developing a singularity at a finite mass (vertical line). It was reported(61) recently, however, that the existence of such a small second hump (maximum) was observed in models in the ultrahigh density regions constructed by Misner and Zalolsky(24) who used the limiting equation of state $P = \mathcal{E}$ or $P = \mathcal{E}/3$. We shall return to the discussion on this topic later (IV-4e).

The solid curve in Figure 30 represents proper mass (the mass before it was assembled into a star) as a function of central density. It is quite interesting to see that the proper mass becomes less than the gravitational mass for log $\mathcal{E}^c \gtrsim 16.7$. This is just what is to be expected as explained later (Section IV-4). In Figure 31, central density is plotted (the dashed curve for an ideal gas) against stellar radius (the radius of the star actually seen by a distant observer). Combining Figures 30 and 31, we see that the radius of the star with the maximum mass (0.72 ☉) is about 9.5 km, as expected.

In Table 10, various physical quantities of interest are listed for ten such models with $\log_{10} \mathcal{E}^c$ (the central density in cgs units) ranging from 12.41 to 18.36. P^c is the central pressure, R is the radius in kilometers, $M/M_{\odot}$ is the gravitational mass U(R) in solar mass units, $M_P/M_{\odot}$ and $M_B/M_{\odot}$ are the proper mass and gravitational binding in solar mass units, α is the ratio of the binding energy in mass units to proper mass, $\zeta(R)$ is the red shift, $g_{44}(R)$ is the time metric and $g_{rr}(R)$ is the radial component of the metric $g_{\mu\nu}$ evaluated at the surface of the star. The first five quantities are obtained by a series of integrations performed in the manner described earlier for given initial values of t_n^c. M_B, α, $g_{44}(R)$, $g_{oo}(R)$ and $\wp(R)$ are calculated through the following simple relations which are derived from the definitions given in Chapter I:

$$M_B/M_\odot = M_P/M_\odot - M/M_\odot \quad \text{(from Appendix 2)} \tag{4-4}$$

$$\wp(R) = \Delta\lambda/\lambda = 1.47\,(M/M_\odot)/R(\text{km}) \tag{4-5}$$

$$g_{44}(R) = 1 - 2\wp(R) = -1/(g_{rr}(R)) \tag{4-6}$$

$$\alpha \equiv M_B/M_P \tag{4-7}$$

Comparing my α defined by (4-7) above with α_1 defined by (4-2) by Saakyan, and examining the definitions of terms involved, we can easily see (Appendix 2) that my α and Saakyan's α_1 mean the same quantity, a fractional binding energy or a packing fraction of gravity. This coincidence applies for a pure neutron configuration (neglecting proton-neutron mass difference), but is no longer true for a configuration of mixtures (Appendix 2). For mixtures, a more exact definition (4-7) with M and M_P which are obtained as the solution of equations (1-8) and (1-45) must be used. Let us compare α in Table 10 and α_1 in Table 9. The small individual deviations seen between α and α_1 are reasonable, considering the errors inherent in the definition of α_1 given by Saakyan (which was just pointed out) and considering that the models of the present section neglect the effect of hyperons in the high density regions entirely. The general agreement is then satisfactory. Both tables 9 and 10 are useful in showing the general relation between t_n^c and $\mathcal{E}^c$. We have seen that the maximum mass occurs at about a central density in the range from 10^{15} to 10^{16} gm/cm^3 which roughly corresponds to $t_n^c \sim 2$ to 3.

The radial distribution of density, mass, g_{oo} and g_{rr} obtained for models in this section have a similar behavior as is obvious from Figures 1, 2, 3, and 4 in reference 15.

c. Neutron Star Models With the Relativistic Skyrme Equation of State

The first set of neutron star models with interaction forces in this research was constructed by the use of the relativistic Skyrme equation of state (3-39), with t_n^c as the free parameter for a pure neutron configuration. As before, the integration was terminated at $\rho = 10^8$ gm/cm^3. The relation between central energy density and mass is shown in Figure 32 (curves marked (1)). The solid curve represents gravitational mass and the dashed curve the proper mass. Comparing this graph with the one in reference 9 which refers to original models of this type, we recognize that the results are identical up to about $\mathcal{E}^c \sim 10^{15}$ gm/cm^3, and that thereafter mass decreases faster in the revised models here. Moreover, the singularity occurs at smaller masses ($M \sim 1.3 \odot$ instead of previous $1.8 \odot$, and $M_p \sim 1.36 \odot$ instead of previous $M_p \sim 2.90 \odot$). The maximum gravitational mass is reduced from about 2 to 1.7 $\odot$ and the maximum proper mass from about 3 to 2.1 $\odot$. In these models crossing of the gravitational mass curve and the proper mass curve does not occur. Comparing the Skyrme-Cameron type models obtained here with models of noninteracting neutrons of the previous section, we note that the equilibrium mass at the same central density is much larger for the former than for the latter: more than twice as large at the maximum point and about three times as large at the singular point (when $\mathcal{E}^c \to \infty$). The fact that the binding energy does not become negative in the present models suggests some complicated effect of nucleon-nucleon forces. These results are summarized also in Tables 11a and 11b.

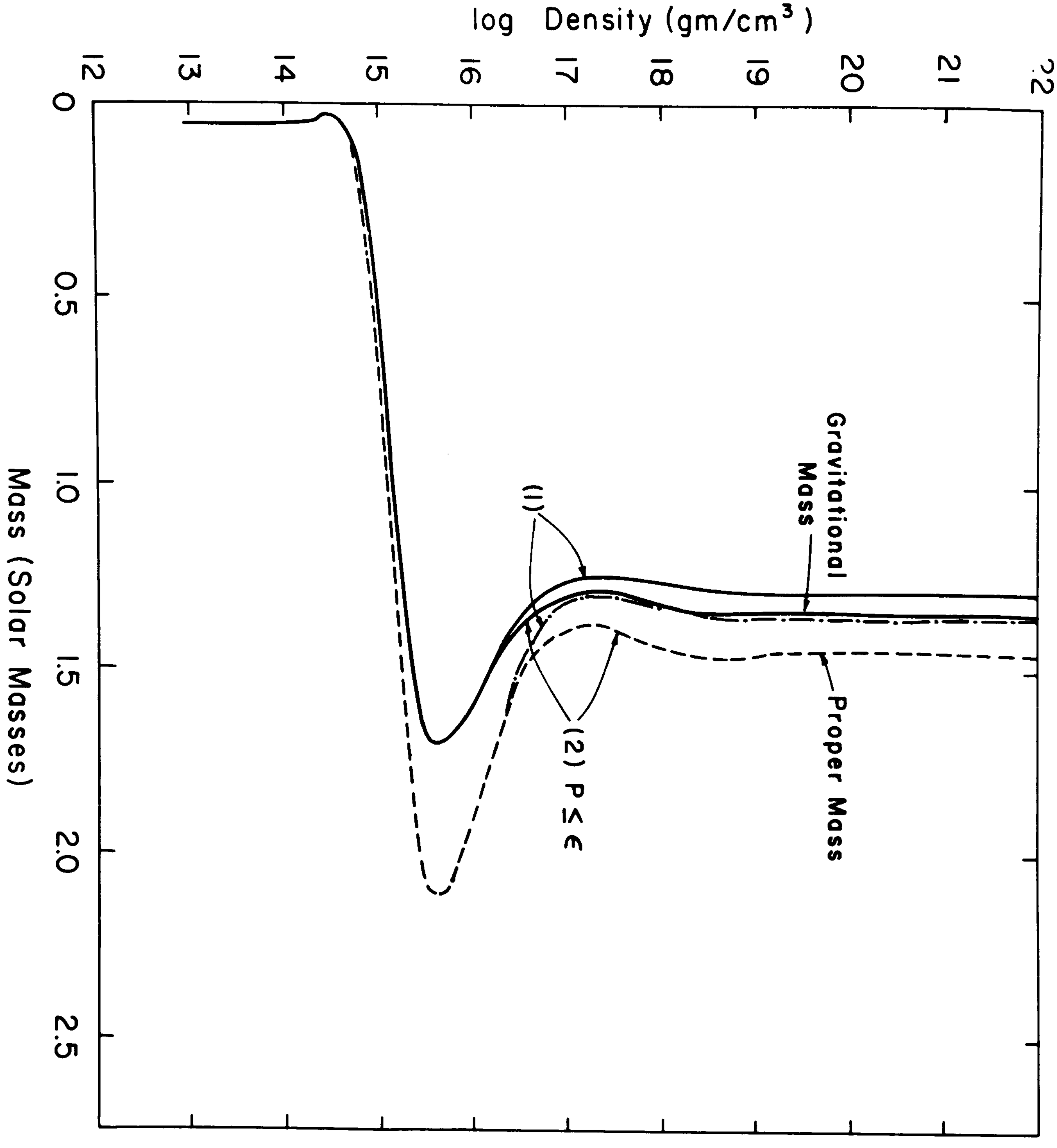
log Density (gm/cm³)
12
13
14
15
16
17
18
19
20
21
22
Mass (Solar Masses)
0
0.5
1.0
1.5
2.0
2.5
Gravitational Mass
Proper Mass
(1)
(2) P ≤ ϵ

Figure 32

TABLE 11a. Relativistic Skyrme-Cameron type models with $P \leq \mathcal{E}$, in medium and high density regions (the symbols are those introduced in Tables 8 and 9).

$\log \mathcal{E}^c$ (cgs)	$\log P^c$ (cgs)	R(km)	$M/M_\odot$	$M_P/M_\odot$	$M_B/M_\odot$	t_n^c
14.947	34.662	8.013	0.4954	0.5423	0.0469	2.0
15.311	35.670	8.768	1.441	1.726	0.285	2.5
15.704	36.478	7.684	1.692	2.078	0.386	3.0
16.165	37.173	6.599	1.503	1.752	0.249	3.5
16.678	37.795	6.221	1.329	1.443	0.114	4.0
17.726	38.906	6.612	1.313	1.413	0.095	5.0
18.726	39.912	6.627	1.345	1.457	0.112	6.0
19.678	40.861	6.599	1.338	1.440	0.102	7.0
20.597	41.778	6.606	1.337	1.438	0.101	8.0
21.496	42.675	6.609	1.338	1.440	0.102	9.0

TABLE 11b. Relativistic Skyrme-Cameron type models without relativistic limitation $P \leq \mathcal{E}$ (the symbols are those introduced in Tables 8 and 9).

$\log_{10} \mathcal{E}^c$ (cgs)	$\log_{10} P^c$ (cgs)	R(km)	$M/M_\odot$	$M_P/M_\odot$	t_n^c
13.6974	31.8256	22.44	0.04612	0.04754	0.8
14.7128	33.8841	6.325	0.12116	0.12523	1.7
14.9470	34.6622	8.013	0.49537	0.54228	2.0
15.3854	35.8435	8.630	1.5595	1.8724	2.6
15.6207	36.3276	7.945	1.6993	2.0890	2.9
15.8805	36.7672	7.186	1.6336	1.9787	3.2
16.1654	37.1733	6.583	1.5026	1.7509	3.5
16.7830	37.9132	6.044	1.2974	1.3343	4.1
17.7261	38.9058	6.192	1.2584	1.3136	5.0
18.9199	40.1056	6.274	1.2911	1.3655	6.2
19.7708	40.9543	6.255	1.2886	1.3611	7.1
20.5968	40.7779	6.255	1.2870	1.3533	8.0
21.6741	42.8532	6.258	1.2877	1.3592	9.2
22.4712	43.6493	6.259	1.2880	1.360	10.1

We noted in the previous chapter (III-5) that pressure must not exceed energy density so that the speed of sound will not exceed the speed of light. We also noted that a potential of the Skyrme type does exceed the limit $P = \mathcal{E}$ as $\mathcal{E} \rightarrow \infty$. To take this requirement into account, the pressure calculated through the relativistic Skyrme equation of state (3-39) was switched over to the asymptotic equation $P = \mathcal{E}$ as soon as the pressure started to exceed the energy density. In this way, curves marked (2) in Figure 32 were obtained. These show the relation between central energy density and gravitational mass (solid curve) and central energy density and proper mass (dashed curve), with the relativistic limitation $P < \mathcal{E}$. Comparing curves (1) with curves (2) in Figure 32 we see that the effect of the requirement $P < \mathcal{E}$ is appreciable only for $\mathcal{E}^c > 10^{16.4}$ gm/cm^3, and that the asymptotic mass (mass with infinite central density) with $P < \mathcal{E}$ appears to be increased somewhat from the value for models with the pure Skyrme equation of state (without the limitation $P < \mathcal{E}$). The effect of the relativistic limit is seen to discourage any further change of equilibrium mass in the same direction with increasing central density. This general conclusion will be further confirmed in Section IV-4i.

The radial distribution of $t_n(r)$ (which specifies the density distribution) and that of mass M_r (or $u(r)$) of a typical model of the type introduced above (the last type with the relativistic correction $P < \mathcal{E}$), in the high density region, are shown in Figure 33. This corresponds to a model with $t_n{}^c = 6.3$, $\mathcal{E}^c = 10^{19}$ gm/cm^3, $P^c \sim 10^{40}$ dynes/cm^2, $M \sim 1.35\ \odot$ and $R \sim 6.5$ km. The general shape of this kind of curve is not only typical of Skyrme-Cameron type models, but applies to almost all kinds of models from those of an ideal Fermi gas to the most complicated models of mixtures under complicated interaction forces, provided that the central density is the same. For instance, the density profile in Figure 33 is similar to the one of the curve (1) in Figure 36 obtained for a model of a Levinger-Simmons type potential v_β applied to pure neutron gas. The conclusion is that the shape of the density profile (and also of the mass profile) is determined by the value of the central density. This point is to be investigated later.

Some of the interesting properties of the final models of the Skyrme-Cameron type are summarized in Tables 8 and 11a. Table 8 presents the results obtained by Cameron and introduced in Section IV-2f which are found to be identical with the results of this section for $\mathcal{E}^c < 10^{15}$ gm/cm^3, and Table 11a presents models constructed by the present writer in higher density region where all the required modifications have been applied ($P \leqslant \mathcal{E}$, etc.). Those results will be compared, shortly, with the other models of a real gas.

d. Neutron Star Models of the Levinger-Simmons Type

The next series of neutron star models have been constructed through the use of the equation of state for a real gas consisting of a pure neutron configuration in which the interaction potentials are of Levinger-Simmons type introduced in Section III-4f. Because of the importance of this type of model in the present research, let us review some of the conclusions of that section. The equation of state was constructed in a parametric form, namely $P = P(t)$ and $\mathcal{E} = \mathcal{E}(t)$. Both $P(t)$ and $\mathcal{E}(t)$ consist of a kinetic energy term and an interaction potential term. The kinetic energy part denoted by subscript KE is just the relativistic expression for non-interacting particles

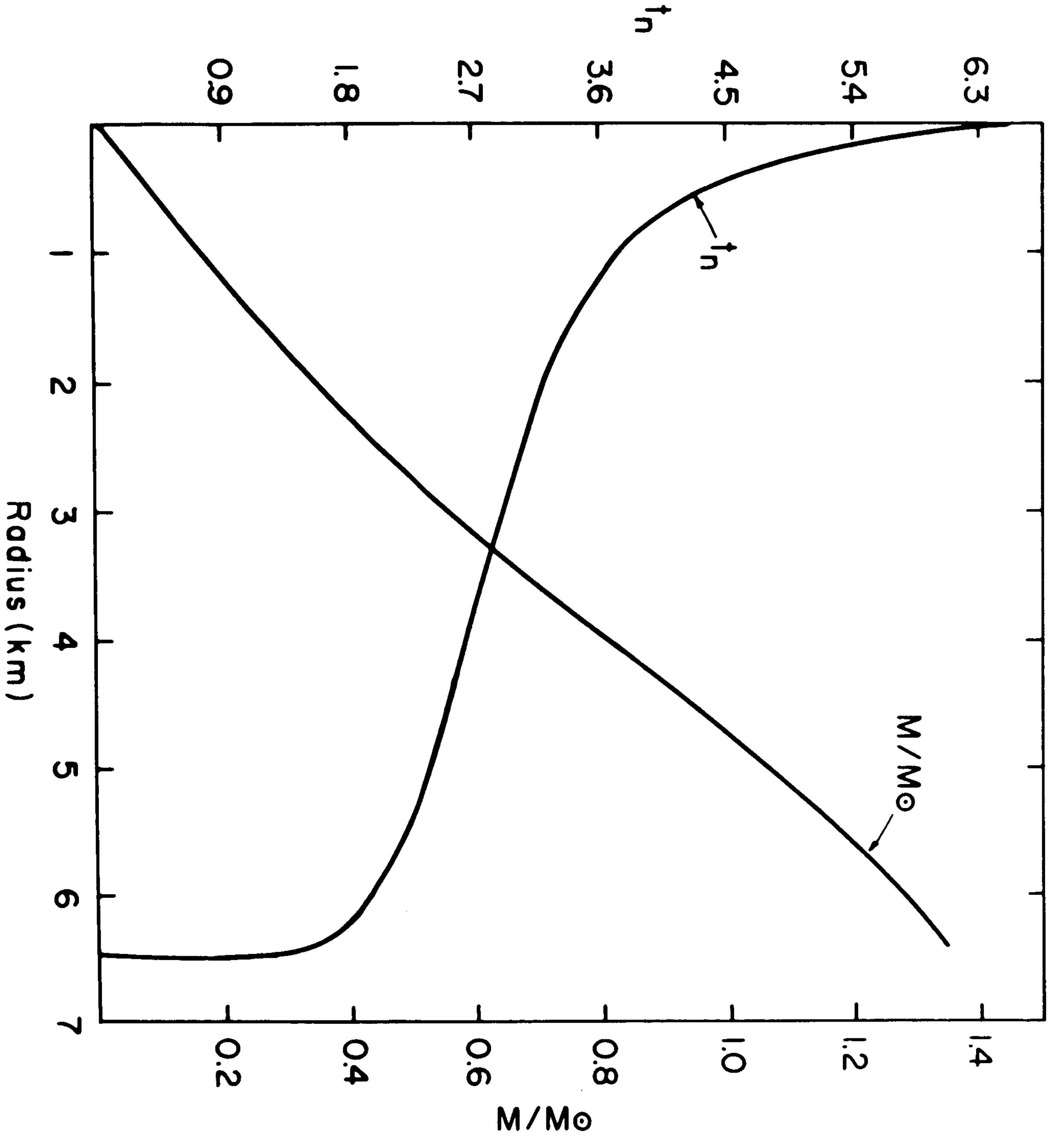
t_n
0.9
1.8
2.7
3.6
4.5
5.4
6.3
Radius (km)
1
2
3
4
5
6
7
M/M⊙
0.2
0.4
0.6
0.8
1.0
1.2
1.4
t_n
M/M⊙

Figure 33

$$\mathcal{E}_{KE} = K\,(\sinh t - t) \tag{4-8}$$

$$P_{KE} = \frac{1}{3}\,K\,(\sinh t - 8\sinh\frac{t}{2} + 3t) \tag{4-9}$$

The potential term involves the static and velocity-dependent parts of the ordinary and the exchange integrals v_o, ω_o, v_e, ω_e. v_o and ω_o are given in the analytic forms $-C_1 k^3$ and $C_2 k_f^5$ respectively, where C_1 and C_2 are constants, and v_e and ω_e depend on the Fermi wave number k_f in a complicated way and were solved for graphically. Three types of potential were suggested, v_α, v_β and v_γ, which depend on the different coefficients of the four terms introduced. Due to a poor fit to the experimental data in the region of greatest interest, v_α was simply discarded in the present research, and v_β and v_γ were used. The basic properties of these two types of potential are summarized in (3-51) and (3-52). It will be recalled that v_β is a square well potential with a tail of the Yukawa type and v_γ is a complicated combination of exponentially decreasing terms which in effect gives rise to same kind of properties as v_β. The major difference between v_β and v_γ is that the coefficients, especially of the repulsive terms, are much larger for v_γ than for v_β. In low density regions (up to about $\rho \sim 10^{13}$ gm/cm^3) the difference between the two is quite small as Figure 24 indicates, but as the repulsive terms begin to dominate over the rest, the potential v_γ goes up much faster than v_β, giving higher pressure at a given density. Larger pressure at the same density produces the possibility of a larger total mass of the star, and we expect larger masses to be associated with v_γ than with v_β at the same central density. This will be confirmed shortly. These two potentials of course do not exhaust all the possibilities of interaction forces, nor do they give upper and lower limits to the possible models of different nuclear forces. However, noting the highly different behavior of the two in high density regions (the regions which are critical in setting an upper limit to stable configurations), it is hoped that these two contrasting models which are fairly consistent with experimental data may represent the probable limits of uncertainty of physical reality. Besides v_β and v_γ, the straight average of the two, $v_{\beta\gamma}$, was also used in constructing a third kind of model of the Levinger-Simmons type.

We have seen that the Levinger-Simmons nuclear potentials are expressed as a function of k_f, but because k_f is directly related to t through (3-30a) and (3-47) the potential terms are expressible in terms of t also. In this way, by choosing t as the constant of integration, we may proceed to carry out the integrations as before. However, due to some technical problems it was concluded that it is more convenient to choose P^o, the pressure at the center of the star in relativistic units, as the parameter of integration this time. Since the equation of state is expressed as a function of t, it is simplest if P and $\mathcal{E}$ (and ρ_m) are calculated in terms of t first. Therefore, the following method was adopted in the actual integration: In a separate subroutine, pressure, energy density, matter density, number density, etc., and other related interesting quantities have first been calculated separately and then listed in terms of t, with the interval Δt of 0.01, extending from $t = 0$ to $t = 16$, which should cover a region far beyond the major region of interest. The table of 1600 such sets of values was used as the input to the main program. Therefore, once P is specified, the densities $\mathcal{E}$ and ρ_m, t, and other interesting quantities were obtained by the use of the interpolation subroutine operating on this input table. Except for this minor change of procedure, the integrations were carried out in the same manner as outlined in earlier sections (IV-3, a, b, and c). As before, the equation of state was switched over to $P = \mathcal{E}$ as soon as this asymptotic value was reached.

The results are summarized in Tables 12, 13, 14 and 15, and Figures 34, 35 and 36. In the first three tables the notation is as follows: P^o is the central pressure in relativistic units (i.e., $c = G = \hbar = 1$), P^c is the same in dynes/cm^2, R is the coordinate radius (or the observable radius), M, M_p, M_B and M'_B are gravitational mass, proper mass, and two kinds of binding energy, respectively, in solar mass units $M_\odot$. t_n^c is the relativistic parameter t of neutrons at the center of the star. In Table 15, α and α_2 are two kinds of packing fractions, $g_{44}(R)$ and $g_{rr}(R)$ are time metric and the radial component of the metric $g_{\mu\nu}$ evaluated at the surface of the star. $\mathcal{P}(R)$ is the gravitational red shift. To make the physical meaning of these quantities clearer, some of the definitions given earlier are summarized below:

$$M = U(R) = \int_0^R 4\pi \mathcal{E} r^2 dr \; ; \; M_p = \int_0^R 4\pi \rho_m r^2 \sqrt{-g_{rr}}\, dr$$

$$M_B = \int_0^R 4\pi r^2 \{\sqrt{-g_{rr}}\, \rho_m - \mathcal{E}\} dr = M_p - M \tag{4-10}$$

$$M'_B = \int_0^R 4\pi r^2 \mathcal{E} (\sqrt{-g_{rr}} - 1) dr = M_0 - M$$

where

$$M_0 \equiv \int_0^R 4\pi \mathcal{E} r^2 \sqrt{-g_{rr}}\, dr = \int_0^R \mathcal{E}\, dV_p$$

$$\alpha = M_B/M_p \; ; \; \alpha_2 = M'_B/M$$

TABLE 12. Neutron star models with v_β ($P \leq \epsilon$), where P^o is the central pressure in relativistic units, M'_B is a quantity as defined by (4-10), and other symbols are those introduced in Tables 8 and 9.

P^o	$\log \epsilon^c$(cgs)	$\log \rho_m^c$(cgs)	$\log P^c$(cgs)	R(km)	$M/M_\odot$	$M_P/M_\odot$	$M_B/M_\odot$	$M'_B/M_\odot$	f_n^c
5×10^{-7}	12.5168	12.5158	30.5072	35.7977	0.04850	0.04857	0.00007	8.48×10^{-5}	0.325
5×10^{-6}	13.1571	13.1155	31.5072	27.4937	0.08406	0.08442	0.00036	3.42×10^{-4}	0.531
5×10^{-5}	13.8357	13.8316	32.5072	20.1809	0.12654	0.12743	0.00089	0.001107	0.887
5×10^{-4}	14.5864	14.5754	33.5072	14.2981	0.14723	0.14891	0.00168	0.00237	1.544
5×10^{-3}	15.1432	15.1167	34.5072	8.5150	0.19025	0.19375	0.00350	0.00692	2.274
5×10^{-2}	15.5300	15.4763	35.5072	6.1902	0.54178	0.57160	0.02982	0.06701	2.899
5×10^{-1}	15.9545	15.8163	36.5072	5.2031	0.95919	1.0914	0.1322	0.3064	3.598
5×10	16.5535	16.1661	37.5072	4.0716	0.88715	0.95762	0.07047	0.4365	4.414
5×10^{1}	17.5535	16.5909	38.5072	3.7859	0.74294	0.72631	-0.01663	0.3938	5.514
5×10^{2}	18.5535	16.9671	39.5072	3.9517	0.75814	0.74640	-0.01174	0.3976	6.560
5×10^{3}	19.5535	17.3366	40.5072	3.9392	0.76916	0.76264	-0.00652	0.4086	7.630
5×10^{4}	20.5535	17.7069	41.5072	3.9256	0.76461	0.75592	-0.00869	0.4079	8.73
5×10^{5}	21.5535	18.0788	42.5072	3.9303	0.76468	0.75794	-0.00674	0.4091	9.85
5×10^{7}	23.5535	18.8258	44.5072	3.9299	0.76501	0.75651	-0.00850	0.4082	12.12

TABLE 13. Neutron star models with v_γ $(P \leqslant \mathcal{E})$. (The symbols are those introduced in Table 12.)

P^o	log $\mathcal{E}^c$(cgs)	log ρ_m^c(cgs)	log P^c(cgs)	R(km)	$M/M_\odot$	$M_P/M_\odot$	$M_B/M_\odot$	$M'_B/M_\odot$	t_n^c
5×10^{-4}	14.3375	14.3178	33.5072	14.154	0.25489	0.25517	0.00028	0.00607	1.277
10^{-3}	14.4713	14.4476	33.8082	13.313	0.34958	0.35088	0.00130	0.01184	1.406
5×10^{-3}	14.7569	14.7261	34.5072	12.371	0.77254	0.79504	0.02250	0.06152	1.723
10^{-2}	14.8724	14.8402	34.8082	12.151	1.0598	1.1177	0.0579	0.1212	1.871
5×10^{-2}	15.1619	15.0995	35.5072	11.333	1.7674	2.0274	0.2600	0.4183	2.247
10^{-1}	15.3035	15.2100	35.8082	10.707	1.9385	2.2844	0.3459	0.5804	2.425
5×10^{-1}	15.6908	15.4660	36.5072	9.008	1.9274	2.2812	0.3638	0.8313	2.880
10	15.8905	15.5763	36.8082	8.366	1.8164	2.0998	0.2834	0.8590	3.094
5×10	16.5535	15.8842	37.5072	7.586	1.5571	1.6589	0.1018	0.8079	3.75
10^{1}	16.8546	16.0081	37.8082	7.579	1.4961	1.5649	0.0688	0.7859	4.034
5×10^{1}	17.5535	16.2807	38.5072	7.857	1.4915	1.5488	0.0573	0.7751	4.700
5×10^{2}	18.5535	16.6573	39.5072	7.954	1.5414	1.6260	0.0846	0.8070	5.695
5×10^{3}	19.5535	17.0307	40.5072	7.898	1.5345	1.6160	0.0815	0.8106	6.742

TABLE 15. Neutron star models with v_β, v_γ and $v_{\beta\gamma}$ (the symbols are those introduced in tables 8, 9 and 10).

CLASS	$\log \rho_m^c$(cgs)	$\log_{10} N$	α	α_2	$g_{44}(R)$	$-g_{rr}(R)$	$\mathcal{P}(R)$
Neutron gas with v_β	12.5158	5.81×10^{55}	0.00144	1.75×10^{-3}	0.996	1.003	0.0020
	13.8316	1.524×10^{56}	0.00700	0.00874	0.982	1.018	0.00924
	15.1167	2.32×10^{56}	0.0181	0.0364	0.9342	1.07	0.0329
	15.4763	6.85×10^{56}	0.0524	0.124	0.744	1.348	0.128
	15.8163	1.32×10^{57}	0.121	0.320	0.460	2.18	0.270
	16.1661	1.146×10^{57}	0.0735	0.493	0.360	2.78	0.320
	16.9671	8.94×10^{56}	-0.0157	0.524	0.616	1.62	0.192
	17.7069	9.05×10^{56}	-0.0115	0.535	0.612	1.63	0.194
	18.8258	9.05×10^{56}	-0.0112	0.535	0.610	1.64	0.195
Neutron gas with v_γ	14.3178	3.05×10^{56}	0.0011	0.0238	0.947	1.056	0.0265
	14.7261	9.51×10^{56}	0.0287	0.0799	0.816	1.224	0.0920
	15.0995	2.42×10^{57}	0.128	0.237	0.542	1.845	0.229
	15.2100	2.74×10^{57}	0.151	0.300	0.468	2.14	0.266
	15.4660	2.30×10^{57}	0.159	0.431	0.372	2.69	0.314
	15.8842	1.98×10^{57}	0.0615	0.519	0.396	2.52	0.3018
	16.2807	1.85×10^{57}	0.0370	0.520	0.440	2.28	0.280
	17.0307	1.93×10^{57}	0.0505	0.533	0.427	2.34	0.2865
Neutron gas with $v_{\beta\gamma}$	12.3842	4.93×10^{55}	4.85×10^{-3}	1.42×10^{-3}	0.997	1.002	0.00159
	13.6739	1.374×10^{56}	0.00646	0.00737	0.984	1.017	0.00790
	14.7312	5.66×10^{56}	0.0354	0.0520	0.883	1.13	0.0583
	15.3069	2.12×10^{57}	0.135	0.263	0.516	1.94	0.242
	15.8654	1.80×10^{57}	0.1462	0.500	0.376	2.66	0.312
	16.4847	1.50×10^{57}	0.0283	0.520	0.450	2.22	0.275
	17.4107	1.55×10^{57}	0.0217	0.528	0.438	2.28	0.281
	18.5327	1.55×10^{57}	0.0274	0.528	0.440	2.27	0.280

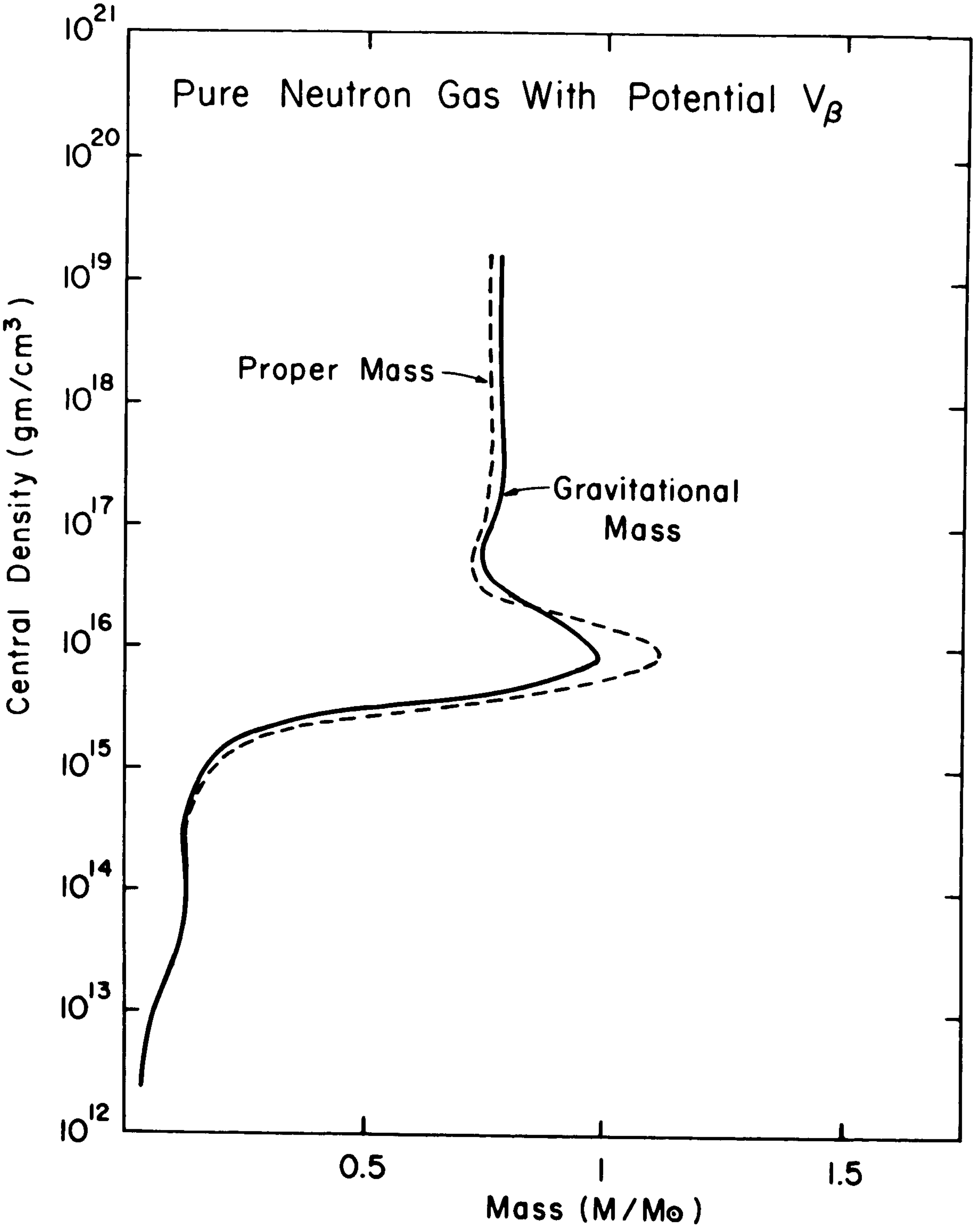
Pure Neutron Gas With Potential V_β
Proper Mass
Gravitational Mass
Central Density (gm/cm^3)
10^{21}
10^{20}
10^{19}
10^{18}
10^{17}
10^{16}
10^{15}
10^{14}
10^{13}
10^{12}
0.5
1
1.5
Mass (M/M⊙)

Figure 34

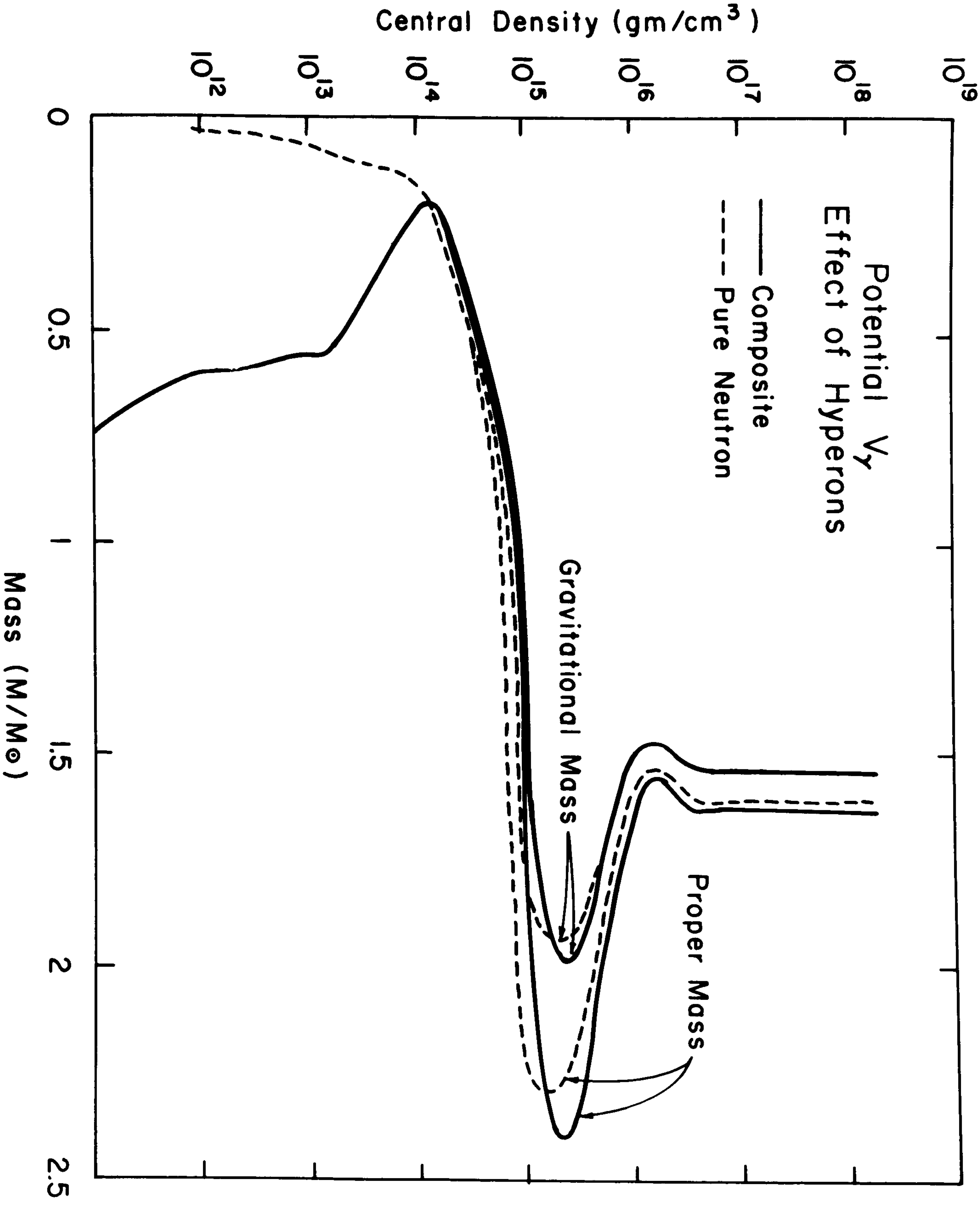
Potential V_γ
Effect of Hyperons
Composite
Pure Neutron
Central Density (gm/cm^3)
10^{12}
10^{13}
10^{14}
10^{15}
10^{16}
10^{17}
10^{18}
10^{19}
Mass (M/M⊙)
0
0.5
1
1.5
2
2.5
Gravitational Mass
Proper Mass

Figure 35

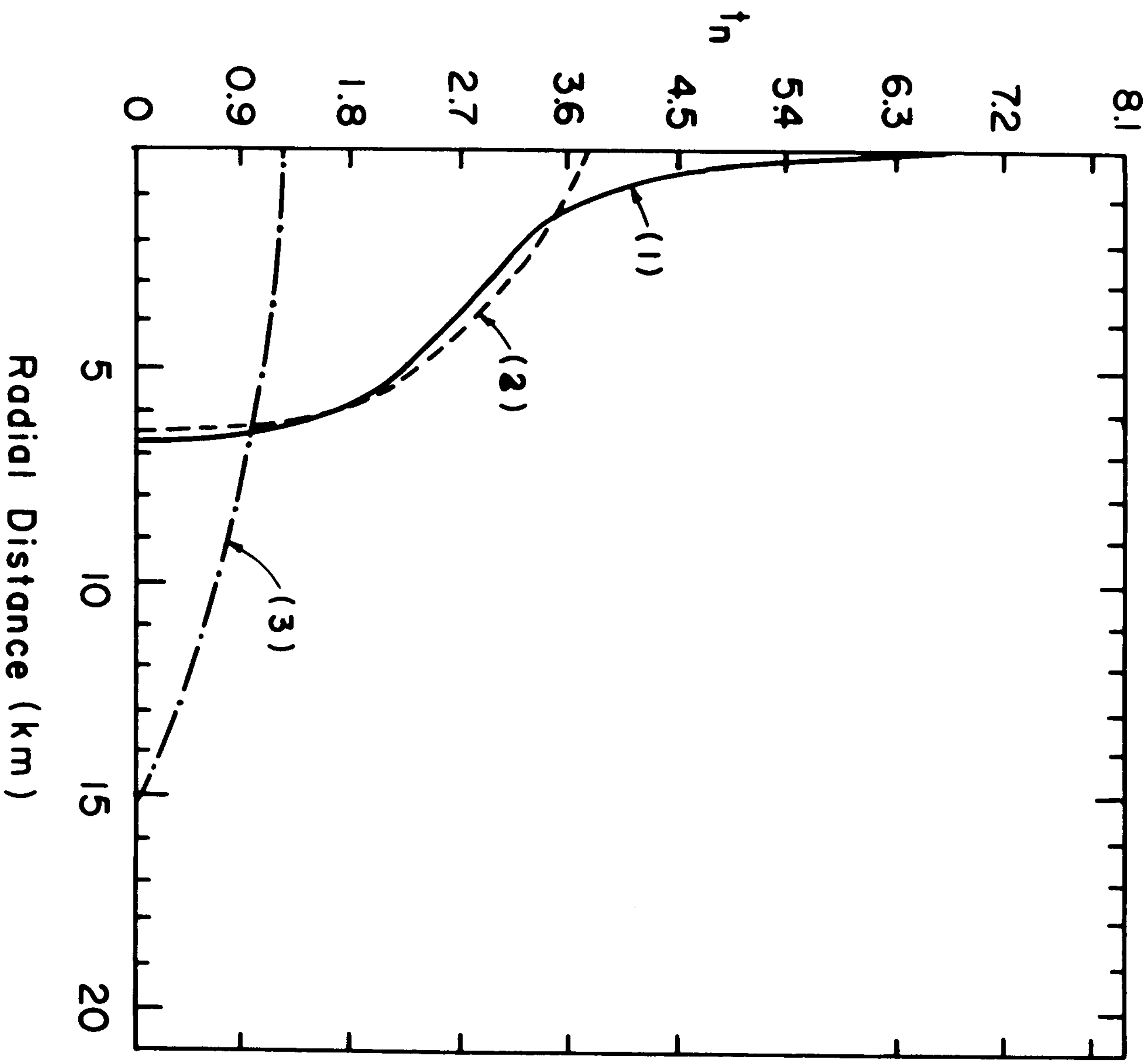

Figure 36

$\mathcal{E}$ is the total energy density, and ρ_m is the total matter density ($=m_n n_n$ for a pure neutron configuration, where m_n is the neutron mass and n_n is the neutron number density).

$$N = \int 4\pi n(r) r^2 \sqrt{-g_{rr}}\, dr \quad (= M_P/m_n \text{ for a pure neutron gas}).$$

n(r) is the total baryon number density at r.

$$-g_{rr} = (1 - 2u(r)/r)^{-1}$$

$$\varphi(R) = \frac{M}{R} = 1.47\,(M/M_\odot)/R(km) \qquad (4\text{-}11)$$

$$g_{44}(R) = 1 - 2\varphi(R) = -1/g_{rr}(R)$$

The relativistic system of units is adopted unless otherwise specified. From these definitions it is clear that M_B is the binding energy with respect to the total mass before it has been assembled as a star or the total binding energy; while M'_B, the macroscopic mass defect, is the difference between the total mass in the absence and in the presence of a gravitational field (note that in the absence of a gravitational field, $g_{rr} = -1$ and M'_B is zero), and thus it corresponds to the binding due to gravity only (with microscopic binding energies excluded).

We noted that M_B, and hence a, becomes negative when $\log \mathcal{E}^c \gtrsim 16.7$ for an ideal gas (Table 10). Negative binding energies do also occur for models with v_β (see Table 12 and 15 or Figure 34), but the gravitational masses are always smaller than the proper masses for other configurations (i.e. for v_γ, $v_{\beta\gamma}$ and the Skyrme potential). An explanation of this will be attempted in the next section (IV-4). For the sake of comparison, it is more convenient to speak of the fractional bindings a and a_2 than of M_B and M'_B. For the ideal gas (Table 10), the maximum a is around 0.07, while for v_β, v_γ, and $v_{\beta\gamma}$, it is 0.12, 0.15, and 0.16, respectively.

For the final Skyrme-Cameron type models (Table 8 and 11 a), α goes as high as about 0.2. The α_1 obtained by Ambartsumyan and Saakyan for a real hyperon gas behaves somewhat differently from those of v_β, v_γ, $v_{\beta\gamma}$ and of the Skyrme-type. Their α_1 was defined improperly, especially for a mixture of hyperons, and this may be a cause of the difference. α_2 increases with the increase of central density in all models, approaching asymptotic values of about 0.53 to 0.55 as $\mathcal{E}^c \rightarrow \infty$, depending on the model. This means that in the high density limit, the macroscopic mass defect due to the presence of gravity becomes even greater than half the observable mass.

Values of $g_{44}(R)$ and $g_{rr}(R)$ in Table 15 reveal that even at the surface, curvature of space due to the gravitational field is quite large for some of the dense stars (of central density $\rho_m{}^c \gtrsim 10^{15}$ gm/cm^3). The deviation of the metric from the Euclidean metric is much larger for models of the Levinger-Simmons type than for models of an ideal Fermi gas. This is because the effect of the interaction forces between nucleons (or baryons) is to make the ratio M/R larger than for the case of non-interacting particles and the curvature depends on M/R through the gravitational potential. On examining these tables, we see that the maximum curvature at the surface and the maximum red shift both occur when the central density is somewhat higher than that corresponding to the maximum mass. For instance, for v_γ the maximum mass of about 1.94 $M_\odot$ occurs when log $\rho_m{}^c \sim 15.3$, while maximum surface curvature and red shift occur at log $\rho_m{}^c \sim 15.47$. The solid curves in Figure 31 shows the central density-radius relation for a mixture of baryon gases, but similar curves are obtained for the models v_β and v_γ of pure neutron gases also.

The general behavior of the radius exhibited in Figure 31 applies also to pure neutron gases, except for the exclusion of the envelope effect.

The total baryon numbers N of the star are listed in Table 15. On comparing the values in Table 15 with those given by Saakyan (Table 9), we note that the N of all our models are much larger than those of his ideal gas models, and that the N of the models V_γ and $V_{\beta\gamma}$ are somewhat larger than those of his "real" gas models, while our models V_β and his "real" gas models have more or less the same values for N. This is easily seen from the fact that for a pure neutron configuration N is just the total proper mass divided by the neutron mass, that the proper masses of all our models are much larger than that of an ideal Fermi gas, and that these of our models V_γ and $V_{\beta\gamma}$ are larger then those of Saakyan's "real" gas models, while the masses associated with our V_β models and his "real" gas models are similar. A very interesting property of N is that with an increase of central density, N first increases, reaching a maximum and then decreases; after reaching a minimum it increases again a little, before reaching a constant value at $\rho_m{}^c = \infty$. When the total baryon number N is plotted against total gravitational mass M, the general behavior of Figure 5 in reference 15 is also revealed for all our models; that is, an assembly of N nucleons generally has one equilibrium configuration when N is smaller than a certain value, say N_1; three equilibrium configurations with different values of M exist in the intermediate region, $N_1 < N < N_2$; two equilibrium configurations in the higher N region $N_2 < N < N_3$ (where $N_3 > N_2 > N_1$); and no equilibrium solutions for $N > N_3$.

Let us now turn to Figure 34 where the central density of V_β models is plotted against total gravitational mass (the solid curve) and total proper mass (the dashed curve) of the star. The maximum mass comes at about $M \sim 0.98\ M_{\odot}$ and $M_p \sim 1.1\ M_{\odot}$ where $\log\ \rho_m{}^c \sim 15.96$ and $R \sim 5$ km. Then crossing of the gravitational mass track and the proper mass track in the $\rho_m{}^c - M$ plane occurs at $\log\ \rho_m{}^c \sim 16.3$, $M \sim M_p \sim 0.85\ M_{\odot}$ and $R \sim 4$ km. The central singularity develops at $M \sim 0.77\ M_{\odot}$, $M_p \sim 0.76\ M_{\odot}$ and $R \sim 3.93$ km. By using the same argument employed by Oppenheimer and Volkoff, we find that all the stellar configurations in the upper branch of the big hump are unstable. Stable models lie in the region $10^{15} \lesssim \rho_m{}^c < 10^{16}$ gm/cm^3. The second small maximum exists at around $\log\ \rho_m{}^c \sim 17.4$ and can be seen in Table 12 but is hardly noticable in Figure 34. Next, let us turn to Figure 35 where the central matter density of V_γ models is plotted against gravitational and proper mass (both dashed curves refer to pure neutron stars). The maximum masses ($M \sim 1.94\ M_{\odot}$ and $M_p \sim 2.3\ M_{\odot}$) occur at $\log\ \rho_m{}^c \sim 15.3$, where $R \sim 10.5$ km. A singularity develops at the center when $M \sim 1.54\ M_{\odot}$, $M_p \sim 1.62\ M_{\odot}$ and $R \sim 7.9$ km. Again the second maximum is hard to see in this figure but it is easily recognized in Table 13. For $\log\ \rho_m{}^c \lesssim 13.7$, models of type V_β and V_γ with the same central density almost coincide. That this should occur is obvious from the fact that these two potentials are almost identical in regions of small density. A striking result is that the maximum mass of V_γ is twice as large as that of V_β. The major difference between V_γ and V_β lies in the larger repulsive term for V_γ which is due to the higher value of the coefficient of this term. One important conclusion deduced from the above result is that one of the decisive factors for determining the parameters of neutron stars is the exact form of the interaction forces between neutrons (or between baryons in the case of a baryon gas).

It is interesting to compare these results with Skyrme type models (Figure 32). In Figure 32, the central density refers to the energy density ϵ^c while that in Figures 34 and 35 refers to the matter density $\rho_m{}^c$. But by inspection of these figures we easily recognize that Skyrme's curve comes between the V_β curve and the V_γ curve in the $\rho^c - M$ plane. One major difference between the Skyrme type models and those of the Levinger-Simmons type is seen in the low density region; namely, in the former, the minimum mass (about 0.02 $M_\odot$) comes at $\log \rho^c \sim 14.5$, while in the latter the minimum mass (at the same ρ^c) is much larger at about 0. 2 $M_\odot$. This is seen to be due to the large difference between the Skyrme potential and Levinger-Simmons potential in the region $10^{14} \lesssim \rho < 10^{15}$ gm/cm^3 covered in Figure 24. In this region the Skyrme potential has a much larger attractive term which lowers the pressure considerably and results in smaller masses. For $\rho^c < 10^{13}$ gm/cm^3, V_β, V_γ, $V_{\beta\gamma}$ and Skyrme all approach the asymptotic line of non-interacting particles in Figure 24 and all models of the pure neutron configuration converge to the same curve for $\rho^c < 10^{13}$ gm/cm^3.

The $V_{\beta\gamma}$ models come nearly midway between those of V_β and V_γ. Characteristic features seen in other models of real gases (V_β, V_γ and the Skyrme type) are seen in the $V_{\beta\gamma}$ models also (Tables 14 and 15). The maximum masses are $M \sim 1.65\ M_\odot$ and $M_p \sim 1.93\ M_\odot$ at $\rho_m{}^c \sim 10^{15.5}$ gm/cm^3 with $R \sim 8$ km. The deviation of the $V_{\beta\gamma}$ models from those of V_β takes place at around $\rho^c \sim 10^{14}$ gm/cm^3. Another small maximum is seen at $\log \rho_m{}^c \sim 16.9$. The central density-mass curves are not shown for the $V_{\beta\gamma}$ models because they are similar to the final Skyrme-Cameron type models (Figure 32) in high density regions, while in low density regions, they converge to other Levinger-Simmons type models. The central singularity develops for $V_{\beta\gamma}$ when $M \sim 1.26\ M_\odot$, $M_p \sim 1.3\ M_\odot$ and $R \sim 6.6$ km.

To see the general features of the density distribution within a star, the density profile (in the form of $t_n{}^c$ vs. r curve) of three different models of the $V_{\beta\gamma}$ type with the low, medium and high central densities are plotted in Figure 36 and labled (3), (2), and (1). Some of the characteristics of these models are listed below:

Models	P^o	Log P^c	Log $\mathcal{E}^c$	Log ρ_m^c	M	R	M_p	$t_n{}^c$
(1)	3×10^4	41.23	20.33	17.41	1.254	6.58	1.292	7.85
(2)	3	37.29	16.29	15.8	1.4	6.6	1.6	3.7
(3)	3×10^{-4}	33.29	14.28	14.27	0.185	15.1	0.188	1.24
Units	$c=\hbar=G=1$	cgs	cgs	cgs	$M_\odot$	km	$M_\odot$	-

This graph clearly shows how the singularity is developed at the center at a finite stellar radius and mass. With a further increase in the central density, the distortion in shape of the type seen in the curve (1) becomes more and more exaggerated until in the limit as $\rho^c \to \infty$, we have all of the matter located at the center. It is very hard to understand why such a configuration can still possess a finite radius. However, the present treatment of the problem may break down before such a limit is reached. We come back to the discussion of the difficulty associated with these singularities later. The general behavior of density profiles exhibited in Figure 36 (which was obtained for $v_{\beta\gamma}$ type models of pure neutrons) with an increase of central density has also been seen in all the other kind of models constructed in this research.

e. Composite Models of the Levinger-Simmons Type

So far all the models constructed in this section had pure neutron configurations, that is, they are "neutron star models" in the literal sense. In reality, we have seen that such a gas is contaminated with other sub-atomic particles, whose kind and concentration depends on the density we are dealing with. In highest density regions, it is a mixture of various kinds of baryons, mesons and leptons. In lowest density regions neutrons are not even allowed to exist and the equilibrium matter consists of heavy nuclei and electrons. In the final set of models, the final composite equation of state constructed in Section III-6 was used. Before proceeding, let us review the conclusions of that section. The equation of state in the major region was expressed as equations (3-73) and (3-74), the relativistic Levinger-Simmons type equations, where in effect everything was expressed as a function of a single parameter t_n. As soon as this equation of state starts to violate the relativistic requirement $P \leq \mathcal{E}$, the equation of state was replaced by the asymptotic equation $P = \mathcal{E}$ as before. In the region $\rho \lesssim 10^{13.8}$ gm/cm^3, we are dealing with a mixture of neutrons, electrons and positive ions (as we lower the density, more heavy ions appear while proton numbers decrease rapidly). When the density becomes less than about $10^{11.3}$ gm/cm^3, the neutron concentration rapidly decreases to zero and the main pressure comes from degenerate electrons. There is a transition region in this vicinity where the main pressure contributor changes from electrons to neutrons or vice versa. In a stellar interior the density decreases as we go radially outward and there is this transition from the neutron phase to the electron-nuclear phase at some boundary within the star. We call the interior part whose major constituent is neutrons and other baryons the "neutron core," and the outer layers of an electron-nuclear configuration "the electron-ion envelopes" for convenience. In most of the previous models such envelopes were simply neglected. However,

our results soon reveals that such a simplification is not justified. The final composite equation of state in Section III-6 automatically goes over into the electron-nuclear equation of state in low density regions, takes interaction forces between baryons into account in higher density regions through a Levinger-Simmons type potential acting on all baryons, and transfers to the asymptotic equation $P = \mathcal{E}$ in the high density limit.

Up to $\rho = 10^{13.86}$ gm/cm^3, the equations are expressed in terms of ρ and thereafter in terms of t_n. The general procedure employed was as follows: First, from log $\rho = 0$ to log $\rho = 13.86$ with the interval $\Delta(\log \rho) = 0.02$; P, $\mathcal{E}$, ρ, t_n and all other related quantities of interest (electron number densities n_e, baryon number densities n, partial densities and pressures of components, etc.) were calculated in the manner described in Section III-6. All the parameters and quantities absent at a given density ρ were set equal to zero (for instance, in the regions of lowest density there are no neutrons and $n_n = t_n = 0$, etc.,). At the transition point the value of t_n corresponding to log $\rho = 13.8$ was used as the initial value and thereafter all quantities P, $\mathcal{E}$, ρ, etc., were calculated as functions of t_n from the initial t_n to $t_n = 16$, with the interval $\Delta t_n = 0.02$. The equation of state thus appears as an input table which lists a set of values of P, $\mathcal{E}$, ρ, etc., to the main program of integration. Special care was taken to see that everything is continuous at log $\rho = 13.86$.

In the main program, the central pressure P^o in relativistic units was chosen as the parameter of integration, and for each P, the corresponding $\mathcal{E}$, ρ, t_n, etc., were interpolated through the interpolation subroutine. In this manner the input table of the equation of state was prepared. The step by step integration was carried out by Adams' method as explained earlier. Another major difference (besides the difference in the equation of state) is that the integration was carried out to the point were $\log \rho = 0$ (that is, $\rho = 1$ gm/cm^3). (Our equation of state now includes the white dwarf region and the former method of terminating the integration at $\log \rho = 8$ is certainly no longer justified.)

The results obtained in this way explain the general behavior of dense stars from the lightest of these (in the white dwarf region) to the densest (with infinite central density). Some of the models obtained in this way are listed in Tables 16, 17 and 18. In the first, the various interesting quantities introduced in the previous sections are listed for composite models of the type v_β, in the second, for composite models of the v_γ type, and in the third for composite models of the type of either V_β or V_γ in the low density region where these two types of models are identical because of the absence of nuclear forces. In the previous section, the same quantities were calculated for models of a pure neutron configuration with V_β , V_γ and $V_{\beta\gamma}$.

To better see the effect of hyperons, pure neutron models of the v_γ type (dashed curves) and composite models of type v_γ (solid curves) are plotted together in the ρ^c-M plane in Figure 35. Here, the difference is clearly noticable. The major differences are that: (1) at the same central density, composite models have smaller masses than pure neutron models near $\rho^c \lesssim 10^{15}$ gm/cm^3; (2) for

TABLE 16. Composite models with V_β. (The symbols are those introduced in Tables 3 and 10.)

$\log \mathcal{E}^c$(cgs)	$\log \rho_m^c$(cgs)	$\log P^c$(cgs)	R(km)	$M/M_\odot$	$M_p/M_\odot$	$M_B/M_\odot$	α	$g_{44}(R)$	$-g_{rr}(R)$	$\mathcal{P}$ (R)
13.6798	13.6732	32.2853	407.33	0.13409	0.13387*	-0.00062	-0.00464	0.9906	1.008	0.00469
13.8352	13.8281	32.5072	124.847	0.13367	0.13355*					
14.4232	14.4119	33.2853	36.777	0.14604	0.14650	0.00046	0.00314	0.9886	1.013	0.00567
14.5943	14.5805	33.5072	30.435	0.14624	0.14688					
15.2588	15.2316	34.6533	10.032	0.19423	0.19701	0.00278	0.0141	0.9430	1.06	0.0285
15.4983	15.4677	35.2853	6.602	0.35286	0.36285					
15.6213	15.5833	35.6533	5.898	0.52948	0.57260	0.04512	0.0789	0.736	1.358	0.132
15.8543	15.7798	36.2853	5.263	0.85488	0.99961					
16.0952	15.9489	36.8082	4.713	0.96640	1.17409	0.2077	0.177	0.398	2.51	0.301
16.3740	16.1101	37.2853	4.210	0.93285	1.10785					
16.5535	16.2004	37.5072	4.011	0.89501	1.04442	0.1494	0.143	0.344	2.91	0.328
16.8546	16.3369	37.8082	3.820	0.83741	0.96986					
17.3317	16.5321	38.2853	3.708	0.76583	0.82676	0.06103	0.0738	0.392	2.55	0.304
17.5535	16.6182	38.5072	3.720	0.74908	0.79846					
17.8546	16.7326	38.8082	3.768	0.74278	0.78790	0.04512	0.0574	0.420	2.38	0.290
18.3317	16.9108	39.2853	3.848	0.75477	0.80536					
18.8546	17.1043	39.8082	3.874	0.76981	0.82915	0.05934	0.0717	0.416	2.40	0.292
19.8546	17.4736	40.8082	3.851	0.77250	0.83492					

TABLE 17. Composite models with V_γ. (The symbols are those introduced in Tables 8 and 10.)

$\log \mathcal{E}^c$(cgs)	$\log \rho_m^c$(cgs)	$\log P^c$(cgs)	R(km)	$M/M_\odot$	$M_p/M_\odot$	$M_B/M_\odot$	α	$g_{44}(R)$	$-g_{rr}(R)$	$\mathcal{P}$ (R)
13.5628	13.5571	32.1092	2.609×10^3	0.40238	0.40172*	-0.00066	-0.00164	0.9996	~ 1	2.26×10^{-4}
13.9795	13.9729	32.8082	47.388	0.15115	0.15194					
14.1366	14.1290	33.1092	29.531	0.18582	0.18751	0.00169	0.00902	0.982	1.02	0.00928
14.3900	14.3799	33.6533	18.079	0.30989	0.31507					
14.4567	14.4456	33.8082	16.663	0.36781	0.37567	0.00786	0.0210	0.935	1.07	0.0324
14.5826	14.5687	34.1092	14.869	0.51991	0.53740					
14.8027	14.7795	34.6533	13.314	0.95050	1.10634	0.1485	0.132	0.790	1.265	0.105
14.9896	14.9504	35.1092	12.505	1.41955	1.58181					
15.0644	15.0155	35.2853	12.165	1.59302	1.80608	0.2131	0.118	0.614	1.63	0.193
15.1631	15.0999	35.5072	11.689	1.77842	2.05876					
15.2310	15.1557	35.6533	11.3418	1187125	2.19331	0.3220	0.147	0.514	1.95	0.243
15.3055	15.2143	35.8082	10.9513	1.94107	2.30023					
15.5574	15.3938	36.2853	9.6878	1.97802	2.37465	0.3966	0.167	0.400	2.50	0.300
15.6893	15.4769	36.5072	9.1320	1.92512	2.29567					
16.3317	15.8043	37.2853	7.8146	1.62779	1.81039	0.1826	0.1006	0.388	2.58	0.306
16.5535	15.9002	37.5072	7.7026	1.55782	1.68273					
17.3317	16.2135	38.2853	7.9106	1.47943	1.55027	0.0709	0.0456	0.452	2.22	0.274
18.3317	16.5953	39.2853	8.1079	1.53742	1.63872					

TABLE 18. Composite models with V_β or V_γ in low density regions. (The symbols are those introduced in Tables 8 and 9.)

$\log \mathcal{E}^c$(cgs)	$\log \rho_m^c$(cgs)	$\log P^c$(cgs)	R(km)	$M/M_\odot$	$M_p/M_\odot$
6.28406	6.28403	22.8082	$9.101\text{x}10^3$	0.42483	0.42599
6.95173	6.95167	23.8082	$6.782\text{x}10^3$	0.66838	0.67001
7.65431	7.65416	24.8082	$4.842\text{x}10^3$	0.90802	0.90988
8.16160	8.16135	25.5072	$3.721\text{x}10^3$	1.03641	1.03827
8.38262	8.38251	25.8082	$3.299\text{x}10^3$	1.07884	1.08067
8.91258	8.91209	26.5072	$2.465\text{x}10^3$	1.14480	1.14480
9.15375	9.15318	26.8082	$2.185\text{x}10^3$	1.13933	1.14079
9.71546	9.71464	27.5072	$1.654\text{x}10^3$	1.05234	1.05321
9.95789	9.95692	27.8082	$1.449\text{x}10^3$	0.99789	0.99857
10.5214	10.5201	28.5072	$1.062\text{x}10^3$	0.86027	0.86067
10.7643	10.7627	28.8082	$9.234\text{x}10^3$	0.80126	0.80158
11.7366	11.7319	29.8082	$5.798\text{x}10^2$	0.62750	0.62765
12.3062	12.3021	30.2853	$6.748\text{x}10^2$	0.59651	0.59581*
12.48	12.47	30.51	$7.069\text{x}10^2$	0.5849	0.5840*
13.0070	13.0022	31.2853	$1.300\text{x}10^3$	0.56300	0.56176*
13.153	13.1474	31.5072	$1.457\text{x}10^3$	0.56893	0.56771*

$\rho^c \gtrsim 10^{15.2}$ gm/cm^3, the composite models have larger masses than pure neutron models; (3) for still higher densities $\log \rho^c \gtrsim 15.8$, the gravitational masses of pure neutrons and composite models almost converge to a common value, while the proper mass of the composite models remains larger than that of pure neutron stars up to the singular point ($\rho^c \rightarrow \infty$). The smaller mass of the composite models in lower density regions is easily explained. In the region $10^{14} < \rho^c < 10^{14.8}$ gm/cm^3, the composite models consist of neutrons, protons and electrons. At slightly higher densities they contain μ^- mesons as well, and for $\rho^c \gtrsim 10^{15}$ gm/cm^3 the appearance of hyperons and excited nucleons lowers the neutron number density appreciably as is seen in Figure 21. As a consequence, the top of the Fermi sea of neutrons is lowered and the partial pressure of the neutrons is depressed. Up to about $\log \rho^c \sim 15.3$ the partial pressures of other baryons are not sufficient to compensate for this decrease of neutron pressure, and the over-all effect is to decrease the total pressure below the value it would have in the absence of other baryons. Lower pressure results in smaller total mass of a star with the same central density, as can be seen in Figure 35. To explain the larger masses of composite models as compared with pure neutron models in higher density regions, it may be pointed out that in general the balance between gravity and degeneracy pressure is acquired at higher matter density when the particles responsible for the degenerate pressure are heavier. For instance, we have seen that the electron degeneracy fails to support the gravitational force for $\rho^c \gtrsim 10^8$ gm/cm^3, while neutron degeneracy pressure is able to balance the gravitational force in the much higher density regions where $10^{16} \gtrsim \rho^c \gtrsim 10^{14}$ gm/cm^3. We have also noted that the second crushing point (Oppenheimer-Volkoff mass limit) is the result of the failure of neutrons to supply sufficient degeneracy pressure to counterbalance the increasing gravity due to increasing density. When some subatomic particles heavier than neutrons supply degeneracy pressure, this crushing is expected to occur at a higher density than in the case of pure neutrons as can be predicted from the same analogy used between electron degeneracy and neutron degeneracy. As a consequence the stable regions of composite models (with heavier baryons than neutrons) are enlarged to include higher density regions and the crushing point occurs at a higher central density and, hence, at a larger mass. Due to the relatively small difference between the masses of ground state nucleons and the heavier baryons, this effect is not so significant as in the case of the difference between the neutron and electron configurations, but it is appreciable enough to increase the maximum mass point from about $1.93\odot$ to $1.98\odot$ for the gravitational mass, and from about $2.28\odot$ to $2.37\odot$ in the case of the proper mass when degenerate hyperons become effective enough as pressure supporters. We have been discussing only v_γ type models above, but hyperons produce exactly the same kind of behavior in the models of type v_β, also, from which it is concluded that the preceding indicates a general effect of hyperons on neutron stars. Saakyan's models also give larger maximum mass for hyperon stars than for pure neutron stars. When all particles become relativistic (the kinetic energy much larger than the rest mass), the mass difference between particles becomes insignificant because Fermi energy and pressure then depend on number density but are independent of mass. This condition, however, is not reached until the total matter density reaches about 10^{17} gm/cm^3 ($E_F = mc^2$ for a neutron gas at $\log \rho^c \sim 16.5$), far beyond the crushing points of either pure neutron stars or hyperon stars. Before this point is reached, the equation of state switches over to the simpler form $P = \mathcal{E}$. That there should be a large divergence between the dashed curve and the solid curve in Figure 35 for densities below 10^{14} gm/cm^3 is obvious from the fact that in the composite models the electron partial pressure is becoming dominant, and with the rapid decrease of neutron numbers with a fall of density the total pressure of the composite models is much larger than that of pure neutron stars due to the presence of electron degeneracy. In effect, qualitatively, we see that the difference between the solid curve and the dashed curve in the region $\rho^c \lesssim 10^{14}$ gm/cm^3 in Figure 35 gives a rough measure of the proportion between the neutron core and the electron-ion envelope. For $\rho^c < 10^{11}$ gm/cm^3, the neutron core completely disappears and we tend toward white dwarfs as the density is further lowered.

A complete set of composite models is exhibited in Figure 37. I think it to be extremely interesting to compare this result with that of Wheeler in Figure 26 and of Salpeter in reference 12. The general agreement between the present models and those of Wheeler and Salpeter is satisfactory in the white dwarf regions. Wheeler's models give a maximum mass of about 1.2 $\odot$ in the white dwarf regions. That of Salpeter ranges from about 1 to 1.4 $\odot$, depending on different choices of composition. The maximum white dwarf mass of our models is about 1.2$\odot$, about the same as Wheeler's, but it occurs at a somewhat higher central density ($\sim 10^9$ gm/cm^3) than Wheeler's ($\sim 10^{8.5}$ gm/cm^3). Our models come in about the middle of the various models of Salpeter. On comparing the equations of state used by Salpeter, Wheeler and by the present writer, it is obvious that in the white dwarf regions, those of the

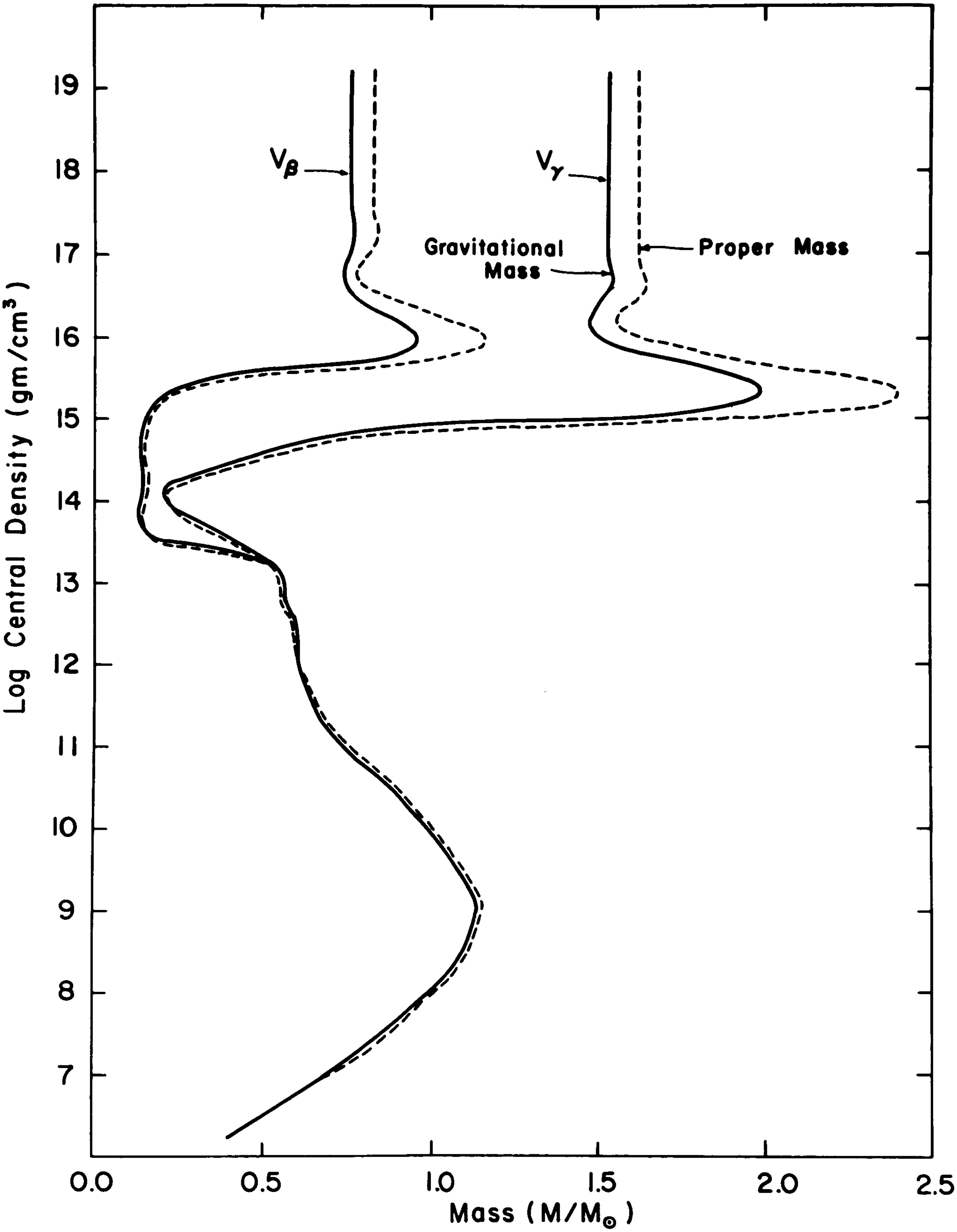
Log Central Density (gm/cm^3)
19
18
17
16
15
14
13
12
11
10
9
8
7
V_β
V_γ
Gravitational Mass
Proper Mass
0.0
0.5
1.0
1.5
2.0
2.5
Mass (M/M$_\odot$)

Figure 37

first two are by far the more complicated and precise. In my models, the more thorough and elaborate treatment of the variation of composition has been applied but all the various correction terms which Salpeter took into account in the non-interacting Fermi gas of electrons are not included. Wheeler neglected such correction terms in the Chandrasekhar white dwarf regions, but his equation of state in the lowest density limit (around atomic regions and solid state regions) is much more elaborate. The conclusion is that for some of the lightest white dwarfs (with the central density $\lesssim 10^4$ gm/cm^3) for which low density effects and the corrections of Salpeter and Wheeler become appreciable, their models are more accurate. However, the main topic of the present research is "neutron stars" not "white dwarfs," and it is not my purpose here to investigate the detailed structure of low density white dwarfs. Therefore, models with central density lower than 10^6 gm/cm^3 are not included in my results. The main purpose for carrying out the calculations down to lower density regions has been to show that the white dwarf regions and neutron star regions are joined smoothly by one curve, which shows two major crushing points (one, Chandrasekhar's and another, Oppenheimer-Volkoff's), without any special assumptions. An effort along the same line was made by Wheeler, but the major difference between Wheeler's models and mine is that I have treated the neutron star regions and the subsequent regions of superdense stars much more thoroughly. Wheeler's results for $\rho \gtrsim 10^{13}$ gm/cm^3 are quite uncertain due to oversimplifications in his equation of state in the heigher density region. Salpeter's main contribution is also to the study of white dwarfs. Salpeter's neutron star models are based on: (1) Newtonian mechanics and (2) the non-relativistic Skyrme equation of state, which causes some uncertainty in his results. But one important result of Salpeter's work is that it pointed out the possibility of a non-negligible contribution of envelopes, which is confirmed in the present research.

In Figure 37, solid curves represent gravitational masses of models of type v_β and v_γ, and the dashed curves their proper masses. In superdense regions the crossing of a solid by a dashed curve does not occur, but an interesting result is that such crossing does occur in the lower density region around $10^{12} < \rho^c < 10^{14}$ gm/cm^3. This is explained as being an effect of the relativistic electrons as will be discussed further in Section IV-4. It may be noted that the proper mass does become less than the gravitational mass in the high density limit for v_β type pure neutron gases (Figure 34), but Figure 37 indicates that this is not the case with composite models of the same type. It is interesting to note that the presence of hyperons prevents the binding energy from becoming negative. In this graph, the last small mass maximums near 10^{17} gm/cm^3 are seen more clearly than in the earlier ones. This hump has been called "the second hump" in previous discussions, but the whole picture exhibited in Figure 37 may suggest that, strictly speaking, this is the 3rd maximum. The first maximum is the Chandrasekhar maximum mass near $\rho^c \sim 10^9$ gm/cm^3, the second maximum is another major one, the Oppenheimer-Volkoff maximum mass, and the 3rd one is a small hump near 10^{17} gm/cm^3 at the neck of the vertical asymptotic lines.

To better compare my composite models with those of Salpeter and Wheeler, central density has been plotted against radius in Figure 38 for each model. Up to log $\rho^c \sim 11.5$ the agreement between these three kinds of models is quite good. This indicates that the absence of various correction terms in the electron equation of

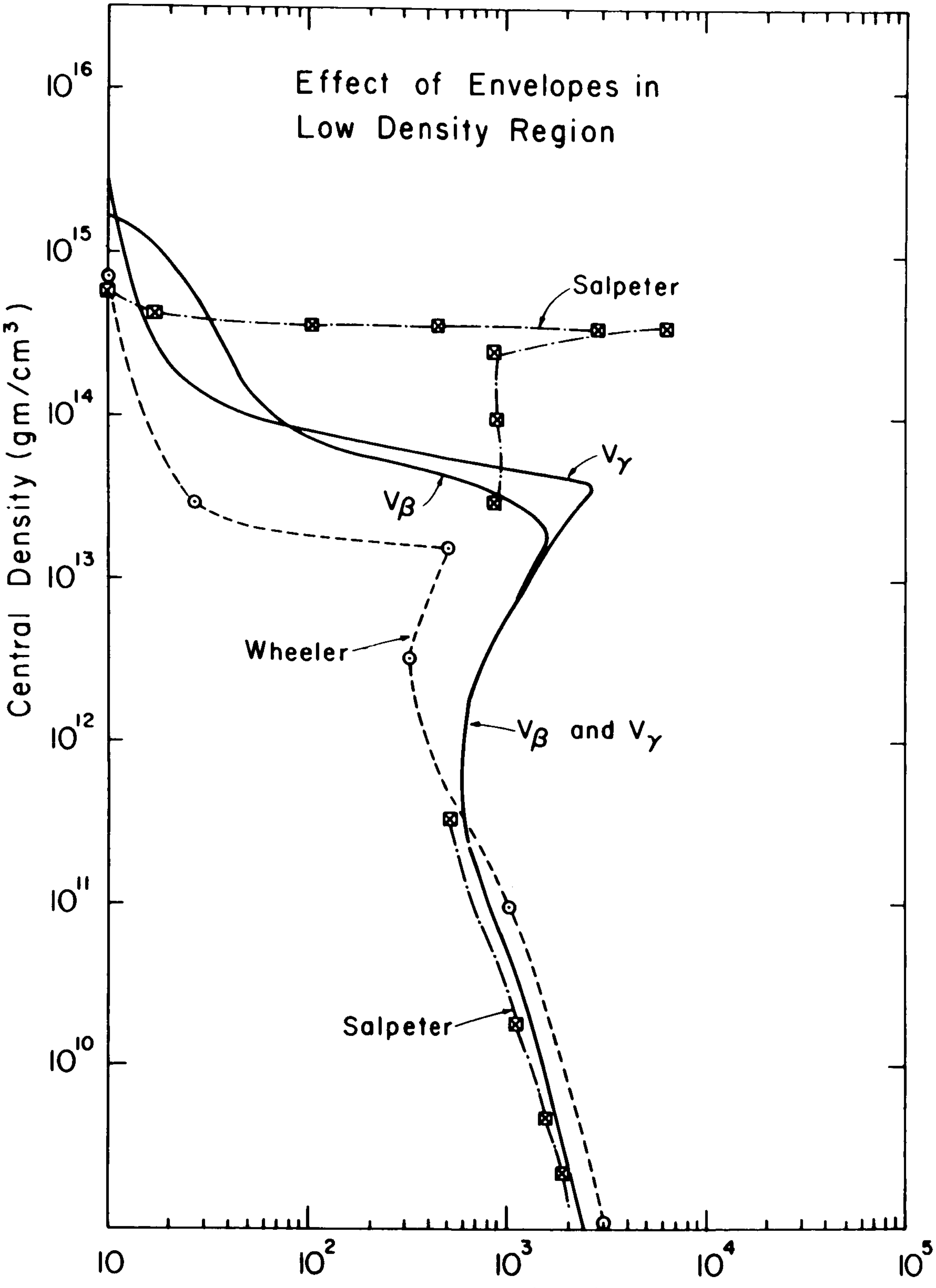
Effect of Envelopes in Low Density Region
Central Density (gm/cm³)
10^{16}
10^{15}
10^{14}
10^{13}
10^{12}
10^{11}
10^{10}
Radius (km)
10
10^2
10^3
10^4
10^5
Salpeter
V_γ
V_β
Wheeler
V_β and V_γ
Salpeter

Figure 38

state is perfectly justified for my purpose (for $\rho^c \gtrsim 10^9$ gm/cm^3). In neutron star regions, Salpeter's second peak is much sharper than the rest, but all four kinds of model (type v_β, type v_γ, and Salpeter's and Wheeler's shown in Figure 38) show the effect of the envelopes. At this critical density, the envelopes of Salpeter's models extend even to the size of some of the largest white dwarfs; those of ours to ordinary white dwarf size. The size of the envelopes in Wheeler's models appear to be much smaller. Most of the models with large extended envelopes lie in unstable regions (IV-4b) and may not be of physical importance, but our final results (particularly Figure 41 to be shown in Section IV-3f) indicate that this statement is not necessarily true.

To better see the dependence of the radius on the central density in neutron star regions, the same relation is plotted on an enlarged scale in Figure 31 for composite models of V_β and V_γ, as well as for the models of an ideal gas obtained in Section IV-3b. The radii of the V_β and V_γ models for $\rho^c < 10^{15}$ gm/cm^3 are much larger than those of ideal gases. This is because in the latter, only neutrons are included, while in models of the V_β and V_γ type considered here, the composite equation of state for electron gases was used. We expect quite an extended envelope in models with central densities in this region. This graph indicates that the effect of nuclear forces and hyperons on the stellar radii is not as significant as on the mass.

The mass-radius relation is shown in Figure 39. Here the portion marked (I) belongs to the white dwarf regions. Around the region marked (II) lie a series of models with extended envelopes. The model with the most extended envelope is

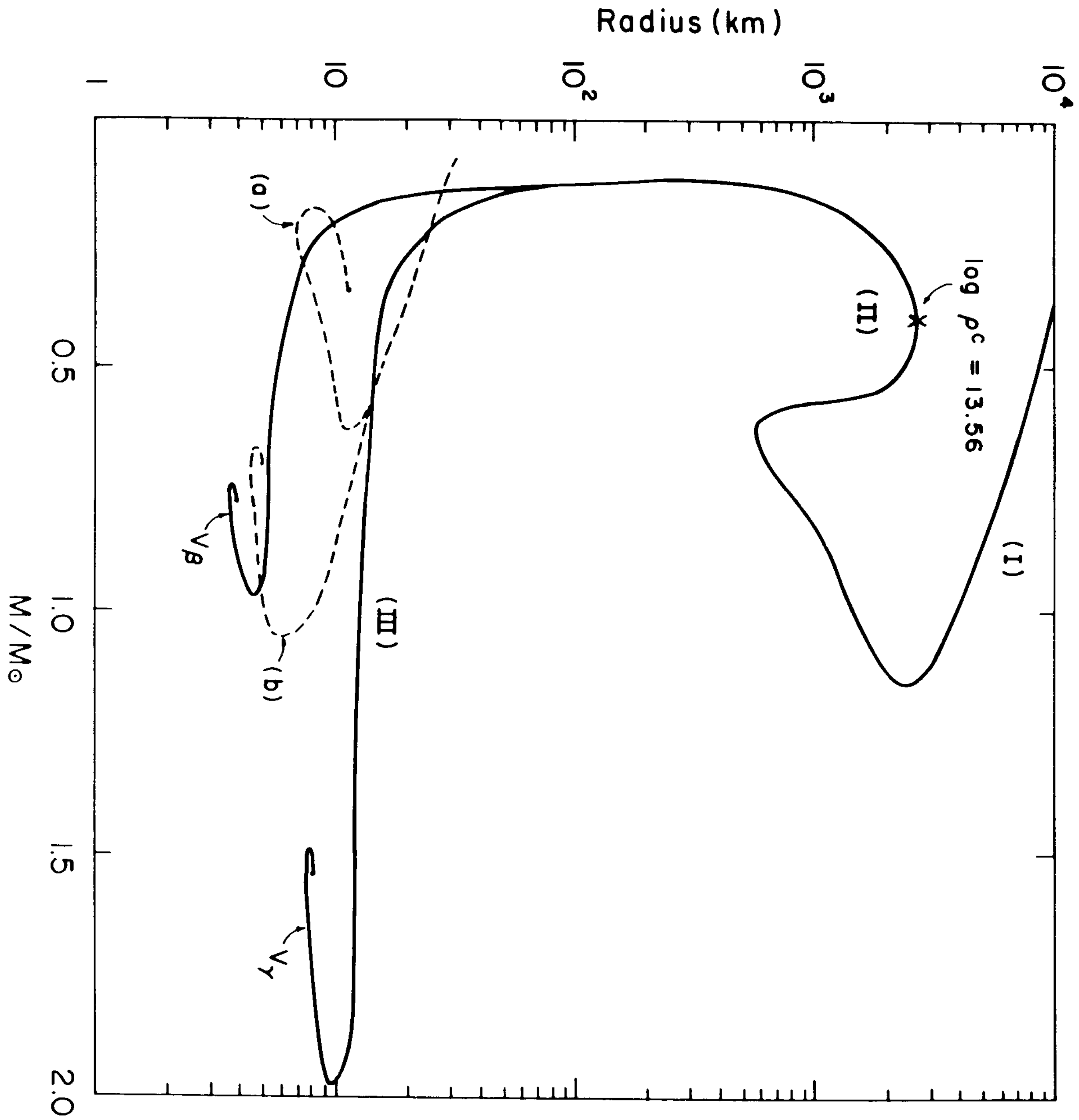
Radius (km)
1
10
10^2
10^3
10^4
log ρ^c = 13.56
(I)
(II)
(III)
(a)
(b)
V_β
V_γ
0.5
1.0
1.5
2.0
M/M⊙

Figure 39

shown by the cross marked with its central density value log $\rho^c = 13.56$. Figure 27 shows Wheeler's results. On comparing these two graphs, we see that the envelopes of Wheeler's models are much smaller. In the lower portion marked (III) lie a series of neutron and hyperon stars. The dotted curves represent Ambartsumyan and Saakyan's models; the branch marked (a) indicates their ideal gas models and that marked (b) their "real" gas models. The branch (a) of the dotted curves and the graphs shown in Figure 27 all refer to ideal gases and are similar to one another. With an increase in central density, we come down from the region (I) to (II) and finally to (III). Due to different assumptions of interaction forces, in region (III) the curves branch off to different individual types of models, first reaching a minimum radius, then increasing slightly, and finally, each branch approaches a point with constant mass and radius as the central density goes to infinity. The center of the curl of each kind of model, therefore, gives the radius and mass of the extreme model which has the central singularity. We notice from this graph that Ambartsumyan and Saakyan's real gas models resemble the V_β type models more than the V_γ type. Larger mass values are associated with V_γ and $V_{\beta\gamma}$ than with V_β and Saakyan's models.

It was pointed out in the last chapter that the absolute limit of the equation of state is $P = \mathcal{E}$. However, there is not yet rigorous physical proof that the state $P > \mathcal{E}/3$ is actually realized. Therefore, it appears worthwhile to calculate models with the more restricted limit $P < \mathcal{E}/3$ as the asymptotic equation instead of $P < \mathcal{E}$. The results are shown in Figure 40, together with the previous models which have $P = \mathcal{E}$ as the asymptotic equation. Again the solid curves represent gravitational masses and dashed curves the proper masses. The crosses represent the points where

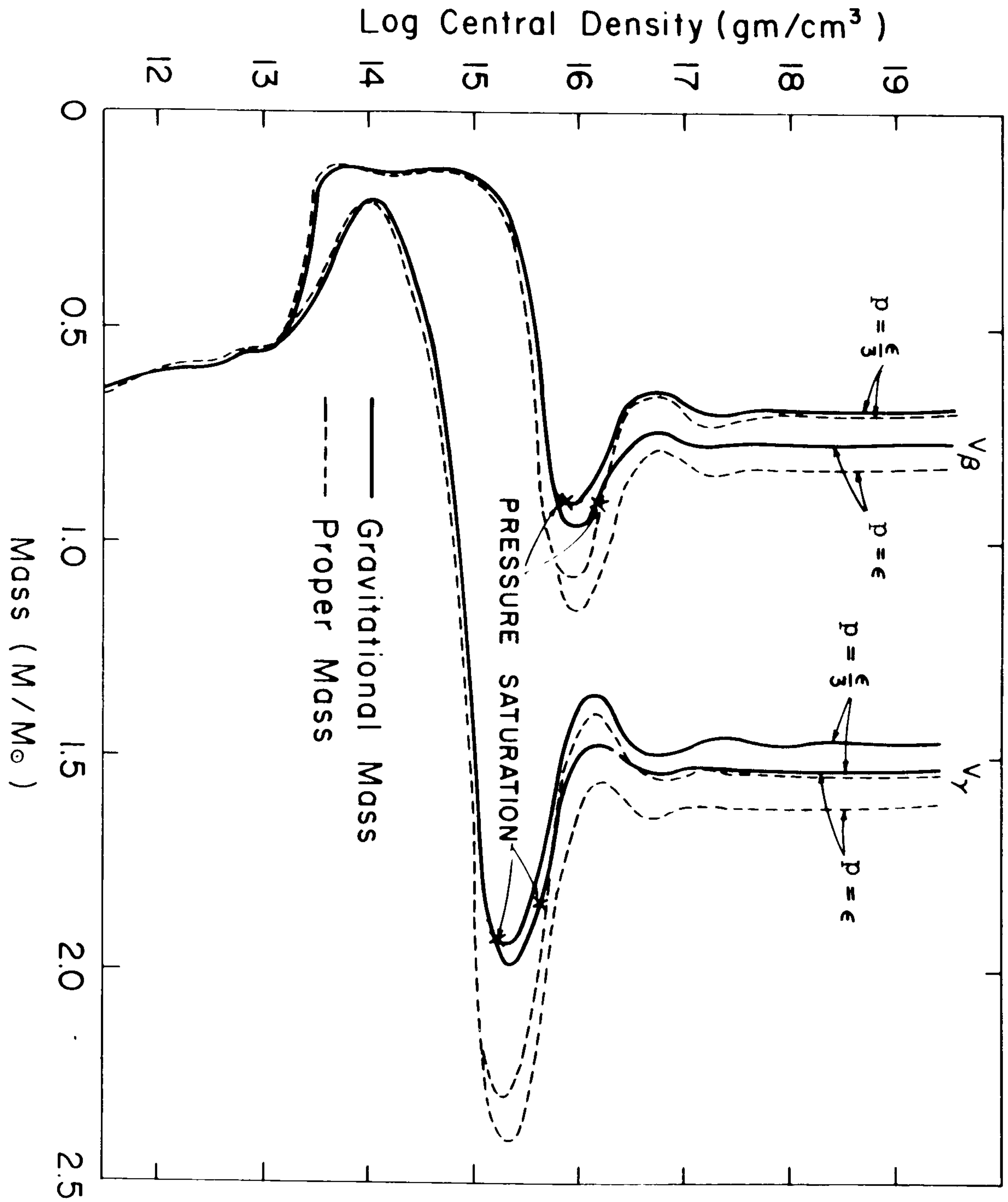
Log Central Density (gm/cm³)
12
13
14
15
16
17
18
19
0
0.5
1.0
1.5
2.0
2.5
Mass (M/M☉)
Gravitational Mass
Proper Mass
PRESSURE SATURATION
p = ε/3
p = ε
p = ε/3
p = ε
V_β
V_γ

Figure 40

pressure saturation takes place, namely, where the pressure becomes equal to $\mathcal{E}$ or $\mathcal{E}/3$. The pressure saturation occurs at lower central densities for $P \leq \mathcal{E}/3$ than for $P \leq \mathcal{E}$. The requirement $P \leq \mathcal{E}/3$ results in slightly smaller maximum masses and in smaller masses at the singular point. But otherwise the effect is small. In particular, most of the models lying in the stable branch (almost horizontal portion of the curve below the Oppenheimer-Volkoff crushing point) are unaffected by the change of the asymptotic equation of state from $P = \mathcal{E}$ to $P = \mathcal{E}/3$.

The internal structure of a model depends on which type of model we have in mind. For V_β type models the following applies: The lightest stable neutron stars have small hyperon cores at their center, an intermediate layer of neutrons (with a small amount of protons and leptons), and rather extended outer envelopes of heavy nuclei and electrons; medium weight stable models have hyperon cores occupying about 1/6 total stellar size with large envelopes of neutrons while the outermost electron-ion envelope is negligible; the heaviest stable models have most of their mass in the concentrated hyperon core whose size increases rapidly with increasing central density. Models with $\rho_m{}^c \gtrsim 10^{16}$ gm/cm^3 are mainly composed of hyperons, with thin neutron envelopes. Due to the lower central densities encountered, the V_γ type models in stable regions have smaller hyperon cores and larger neutron envelopes. The lightest stable neutron star models of the V_γ type possess no central hyperon cores but have larger electron-nuclear envelopes than those of type V_β.

The major differences between the composite models and the pure neutron star models may be summarized as (1) the composite models have larger masses and larger radii in low density regions ($\rho^c < 10^{14}$ gm/cm^3) due to the electron-ion envelopes,

(2) the composite models (V_β , V_γ and $V_{\beta\gamma}$ models) do not possess negative binding energies in high density limit due to the presence of hyperons, (3) the composite models have slightly smaller masses in most of the stable regions due to the presence of other baryons, (4) somewhat larger masses exist for the composite models in higher density regions due to the effect mentioned in (3). The consequent difference in physical properties can be seen in Tables 16-18 as compared with the listings of Tables 12-15. In Tables 16-18 the proper masses which are less than the corresponding gravitational masses in the low density region where $10^{12} < \rho^c < 10^{14}$ gm/cm^3 are marked with asterisks.

f. Final Models of Stable Neutron Stars

Noting that the models constructed in the preceding section are the most realistic at present, three from the V_β and another three from the V_γ type were selected as models to which envelopes were fitted/one near the maximum point, another from the region of minimum mass (among stable models) and the third from the intermediate region. We have noted that the difference between baryon stars and pure neutron stars of the same type (V_β or V_γ, etc.), is relatively small, and that the Skyrme models, the Levinger-Simmons models of type $V_{\beta\gamma}$, and the Ambartusmyan-Saakyan models of real gases all lie between the V_β and V_γ type models. Therefore, on selecting one model at the upper, one intermediate and one at the lower extreme from each of the two types V_β and V_γ, we may safely assume that these six models represent fairly extreme possibilities for neutron stars not only of the restricted kind of Levinger-Simmons, but also, more generally, other possible models using different kinds of potentials. To obtain better values of the model parameters, M, R, etc., the integrations were carried out again for these six models using closer intervals in the interpolation table used as the equation of state (that is, the intervals of t_n and $\log \rho$ were reduced from 0.02 to 0.01).

The characteristic properties of the six models are summarized in Tables 19, 20, 21 and Figure 41. For convenience, in the following discussion the various models are represented by symbols. In the scheme adopted, (1 $M_\odot$, V_β) would, for example, refer to a model of about 1 solar mass (the maximum mass) of the type V_β. Models are also designated by V_β I, V_β II, etc., V_β indicating the type of model and the symbol I indicating stable models with the maximum mass, II with the intermediate mass, and III with the minimum mass of that group. The same notation as was introduced earlier is used in Table 19. The so far undefined symbols, such as C_V/T (specific heat per unit temperature), etc., will be explained later when such quantities become necessary. In the last four rows, M_c represents the mass of the neutron core and R_c the radius of the same core (in the table, they are expressed as the fraction of total mass and radius respectively); and g_0 (R) and g(R) represent the following quantities:

$$g_0(R) = GM/R^2$$

$$g(R) = g_0(R)\left(\frac{P}{\rho c} + 1\right)\left(1 + \frac{4\pi P R^3}{M c^2}\right)\left(1 - \frac{2GM}{R c^2}\right)^{-1} \qquad (4\text{-}12)$$

$g_0(R)$ is the Newtonian gravitational acceleration and g(R) is the general relativistic analogue on the surface of a neutron star. log g on the surface of the sun is around 4, that of a typical white dwarf is around 8, and we notice in Table 19 that log g ranges from about 12 to 15 on the surface of neutron stars. This also indicates

TABLE 19. Detailed parameters for neutron star models.

TYPES	V_β I	V_β II	V_β III	V_γ I	V_γ II	V_γ III
	$(1M_\odot, V_\beta)$	$(0.6M_\odot V_\beta)$	$(0.2M_\odot, V_\beta)$	$(2M_\odot, V_\gamma)$	$(1.1M_\odot, V_\gamma)$	$(0.2M_\odot, V_\gamma)$
$M/M_\odot$	0.9386	0.5992	0.1926	1.9765	1.1055	0.2150
R(km)	4.833	5.658	10.091	9.686	13.032	24.154
$\log \rho_m^c$ (gm/cm^3)	15.9018	15.6379	15.2388	15.3944	14.8380	14.2143
$\varphi = GM/RC^2$	0.285	0.156	0.0282	0.301	0.125	0.0131
$\log(\frac{C}{T}v)$ (cgs)	29.6811	29.6169	29.4078	30.1426	30.1594	29.9572
$M_p/M_\odot$	1.1307	0.6593	0.1949	2.3722	1.1975	0.21686
$M_B/M_\odot$	0.1921	0.06012	0.00227	0.3957	0.09198	0.00189
α	0.170	0.0915	0.0117	0.167	0.0767	0.0087
$\log \mathcal{E}^c$ (cgs)	16.0233	15.6823	15.2660	15.5583	14.8654	14.2226
$\log p^c$ (cgs)	36.6533	35.8082	34.6533	36.2853	34.8082	33.2853
$\log(\frac{C_v}{T})^*$	30.0127	29.6995	29.2698	—	—	—
$\Delta(\frac{C_v}{T})$	~ +50%	~ +20%	~ -30%	(~ +20%)	(~ -20%)	(~ -50%)
$g_{44}(R)$	0.430	0.688	0.944	0.398	0.750	0.974
$-g_{rr}(R)$	2.32	1.45	1.06	2.52	1.33	1.03
M_c/M	~ 1	~ 1	0.996	~ 1	~ 1	0.994
R_c/R	~ 1	~ 1	0.755	~ 1	~ 1	0.607
$g_o(R)$(cgs)	5.31×10^{14}	2.48×10^{14}	2.52×10^{13}	2.79×10^{14}	8.64×10^{13}	4.88×10^{12}
$g(R)$(cgs)	1.23×10^{15}	3.60×10^{14}	2.67×10^{13}	7.05×10^{14}	1.15×10^{14}	5.04×10^{12}

TABLE 20. The radial distribution of mass and the ratio of mass to radius for the model V_γI.

Model V_γI $(2 M_\odot, V_\gamma)$					
r (km)	$u(r)/M_\odot$	$M_p(r)/M_\odot$	u(r)/M	u(r)/r	2u(r)/r
1.061	0.9199×10^{-2}	0.5897×10^{-2}	0.00465	1.28×10^{-2}	2.56×10^{-2}
2.020	0.6076×10^{-1}	0.4115×10^{-1}	0.0338	0.0442	0.0884
3.010	0.1859	0.1460	0.0941	0.0911	0.1822
4.006	0.3974	0.3315	0.201	0.146	0.292
5.011	0.6890	0.6211	0.348	0.202	0.404
6.009	1.029	1.009	0.520	0.252	0.504
7.008	1.381	1.470	0.700	0.292	0.584
8.002	1.698	1.938	0.859	0.313	0.626
9.001	1.921	2.229	0.974	0.313	0.626
9.686	1.977	2.372	1.000	0.301	0.602

TABLE 21. Radial distribution of mass for models V_βIII and V_γ III.

Model V_β III $(0.2 M_\odot, V_\beta)$			Model V_γ III $(0.2 M_\odot, V_\gamma)$		
r(km)	$u(r)/M_\odot$	u(r)/M	r	$u(r)/M_\odot$	u(r)/M
2.07	0.0298	0.154	4.04	0.0208	0.0965
3.00	0.0733	0.380	6.01	0.0601	0.280
4.00	0.1292	0.670	8.01	0.1157	0.537
6.00	0.1846	0.959	10.00	0.1686	0.785
* 7.60	0.1919	0.996	12.01	0.2017	0.936
9.00	0.1921	0.999	* 13.74	0.2129	0.990
10.091	0.1926	1.000	24.15	0.2150	1.000

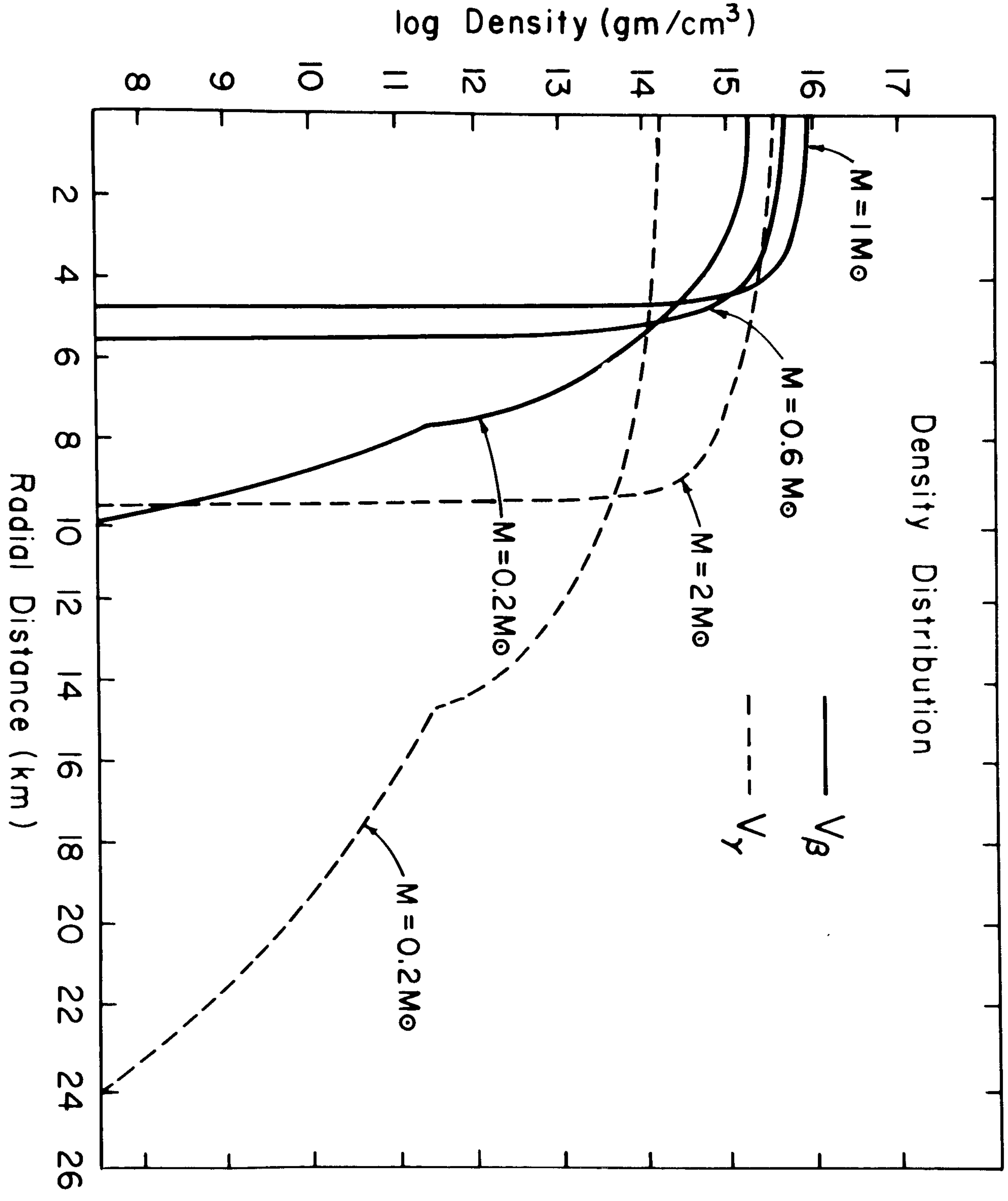
Density Distribution
Vβ
Vγ
M = 1 M⊙
M = 0.6 M⊙
M = 2 M⊙
M = 0.2 M⊙
M = 0.2 M⊙
log Density (gm/cm³)
8
9
10
11
12
13
14
15
16
17
Radial Distance (km)
2
4
6
8
10
12
14
16
18
20
22
24
26

Figure 41

that the general relativistic corrections are significant even on the surface if the neutron star is massive enough (the last two rows in Table 19). $g(R)$ is more than twice as large as $g_o\,(R)$ for models V_β I and V_γ I, though the $|g - g_o|$ is less than 1.0% of the Newtonian value g_o for the lightest stable models, V_β III and V_γ III. This information is quite useful when we come to the discussion of the atmospheres of neutron stars. The curvature of space and the red shifts are relatively small for our lightest models but are quite large for the heaviest ones. All these results point out the importance of general relativity in the problem of neutron stars. We note that larger values of mass and radius are associated with v_γ type models than V_β type models, and lower central densities prevail in the former than in the latter.

To examine the internal structure of these stars in more detail, the radial distribution of density inside the star is shown in Figure 41. Models of type V_γ are represented by dashed curves and those of type V_β by solid curves. Different models in the same group are specified by their masses. An interesting thing is that the effect of the electron-ion envelope is negligible for the heaviest and medium weight models of both groups, but it is significant for the lightest models, especially for the model ($0.2M_\odot$, V_γ) due to the small central density associated with this model. All these models have been selected from the stable regions. That the proper mass is larger than the gravitational mass (so that the stellar configuration is stable against dispersion to infinity) has been checked. The general assumption that the electron-nuclear envelopes are negligible for stable neutron stars has been found to be invalid. This is shown in what follows. The radius of the neutron core is about 75% and 60% of the total stellar radius for models V_β III and V_γ III, respectively (the third row from the bottom in Table 19). Also, the results of the last two sections indicate that the radii of the stable models of minimum mass of the types V_β and V_γ are about 8.5 km and 14 km, respectively, when the outer electron-ion envelopes are neglected, as compared with 10 km and 24 km when these envelopes are included. By neglecting the envelopes, therefore, we will introduce the error as large as 15% to 40% in the value of the radius of some of the lightest neutron stars.

To see the effect of the envelope on stellar masses, the internal distribution of masses is shown for the two lightest models V_β III and V_γ III in Table 21 and for the heaviest model V_γ I in Table 20. The boundary between the envelope layers and the neutron core is marked by an asterisk for models V_β III and V_γ III for which such envelopes are appreciable. 99.6% of the mass is contained in the core of model V_β III, while about 99.4% is in that of model V_γ III. That is, in spite of the large extended envelope, the mass contained in the envelope is only about 0.5%. The effect of the envelope on mass is negligible even for the lightest stable neutron stars.

As we shall see in the next chapter, one of the decisive factors in determining the surface condition of a star is the gravitational acceleration g on the surface which is proportional to the ratio M/R. That is, by neglecting the heavy-nuclei envelopes we are introducing errors from about 25 to 60% in our surface parameters, especially on the values of red-shift. As a consequence, for instance, if the results of the last section (for a pure neutron configuration) were used, quite a different result for the possible behavior of cooling times, etc., of light neutron stars would be expected.

We have noted that the radial component of the metric becomes infinite, and that we face the Schwarzschild singularity if the factor $2u(r)/r$ becomes equal to or greater than 1. To check that our final models do not lead to this difficulty, the factor $2u(r)/r$ is calculated at different radial distances r from the center. Such values for the heaviest stable model $V_{\gamma}I$ are listed in the last column of Table 20. The maximum of about 0.63 is seen to occur at about 10% of the radial distance inward from the surface. For all of the other five lighter models, the values are less. Our last six stable models therefore do not exhibit the Schwarzschild singularity.

It may be noted that the proper mass is smaller than the gravitational mass from the center up to a certain distance from the center. In this region the total binding energy becomes negative but the larger positive binding energy in the outer half of layers is thought to keep the body stable as a whole.

IV-4 DISCUSSION

In this section, some of the key points of the results will be summarized and explored further.

a. Chandrasekhar Mass Limit

We have noted that in the simple white dwarf models of Chandrasekhar, the solution of the equations of hydrostatic equilibrium gives a finite mass (called "Chandrasekhar's maximum mass") as the central density goes to infinity, and that there is no solution for more massive degenerate stars. This is easily explained by some simple reasoning (as given in Appendix 3). That is, inside a white dwarf star, the gravity is supported by the pressure supplied by non-relativistic degenerate electrons. This pressure depends on the mass and radius through the density (A3-3), while the gravitational force also depends on mass and radius (A3-2). The dependence of those quantities on M and R is such that when the gravitational force and the pressure force are equated to each other to fullfil the hydrostatic equilibrium condition, a relation is gotten between the total mass and radius of a star under hydrostatic equilibrium (A3-7). That is, a star of a given mass can take on only a fixed value of R as determined by this relation. This argument no longer applies when the density becomes so high that the electrons become relativistic. In this case the pressure dependence on density (and hence on M and R) is such that when the condition of hydrostatic equilibrium is applied, the radius term is eliminated (Eq. (A3-8)) and there exists no fixed radius for a given mass. The Chandrasekhar mass limit occurs when the degenerate electrons become relativistic. Therefore, a degenerate star more massive than this limit has no way of adjusting itself to become a stable star unless some catastrophic events such as nova and supernova explosions can eject its excess mass into space so that it can finally end up as a stable white dwarf with a mass smaller than the Chandrasekhar limit, or else that the increase in the internal temperature due to contraction can succeed in causing enough of the star to become non-degenerate.

It has been shown that instead of developing a singularity at Chandrasekhar's critical mass, the solution of the hydrostatic equations with a more realistic equation of state gives a turning point at a finite mass, radius and central density of about 1.2 $M_\odot$, 2×10^3 km and 10^9 gm/cm^3, respectively (due to the inverse beta processes), and that the solutions with higher central densities lie along the curves shown in Figure 37 above the first turning point.

b. Problem of Stability

The problem of stability has been discussed frequently in the last sections. We shall now look into this point in more detail. A star, as a stable mechanical system, must first of all satisfy the hydrostatic equilibrium condition. Therefore, if the hydrostatic equations (1-1) and (1-2) or (1-8) and (1-9) fail to give solutions, it means such configurations do not exist as stable bodies. An example is a degenerate star exceeding the maximum mass of the Chandrasekhar or Oppenheimer-Volkoff type. Consider a star lying on the lower portion of the curve in Figure 37 before the first turning point. Such a star corresponds to a body in which gravity is supported by the degeneracy pressure of non-relativistic electrons under the condition $R = \text{const } M^{-1/3}$, (A3-7). If because of some perturbation a star of a given mass M happens to have a larger R than that given by (A3-7) it will contract to the right size, while if it happens to be too small in size it will expand until the condition (A3-7) is fullfilled. In this way the star can adjust itself to the stability point against external disturbances. If this condition is satisfied, the star is said to be dynamically stable as well as being in a condition of hydrostatic stability. A real, stable star must satisfy both conditions of stability, namely, the hydrostatic and the dynamic ones.

The stars lying along the branch between the first turning point (Chandrasekhar's crushing point at around $\rho^c \sim 10^9$ gm/cm^3) and the next turning point (near

$\rho^c \sim 10^{14}$ gm/cm^3), and which belong to the intermediate region between the white dwarf and neutron star models, are unstable in the following sense: They do satisfy the hydrostatic stability condition(being solutions of hydrostatic equations), but they are not stable against dynamical disturbances. Let us suppose that such a star exists. Should a slight disturbance be given to it, it would contract a little. In this region, the higher density resulting from contraction does not raise the pressure sufficiently (because some electrons to which pressure is due will be lost because of the increased rate of electron capture at the higher density). The gravity, however, increases with the increase in density. The pressure thus fails to support the increasing gravity with an increasing density and the contraction continues, becoming more and more rapid once it is initiated by the slightest disturbance until the star becomes so condensed that it reaches the stable branch for neutron stars. In the same way, if the slightest disturbance produce a small expansion, the pressure does not decrease sufficiently to not over-balance the gravity which, of course, also decreases because of the expansion. This is because, with a decrease in density, and hence a decrease in electron Fermi energy, more free electrons will be liberated. Once begun, therefore, the expansion continues at a higher and higher rate so that it soon reaches the stable branch of white dwarfs.

A similar argument may be applied to the upper and lower branches in the neutron star regions ($10^{14} < \rho^c < 10^{17}$ gm/cm) in Figure 37. In this case, however, it is not electrons, but neutrons and other baryons which may be crushed out of existence. A more rigorous approach to the dynamical stability of stars in the category of general relativity has been recently given by Chandrasekhar(65) and it has been applied to the problem of high density behavior and dynamical stability of neutron stars by Misner and Zapolsky.(24,61) The result is the same as that estimated by Oppenheimer and Volkoff, namely, that between the two branches around the Oppenheimer-Volkoff crushing point, the stars lying along the lower branch (in Figure 30) are completely stable while those lying along the upper branch are dynamically unstable. Even if a star along the upper branch is created by some magic, the slightest perturbation will cause a transition to the lower branch (expansion), or if it starts to contract, it will contract indefinitely.

c. Oppenheimer-Volkoff Mass Limit

All the models constructed and the approximate analysis applied so far point out that this second crushing, or the existence of the second maximum mass, is also inescapable, as is that of the first Chandrasekhar maximum mass. No stable stars with mass exceeding this limit exist. For models with non-interacting particles, this maximum mass has been shown to be about 0.7 $M_\odot$ while it is increased to as much as 2 solar masses in some of the models of real gases (e.g. V_γ). We do not know what is going to happen on superdense stars whose mass exceeds this limit. We have to rely on a non-static approach in dealing with such problems.

d. Fate of Stars Exceeding the Maximum Mass Limit

The fate of massive degenerate stars exceeding Chandrasekhar's limit has been discussed and investigated to a great extent in the past, and these investigations have produced the basis of most of the theories of formation of white dwarfs by loss of mass. The fate of neutron stars with mass exceeding the Oppenheimer-Volkoff mass limit has been speculated upon ever since the existence of this limit was first confirmed by Oppenheimer and Volkoff. The first theory is due to Oppenheimer and Snyder(6) who investigated the problem with the simplified assumption of the equation of state $P = 0$. Recently, in particular, the dynamics of a collapse of such a body has been a hot issue among people in relativistic physics and astrophysics. Various contributions toward a solution of the problem of the fate of massive stars have been given by authors such as Wheeler, Cameron, Chiu, Fuller, Fowler, Hoyle, etc. (e.g. references 8, 9, 17, 29, 32, 33, 60 and 66). This interesting topic however goes beyond the domain of this research, and I shall only mention that (1) if one looks at the problem as a matter of principle, it poses serious paradoxes such as the non-conservation of the baryon numbers, while (2) if the problem is taken as a matter of phenomenon, various possible means of ejecting excessive mass can and have been speculated upon (as has been done for stars with mass exceeding the white dwarf limit), which would enable a star to finally become a neutron star within the mass limit.

e. Existence of the Third Maximum Mass

In most of previous work, the methods commonly adopted were to carry out the integration up to about $\rho_m{}^c \sim 10^{17}$ gm/cm^3, and then join this smoothly to one asymptotic model of a central singularity. Therefore, the exact behavior of superdense stars with $\rho_m{}^c > 10^{17}$ gm/cm^3 was not determined. In carrying out integrations for ideal gas models in these superdense regions, this writer was first disturbed by the fact that the expected singularity (a straight vertical line in the $\mathcal{E}^c$–M plane) was not seen when the integration was carried out up to a limit as high as $\mathcal{E}^c \sim 10^{19}$ gm/cm^3.

To settle this question, the original domain of the equation of state (from $t_n^c = 0$ to 8) was enlarged (to $t_n^c = 16$), and the integrations were repeated with central densities as high as $\mathcal{E}^c \sim 10^{24}$ gm/cm^3. Then finally, the smooth approach to the singularity (the vertical line in the $\mathcal{E}^c - M$ plane) was observed (Figure 30) as expected. The result is that before approaching the singularity, there is another small maximum at a central density $\sim 10^{19.4}$ gm/cm^3 above the Oppenheimer-Volkoff critical point.

This third maximum belongs to the region which was found to be dynamically unstable in previous investigations. However, it is reported$^{(24)}$ that the stability problem at the third maximum cannot be analyzed by the simple methods employed earlier and Wheeler suggested$^{(24)}$ that this peak might be checked by extending the variational method to terms of the second order. The result of such a check may tell whether the third peak has any physical significance.

f. Central Singularity

From Figure 36, we have a glimpse of how the central singularity may be developed for a star of finite mass and radius. The tendency seen in the curve (1) in Figure 36 becomes more and more pronounced as the central density increases. Above a certain value (just after passing the third hump), the mass and radius of a star seems to stay almost constant with increasing central density; the only change being that of the internal distribution of matter. The N baryons which have been spreading over the whole interior of the star seem to assemble more and more at the center, and this readjustment of internal distribution of matter seems to keep the apparent size of the star fairly constant, until at the extreme ($\rho^c = \infty$) all N baryons gather at the center, leaving nothing elsewhere in the star.

The existence of a central singularity has been predicted by various people with various analytic approximations all of which point to the inescapable existence of this singularity. The major difference between different models is in the values of the radius and mass.

An interesting common property of models with $\rho^c = \infty$ is that the time metric at the center vanishes. Equation (1-33) in Chapter I gives an expression for the time metric inside a star ($r < R$); $g_{44}(r) = (1 - \frac{2M}{R}) \{\cos h^2 \frac{t_n(r)}{4}\}^{-1}$, where M and R are the total gravitational mass and radius of the stellar configuration and $t_n(r)$ is the relativistic parameter of neutrons at a radial distance r. Especially at the center $t_n(0) = \infty$ for such stars and the cosh term becomes infinite, giving the value zero to $g_{44}(0)$ for any combination of M and R. The vanishing of the time metric implies that for a distant observer the phenomena occuring at the center of such a star proceed at an infinitely slow rate.

g. Schwarzschild Singularity

In Chapter I, Section 4d, another type of singularity was introduced which is inherent in spherically symmetric bodies of the Schwarzschild type, namely, those where the line element is expressed in a form as given by (1-26) and (1-30). This singularity develops on the surface of radius $R_G = 2\,GM/C^2$ called the gravitational radius. The time metric vanishes and the radial component of the metric becomes infinite on this surface. Therefore, it takes infinite time to cross this surface and due to the infinite curvature of space there, the light emitted from this surface will never reach us. Even though it was pointed out in Chapter I that the Schwarzschild singularity seems to be a coordinate singularity (in the sense that it is removed by coordinate transformations into, for instance, isotropic forms such as (1-48)); nevertheless, in the above sense, it may be regarded as a physical singularity. For instance, if a neutron star of a given mass has a radius equal to the gravitational radius $R_G = 2GM/C^2$, we are then in serious trouble because this star might never be seen even if it were located closer to us than the moon.

This point was checked with our models. The conclusion is that all the models constructed in this research have radii larger than R_G, the limit set by the Schwarzschild singularity, from the lightest models to the densest (where $\rho^c = \infty$), and if they do exist, the emitted light will travel into outer space. However, it is not known whether somewhere in the interior of some of the superdense stars, the condition $r > \frac{2GM(r)}{C^2}$ is violated or not. In the extreme case of a central singularity, this condition will be violated in the interior. However, as was checked in Section IV-3f, the Schwarzschild singularity does not occur both in the interior and on the surface of all of the six models selected for further investigation as stable neutron stars (the results for the densest one of them, $V_\gamma I$, are listed in Table 20). After also examining results from my other models I conclude that this applies to all the other models as well, if the central density is not too high.

h. Binding Energies

Two kinds of binding energies (in mass units) have been introduced. One, M_B, represents the total binding energy of a star with respect to the mass before the constituent particles have been assembled in the form of a star; the other, M'_B, is the macroscopic mass defect, or the binding energy due to the presence of only a gravitational field. The results presented reveal that M_B can be either negative or positive, while M'_B is always positive. This can be explained as follows: By definition,

$$M_B = M_p - M \text{ where } M_p = \int_0^R \rho_m \sqrt{-g_{rr}(r)}\, dV ; \quad M = \int_0^R \mathcal{E}\, dV = u(R) \tag{4-13}$$

and

$$M'_B = M_o - M \text{ where } M_o = \int_0^R \mathcal{E} \sqrt{-g_{rr}(r)}\, dV \tag{4-14}$$

where $\mathcal{E}$ is the total energy density which includes the rest mass energy and all internal energies due to microscopic phenomena (kinetic energy, and potential energy due to interaction forces between constituent particles, etc.), while ρ_m is specifically the sum of rest masses of the constituent particles. We can, therefore, decompose $\mathcal{E}$ into a rest mass part ρ_m and an internal energy density $(\mathcal{E}\text{in}.)$

Then, M_B can be re-expressed as

$$M_B = \int_0^R (\rho_m \sqrt{-g_{rr}(r)} - \mathcal{E})\, dV = \int_0^R \rho_m(\sqrt{-g_{rr}(r)} - 1)\, dV + \int_0^R (\rho_m - \mathcal{E})\, dV =$$

$$M_B = \int_0^R \rho_m(\sqrt{-g_{rr}(r)} - 1) 4\pi r^2 dr - \int_0^R \mathcal{E}_{in}\, 4\pi r^2 dr ; \tag{4-15}$$

where $\mathcal{E} \equiv (\mathcal{E}\text{ in}) + \rho_m$

Noting that $\sqrt{-g_{rr}(r)} = \left(\frac{r}{r - 2\,u(r)}\right)^{\frac{1}{2}} > 1$, the first term in (4-15) is always positive, while $(\mathcal{E}\text{in})$ consists, in our case, of the kinetic term (which is positive) and the nuclear potential term which is also positive if a repulsive potential dominates. From earlier discussions we know that the total internal energy density $(\mathcal{E}\text{ in})$ is also positive because the attractive potential never becomes larger than the kinetic term in magnitude. Therefore, the above expression (4-15) shows that M_B can be either positive or negative depending on whether the first term or the second term is larger in magnitude. u(r) appearing in the metric is a function of $\mathcal{E}$, and, therefore, each term depends on the exact expression of the internal energy (especially on the interaction potential used) in a complicated way. This explains why the binding energy M_B became negative in high density limit for an ideal gas and for pure neutron gases of type V_β, but failed to become negative in all the other potentials used in this research. It is interesting to note that the corresponding quantity became negative for high density in Saakyan's real gas model.

When kinetic energy exceeds the rest mass, it appears that binding energy becomes negative; this is true in a flat space because here $\sqrt{-g_{rr}} = 1$ and the first term in (4-15) vanishes. That the curvature increases with an increasing gravitational field which itself increases with increasing density and microscopic kinetic energy, makes the situation more complicated.

The above simple reasoning that the binding energy should become negative (and hence that M_p should be less than M) for the relativistic particles (i.e. KE>> mc^2) applies, however, in the case of electrons. When the electrons become relativistic, the effect of curvature due to gravity is still negligible(where $\rho \sim 10^{13}$ gm/cm^3), and when the electron kinetic energy becomes much larger than its rest mass energy, the binding energy does become negative: this is exhibited in Figures 37 and 40 (the dashed curves are to the left side of solid curves for $10^{12} < \rho^c < 10^{14}$ gm/cm^3). The effect is small, however, due to the small masses and energies associated with electrons as compared with those of baryons.

Equction (4-14) may be re-written as

$$M'_B = \int \varepsilon\left(\sqrt{-g_{rr}(r)} - 1\right) dV = \int 4\pi r^2 \varepsilon\left[\left(\frac{r}{r - 2u(r)}\right)^{1/2} - 1\right] dr \qquad (4\text{-}16)$$

Noting that $\sqrt{r/(r - 2u(r))} > 1$, this quantity is always positive in the presence of a gravitational field, as was noted in our previous results. The large values associated with the macroscopic mass defect also point out the importance of the non-Euclidean nature of space (gravity) on the problems of neutron stars and other superdense objects.

i. Effect of the Upper Limit Set by Relativity

The effect of the requirement that the pressure cannot become larger than a certain function of the energy density is summarized below. The general behavior of models of dense stars (the existence of the first, second and third mass maximums and finally the arrival at a constant mass and radius as the central density becomes infinite in the manner illustrated by the general shape of the trajectory of the solutions of the hydrostatic equations in the ρ_m^c-M plane, such as are shown in Figure 37) does not change, irregardless of whether the relativistic limit has been applied or not and what kind of restriction has been applied (whether it is the type $P \leq \mathcal{E}$ or $P \leq \frac{\mathcal{E}}{3}$, etc.). The main effect of such a restriction seems to be the change in the actual value of the critical mass (Figures 32 and 40). For instance, the Skyrme-Cameron type models have a larger critical mass at $\mathcal{E}^c = \infty$ after the limitation $P \leq \mathcal{E}$ has been observed than before (Figure 32). While Figure 40 reveals that for Levinger-Simmons type models the more restrictive limitation $P \leq \frac{\mathcal{E}}{3}$ causes masses to be smaller than in the case of the less restrictive limitation $P \leq \mathcal{E}$. After examining all the models constructed in this research and their behavior, it is concluded that the general effect of "cutting off" is to discourage any further change in mass with any further increase of central density. For instance, if the pressure saturation is applied in the lower branch of Oppenheimer-Volkoff hump (that is, if the nuclear equation of state becomes equal to the asymptotic equation when the mass is increasing with increasing central density), then the application of the requirement $P \lesssim K\,\mathcal{E}$ (where K is a constant) prevents any further change of mass in the same direction (in this case, the mass does not increase with increasing central density as fast as it would in the case of no restriction, and, therefore, we get smaller masses above the pressure saturation point (refer to the curves for $P \lesssim \mathcal{E}/3$ in Figure 40, for instance). While, if the pressure saturation occurs on the upper branch after the Oppenheimer–Volkoff crushing point has been passed, then on this branch the equilibrium mass decreases with increasing central density, and hence the application of the limit $P \lesssim K\,\mathcal{E}$ discourages any further decrease of mass with increasing central density: as a consequence larger masses obtain beyond the crushing point for models with $P \lesssim K\,\mathcal{E}$ than for the original unrestricted ones (for instance, compare curves (1) and (2) in Figure 32).

It should be emphasized that an exact knowledge of the equation of state near and just above nuclear densities (around $10^{14} < \rho < 10^{16}$ gm/cm^3) is required to determine the properties of the stars not only in this range but also of far denser ones. It is true that denser matter, about $\rho \gtrsim 10^{16}$ gm/cm^3, should follow an asymptotic equation of state such as $P = \mathcal{E}$ or $P = \mathcal{E}/3$ (or most generally the polytropic form $P = cn^{\gamma} = (\gamma - 1)\,\mathcal{E}$, with γ appropriately chosen), but the important question is: to what nuclear equation should this be joined in lower density regions?

j. Red Shift

We may feel that the denser stars have larger red shifts. However, on examining the behavior of red shifts with central density from the list in Tables 10, 15, 16, and 17, we see that the red shift is largest for models just above the Oppenheimer–

Volkoff crushing point, and that with a further increase in central density, red shift first decreases and then stays constant as $\varepsilon^c \rightarrow \infty$. This is because the red shift is determined by the ratio of the total mass of the star to its radius, and mass and radius stay nearly constant as the central density approaches infinity in super-dense regions. It is quite large around the maximum mass point, even as large as about 0.3 for real gas models. This is consistent with the prediction of Burbidge(67) that red shift of such a star can become as large as about 0.5 (= $\Delta\lambda/\lambda$).

IV-5 CONCLUSIONS

(1) By investigating the properties of models based on two contrasting possible forms of interaction potentials (type V_β and type V_γ) both consistent with experimental data in the medium energy regions near and just above nuclear densities, we are led to the conclusion: that models of these two types possess quite different properties, especially their critical mass values and radii. In stable regions, the radii of the V_γ type models are almost twice those of type V_β and the critical mass of models of type V_γ are also about twice as large as the corresponding mass value of type V_β models. It is most desirable to further improve the nuclear equation of state in the critical region of 10^{14} gm/cm$^3 \lesssim \rho \lesssim 10^{16.5}$ gm/cm^3. Through knowing the nature of the interaction forces between baryons, we will be able to construct better neutron star models; or by the reverse process, if in the future we happen to obtain the mass and the radius of neutron stars through observations, we may be able to solve the problem of the interactions between nucleons and strange particles.

(2) The above investigation shows that other effects, like that of the relativistic limit, the effect of hyperons, etc. are relatively small, compared with the effect of the exact form of the interaction potentials. However, we realize that the present research has been based on a very artificial assumption, namely, that all hyperons are under the same interaction potential of either type V_β or V_γ, and this may not be well justified. If a better expression for the interaction forces between strange particles is adopted, the hyperon effect may turn out to be quite important.

(3) Another outcome which may well be noted is the possible importance of the electron-heavy nuclei envelope in some of the lightest neutron stars. The most extended envelopes occur in unstable regions, but it was shown that some of the stable neutron stars could have quite an extended envelope also, almost as large as the neutron core itself, although the mass contained in it would be small.

(4) By calculating the curvature of space, it was demonstrated that general relativity is important in the problem of neutron stars.

(5) It was shown that all the models in hydrostatic equilibrium have radii larger than $R_G = \frac{2MG}{c^2}$ (otherwise $\sqrt{-g_{rr}(R)}$ would have to be infinite or imaginary), and it may be concluded, therefore, that all stable neutron star models do not face the troublesome Schwarzschild singularity.

IV-6 SUMMARY

To summarize the results, some of the interesting physical quantities for different models are listed in Tables 22, 23, 24.

TABLE 22. Properties at critical points (the stellar radius R, the gravitational and proper masses M and M_p in units of solar mass, the central matter and energy densities $\rho_m{}^c$ and $\mathcal{E}^c$, and the red shift) for a real gas model of neutrons with V_β, V_γ and $V_{\beta\gamma}$, for composite models of a real gas of type V_β and V_γ, the Skyrme-Cameron type models, and ideal gas models, are listed at: (1) the second maximum, (2) the third maximum, and (3) the central singularity with $\mathcal{E}^c = \infty$. (Summary of my results.)

Critical Point	Model	Composite ($P \leq \mathcal{E}$)		Pure Neutron ($P \leq \mathcal{E}$)			Skyrme-Cameron-Type	Ideal Gas
		V_β	V_γ	V_β	V_γ	$V_{\beta\gamma}$		
(1) 2nd Max. (Opp.-Volk.)	R (km)	4.7	9.7	5	10	8	7.5	9.5
	$M/M_\odot$	0.96	1.98	0.98	1.94	1.65	1.70	0.72
	$M_p/M_\odot$	1.17	2.40	1.12	2.29	1.92	2.10	0.75
	$\log \rho_m{}^c$	15.95	15.4	15.95	15.3	15.5	15.5	15.4
	$\log \mathcal{E}^c$	16.1	15.6	16.2	15.45	15.7	15.8	15.6
	Red shift	0.301	0.300	0.288	0.285	0.303	0.334	0.11
(2) Third Max.	R (km)	3.86	8.05	3.94	7.9	6.26	6.6	6.4
	$M/M_\odot$	0.78	1.54	0.77	1.55	1.26	1.351	0.44
	$M_p/M_\odot$	0.84	1.64	0.76	1.63	1.31	1.455	0.42
	$\log \rho_m{}^c$	17.3	16.7	17.34	16.6	16.86	16.85	18.8
	$\log \mathcal{E}^c$	19.5	18.8	19.55	18.5	18.86	19.1	19.4
	Red shift	0.29	0.27	0.287	0.288	0.296	0.302	0.10
(3) Central Singularity	R (km)	3.86	8.05	3.93	7.9	6.59	6.61	6.4
	$M/M_\odot$	0.77	1.53	0.765	1.54	1.26	1.34	0.425
	$M_p/M_\odot$	0.83	1.62	0.757	1.62	1.294	1.44	0.398
	Red shift	0.292	0.274	0.286	0.287	0.280	0.298	0.098

TABLE 23. The physical properties (1) near the Chandrasekhar crushing point and (2) in the region of the electron-ion extended envelopes, are listed for various composite models of low density for the purpose of comparison.

		(1) 1st Max. (Chandrasekhar)			(2) Max. Envelopes		
		$\log \rho_m^c$	$M/M_\odot$	R(km)	$\log \rho_m^c$	$M/M_\odot$	R (km)
L.-S.	V_β	9.1	1.18	2.3×10^3	13.25	0.26	1.6×10^3
	V_γ	9.1	1.18	2.3×10^3	13.55	0.4	2.6×10^3
Salpeter (equil.)		9.3	1.02	2.44×10^3	14.54	0.11	6.2×10^3
Wheeler		8.4	1.2	3.5×10^3	13.17	0.24	4×10^2
Chandra.		∞	1.44	0	—	—	—
Rudkjö.		∞	1.2	0	—	—	—

TABLE 24. The models of others are compared with mine at (1) the Oppenheimer-Volkoff crushing points and (2) the point of central singularity.

Models \ Critical Point				(1) OPP.- VOL. MAX. POINT			(2) CENTRAL SINGULARITY	
				ρ_m^c(gm/cm^3)	$M/M_\odot$	R(km)	$M/M_\odot$	R (km)
Others	OP.- VOL.			$\varepsilon^c \sim 10^{16}$	0.7	10	0.34	3.1
	Wheeler			$\varepsilon^c \sim 10^{16}$	0.68	10	1.48 (analytic)	
	Saakyan (Ideal)			$\varepsilon^c \sim 2.34 \times 10^{15}$	0.64	11	0.324	11.1
	Saakyan (real)			$\varepsilon^c \sim 10^{16}$	1.06	6	0.691	4.95
Models in this research	Ideal			2.5×10^{15}	0.72	9.5	0.425	6.4
	S.-C.			3.2×10^{15}	1.70	7.5	1.30	6.7
	S.-C.($P \leq \mathcal{E}$)			3.2×10^{15}	1.70	7.5	1.34	6.61
	$P \leq \mathcal{E}$	Neutron	V_β	9×10^{15}	0.98	5	0.765	3.93
			$V_{\beta\gamma}$	3.2×10^{15}	1.65	8	1.26	6.59
			V_γ	2×10^{15}	1.94	10	1.54	7.9
		Composite	V_β	9×10^{15}	0.96	4.7	0.77	3.36
			V_γ	2.5×10^{15}	1.98	9.7	1.53	8.05
	$P < \mathcal{E}/3$		V_β	8×10^{15}	0.91	5	0.72	4
			V_γ	2×10^{15}	1.935	10	1.47	8.1

In Table 22, the stellar radius R, the gravitational and proper masses M and M_p, the central matter and energy densities $\rho_m{}^c$ and $\mathcal{E}^c$, and the red shift, for models constructed in this research (the Levinger-Simmons type real gas models of a pure neutron configuration (V_ρ, V_γ and $V_{\beta\gamma}$) and of composite configurations (V_β and V_γ), the Skyrme-Cameron type real gas models, and ideal gas models), are listed at: (1) the second maximum point (the Oppenheimer-Volkoff crushing point), (2) the third maximum point, and (3) the point where the central singularity developes. From this table it can be seen that the red shift in ideal gas models is about 1/3 that in real gas models, the difference in red shifts between different real gas models being quite small. The red shift is only about 1% or less for light neutron star models, is about 0.1 to 0.3 near the Oppenheimer-Volkoff crushing point, becomes somewhat less at the third maximum point and stays constant thereafter as the central density becomes infinite. In Table 23, the physical properties near (1) the Chandrasekhar crushing point and (2) in the region where the electron-ion envelopes become most extended, are listed for various composite models of low density: the first two rows give properties of composite models of the Levinger-Simmons type V_β and V_γ. . Listed together with these for the purpose of comparison are the corresponding properties of Salpeter (equilibrium models) and the Wheeler, Chandrasekhar, and Rudkjöbing's models. In Table 24, the models of others and those constructed in this research are compared, at (1) the Oppenheimer-Volkoff crushing point and (2) at another important critical point where the central singularity developes. By examining this table, we may obtain a quick view of the effect of the interactions between particles, of the presence of hyperons and other baryons, and of the relativistic upper limit $P \lesssim \mathcal{E}$ or $P \lesssim \mathcal{E}/3$. It should be noted that Saakyan's ideal gas models are for baryon gases while the ideal gas models of Oppenheimer-Volkoff and those of the present research are for pure neutron gases, while Wheeler's models are for a relativistic proton-neutron-electron system. The critical mass at which central singularity occurs as obtained by Wheeler has no connection with the rest of his ideal gas models, because it was obtained through an independent analytical method. His maximum mass of about 1.48 $M_\odot$ therefore represents an approximation for real gases and agrees roughly with the other real gas models presented in this table. In Tables 23 and 24, L.-S. means models of the Levinger-Simmons type and S.-C. indicates models of the Skyrme-Cameron type obtained in this research. The models of other authors are indicated by the full or abbreviated names of the respective authors. For instance, Chandra. means the models constructed by Chandrasekhar, etc. Other symbols in Tables 23 and 24 are the same as those introduced in Table 22.

CHAPTER V

HOT NEUTRON STAR MODELS

V-1 INTRODUCTION

In the last chapter the hydrostatic structure of degenrate stars was analyzed. Some important questions, such as those pertaining to the internal temperature, luminosity, cooling, and detectability of these dense stars, were, however, completely left out. This chapter is devoted to these problems to complete our investigation.

It was noted in Chapter I that the integrations through the degenerate core from the center do not contain temperature and that all the temperature-dependent properties are determined through the integrations over the thin non-degenerate outer layers from the surface. The structure equations in these outer layers are, from Chapter I,

$$\frac{dP_r}{dr} = -\frac{[P_r/c^2 + \rho(r)]\,G(4\pi r^3 P_r/c^2 + M_r)}{r(r - 2M_r G/c^2)} \tag{5-1}$$

$$\frac{dM_r}{dr} = 4\pi r^2 \rho(r) \tag{5-2}$$

$$\frac{dT_r}{dr} = -\frac{3}{4ac}\,\frac{\kappa(r)\,\rho(r)}{T_r^3}\,\frac{L}{4\pi r^2} \quad \text{(radiative or electron conduction) or} \tag{5-3}$$

$$\frac{dT_r}{dr} = \left(1 - \frac{1}{\gamma}\right)\frac{T_r}{P_r}\,\frac{dP_r}{dr} \quad \text{(convective)} \tag{5-4}$$

where M_r, T_r, P_r, $\rho(r)$, and $\kappa(r)$ are the mass, temperature, pressure, density and opacity at a distance r from the center, L is the total luminosity of the star, and other notation is the same as in Chapter I. The general relativistic expressions are used in hydrostatic equations because the result of the last chapter (Table 19, last two rows) reveals that the general relativity effects are not negligible near the surface.

To solve these differential equations, the density and opacity must be eliminated through the explicit relations

$$P_r = P_r(\rho(r), T_r) \tag{5-5}$$

$$\kappa(r) = \kappa(\rho(r), T_r) \tag{5-6}$$

for a given composition. In the core integrations of Chapter IV, we saw that the most troublesome task is making a correct choice of equation of state (5-5). In the non-degenerate outer layers the equation of state is relatively simple (Section V-4a), but here it is the opacity, (5-6), which poses the most complicated problem. The next section (V-2) is, therefore, devoted to the subject of opacity.

Also, we must have a suitable boundary condition at the surface. The simple condition (1-6b) is no longer adequate when we are concerned with the outermost layers. More accurate boundary conditions for surface integrations are obtained in Section V-3 through the construction of simple model atmospheres. The actual integrations of the structure equations over the surface layers are carried out in Section V-4. Some temperature-dependent properties of neutron stars, such as central and surface temperature, and the distribution of pressure, density, and temperature near the surface, are investigated in this same section. The total energy contents of neutron stars are then found in Section V-5. Luminosity, both optical and neutrino, is calculated in Section V-6, and cooling curves are obtained in Section V-7. The observational problems are investigated in Section V-8. The conclusion is given in Section V-9.

The temperature-independent properties of hot neutron stars are the same as those of the cold models obtained in the last chapter, as long as the internal temperature does not exceed about 5×10^{11} °K. This criterion applies to any hot neutron stars of appreciable duration as will be seen in Section V-7.

V-2 OPACITY

a. General Remarks

The opacity is the most decisive factor in the envelopes of neutron stars. Both radiative and conductive energy transport are expressed by (5-3) together with a suitable expression for $\kappa(r)$. Let us call the radiative opacity κ_R, and the conductive opacity κ_c, then the total opacity κ is given by

$$\frac{1}{\kappa} = \frac{1}{\kappa_R} + \frac{1}{\kappa_c} \, . \tag{5-7}$$

Radiative opacity is due to the various processes of atomic and molecular absorption, emission and scattering of radiation in which electrons play the major role. The relative importance of these processes depends strongly on the temperature-density combination. For instance, in matter of high temperature and of relatively low density, electron scattering is dominant, while in the region of intermediate density and temperature the various photoelectric effects such as the bound-free and free-free processes are the most important. In degenerate matter of high density electron conduction is in general the most efficient mechanism. The major processes of atomic absorption are (1) bound-free process where bound electrons are ionized through the absorption of photons, (2) free-free process in which free electrons are excited to higher states through the absorption of photons, and (3) bound-bound process where bound electrons are excited to higher bound states through the absorption of photons. Excited electrons emit photons in the inverse processes. The scattering processes are (1) Thomson scattering if the temperature is not too high and (2) compton scattering for $T > 5 \times 10^8$ °K.

In general, the radiative absorption coefficient depends on the frequency of radiation ν. There are various ways of obtaining the mean coefficient of absorption. The most commonly used of these is the following, called the Rosseland mean,

$$\frac{1}{\kappa_R} = \frac{\rho \int_0^\infty \ell(\nu)[dB(\nu,T)/dT]\,d\nu}{\int_0^\infty [dB(\nu,T)/dT]\,d\nu} \tag{5-8}$$

where

$$\ell(\nu) = \left\{\mu_a(\nu)\left[1 - \exp\left(-\frac{h\nu}{kT}\right)\right] - \mu_s(\nu)\right\}^{-1} \tag{5-9}$$

is the mean free path of a photon of frequency ν; $\mu_a(\nu)$ and $\mu_s(\nu)$ are the usual coefficients of absorption and scattering, given by

$$\mu_a(\nu) = \sum_i n_i \sigma_i(\nu) \quad \text{and} \quad \mu_s(\nu) = n_e \sigma_s \tag{5-10}$$

where n_i is the number of atoms per unit volume in state i; $\sigma_i(\nu)$ is the cross section for absorption of radiation of frequency ν by these atoms; n_e is the number of electrons per unit volume; and σ_s is the compton scattering cross section which becomes σ_o, the Thomson scattering cross section, in the low temperature limit. The factor $\left[1 - \exp\left(-\frac{h\nu}{kT}\right)\right]$ in (5-9) is to account for stimulated emission. h and k are Planck's and Boltzmann's constants, respectively, and ρ is matter density.

$$B(\nu,T) = (2h\nu^3/c^2)\left[\exp\left(+\frac{h\nu}{kT}\right) - 1\right]^{-1} \tag{5-11}$$

is the Planck distribution function corresponding to a temperature T.

Conductive opacity is obtained through the thermal conductivity λ_c, which is defined by

$$\lambda_c \frac{dT}{dr} = - Q \qquad (5\text{-}12)$$

where dT/dr is the temperature gradient in the direction r and Q is the flux of energy. Noting that the temperature gradient is expressible also as

$$\frac{dT}{dr} = - \frac{3\kappa_c \rho}{4aT^3 c} \frac{L}{4\pi r^2} \qquad (5\text{-}13)$$

and that $L/4\pi r^2$ is the energy flux, we see that these two equations are identical if

$$\kappa_c \equiv \frac{4acT^3}{3\rho\lambda_c} \qquad (5\text{-}14)$$

That is, the solution of the problem of conductive opacity boils down to the determination of λ_c, the thermal conductivity.

If $\mu_a(\nu)$, $\mu_s(\nu)$ and λ_c are known, therefore, the above equations enable us to find the total opacity κ, in principle. The opacity obtained in this way usually has quite a complicated dependence on density and temperature and is expressed as

$$\kappa = \kappa(\rho, T), \qquad (5\text{-}15)$$

In recent years, various extensive tables based on detailed computations have been published which give the absorption coefficient for many different compositions and for a large number of points in the temperature-density diagram. The most accurate method of obtaining opacities at present is thought to be through the computer programming code for stellar absorption coefficients and opacities constructed by A. N. Cox and his colleagues of the Los Alamos Scientific Laboratory, which includes most of the possible major processes contributing to opacity.

b. Cox's Opacity Code

The code was constructed so that it could be run for a mixture of as many as 11 elements. It includes bound-bound, bound-free, and free-free absorption, electron scattering (both Thomson and compton scattering), negative ion absorption and electron conduction, and can be run for 50 discrete values of density and 50 discrete values of temperature. The bound-free absorption depends on the equilibrium number of electrons which are bound in the various atomic states. When the ionization of one element is completed, no more bound-free absorption due to that element can occur. For high densities the effect of degeneracy is taken into account in all but the electron scattering term. At low densities and low temperatures not all electrons are ionized. An ionization code should be used in conjunction with the opacity code in these regions to calculate the degree of ionization, the partial pressure of electrons, and the number of free electrons and bound electrons in the opacity calculations.

At temperatures above about 5×10^7 °K, almost all elements (even the heaviest elements) are ionized. The existing tables mentioned in the previous subsection are also used to obtain absorption cross sections $\sigma_i(\nu)$ for the various kinds of processes: bound-free, free-free, negative ion, etc.). The electron scattering term is obtained for the non-degenerate case in which pair production of electrons and positrons is neglected, and it is, therefore, independent of density but dependent on temperature in the high temperature region where compton scattering is dominant. Different approximations are applied for different degrees of degeneracy to evaluate the conductive opacity κ_c.

c. Opacity Calculations

Cox's opacity code was run by Mr. B. Sackaroff, a member of the computer staff at the Goddard Institute for Space Studies, on an IBM 7094 computer for (1) a pure iron composition and (2) a pure magnesium composition*, in the range of temperature from $10^{3.7}$ °K to 10^{10} °K, and of density from $10^{-4.3}$ gm/cm^3 to 10^{14} gm/cm^3. For a pure Fe^{56} or Mg^{24} composition, Cox's code did not work for temperatures below $10^{3.7}$ °K and densities below $10^{-4.3}$ gm/cm^3. Opacities at densities higher than 10^{14} gm/cm^3 have not been included in this calculation because degeneracy sets in at densities far below this. Calculation of the same quantities at temperatures higher than 10^{10} °K has not been carried out because the assumption of electron scattering in non-degeneracy and no electron-positron pair creation causes serious errors there. The opacities ($\ln \kappa$) thus obtained have been stored as an input deck of cards in the form of a two-dimensional table corresponding to a given $\ln T$ and $\ln \rho$ combinations, for later use.

The ionization code was run in conjunction with the opacity code of Cox in the low density and temperature regions where the ionization code works (roughly, the region where photoelectric effects predominate) to obtain the correct degree of ionization at a given combination of temperature and density.

d. Results

Results obtained in this manner are plotted in Figure 42. The solid curves represent the opacity of iron 56 as a function of density at different temperatures, while the dashed curves represent the same for magnesium 24. The opacity shows quite a complicated dependence on density and temperature in the region $\rho \lesssim 10^6$ gm/cm^3 and $T \lesssim 10^8$ °K, where the transition from electron scattering

---

*The reason for these particular choices is explained in Section V-4d.

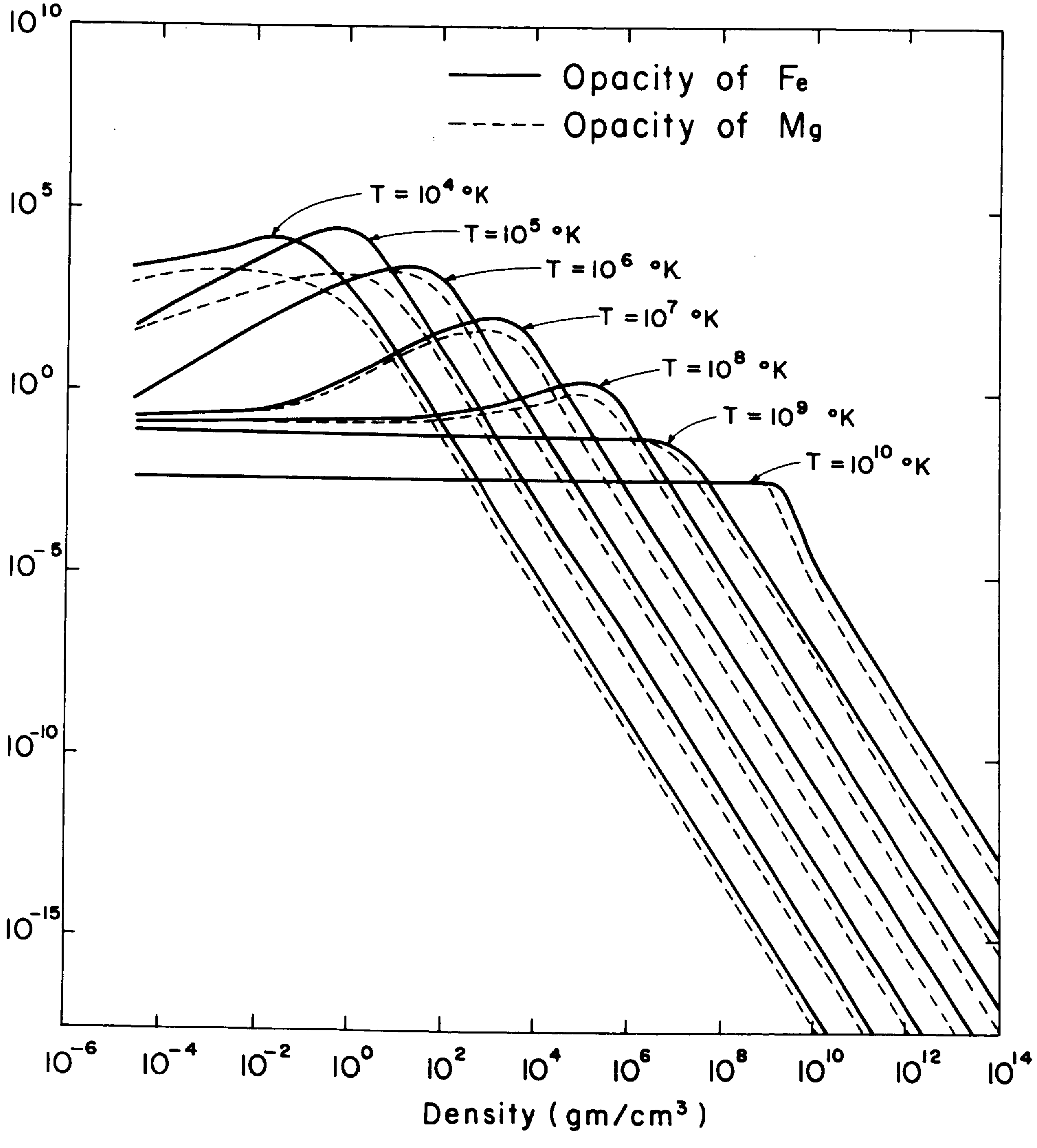
Opacity of Fe
Opacity of Mg
T = 10⁴ °K
T = 10⁵ °K
T = 10⁶ °K
T = 10⁷ °K
T = 10⁸ °K
T = 10⁹ °K
T = 10¹⁰ °K
10¹⁰
10⁵
10⁰
10⁻⁵
10⁻¹⁰
10⁻¹⁵
Opacity (cm²/gm)
10⁻⁶
10⁻⁴
10⁻²
10⁰
10²
10⁴
10⁶
10⁸
10¹⁰
10¹²
10¹⁴
Density (gm/cm³)

Figure 42

or electron conduction to Kramer's opacity (mainly various kinds of photoelectric effects) occurs. In Figure 42, the almost straight horizontal lines in the region of $T > 10^9$ °K and $\rho < 10^6$ °K are due to compton scattering, while the almost straight lines of negative slope in regions of higher density are an indication that electron conduction is the dominant factor in the transport of energy there. We can assume that degeneracy starts as soon as the opacity curve in Figure 42 starts to follow one of these straight negatively sloping lines.

In order to understand the meaning of these opacity curves more clearly and to check the results obtained through Cox's opacity code, it was thought to be helpful to investigate some of the asymptotic forms of the complicated opacity formulae presented in Section V-2a.

e. Kramer's Formula for Bound-Free Transitions

We noted that in intermediate temperature and density regions, bound-free, free-free and bound-bound processes are in general the most important. Besides these, some negative ion absorption, especially in the case of H^-, is quite important in low temperature regions. However, in the particular case of a composition of pure iron or pure magnesium and also in the outermost layers of neutron stars, only the bound-free process is thought to be important. This is mainly because of the extraordinary composition and the extraordinary high temperatures which are associated with the surface of neutron stars (about $10^{6 \sim 7}$ °K as compared with about several thousand degrees of most typical stars such as the sun). Due to the absence of hydrogen and helium we do not have a source of negative ions. In the presence of heavy elements, the bound-free process is possible even under temperatures up to about 5×10^7 °K. In the presence of the bound-free processes, the contribution from the free-free and bound-bound ones is usually negligible, as will be seen shortly.

Various molecular processes become important at lower temperatures, but the surface temperatures of neutron stars of interest are too high to let these molecular processes enter into our consideration.

The conclusion is, that to analyze the behavior of opacity in the low temperature low density limit associated with neutron stars (that is, the upper-left corner in Figure 42), we need consider only the ordinary bound-free transitions in the non-degenerate case.

The absorption coefficient per atom and per electron for bound-free transitions is given by

$$a_{bf} = 64\pi^4 m e^{10} (Z')^4 g / (3\sqrt{3}\, c\, \hbar^6 n^5 \nu^3) \tag{5-16}$$

where Z^1 is the effective charge of the ion, n is the principle quantum number of the electron, and g is a non-dimensional factor called the Gaunt factor, which is of order of 1 and varies slowly with n and ν. The over-all absorption coefficient for bound-free transitions is then,

$$\mu_{bf}(\nu) = \sum_{A,n} a_{bf} \left(\frac{\chi_A \rho}{A H}\right) N_{A,n} \tag{5-17}$$

χ_A is the concentration of the atom in question, H is the mass of hydrogen, $(\chi_A \rho / AH)$ is the total number of atoms of atomic weight A per unit volume and $N_{A,n}$ is the number of electrons per atom bound in the nth state. On substituting (5-16) and (5-17) in (5-8) and (5-9) in the absence of the scattering term and of hydrogen and helium, the following approximation, called Kramer's formula, results

$$\kappa_{bf}(\rho, T) = 4.34 \times 10^{25} \left(\frac{\bar{g}}{t}\right) \rho T^{-3.5} \tag{5-18}$$

$\bar{g}$ is the mean Gaunt factor, and t, called guillotine factor, takes care of all the required modifications and corrections. $t/\bar{g}$ is in general on the order of 1 to 10.

After applying a similar argument, Kramer's formula for free-free transitions in the absence of hydrogen and helium takes the form,

$$\kappa_{ff}(\rho, T) = 3.68 \times 10^{22}\ \bar{g}\ \rho\ T^{-3.5} \qquad (5\text{-}19)$$

From these two equations, it is clear that for the composition of interest, free-free opacity is about 10^{-3} times that of the bound-free process, which proves the original assumption that the former is negligible compared with the latter. (5-18) applies in the low density-temperature region where degeneracy is not important (the outermost layers of neutron stars), or, referring to Figure 42, in the upper-left hand corner.

In the presence of degeneracy (in the region of transition from Kramer's opacity to conductive opacity), each term in (5-17) for the bound-free absorption coefficient must be multiplied by the probability that the final state of the ionized electron is empty, namely,

$$1 - \frac{1}{1 + \exp\left((E - \mu)/kT \right)} ,$$

where E is the energy of the final free state of the electron and μ is the chemical potential of the electron. The result is that in the presence of degeneracy, the bound-free opacity is somewhat lower than that obtained by (5-18). Equation (5-18) is, however, still valid if the degeneracy correction is included in the factor t.

f. Electron Scattering

The electron scattering term in (5-9), $\mu_s(\nu)$, is evaluated as follows. Starting from the equation of radiative transfer with electron scattering, which holds for local thermodynamic equilibrium, and retaining only the first term in the expansion of $F_n(\nu)$, the flux of radiant energy of frequency ν across a surface with normal n, Sampson(68) found that,

$$\mu_s(\nu)=\iint_{P\,\Omega_2} N(P)\,4\pi P^2 dP \frac{d\sigma}{d\Omega_2} d\Omega_2 \left[\frac{1-\exp(-h\nu/kT)}{1-\exp(-h\nu_2/kT)}\right]\left[1-\frac{\nu_2 \ell(\nu_2)\cos\theta}{\nu \ell(\nu)}\right] \tag{5-20}$$

Here, N(P) is the number density of electrons with momentum P ; ν, ℓ (ν), and Ω without the subscript 2 are, respectively, the frequency, mean free path and solid angle before scattering and those with the subscript 2 are the corresponding quantities after scattering. The differential cross section $\frac{d\sigma}{d\Omega_2}$ is given by the Klein-Nishina formula for a system in which the electrons are initially at rest, denoted by primes, as

$$\frac{d\sigma'}{d\Omega_2'}=r_0^2\frac{(1+\cos^2\theta')}{2}\frac{1}{[1+\gamma'(1-\cos\theta')]^2}\left\{1+\frac{\gamma'^2(1-\cos\theta')^2}{(1+\cos^2\theta')[1+\gamma'(1-\cos\theta')]}\right\} \tag{5-21}$$

where $\gamma' = h\nu'/mc^2$ and $r_o = e^2/mc^2$. On substituting (5-21) into (5-20) and applying the transformation from the primed to the unprimed system, we obtain

$$\mu_s(\nu)=n_e\sigma_{eff}(\nu,T)= n_e\,\sigma_0\,G(U,T') \quad \text{where} \tag{5-22}$$

$$G(U,T')=\frac{1}{C(T')}\int_0^\infty g(\gamma,E)(E+1)(E^2+2E)^{1/2}\exp\left(-\frac{E}{T'}\right)dE \tag{5-23a}$$

$$\begin{aligned} C(T') &= \int_0^\infty (E+1)(E^2+2E)^{1/2}\exp\left(-\frac{E}{T'}\right)dE \\ &=\left(\frac{\pi}{2}\right)^{1/2}T'^{3/2}\left(1+\frac{15}{8}T'+\frac{105}{108}T'^2-\frac{315}{1024}T'^3+\frac{10395}{37268}T'^4\cdots\right) \end{aligned} \tag{5-23b}$$

where γ, E and T' are the photon energy, the electron kinetic energy and the temperature in units of mc^2, $g(\gamma, E)$ is a complicated function of γ and E as given in reference 68, $u = h\nu/kT$, and

$$\sigma_0 = \frac{8\pi r_0^2}{3} = \frac{8\pi}{3}\left(\frac{e^2}{mc^2}\right)^2 = \text{constant} \tag{5-24}$$

is the Thomson cross section for scattering of radiation by electrons. If all electrons are ionized (which is the case when electron scattering is dominant as for $T > 10^7$ °K) in the absence of electron-positron pair creation, the electron number density is simply $n_e = \sum_i \frac{\rho Z_i}{A_i} N_o X_i$, where X_i is the concentration of the ith atom and N_o is the Avogadro's number. When only the element of mass number A and atomic number Z is present (as in the present case),

$$n_e = \frac{\rho Z}{A} N_o \quad \text{(for nucleus (A, Z))} \tag{5-25}$$

In the absence of absorption and emission processes, if we substitute $\mu_s(\nu)$ of (5-22) into (5-9) and use (5-8), we get for the radiative opacity due to electron scattering,

$$k_s = \frac{n_e \sigma_0 \bar{G}(T)}{\rho} = \left(\frac{Z}{A}\right) N_0 \sigma_0 \bar{G}(T) \quad \text{(for nucleus (A,Z))} \tag{5-26}$$

where $\bar{G}(T)$ is a function of temperature only, which can be calculated from

$$\bar{G}(T) = \left\{\frac{15}{4\pi^4}\int_0^\infty u^4 e^u (e^u - 1)^{-2} \left[G(u,T')\right]^{-1} du\right\}^{-1} \tag{5-27a}$$

Values of $\bar{G}(T)$ calculated in this manner are listed in a table in reference 68, which is reproduced below:

kT(kev)	2	4	6	9	14	20	30	50	80	125
$\bar{G}(T)$	0.95005	0.9044	0.8626	0.8067	0.7279	0.6525	0.5590	0.4408	0.3411	0.2579

------(5-27b)

In the limited range of 20 kev $\leq kT \leq$ 125 kev, we have

$$\bar{G}(T) = -\,0.13887 + 4.9371\,(kT)^{-\frac{1}{2}} - 5.9479(kT)^{-1} - 2.362(kT)^{-3/2} \qquad (5\text{-}27c)$$

The conversion from kT in Kev to temperature in units of 10^9 °K is

$$T_9 \sim kT(\mathrm{kev})/85.2 \qquad (5\text{-}28)$$

For an element where $A/Z = 2$, (5-26) reduces to

$$\kappa_s = 0.2\,\overline{G}(T)\ \mathrm{cm}^2/\mathrm{gm} \qquad (5\text{-}26')$$

the constant term is, in fact, opacity due to Thomson scattering, and the extra temperature dependent term $\bar{G}(T)$ can be considered as a correction to the pure Thomson scattering in the region of compton scattering. The above results show that the compton scattering effect is negligible at $T \lesssim 10^7$ °K, but with increase of temperature, the opacity decreases. It shows also that opacity due to electron scattering is independent of density in the absence of degeneracy and of electron-positron pair creation, while it depends on temperature through the term $\bar{G}(T)$. Pair creation of electrons and positrons is always negligible in the problem of neutron stars, because the density is too high for this process even at the high temperatures which obtain here. The degeneracy effect may, however, become important, especially in the transition region between radiative and conductive energy transport. In the presence of degeneracy, the integrand in (5-20) should be multiplied by the probability that the final electron state will be empty, as in V-2e. This results in opacity in the presence of degeneracy being lower than the non-degenerate value.

g. Electron Conduction

The thermal conductivity of electrons has been derived by the use of the electron theory of metals$^{(31)}$ as,

$$\lambda_c = \frac{2}{3}\frac{m_e^5 c^8}{\hbar^3 e^4 I}\frac{m_e c^2}{T}\frac{G_3 G_5 - G_4^2}{G_3} \tag{5-29a}$$

where

$$I = \frac{\rho}{H}\sum_i \frac{x_i Z_i^2}{A_i}\left\{\frac{1}{3}\log 6\pi + \frac{1}{3}\log Z_i + \frac{1}{2}\log K - \frac{5}{6}\log L\right\} \tag{5-29b}$$

G_3, G_4, G_5, K and L are integrals of the form

$$\int_0^\infty [1 + \exp(\theta(m_e c^2 \cosh t - \mu)]^{-1} f(t)\,dt \;;\quad \theta = (kT)^{-1};$$

where f(t) is some function of t. For the non-relativistic case, these equations reduce to $\lambda_c = \frac{64}{3}\frac{m_e k^5 J^4}{\hbar^3 e^4 I}\left\{\left(\frac{15}{4}\right)F_2 F_4 - 4F_3^2\right\}\Big/(3F_2)$

$$\text{where } F_n = \int_0^\infty \frac{u^n\,du}{1 + e^u \Lambda^{-1}} \;;\quad \Lambda = e^{\mu/kT}\;; \tag{5-30a}$$

and

$$I = \frac{\rho}{H}\sum_i \frac{x_i\ Z_i^2}{A_i}\left(\frac{1}{3}\log 12\pi + \frac{1}{3}\log Z_i + \frac{1}{2}\log F_{3/2} - \frac{5}{6}\log F_{1/2}\right) \tag{5-30-b}$$

For the non-degenerate, non-relativistic case, it simplifies to

$$\lambda_c = 128 m_e k^5 T^4 \Lambda \big/ (\hbar^3 e^4 I) \tag{5-30c}$$

and for the degenerate, non-relativistic case

$$\lambda_c = \frac{2\pi^2}{9}\frac{m_e^4 c^6 k^2 T}{\hbar^3 e^4 I}\frac{x^6}{(x^2+1)} \text{ with } x = p_F/m_e c \tag{5-30d}$$

The conductive opacity in the corresponding asymptotic regions is calculated by substituting λ above into (5-14).

h. Discussion of the Results

First, let us consider the region where all but the Kramer's opacity are negligible. When T = 10^6 °K, this condition is fulfilled as long as 10^{-4} gm/cm$^3 \lesssim \rho \lesssim 10^2$ gm/cm^3. Noting that t/$\bar{g}$ in the absence of degeneracy is about 1 to 10 Kramer's opacity for bound-free transitions calculated from (5-18) is about 10 cm^2/gm at $\rho = 10^{-3}$ gm/cm^3 and about 10^3 cm^2/gm at $\rho = 1$ gm/cm^3. These values agree almost perfectly with the curve of $T = 10^6$ °K shown in Figure 42. For $T = 10^6$ °K and $\rho = 10^3$ gm/cm^3, the quantity $E_F/kT \sim 1$ and degeneracy is no longer negligible, although still small. At this particular point, the results calculated through Cox's opacity code are

$$\kappa_R = 10^5 \ cm^2/gm \ \text{and} \ \kappa_c = 10^{1.8} \ cm^2/gm \cong \kappa = \frac{\kappa_R \ \kappa_c}{\kappa_R + \kappa_c} \ .$$

Conductive opacity is already the more important. However, the Kramer's opacity calculated from (5-18) still agrees with the radiative opacity κ_R from Cox's code if $\bar{g}/t$ is taken to be about 1/300. It has been noted that the effect of degeneracy is to lower the opacity and that this effect can be included in the guillotine factor t. Therefore, it seems quite in order that $\bar{g}/t$ has been decreased from 1/10 to 1/300 in the presence of degeneracy. Next, let us consider $T = 10^5$ °K. Kramer's opacity becomes $\sim 10^{2.5}$ cm^2/gm at $\rho = 10^{-3}$ gm/cm^3 if $\bar{g}/t$ is taken to be about 1/50; while $\kappa_{bf} \sim 10^{4.5}$ cm^2/gm at $\rho = 1$ gm/cm^3 if $\bar{g}/t$ is taken to be 1/500. Both values agree well with the radiative opacity from Cox's code. When $T = 10^5$ °K, E_F, the electron Fermi energy, and kT become comparable with each other when $\rho \sim 1$ gm/cm^3, and the increase of t in this case is again as should be expected. When $T = 10^4$ °K, E_F/kT is already comparable to unity at about $\rho \sim 10^{-3}$ gm/cm^3 and the non-degenerate κ_{bf} from (5-18) at this density is much larger than the value from Cox's code if the ordinary value of $\bar{g}/t = 1 \sim 10$ is used. The conclusion is that the general behavior of Cox's opacity for iron composition and magnesium composition is reliable in the region where Kramer's law of opacity applies, if degeneracy is correctly taken into account. It should be noted that the simple approximation (5-18) is good only for checking the order-of-magnitude.

Next, let us turn to electron scattering. For $T = 10^6$ °K, electron scattering is negligible unless the density becomes less than about 10^{-4} gm/cm^3, which is outside the region of our major interest. At $T = 10^7$ °K, the opacity due to electron scattering dominates over Kramer's opacity for $\rho < 10^{-1}$ gm/cm^3. At $T = 10^7$ °K, kT is about 1 kev and Thomson scattering applies. Here, $\kappa_s \sim 0.2$ cm^2/gm, which agrees well with the $T = 10^7$ °K curve for $\rho \lesssim 10^{-2}$ gm/cm^3 in Figure 42. At $T = 10^8$ °K, kT is about 8.5 kev, $\bar{G}(T)$ is about 0.8 from (5-27b), and the scattering opacity $\kappa_s \sim 0.16$ cm^2/gm from equation (5-26'), agreeing perfectly with the curve of $T = 10^8$ °K in Figure 42 for $\rho < 10^3$ gm/cm^3. In the small range around $\rho \sim 10^5$ gm/cm^3, Kramer's opacity contributes appreciably, but for higher densities, electron conduction takes dominance over the rest. At $T = 10^9$ °K, Kramer's opacity never enters. In this region of high temperature, most of the electrons are ionized and bound-bound and bound-free transitions can give hardly any contribution, the effect of free-free transitions is also too small to be important. At $T = 10^9$ °K, kT is about 85 kev, $\bar{G}(T)$ is about 0.34, and (5-26') gives $\kappa_s \sim 0.07 \sim 10^{-1.1}$ cm^2/gm = constant, which agrees well with the result shown in Figure 42. At this temperature, degeneracy starts at about 10^6 gm/cm^3, and radiative opacity is replaced by conductive opacity at higher densities. When $T = 10^{10}$ °K, kT is about 0.85 Mev and E_F/kT becomes comparable with 1 when $\rho \sim 10^9$ gm/cm^3. At lower densities the main mechanism for radiative transport of energy is compton scattering with $\kappa_s \sim 10^{-2.5}$ cm^2/gm, while at higher densities electron conduction is the most efficient process (see Figure 42).

The degeneracy effect on electron scattering is negligible for $T \lesssim 10^8$ °K, because E_F/kT is less than about 0.05 (that is, degeneracy is negligible for $\rho \lesssim 10^3$ gm/cm^3 at $T = 10^8$ °K. At this same temperature but at higher densities, Kramer's opacity dominates over electron scattering before real degeneracy sets in and makes conduction the most efficient mechanism. At temperatures below $T = 10^8$ °K Kramer's opacity predominates over electron scattering at densities even lower than above. For higher temperatures, a non-degenerate treatment of electron scattering may not be well justified in the transition region. At $T = 10^9$ °K, however, E_F/kT is already around 0.1, at $\rho \sim 10^5$ gm/cm^3, and we expect that the only effect of including degeneracy at this temperature will be to lower slightly the corner of the curve for $T = 10^9$ °K in Figure 42 in the approximate density range 10^5 to 10^7 gm/cm^3. This decrease in scattering opacity with increasing density due to degeneracy is expected to start at about $\rho \gtrsim 10^6$ gm/cm^3 for temperatures $\gtrsim$ 10 billion degrees.

If electron-positron pair production is included in these extremely high temperature regions ($10^8 \lesssim T < 10^9$ °K), the opacity would increase with decreasing density if $\rho \lesssim 1$ gm/cm^3, but the actual solutions of the structure equations of the envelopes of neutron stars in later sections reveal that this combination of temperature and density is not encountered in the problem of neutron stars.

Finally, let us check the conductive opacity. Because the term in the bracket in (5-30b) is on the order of unity, and $A/Z \sim 2$ and $x_i \sim 1$ for the composition of our interest (pure Fe or pure Mg), the conductive opacity for the non-relativistic, extremely degenerate case becomes, from (5-14), (5-30b) and (5-30d),

$$\kappa_c = 5.57 \times 10^{-19}\, T^2 \left(\frac{x^2+1}{x^6}\right)\left(\frac{Z}{26}\right) \tag{5-31}$$

with $x = p_F/mc$. Let us consider that $\rho = 10^6$ gm/cm^3. Ionized electron gases of heavy nuclei are still non-relativistic at this matter density, with a corresponding Fermi energy of about $E_F \sim 0.2$ Mev and with $x \sim 0.4$. Then, (5-31) gives us the following values at $\rho = 10^6$ gm/cm^3; conductive opacity is $\kappa_c^{Fe} = 1.22 \times 10^{-9}$, 1.22×10^{-7}, and 1.22×10^{-5} cm^2/gm for pure iron, and is $\kappa_c^{Mg} = 5.65 \times 10^{-10}$, 5.65×10^{-8}, and 5.65×10^{-6} cm^2/gm for pure Mg, at $T = 10^4$ °K, 10^5 °K, and 10^6 °K, respectively. These values agree perfectly with the results of the Los Alamos opacities shown in Figure 42, as they should.

Next, consider $\rho = 10^9$ gm/cm^3 with $E_F \sim 5$ Mev and $x \sim 10$, and note that the electrons are relativistic here. At this density, equation (5-31) gives $\kappa_c^{Fe} = 5.6 \times 10^{-15}$, 5.6×10^{-13}, and 5.6×10^{-11} cm^2/gm for Fe, and $\kappa_c^{Mg} = 2.6 \times 10^{-15}$, 2.6×10^{-13}, and 2.6×10^{-11} cm^2/gm for Mg, at $T = 10^4$ °K, 10^5 °K, and 10^6 °K, respectively. These values deviate from the results shown in Figure 42 to a small extent, but this degree of deviation is just what is to be expected because the non-relativistic approximation was used in the derivation of (5-31) and this does not apply well at this density. However, the condition of extreme degeneracy is satisfied at all the points selected to be checked. In most of the electron conduction regions shown in Figure 42 electrons are degenerate. However, at the lowest density for which conduction is still dominant at $T = 10^{10}$ °K, the highest temperature considered (that is, at the corner of the $T = 10^{10}$ °K curve near $\rho \sim 10^9$ gm/cm^3 in Figure 42), E_F/kT is only about 5 and the assumption of extreme degeneracy is not well justified. The small hump at this corner (in the transition region between the compton scattering and electron conduction at $T = 10^{10}\ ^{\circ}K$) occurs because of deviation from perfect degeneracy as expressed by the approximate relation of (5-31). Using the relation $x = P_F/mc \propto n^{1/3} \propto \rho^{1/3}$, equation (5-31) can be rewritten as

$$\log \mathcal{K}_c \cong (\text{const} \times T^2) - 2 \log \rho \ (\text{if } P_F < m_e c^2), \qquad (5\text{-}31')$$

which indicates that conductive opacity of degenerate matter should give roughly straight lines of negative slope when plotted in the $\log \mathcal{K}_c - \log \rho$ plane, and the intercepts should be larger for higher temperatures. This agrees with Figure 42. The conductive opacity of Mg is lower than that of Fe due to the appearance of Z in (5-31). It also depends on $Z/A \doteq \mu^{-1}$ but this dependence is too small to be seen in a graph such as Figure 42. It is reasonable that opacity of iron in the region of photoelectric effects should be somewhat larger than that of magnesium, because in general more bound electrons are available at a given temperature and density for the heavier than for the lighter elements, and therefore more bound-free transitions will occur in the former.

Compton scattering depends on composition only through the ration Z/A, as seen in (5-26), which effect is also too small to be seen in Figure 42.

After examining the various asymptotic values, we can conclude that the opacity table prepared through the Los Alamos code for pure Fe and pure Mg in Section V-2c is sufficiently accurate for our neutron star problem.

In the above discussion, the temperature-density diagram for opacity on p.72 of reference 26 was used qualitatively to determine which particular kind of opacity should be dominant in each of the temperature-density regions of interest.

V-3 ATMOSPHERIC CALCULATIONS

We have noted that the simple boundary condition (1-6b) does not lead to a proper representation of the surface layers. Somewhat better boundary values at the surface are obtained as follows.

Let us define the surface as the point where the actual temperature is equal to the effective temperature, that is, $T_s = T_e$, where the effective temperature T_e is defined as the temperature of the black body which would radiate the same flux F as the star itself. That is, $F = \sigma T_e^4$, where σ is Stefan's constant (5.670 x 10^{-5} ergs/cm^2 - sec-deg.^{4}). By definition, the total optical luminosity L of the star is related to the total flux per cm^2 per sec, F, as $L = 4\pi R^2 F$, where R is the radius of the star. Therefore, we have

$$L = 4\pi \sigma R^2 T_e^4 \tag{5-32}$$

In the atmospheric layers above the surface of neutron stars as defined above, it is assumed that the ordinary theory of stellar atmospheres applies, provided that general relativity effects are correctly taken into account in some of the denser models. According to the theory of radiative transfer in stellar atmospheres, the first approximation (due to Eddington) to the temperature distribution in grey atmospheres in radiative equilibrium is,

$$T^4 = T_o^4 (1 + \frac{3}{2} \tau) \tag{5-33}$$

where T_o is the temperature at $\tau = 0$ and τ is the optical depth defined as

$$d\tau = - \kappa \rho (r) dr \quad \text{where } \kappa \text{ is the opacity.} \tag{5-34}$$

If κ_ν is independent of ν the theory of radiative transfer leads us to the relation

$T_e = 2^{1/4} T_o$, and from (5-33) we find that the optical depth at the surface where $T_s = T_e$ is $\tau_s = 2/3$. The thickness and mass content of an atmosphere is negligible in general, and, therefore, equation (1-1) when applied to regions within atmospheres, takes the simple form,

$$\frac{dP}{d\tau} = \frac{g}{\kappa(\rho, T)} \tag{5-35a}$$

where $g = GM/R = \text{constant}$. In the above derivation, (5-34) was used to eliminate r. The general relativistic equation (5-1) leads us to the same atmospheric equation (5-35a) if g is re-defined as

$$g = g_o \left(\frac{P_{ph}}{\rho_{ph} c} + 1 \right)\left(1 + \frac{4\pi R^3 P_{ph}}{M c^2}\right)\left(1 - \frac{2GM}{R c^2}\right)^{-1} \tag{5-35b}$$

and $g_o = GM/R$.

To determine the pressure P_{ph}, density ρ_{ph}, temperature T_e, and opacity $\kappa(\rho_{ph}, T_e)$ at the surface as defined above, the general procedure followed by Ezer and Cameron in reference 69 was adopted here. That is, we assume that the opacity κ is independent of both height and wave length in the atmosphere but that it has the value determined at the photosphere, $\kappa(\rho_{ph}, T_e)$: then we find from (5-35a) that

$$P_{ph} = \int_0^{P_{ph}} dP = \int_0^{\tau_s} \frac{g(P_{ph}, \rho_{ph})}{\kappa(\rho_{ph}, T_e)} d\tau \simeq \frac{g(P_{ph}, \rho_{ph})}{\kappa(\rho_{ph}, T_e)} \frac{2}{3} \tag{5-36}$$

For a given stellar radius, mass and luminosity, we first guess a value of ρ_{ph}, then find T_e from (5-32), and finally we calculate P_{ph} through (5-36). The equation of state at the photosphere is simply

$$P_{ph} = \frac{(Z+1)}{A} \frac{k}{H} \rho_{ph} T_e + \frac{1}{3} a T_e^4 \; ; \; a = 7.569 \times 10^{-15} \tag{5-37}$$

The first term is the gas pressure of non-degenerate fully ionized electrons and heavy nuclei of pure (A,Z) composition, and the last term is the radiation pressure. The notation used in equation (5-37) is the same as that introduced in Section III-1. Radiation pressure is negligible in dense interiors and even at the surface in most cases. For instance at a temperature of one million degrees, radiation pressure P_γ is 2.5×10^9 dynes/cm^2, which is negligible when compared with the gas pressure Pg $(= 5 \times 10^{12}$ dynes/cm$^2)$ at the photosphere of a typical neutron star at this same temperature. However, when the temperature goes up to about 10 million degrees then $P_\gamma = 2.5 \times 10^{13}$ dynes/cm^2 while according to Table 25 Pg $\sim 2 \times 10^{14}$ dynes/cm^2 at the photosphere. At even higher temperatures, radiation pressure becomes larger than 10% of the gas pressure near the photosphere of neutron stars. On substituting P_{ph} as calculated through (5-36) into (5-37), we obtain a new value for ρ_{ph}. We then repeat the procedure using this new value as the starting point. This process is continued until we get the desired degree of agreement between subsequent values of ρ_{ph}.

The above calculations are performed with (1) a pure Fe^{56} composition, and (2) a pure Mg^{24} composition, because of the reason given in Section V-4d. The photospheric properties of a neutron star depend on the specific model (that is, the specific combination of M and R) and on the period in its lifetime (that is, the surface temperature).

The result of the present calculation shows that as a neutron star cools from $T_e = 5 \times 10^7$ °K to $T_e = 2 \times 10^4$ °K, (1) optical luminosity is reduced from about 10^6 times to 10^{-8} times the solar luminosity, (2) the ρ_{ph} decreases slightly from about

TABLE 25. Photospheric properties of typical neutron stars (V_β, $0.6M_\odot$) and (V_γ , $2M_\odot$) at different surface temperatures T_e. L is the luminosity, ρ_{ph}, P_{ph} and κ_{ph} are the photospheric density, pressure and opacity, respectively, and λ^o_{max} is the maximum wavelength without red shift.

T_e	V_β, $M = 0.60\ M_\odot$, $R = 5.66$ km				V_γ, $M = 1.977\ M_\odot$, $R = 9.686$ km				λ^o_{max}
(°K)	$\log(\frac{L}{L_\odot})$	$\log\rho_{ph}$(gm/cm^3)	P_{ph}(dynes/cm^2)	$\log\kappa_{ph}(\frac{cm^2}{gm})$	$\log(\frac{L}{L_\odot})$	$\log\rho_{ph}(\frac{gm}{cm^3})$	$P_{ph}(\frac{dynes}{cm^2})$	$\log\kappa_{ph}(\frac{cm^2}{gm})$	(Å)
2×10^4	-8.0153	-1.8198	1.214×10^{10}	4.2955	-7.5484	-1.6708	1.731×10^{10}	4.4338	1459
5×10^4	-6.424	-1.8616	2.757×10^{10}	3.9394	-5.9566	-1.7177	3.840×10^{10}	4.0832	583.6
10^5	-5.22	-1.8134	6.166×10^{10}	3.5898	-4.7525	-1.6490	9.009×10^{10}	3.7129	291.8
2×10^5	-4.015	-1.5985	2.021×10^{11}	3.0743	-3.5484	-1.4499	2.846×10^{11}	3.2133	145.9
5×10^5	-2.424	-1.0739	1.693×10^{12}	2.1513	-1.9567	-0.8650	2.741×10^{12}	2.2298	58.36
10^6	-1.220	-0.9310	4.704×10^{12}	1.7074	-0.7526	-0.7275	7.519×10^{12}	1.7915	29.18
2×10^6	0.0154	-0.9447	9.102×10^{12}	1.4207	0.4516	-0.7523	1.418×10^{13}	1.5160	14.59
5×10^6	1.576	-0.8647	2.735×10^{13}	0.9430	2.0433	-0.6900	4.085×10^{13}	1.0564	5.836
10^7	2.780	-0.4408	1.452×10^{14}	0.2180	3.2474	-0.2596	2.201×10^{14}	0.3250	2.918
2×10^7	3.985	-0.3963	3.212×10^{14}	-0.1269	4.4515	-0.2012	5.051×10^{14}	-0.0358	1.459
5×10^7	5.576	-0.2744	1.065×10^{15}	-0.6474	6.0433	-0.0578	1.757×10^{15}	-0.5772	0.584

1 gm/cm^3 to about 0.01 gm/cm^3, (3) P_{ph} decreases from about 2×10^{15} to 10^{10} dynes/cm^2, and (4) its opacity at the surface changes from about 0.1 to $10^{4.5}$ cm^2/gm. In general, at the same surface temperature, higher values of P_{ph}, ρ_{ph} and K_{ph} seem to be associated with heavier models.

The surface boundary values of two typical models of stable neutron stars (v_β, $0.6M_\odot$) and (v_γ, $2M_\odot$) with pure iron atmospheres are shown in Table 25. For our lightest model (v_β, $0.2\,M_\odot$) at the lowest temperature considered at present, $T_e = 2 \times 10^4$ °K, we have $L = 10^{-7.5}\,L_\odot$, $\rho_{ph} = 3.16 \times 10^{-2}$ gm/cm^3 and $P_{ph} = 2.54 \times 10^9$ dynes/cm^2, which indicates that for $T_e > 10^4$ °K we need not be concerned about opacity at densities lower than 10^{-3} gm/cm^3. Surface temperatures lower than 10 thousand degrees are not included because the opacity code does not work in these regions . (In the above, $L_\odot = 3.780 \times 10^{33}$ ergs/sec is the sun's luminosity.)

In evaluating the opacity $\kappa(\rho_{ph}, T_e)$, the $\ln\kappa$-$\ln\rho$ -ln T table prepared in Section V-2c and the interpolation subroutine are used to obtain the desired value of ln κ_{ph} corresponding to a given ln ρ_{ph}-ln T_e combination.

V-4 ENVELOPES OF NEUTRON STARS

a. Surface Integration

In the surface layers where the pressure gradient is quite high, it is most convenient to express everything in logarithms and in terms of ln P. Then, the structure equations introduced in Section V-1 become:

$$\begin{aligned}
\frac{d(\ln r)}{d(\ln P_r)} &= -\exp(\ln P_r + \ln A - \ln B - \ln G - \ln D) \\
\frac{d(\ln M_r)}{d(\ln P_r)} &= -\exp[3\ln r - \ln M_r + \ln\left(\frac{4\pi}{G}\right) + \ln \rho(r) + \ln P_r + \ln A \\
&\qquad - \ln B - \ln D] \\
\frac{d(\ln T_r)}{d(\ln P_r)} &= \exp[\ln(3/16\pi a c G) + \ln \kappa(r) + \ln \rho(r) \\
&\qquad + \ln L - 4\ln T_r - \ln r + \ln P_r + \ln A - \ln B - \ln D]
\end{aligned} \tag{5-38}$$

where

$$\begin{aligned}
A &= \exp(\ln r) - \exp(\ln 2 + \ln M_r - 2\ln c + \ln G) \\
B &= \exp(\ln \rho(r)) + \exp(\ln P_r - 2\ln c) \\
D &= \exp(\ln M_r) + \exp(\ln 4\pi + 3\ln r + \ln P_r - 2\ln c)
\end{aligned}$$

where $a = 7.569 \times 10^{-15}$, $G = 6.67 \times 10^{-8}$ dynes-cm^2/gm^2, $c = 2.9978 \times 10^{10}$ cm/sec.

The equation of state in non-degenerate layers is

$$P = \frac{1}{\mu}\frac{k\rho T}{H} + \frac{1}{3}aT^4 \quad ; \quad \frac{1}{\mu} = \frac{1}{\mu_e} + \frac{1}{\mu_{ion}} \tag{5-39}$$

with μ_e and μ_{ion} as defined as (2-44) and obtained from Table 6 in Chapter II. In degenerate envelopes, all pressures except the degenerate pressure of electrons are negligible and the equation (4-1) of Chapter IV for degenerate electron gases replaces (5-39). μ_e in (4-1) is again evaluated from the result of Chapter II.

A computing program, which consists of a main program working in conjunction with the integration subroutine, the interpolation subroutine, the opacity table prepared in Section V-2c as an input, and with the subroutine for the equation of state and that for the atmospheric calculations, has been constructed for the 7094 computor which carries out the integration and all the other computations automatically. For instance, the program is constructed so that the equation of state automatically switches over from (5-39) to (4-1) as soon as the point is reached where these two become equal; the surface boundary values are calculated through the subroutine for the atmosphere whenever a new set of values of R, M and T_e are given; the interval of integration $\Delta \ln P$ is automatically adjusted so that the change of every variable is kept smaller than a preassigned suitable limit; and any desired value of opacity is calculated for any given set of density and temperature through the input opacity table and the interpolation subroutine. The integrations were terminated when the temperature gradient completely vanished.

b. Atmospheric Temperatures

To determine the temperature distribution in the interior of the atmosphere, the integration was first carried out from the photosphere down to the point where $\rho = 10^{14}$ gm/cm^3, for a typical model of $M = 1\ M_\odot$ and $R = 10$ km. This was repeated at several different surface temperatures. The result is shown in Table 26. The temperatures T at different densities (corresponding to different radial distances from the center of the star) are listed in terms of the given effective temperatures T_e. T_b and ρ_b are the temperature and density where degeneracy starts (where the equation of state switches over from the non-degenerate expression (3-39) to the degenerate expression (4-1)). It shows that degeneracy starts at about $\rho_b = 10^6$ gm/cm^3 when the surface temperature is about 10 million degrees. But when the surface has cooled down to about one million degrees, degeneracy sets in already at $\rho_b = 10^4$ gm/cm^3. A significant result is that even after the degeneracy boundary has been passed, the temperature still goes up considerably as we go inwards. Let us compare the internal temperature at $\rho = 10^6$ gm/cm^3 and that at

TABLE 26

Atmospheric temperature distribution of neutron star models with $M=1\,M_\odot$ and $R=10$ km. The temperature T at a specified ρ, the temperature Tb and density ρ_b where the degeneracy starts are listed as a function of surface temperatures T_e.

SURFACE TEMPERATURE	INTERNAL TEMPERATURE T (°K)				T_b(°K)		ρ_b
T_e (°K)	AT $\rho=10^6$ gm/cm^3	AT $\rho=10^9$ gm/cm^3	AT $\rho=10^{12}$ gm/cm^3	AT $\rho=10^{14}$ gm/cm^3	This Research	Morton	(gm/cm^3)
1.6×10^7	9.08×10^8	3.47×10^9	3.65×10^9	3.65×10^9	1.4×10^9	2×10^9	4.3×10^6
1.2×10^7	6.86×10^8	2.34×10^9	2.425×10^9	2.425×10^9	7.7×10^8	1×10^9	1.5×10^6
1×10^7	5.92×10^8	1.825×10^9	1.88×10^9	1.88×10^9	5.92×10^8	–	1×10^6
9.4×10^6	5.75×10^8	1.68×10^9	1.73×10^9	1.73×10^9	4.8×10^8	5×10^8	5.4×10^5
6.7×10^6	4.51×10^8	1.10×10^9	1.125×10^9	1.125×10^9	2.6×10^8	2×10^8	1.4×10^5
5.1×10^6	3.79×10^8	8.09×10^8	8.21×10^8	8.21×10^8	1.5×10^8	1.19×10^8	6.2×10^4
4.3×10^6	3.395×10^8	6.765×10^8	6.83×10^8	6.83×10^8	1.03×10^8	10^8	4.8×10^4
3×10^6	2.64×10^8	4.62×10^8	4.64×10^8	4.64×10^8	7.6×10^7	-	4×10^4
1×10^6	9.61×10^7	1.12×10^8	1.125×10^8	1.125×10^8	3.5×10^7	-	10^4
7.7×10^5	6.5×10^7	7.18×10^7	7.35×10^8	7.35×10^8	2.3×10^7	2×10^7	4.2×10^3

$\rho = 10^9$ gm/cm^3 with the same temperature of the surface. The fractional rise in temperature as the density increases from 10^6 to 10^9 gm/cm^3 is about 10% when $T_e = 7.7 \times 10^5$ °K, but at $T_e = 10$ million degrees the temperature at the point $\rho = 10^9$ gm/cm^3 is about 3 times that at $\rho = 10^6$ gm/cm^3. As we go in toward the center from any point where $\rho = 10^9$ gm/cm^3 to $\rho = 10^{12}$ gm/cm^3, the fractional rise in temperature is about 0.5% for $T_e = 10^6$ °K, while that for $T_e = 10^7$ °K is about 3%. Even at the highest temperature considered, $T_e = 1.6 \times 10^7$ °K, the increase is only about 5%. This shows that the temperature gradient is completely negligible for $\rho > 10^{12}$ gm/cm^3.

As we go inwards from the surface we find that the temperature gradient is very high in the outermost thin non-degenerate layers and that the temperature continues to rise as we go through the degenerate layers inwards. According to the result shown in Table 26, however, the inner neutron core (with $\rho > 10^{12}$ gm/cm^3) is isothermal even for the models of the hottest neutron stars of appreciable duration.

To determine the core temperature of neutron stars (or the central temperature), let us go back to the graph shown in Figure 41 and some of the discussion of the last chapter. Typical stable neutron stars have the following internal structure. Except in some of the lightest models, density and pressure are practically constant from the center out to the very edge where neutrons (and hyperons if density is sufficiently high) form the main composition. The abrupt fall of density (and pressure) from their central value ($\rho^c = 10^{14} \sim 10^{16}$ gm/cm^3) down to the photospheric value ($\rho_{ph} = 0.01 \sim 1$ gm/cm^3) and a change in composition from neutrons to electrons and heavy nuclei is expected at the very edge of the star. Even for some of the lightest stable neutron stars with large degenerate envelopes of electrons and ions, the outermost non-degenerate envelopes are very thin (which is shortly to be shown numerically), while the mass contained outside the central neutron core where $\rho < 10^{12}$ gm/cm^3 is still negligible. The boundary between the degenerate electron-ion envelopes and the neutron cores has $\rho \sim 10^{11 \sim 12}$ gm/cm^3. Therefore we conclude that the neutron core is isothermal even for the lightest (stable) neutron stars and for the hottest of those of appreciable duration, and that the core temperature T_c (which is also the central temperature of the star) can, according to Table 26 and the above, be defined as that temperature where $\rho = 10^{12}$ gm/cm^3.

Next to the last column in Table 26 lists T_b, the temperature at the degeneracy boundary obtained by Morton. Morton's models have $M = 1.3\ M_\odot$, $R = 9.25$ km, and $\rho^c = 14.6 \times 10^{14}$ gm/cm^3. Also they have non-degenerate outer layers where the opacity is expressed as $\mathcal{K} = 1.4 \times 10^{25}\ \rho^{\frac{1}{2}}\ T^{-3.5}$ cm^2/gm (a modification of Kramer's formula) if $T_b < 1.19 \times 10^8$ °K. However, the non-degenerate envelopes consist of two layers if $T_b > 1.19 \times 10^8$ °K; in the inner layer electron scattering is the main source of opacity ($K_s = 0.19$ cm^2/gm), while in the outer layer the modified Kramer's opacity is dominant. The opacity is set equal to zero as soon as the degeneracy starts, that is, Morton defined the core temperature, or the central temperature T^c of the star, as T_b, the temperature where the degeneracy starts.

For $T_e < 10^7$ °K, the general agreement between Morton's results and mine is satisfactory. The deviation between our results in the high temperature regions is thought to be due to the temperature dependence of compton scattering for which I made allowance in my use of Cox's opacity code but which was neglected by Morton.

Figure 42 shows that the compton scattering has, at $T \sim 10^9$ °K, already reduced the opacity from the simple value 0.19 cm^2/gm of Thomson scattering. The density values at the degeneracy-boundary ρ_b calculated by Morton and myself agree well. The major error in Morton's procedure is that he set T_b to be the core temperature, that is, he neglected the temperature gradient at $\rho > \rho_b$. Our results show that temperature increases even after density is increased beyond the point ρ_b, up to $\sim 10^8$ gm/cm^3, for some of the hottest models.

The central temperatures are plotted against surface temperature in Figures 43 and 44. The solid curves are for iron and the dashed curves are for Mg. Curves drawn for three models of the V_ρ type in Figure 43 and for three models of the V_γ type in Figure 44 are marked by the appropriate mass. In Figure 43, Chiu's models and Morton's models are also shown. Chiu's models have $M = 1 M_\odot$ and $R = 10$ km. His treatment of opacities and the method for determining the central temperatures are similar to those used by Morton. Note that our central temperature is defined as that at $\rho = 10^{12}$ gm/cm^3, while theirs is defined as that at $\rho = \rho_b \sim 10^{4 \sim 6}$ gm/cm^3, also there is some non-negligible temperature rise as the density goes up from ρ_b to 10^{12} gm/cm^3. Therefore, our central temperature should be higher than theirs for given surface temperature. This explains why Morton's points for $T_e < 10^7$ °K (dotted square) in Figure 43 are much lower than ours. At higher temperatures ($T_c \gtrsim 10^9$ °K), the compton scattering in Cox's code lowers the opacity from the constant value of ~ 0.2 cm^2/gm (Thomson scattering) and this is expected to lower our values of central temperature. These two causes of discrepancy, however, compensate for one another and therefore there is good general agreement among the three for $T_c \gtrsim 10^9$ °K.

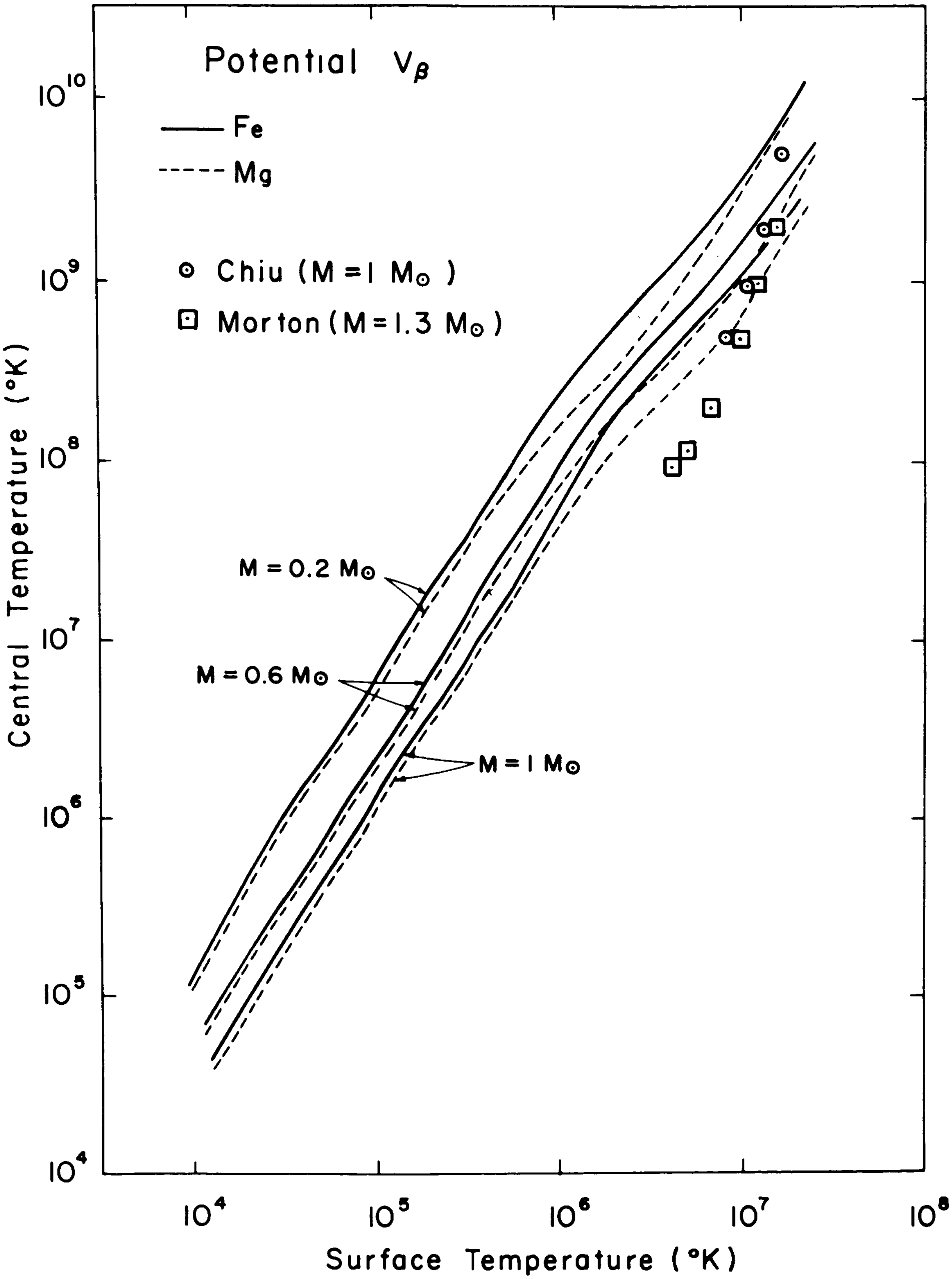
Potential V_β
Fe
Mg
Chiu (M = 1 M⊙)
Morton (M = 1.3 M⊙)
M = 0.2 M⊙
M = 0.6 M⊙
M = 1 M⊙
Central Temperature (°K)
Surface Temperature (°K)
10^4
10^5
10^6
10^7
10^8
10^9
10^{10}

Figure 43

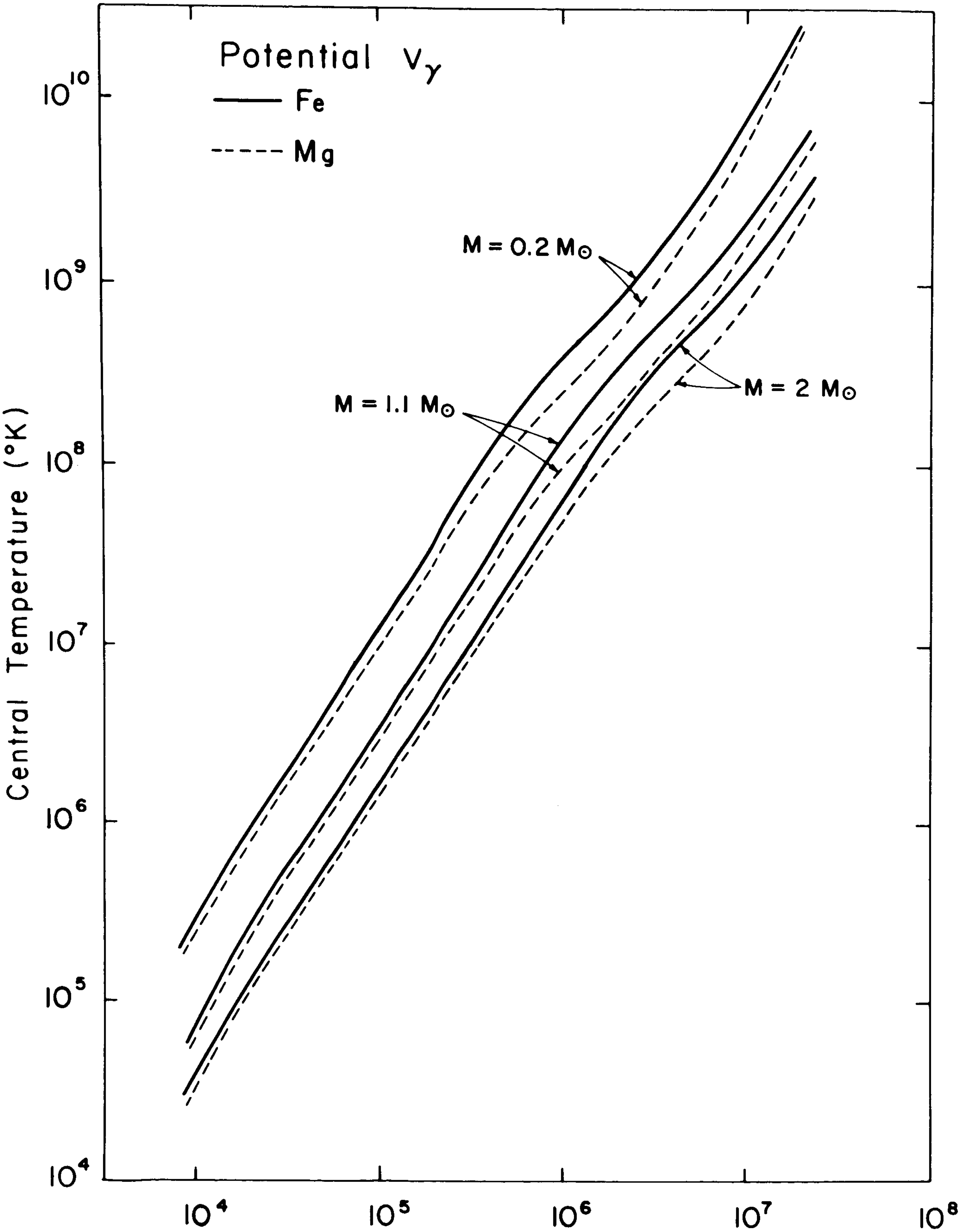
Potential V_γ
Fe
Mg
$M = 0.2\,M_\odot$
$M = 1.1\,M_\odot$
$M = 2\,M_\odot$
Central Temperature (°K)
10^4
10^5
10^6
10^7
10^8
10^9
10^{10}
10^4
10^5
10^6
10^7
10^8
Surface Temperature (°K)

Figure 44

It might be argued that the large discrepancy between Morton's and our results might be reduced considerably if Cox had taken the degeneracy effect on electron scattering into account. However, this argument is not valid, because the discrepancy is greatest for $T < 10^8$ °K, while in this same temperature region, Cox's opacity plot in Figure 42 shows that the electron scattering becomes important only in the non-degenerate region (low density region) if it ever becomes important.

Figures 43 and 44 show that the central temperature is somewhat lower for Mg than for Fe at the same surface temperature. This is due to the fact that somewhat lower opacities are associated with Mg than Fe as is revealed in Figure 42.

We also see that for some of the coolest stars ($T_e \sim 10^4$ °K), the central temperature is only about 10 times the surface temperature, while for hot models (of $T_e \sim 10^7$ °K), the core is about 100 times as hot as the surface. In any case the difference between the central temperature and surface temperature is quite small as compared with that of typical stars, where in general T_c is at least about 1,000 times T_e. (For instance, the internal temperature of the sun is about 5×10^6 °K and its surface temperature is 5760 °K, while a typical white dwarf with $T_e \sim 10^4$ °K is supposed to have an internal temperature of about 10 million degrees.)

The conclusion according to the present calculation is that neutron stars of about 3 times solar luminosity are as hot as 10 million degrees at the surface and about a billion degrees in the interior, those which are as bright as the sun have a surface temperature of $1 \sim 2 \times 10^6$ °K and an internal temperature of about 10^8 °K, and that by the time they cool down to the point where $T_c \sim 10^{6 \sim 7}$ °K and $T_e \sim 10^5$ °K, they are too faint to be seen ($L \sim 10^{-5} L_\odot$).

c. Temperature and Density Distribution Near the Surface

The internal distribution of temperature can be roughly seen from Table 26. To examine the region near the surface in more detail, temperature is plotted against distance from the photosphere as measured inward in Figure 45. Each curve is marked by the surface temperature. The model with $M = 1\ M_\odot$ and $R = 10$ km is used here and hereafter in this sub-section to illustrate the general behavior of the surface properties.

The crosses marked by $X = 2.5$ represents points where the degeneracy starts. This criterion for degeneracy is derived from the fact that the kinetic energy of a non-relativistic fermion (about 3/5 of the Fermi energy E_F) and the thermal energy of a free particle with no internal degrees of freedom ($(3/2)kT$) should be equal at the boundary between the non-degenerate and degenerate layers. For the hottest model shown ($T_e = 1.6 \times 10^7\ {}^\circ K$), the cross is outside the range shown in the figure. The result of the present calculations shows that even for the hottest models degeneracy starts before we go inward by 100 meters from the surface, and that the non-degenerate layers are less than 1% in thickness for even the hottest models. The mass contained in the non-degenerate envelopes is practically zero. (We saw in the last chapter that the amount of mass contained even in the inner degenerate electron-ion envelopes is very small compared to the total stellar mass.) These results more than justify our previous assumption of constant mass and radius in the atmospheric calculations and also the neglect of non-degenerate layers in determining the total mass and radius of neutron stars in the previous chapter. Hot neutron stars with $T_e \sim 10^7\ {}^\circ K$ have non-degenerate envelopes of about 10 to 20 meters in thickness, but when the surface

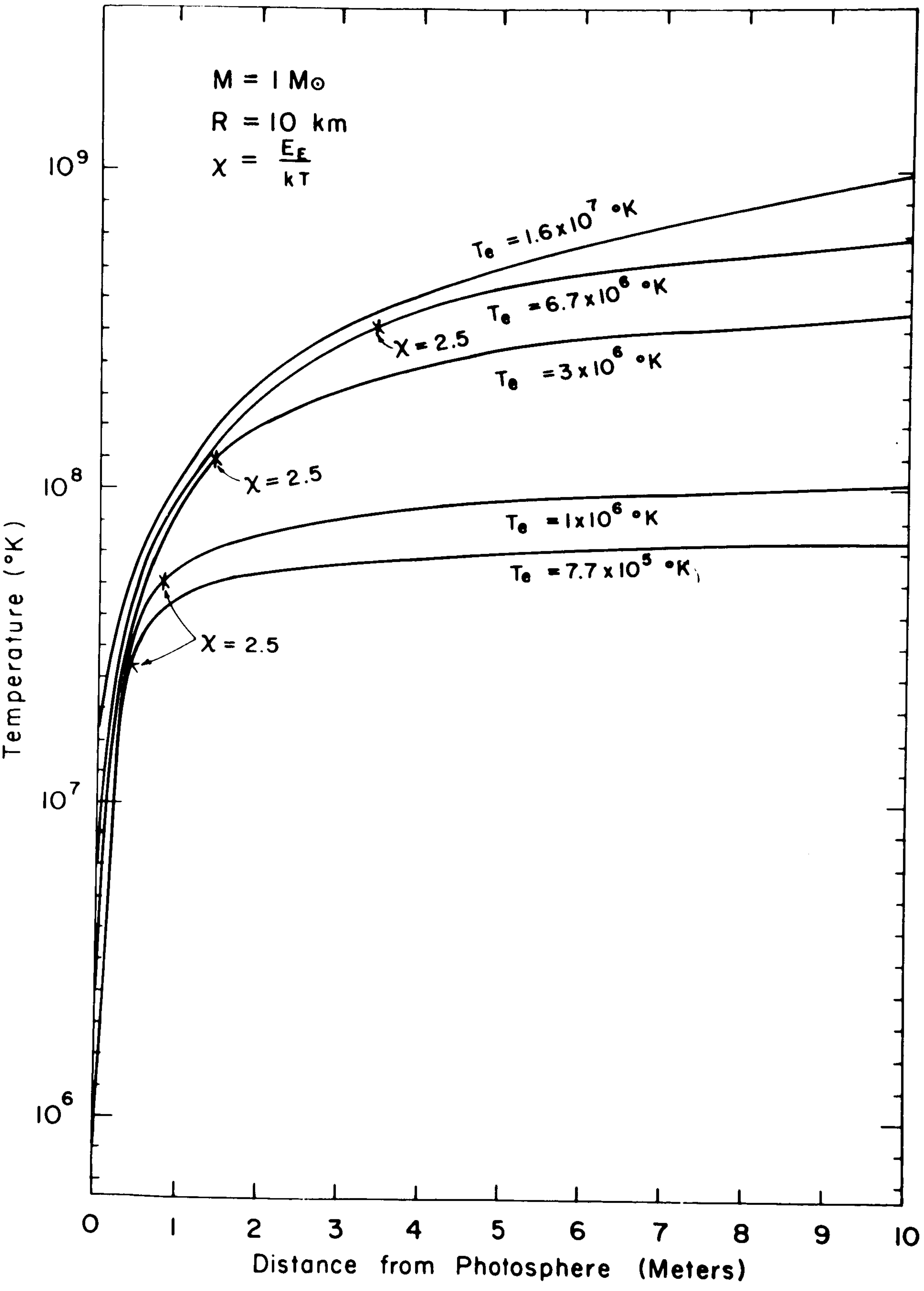
M = 1 M⊙
R = 10 km
χ = E_F / kT
10^9
10^8
10^7
10^6
Temperature (°K)
Te = 1.6 x 10^7 °K
Te = 6.7 x 10^6 °K
Te = 3 x 10^6 °K
Te = 1 x 10^6 °K
Te = 7.7 x 10^5 °K
χ = 2.5
χ = 2.5
χ = 2.5
0
1
2
3
4
5
6
7
8
9
10
Distance from Photosphere (Meters)

Figure 45

temperature falls to about a million degrees the thickness of the non-degenerate layers becomes about a meter or so. A typical neutron star with the sun's mass, a radius of 10 km and a surface temperature of 6.7×10^6 °K (about 100 times as bright as the sun) is shown to have non-degenerate envelopes of about 3 to 4 meters in thickness.

The density profile near the surface is plotted in Figure 46 for the same model. The distance from the surface is now shown by a cm-scale. This shows that within about a meter (0.01% of radius) from the photosphere the density rises to about 10^5 gm/cm^3 for cooler stars (when $T_e \sim 10^6$ K) and to about $10^{2.5}$ gm/cm^3 for hotter stars ($T_e = 1.6 \times 10^7$ °K). In the photosphere, the density rises within a thickness of 10 cm by a factor of about 100 for cooler models ($T_e \sim 10^6$ °K) and about 5 to 8 for hotter ones ($T_e = 1 \sim 2 \times 10^7$ °K). Such small scale heights may cause the diffusion process to become important.

The distribution of density, temperature and degree of degeneracy E_F/kT within the thin layers about 20 meters from the surface are numerically shown in Table 27 at several different interesting values of surface temperatures. On comparing Table 27 with Table 26, we see that the degeneracy criterion used in Table 26 (where the non-degenerate equation of state becomes equal to the degenerate one) agrees well with that used in Table 27 ($E_F/kT = 2.5$).

d. Diffusion, Convection, and the Composition of Envelopes

In Chapter II, it was concluded that the composition of the surface layers changes sharply from layer to layer near the surface. Starting from the boundary between the neutron core and the degenerate electron-ion envelopes, the composition

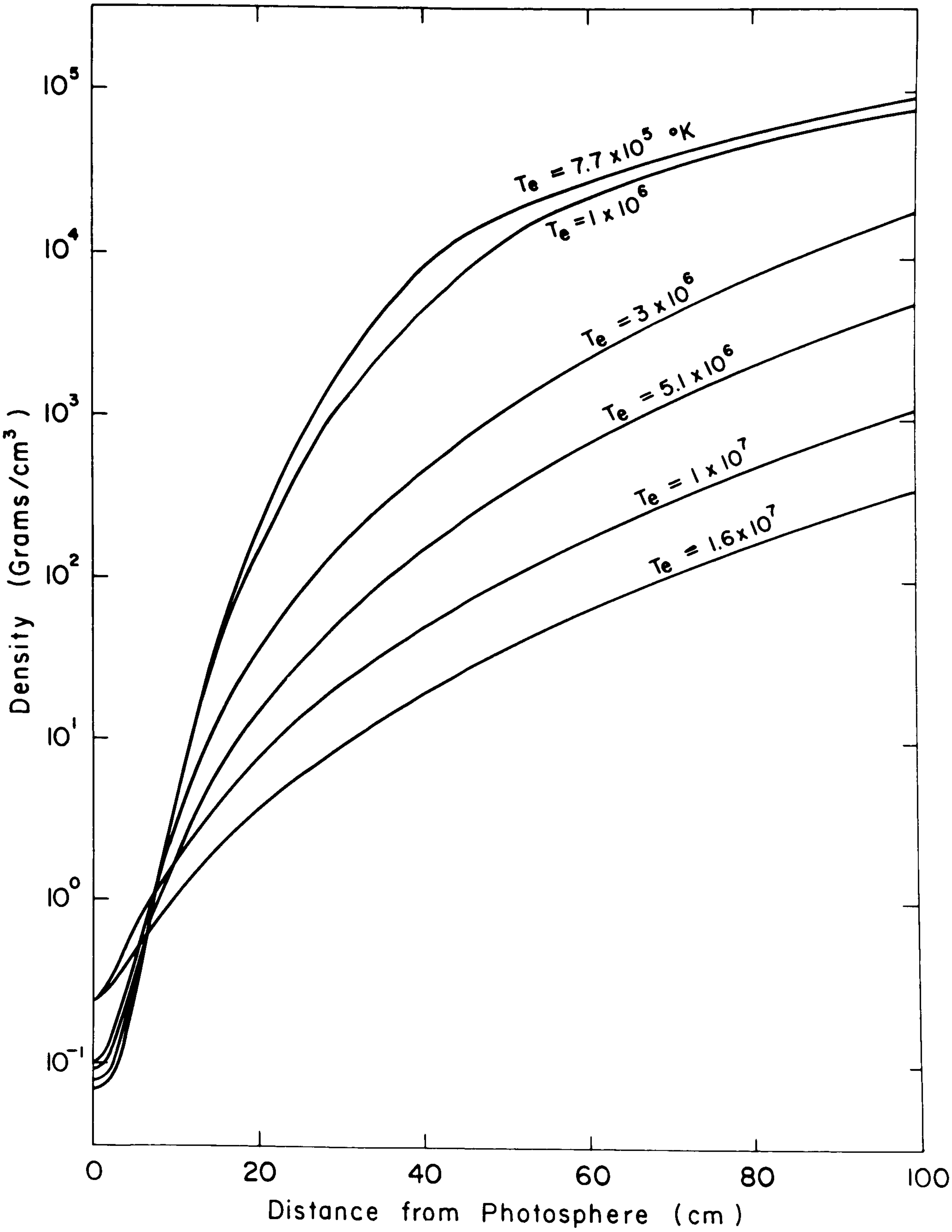
Density (Grams/cm^3)
10^5
10^4
10^3
10^2
10^1
10^0
10^{-1}
0
20
40
60
80
100
Distance from Photosphere (cm)
$T_e = 7.7 \times 10^5$ °K
$T_e = 1 \times 10^6$
$T_e = 3 \times 10^6$
$T_e = 5.1 \times 10^6$
$T_e = 1 \times 10^7$
$T_e = 1.6 \times 10^7$

Figure 46

TABLE 27. (Models with $M = 1\ M_\odot$, $R = 10$ km) Temperature and density distribution near the surface at different depths (R-r) at given surface temperature T_e. The point where $E_F/kT = 2.5$ indicates the thickness of the non-degenerate envelopes.

T_e(°K) / (R-r) (meters)	$T_e = 7.7 \times 10^5$ °K			$T_e = 3 \times 10^6$ °K			$T_e = 6.7 \times 10^6$ °K			$T_e = 1.6 \times 10^7$ °K		
	(gm/cm^3) log ρ	(°K) log T	E_F/kT	log ρ	log T	E_F/kT	log ρ	log T	E_F/kT	log ρ	log T	E_F/kT
0	-1.176	5.887	0.039	-1.095	6.477	0.0114	-0.854	6.826	0.0074	-0.605	7.204	0.0045
0.1	0.614	6.48	0.166									
0.2	2.317	7.002	0.63	1.55	7.23	0.118						
0.3	3.275	7.261	1.53									
0.4	3.888	7.432	2.765	2.637	7.565	0.284						
0.5	4.201	7.509	3.59				2.28	7.714	0.118	1.576	7.794	0.0332
0.6	4.430	7.561	4.61	3.337	7.734	0.564						
0.8												
1	4.930	7.661	7.66	4.286	7.931	1.564	3.42	7.97	0.376	2.558	8.028	0.0865
2	5.49	7.73	15.7	5.315	8.210	3.935	4.628	8.284	1.165	3.567	8.339	0.203
3				5.69	8.32	5.43	5.317	8.463	2.215	4.166	8.505	0.348
4				5.92	8.40	6.38	5.710	8.576	3.14	4.638	8.623	0.539
5	5.89	7.80	24.3	6.09	8.45	7.42	5.939	8.638	3.865	5.004	8.709	0.770
6							6.106	8.680	4.52	5.312	8.783	1.054
7				6.23	8.50	8.32						
8							6.27	8.74	5.04	5.784	8.902	1.673
9												
10	6.463	7.835	55	6.54	8.55	11.75	6.474	8.782	6.265	6.15	8.996	2.34

changes from more neutron-rich nuclei to less neutron-rich nuclei as we go outwards, as determined in Chapter II. In the outermost non-degenerate envelopes with $\rho < 10^6$ gm/cm^3, the main composition was found to be of ordinary iron group elements. This is why iron was chosen in the earlier opacity and atmospheric calculations.

As was mentioned in Chapter II, a possible change in the above result is caused by diffusion. We have just seen in the last subsection (c) how small the density scale heights are. Small scale heights and large gravity effects can make the diffusion process quite important.

Chiu and Salpeter$^{(22)}$ made the following estimates, regarding the surface composition of neutron stars: H and He on the surface go down to the interior and are burned up rapidly so that, consequently, these elements should be completely absent in neutron stars; carbon is probably strongly depleted in a neutron star about 1000 years old; O and Ne are depleted slightly, while Mg or any heavier elements remain unburned.

No quantitative investigation of the diffusion problem has been made (as far as I know), but qualitatively it is estimated that under the circumstances mentioned above, lighter elements such as Mg, O, and Ne, if present, are more probably the composition of the photosphere than is iron, due to a relatively fast diffusion process. If it is assumed that the O and Ne are appreciably depleted, then Mg is the most probable composition of the atmosphere of neutron stars. This is why not only Fe but also Mg was selected in the opacity and atmospheric calculations earlier. At the present time, the degree of importance of the diffusion effects is not known, but

I hope that this effect will be quantitatively accounted for in my models sometime in the future. At the present stage, it appears that the treatment applied in this research is adequate enough, because the uncertainties due to other causes may be more serious than the effect of diffusion on surface composition, as will be shown in more detail in subsequent sections.

The change of composition due to diffusion, however, does not occur if convective mass motions in non-degenerate layers cause efficient mixing of elements. In this case, the original statistical equilibrium composition of iron will be maintained. However, convection appears to play no important role in neutron stars. This is estimated as follows. The condition of stability against convection may be written as*

$$\left(\frac{\Delta \ln T}{\Delta \ln P}\right)_{\text{actual}} < \left(\frac{\Delta \ln T}{\Delta \ln P}\right)_{\text{adiabatic}} = \left(1 - \frac{1}{\Gamma_2}\right) \qquad (5\text{-}40)$$

Γ_2, an adiabatic exponent, is in general 5/3 for non-relativistic simple ideal gases, 4/3 for radiation or extremely relativistic gases, and varies between these limits in most general cases of stable matter. Γ_2 can locally become less than 4/3 quite often. An example is the hydrogen ionization zones in the outer layers of ordinary stars. Another example is a mixture of radiation and electron-positron pairs at extremely high temperatures and low densities.(70) In the outer envelopes of neutron stars, however, due to the high temperatures encountered there, the ionization effect on Γ_2 is likely to be negligible and Γ_2 will most probably not go appreciably below 4/3. In this case, the above inequality demands that

$$\left(\frac{\Delta \ln T}{\Delta \ln P}\right) < 0.25. \qquad (5\text{-}41)$$

---

*For instance, see reference 69 for the inequality relation and reference 70 for the equality relation of (5-40)

The quantity $(\Delta \ln T/\Delta \ln P)$ in my final six models of neutron stars has been calculated at different layers. As we go inwards from the photospheres $(\Delta \ln T/\Delta \ln P)$ was found to vary from about 0.1 to 0.15 at the photospheres, to about 0.2 to 0.24 just below the photospheres, and then to go to zero smoothly before we reach a point about 1 km below the surface. In no case was $(\Delta \ln T/\Delta \ln P)$ found to exceed 0.25. Even if the above inequality breaks down at a particular point in some other types of models it is not likely that this can occur in a region sufficiently extended to make convection important.

V-5 ENERGY CONTENT OF A NEUTRON STAR

If we assume that a neutron star belongs to the end state of a thermonuclear evolution, then there can be no energy generation within it. Any stable neutron star is already so dense that the gravitational energy due to contraction is not available. Even though the matter is highly degenerate, the only contribution to the total energy of the star comes from the small tail of the Fermi distribution function of the particles which constitute the star. This is evaluated by retaining the first two terms in the expansion of the energy density integral, the second equation of (3-26) in Chapter III, for a nearly zero-temperature ideal Fermi gas. The result obtained in reference 7 is quoted below.

$$\frac{C_v}{N} = \frac{\pi^2 k^2}{mc^2}\,\frac{(x^2+1)^{1/2}\,T}{x^2} \tag{5-42}$$

where

$$C_V = \left(\frac{\partial U}{\partial T}\right)_{N,V} \tag{5-43}$$

is the specific heat at constant volume, for a fixed number of particles, U is the total internal energy, and $x = p_F/mc$ is the relativistic parameter. The total thermal energy of the star U is then given in principle by carrying out the integration,

$$U = \int_0^T C_V(T)\,dT \tag{5-44}$$

The actual procedure adopted in this research is as follows: Noting that C_V depends linearly on T, we calculate the following quantity, the specific heat per particle per unit temperature, which is independent of temperature for all fermions present at a given point in the star:

$$\left(\frac{C_V}{NT}\right)_k = \frac{\pi^2 k^2}{m_k c^2}\,\frac{(x_k^2+1)^{1/2}}{x_k^2} \qquad \text{with} \quad x_k = p_k^F/m_k c \tag{5-45}$$

where m_k and $p^F{}_k$ are the mass and Fermi momentum of the component k. $p_k{}^F$ is expressible as a function of the number density of the kth particle, n_k. At each point in the star, $(C_V/NT)_k$ times the number density n_k of all components present are added together: This sum then expresses the total specific heat per unit volume per unit temperature at a particular point in the star. Due to the spherical symmetry of the star, the star's total specific heat per unit temperature is then obtained by carrying out the integration

$$\frac{C_V}{T} = \int_0^R \sum_k \left(\frac{C_V}{NT}\right)_k n_k\, 4\pi r^2\, dr \tag{5-46}$$

This quantity is independent of temperature, and is a constant for a model of a given mass and radius. Values of (C_V/T) for each of the six final models are listed in Table 19 in the c.g.s. system on a logarithmic scale.

The total energy U is obtained by integrating C_V over temperature, as in (5-44). Noting that (C_V/T) is independent of temperature, we get

$$U=\left(\frac{C_v}{T}\right)\int_0^T T\,dT=\left(\frac{C_v}{T}\right)\frac{T^2}{2} \qquad (5\text{-}44')$$

T in the above expression is the internal temperature of the isothermal core, which has been calculated in Section V-4b for all six models (Figure 43 and 44) for both pure iron atmospheres and pure Mg atmospheres. The energy content of our six final models at various different ages (different surface temperatures) has been computed in this manner for Fe and Mg. That for Fe is plotted in Figure 47 in terms of the surface temperature.

It is seen that as the surface temperature of a star decreases from about 5×10^7 °K to 10^4 °K the energy content of the star decreases from about 10^{50} ergs to 10^{40} ergs, although the precise value depends on the type of model in question.

In the above calculations the thermal energy of all components present (ground and first excited states of nucleons, the ground states of hyperons, muons and electrons) are included.

It may be worthwhile to comment at this point that the above discussion does not exhaust all possible contributions to the total energy content of the star. This is because in the above derivation of specific heats, E in (3-26) and (3-27) is the kinetic energy only and the potential energy has been left out.

The effect of the potential term is taken into account as follows. Let us define the reduced mass, m*, as(71)

$$\frac{1}{m^*}=\frac{1}{m}+\frac{1}{P_F}\left(\frac{dV(P)}{dP}\right)_{P_F} \qquad (5\text{-}47)$$

where v is the potential energy per particle. Then, rather than using $(C_V/NT)_k$, we multiply $(C_V/TN)^*_k$ as defined below by n_k, sum over all k and integrate

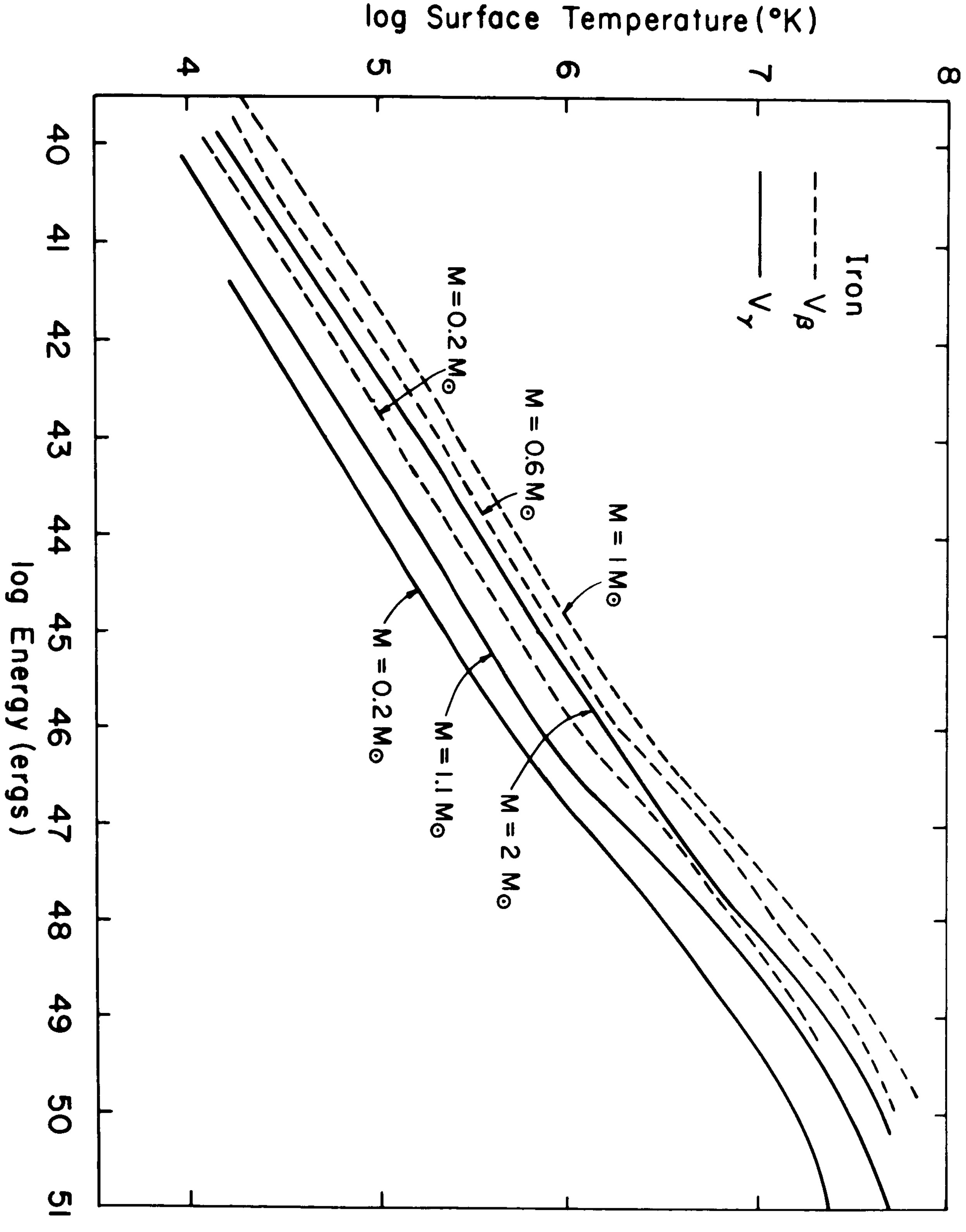
log Surface Temperature (°K)
4
5
6
7
8
log Energy (ergs)
40
41
42
43
44
45
46
47
48
49
50
51
Iron
V_β
V_γ
M = 0.2 M⊙
M = 0.6 M⊙
M = 1 M⊙
M = 0.2 M⊙
M = 1.1 M⊙
M = 2 M⊙

Figure 47

over the total volume in (5-46) to get the total energy.

$$\left(\frac{C_V}{TN}\right)^{*}_{k} = \frac{\pi^2 k^2}{m^{*}_{k} c^2}\left(\frac{(x_k^2+1)^{1/2}}{x_k^2}\right) = \left(\frac{C_V}{NT}\right)^{0}_{k}\left(\frac{m}{m^{*}}\right) \qquad (5\text{-}45')$$

where $(C_V/NT)^{0}_{k}$ is the original unmodified expression.

The second term in (5-47) is evaluated as follows: Because the Levinger-Simmons potentials introduced in Chapter III are functions of both the separation distance r and the momentum p, and (dP/dP_F) is 1 at the top of the Fermi sea we have

$$\frac{1}{P_F}\left(\frac{dV(P)}{dP}\right)_{P_F} = \frac{1}{P_F}\left[\left(\frac{\partial V(P,r)}{\partial r}\frac{dr}{dp}\right)_{P_F} + \frac{dV(k_f)}{dk_f}\frac{dk_f}{dP_F}\right] \qquad (5\text{-}48)$$

The potential V_β introduced in Chapter III is a square-well potential with a finite range and with a Yukawa tail outside this range. For the densities we are interested in (those within a neutron star), the interparticle distance r is less than the range of the nuclear forces (that is, inside the well), dv/dr in the above equation is 0, and

$$\frac{1}{P_F}\left(\frac{dV(P)}{dP}\right)_{P_F} = \frac{1}{P_F}\frac{dV(k_f)}{dk_f}\frac{dk_f}{dP_F} \qquad (\text{for } V_\beta) \qquad (5\text{-}47')$$

This simple expression, however, does not apply for V_γ, because V_γ has a complicated dependence on r, and dv/dr is not zero even for small r.

Due to the difficulty in evaluating the term $\frac{1}{P_F}\left(\frac{dV(P)}{dP}\right)_{P_F}$ for V_γ, the above correction has been applied in the case of V_β only. Values of the modified expression $(C_V/T)^*$ on a logarithmic scale for three models of type V_β are listed in Table 19. For the heaviest model, $(V_\beta, 1\ M_\odot)$, the total energy content is increased by a factor of 2: for the lightest model (V_β, $0.2M_\odot$) it is decreased by a factor of 1.3, and for the medium weight model (V_β, $0.6\,M_\odot$) it is increased by a factor of 1.2. This is because the nuclear potential is attractive, that is, negative, in the major part of the lightest star, and m/m^* in (5-45') is consequently less than 1, as can be seen from (5-47), thus making $(C_V/T)^*$ and the modified energy smaller than the original unmodified quantities. We note that for this model, the central density is $10^{15.2}$ gm/cm^3, and mean density is less than 10^{15} gm/cm^3, and an attractive, negative potential is dominant in this region of density. On the other hand, the medium weight and the heaviest model of type V_β selected above have the central densities $10^{15.6}$ and $10^{15.9}$ gm/cm^3 respectively, and in both of these the density is constant throughout the major part of the volume. Therefore, the repulsive, positive potential term is dominant in this case, $(m/m^*) > 1$, and the over-all energy content is increased. Even though numerical calculations have not been carried out for V_γ, it is possible to make a qualitative estimate of the correction due to the potential term. The central densities of V_γ type models are lower than those of V_β type models in general. For V_γ, $\log \rho^c$ of the lightest model is 14.2 and that of the heaviest model is 15.4. We expect that the potential is negative in most parts of the model (V_γ, $0.2\,M_\odot$), slightly negative for the model (V_γ, $1.1\,M_\odot$), while it is expected to be slightly positive and repulsive in the major part of the model (V_γ, $2\,M$). $\triangle(Cv/T)$ $\left(= \dfrac{(Cv/T)^*-(Cv/T)}{(Cv/T)}\right)$ for the lightest, intermediate and heaviest models of type V_γ is estimated to be roughly - 50%, - 20% and + 20%, respectively.

The above correction for the interaction potential, however, turns out to be rather small and unimportant in our final results (Section V-7) as compared with the corrections required for some other effects, for instance, that for the URCA neutrino process in the next section.

V-6 LUMINOSITY

We expect that a neutron star cools off rapidly, starting right after its formation at an extremely high temperature (say, 10^{10-11} °K), first by neutrino energy dissipation, and then after it has cooled down to about 10^9 °K, through optical radiation from the still hot surface. The energy loss rate due to these two mechanisms is calculated in this section.

a. Optical Luminosity

The optical luminosity of the star, L_{ph}, is related to its radius and its effective temperature through the simple equation (5-32). We see, therefore, that L_{ph} varies among different models (different R) of different ages (different T_e). The results are shown in Tables 28-33 for our six models (V_β I, V_β II, V_β III, V_γ I, V_γ II, and V_γ III) at different surface temperatures ranging from the highest value, 5×10^7 °K, to the lowest value, $1 \sim 2 \times 10^4$ °K. To visualize these values more clearly, let us go back to Table 25 in Section V-3. For a neutron star of radius about 10 km, it is seen that the optical luminosity changes from about 10^6 times solar luminosity at $T_e = 5 \times 10^7$ °K to about $10^{-7.5}$ times solar luminosity at $T_e = 2 \times 10^4$ °K, and that a star as luminous as the sun has a surface temperature of about 1 to 2 million degrees and an internal temperature of about 10^8 °K. A neutron star of R = 5-6 km has $L_{ph} = 10^{5.6} L_\odot$ at $T_e = 5 \times 10^7$ °K, and $L_{ph} \cong 10^{-8} L_\odot$ at $T_e = 2 \times 10^4$ °K.

TABLE 28. Atmospheres of model (V_β, I); $M = 0.939\ M_\odot$, $R = 4.333$ km, $\Delta\lambda/\lambda = 0.235$. (Photon luminosity L_{ph}, plasma neutrono luminosity L_ν, core temperature T_c, total energy U, maximum wave length with red shifts λ_{max}, and cooling time τ, as a function of T_e, are listed. $\Delta\lambda/\lambda$ is the red shift.)

T_e (°K)	log L_{ph} (ergs/sec)	log L_ν (ergs/sec)	log T_c (°K)		log U (ergs)		λ_{max} (Å)	log τ (years)	
			Fe	Mg	Fe	Mg		Fe	Mg
5×10^7	39.0169	44.86	9.9881	9.9787	49.3563	49.3375	0.75	-3.7	-3.3
2×10^7	37.4251	38.92	9.4089	9.3068	48.1979	47.9937	1.88	0.89	1.38
1×10^7	36.2210	34.82	9.0139	8.8724	47.4079	47.1249	3.75	3.41	3.45
5×10^6	35.0169	31.25	8.6846	8.4890	46.7493	46.3581	7.50	4.355	4.08
2×10^6	33.4251	–	8.1913	8.0773	45.7627	45.5347	18.75	5.14	4.67
1×10^6	32.2210	–	7.7127	7.6264	44.8043	44.6329	37.50	5.54	5.26
5×10^5	31.0169	–	2.7645	7.1736	43.9091	43.7273	74.96	5.955	5.71
2×10^5	29.4252	–	6.5963	6.5542	42.5727	42.4885	187.5	6.424	6.092
1×10^5	28.2211	–	6.1520	6.0937	41.6841	41.5675	375.0	6.727	6.404
5×10^4	27.0170	–	5.6728	5.5649	40.7257	40.5099	749.6	6.954	6.701
2×10^4	25.4252	–	5.0349	–	39.4499	–	1875	7.127	7.028

TABLE 29. Model (V_β, II); $M = 0.5992\ M_\odot$, $R = 5.658$ km, $\Delta\ \lambda/\lambda = 0.156$.
(Symbols are the same as those in Table 28)

T_e (°K)	Log L_{ph} (ergs/sec)	log L_ν (ergs/sec)	log T_c (°K)		log [U(ergs)]		λ_{max} (Å)	log τ (years)	
			Fe	Mg	Fe	Mg		Fe	Mg
5×10^7	39.1538	47.23	10.2516	10.4603	49.8191	50.2365	0.675	~ -7	~-6
2×10^7	37.5627	42.18	9.5976	9.5092	48.5111	48.3343	1.686	-1.36	-0.395
1×10^7	36.3579	37.26	9.1803	9.0662	47.6765	47.4483	3.373	2.21	3.101
5×10^6	35.1538	33.49	8.8289	8.6510	46.9737	46.6179	6.746	4.26	4.454
2×10^6	33.5621	29.2	8.3778	8.2099	46.0715	45.7357	16.86	5.208	5.024
1×10^6	32.3580	-	7.9293	7.8502	45.1745	45.0163	33.73	5.717	5.328
5×10^5	31.1539	-	7.4726	7.3638	44.2611	44.0435	67.46	6.148	5.825
2×10^5	29.5621	-	6.7953	6.7608	42.9065	42.8375	168.6	6.604	6.298
1×10^5	28.3580	-	6.3521	6.3056	42.0201	41.9271	337.3	6.871	6.589
5×10^4	27.1539	-	5.8850	5.7990	41.0859	40.9139	674.6	7.111	6.886
2×10^4	25.5622	-	5.2634	-	39.8427	-	1686.2	-	7.244

TABLE 30. Model (V_β, III); $M = 0.1926\ M_\odot$, $R = 10.09$ km, $\frac{\Delta\lambda}{\lambda} = 0.0282$.

(Symbols are the same as those used in Table 28.)

T_e (°K)	Log L_{ph} (ergs/sec)	Log L_ν (ergs/sec)	Log T_{in}(°K)		Log [U (ergs)]		λ_{max} (Å)	log τ (years)	
			Fe	Mg	Fe	Mg		Fe	Mg
2×10^7	38.0645	45.31	10.0223	10.0223	49.1514	49.0134	1.500	-4.27	-3.89
1×10^7	36.8604	41.78	9.5736	9.4813	48.2540	47.9314	3.000	-1.86	-0.95
5×10^6	35.6563	38.21	9.1570	9.0392	47.4208	47.0472	6.000	0.902	2.36
2×10^6	34.0640	33.75	8.7057	8.5109	46.5182	45.9906	15.00	4.553	4.49
1×10^6	32.8005	30.01	8.3510	8.1939	45.8160	45.3566	30.00	5.656	5.061
5×10^5	31.0564	–	7.8990	7.8215	44.9048	44.6118	60.00	6.281	5.598
2×10^5	30.0646	–	7.2957	7.2024	43.6982	43.3736	150.0	6.744	6.49
1×10^5	28.8605	–	6.7651	6.7355	42.6370	42.4398	300.0	7.088	6.655
5×10^4	27.6564	–	6.3248	6.2789	41.7564	41.5266	600.04	7.308	6.963
2×10^4	26.0647	–	5.7052	–	40.5172	–	1500.1	–	7.326
1×10^4	24.8006	–	–	5.0936	–	39.1560	3000.3	–	7.598

TABLE 31. Model (V_γ I); M = 1.9765 $M_\odot$, R = 9.686, $\Delta\lambda/\lambda$ = 0.301. (Symbols are the same as those used in Table 28.)

T_e (°K)	log L_{ph} (ergs/sec)	log L_ν (ergs/sec)	log T_{in} (°K)		log U (ergs)		λ_{max} (Å)	log τ (years)	
			Fe	Mg	Fe	Mg		Fe	Mg
5 x 10^7	39.6208	46.75	10.1015	10.1371	50.0446	50.1158	0.759	~-5	-5.25
2 x 10^7	38.0290	40.988	9.4999	9.3988	48.8414	48.6392	1.898	-0.37	0.388
1 x 10^7	36.8247	37.24	9.0888	8.9006	48.1192	47.7628	3.794	2.948	3.238
5 x 10^6	35.6208	33.38	8.7528	8.5625	47.3472	46.9666	7.591	4.338	4.03
2 x 10^6	34.0291	~ 24	8.2760	8.1397	46.3936	46.1210	18.98	5.127	4.72
1 x 10^6	32.8249	-	7.8077	7.7335	45.4570	45.3086	37.94	5.508	5.18
5 x 10^5	31.6208	-	7.3620	7.2624	44.5056	44.3064	75.9	6.001	5.604
2 x 10^5	30.0261	-	6.6845	6.6506	43.2146	43.1428	189.8	6.388	6.048
1 x 10^5	28.8250	-	6.2467	6.1957	42.3350	42.2330	379.4	6.774	6.348
5 x 10^4	27.6209	-	5.7720	5.6727	41.3856	41.1970	759.1	6.998	6.655
2 x 10^4	26.0291	-	5.1493	-	40.1402	-	1898	7.156	6.95

TABLE 32. Model (V_{γ} II); $M = 1.1055\ M_{\odot}$, $R = 13.032$ km; $\frac{\Delta \lambda}{\lambda} = 0.125$.
(Symbols are the same as those used in Table 28.)

T_e (°K)	log L_{ph} (ergs/sec)	log L_{ν} (ergs/sec)	log T_{in} (°K)		log U (ergs)		λ_{max} (Å)	log τ (years)	
			Fe	Mg	Fe	Mg		Fe	Mg
5×10^7	39.8785	48.8281	10.5691	-	50.9876	-	0.6566	-	-5.4
2×10^7	38.2867	44.1172	9.7680	9.7118	49.3954	49.2820	1.641	-2.788	-2.71
1×10^7	37.0826	40.0833	9.3485	9.2459	48.5564	48.3502	3.283	0.088	0.855
5×10^6	35.8785	36.0542	8.9645	8.8140	47.7884	47.4864	6.566	3.516	3.903
2×10^6	34.2867	31.7498	8.5378	8.3355	46.9368	46.5294	16.41	5.001	4.808
1×10^6	33.0826	-	8.1317	8.0292	46.4228	45.9168	32.33	5.898	5.431
5×10^5	31.8785	-	7.6528	7.5562	45.4650	44.9708	65.66	6.516	6.003
2×10^5	30.2368	-	7.0251	6.9619	44.2096	43.7822	164.1	7.048	6.499
1×10^5	29.0827	-	6.5336	6.4923	43.2266	42.8430	328.3	7.363	6.77
5×10^4	27.8786	-	6.0347	6.0201	42.3288	41.8986	656.6	7.698	7.083
2×10^4	26.2868	-	5.4511	-	41.0616	-	1641.3	8.003	7.403
1×10^4	25.0827	-	-	4.8043	-	39.4670	3283	-	7.63

TABLE 33. Model ($V_\gamma III$); $M = 0.2150\ M_\odot$, $R = 24.154$ km, $\frac{\Delta\lambda}{\lambda} = 0.0131$.
(Symbols are the same as those used in Table 28)

T_e (°K)	log L_{ph} (ergs/sec)	log L_ν (ergs/sec)	log T_{in} (°K)		log U (ergs)		λ_{max} (Å)	log τ (years)	
			Fe	Mg	Fe	Mg		Fe	Mg
2×10^7	38.8227	45.74	10.4108	-	50.4778	-	1.478	-4.9	-4.46
1×10^7	37.6186	43.999	9.8275	9.7873	49.3111	49.2308	2.956	-2.34	-2.55
5×10^6	36.4145	42.03	9.4039	9.3018	48.4640	48.2598	5.913	-0.78	-0.298
2×10^6	34.8227	36.81	8.8997	8.7365	47.4556	47.3292	14.78	2.47	3.203
1×10^6	33.6186	33.69	8.5800	8.3767	46.8162	46.4096	29.56	5.098	5.29
5×10^5	32.4145	28.1	8.1865	8.0736	46.0292	45.8034	59.13	6.326	5.998
2×10^5	30.8228	-	7.5703	7.4637	44.7968	44.5836	147.8	7.14	6.601
1×10^5	29.6186	-	7.0965	7.0207	43.8492	43.6976	295.6	7.561	7.078
5×10^4	28.4145	-	6.5901	6.5484	42.8364	42.7530	591.3	7.948	7.441
2×10^4	26.8228	-	5.9904	-	41.6370	-	1478.1	8.368	7.728
1×10^4	-	-	-	5.4020	-	40.4602	2956	-	7.826

Optical luminosity is plotted against internal energy for the model (2 $M_\odot$, V_γ) in Figure 48 (the curves marked "Optical"). The solid curve corresponds to an atmosphere of iron and the dashed curve to one of Mg. Similar curves have been obtained for the rest of the models also. Such graphs are very useful in obtaining the cooling curves, as seen in Section V-7.

b. Neutrino Luminosity

The universal Fermi interaction predicts that an electron could radiate a neutrino pair as well as electromagnetic radiation.(72) Even though the probability for the neutrino radiation is enormously small, it plays an extremely important role in some stages of stellar evolution, because of the fact that the neutrino mean free path is so large that it could escape even from a dense star with hardly any interaction, while electromagnetic radiation can only diffuse out very slowly from the interior to the surface. In a very hot neutron star ($T_{in} > 10^9$ °K), the cooling through neutrino radiation is found to be much faster than that through electromagnetic radiation, as seen in detail in Section V-7. Various different neutrino processes possible in a stellar interior have been proposed. These are,(73,74) assuming that temperature is not too high ($T < 10^{10}$ °K):

(i) $\gamma + e^- \rightarrow e^- + \nu_e + \bar{\nu}_e$ (Photoneutrino process)

(ii) $\gamma + \gamma \rightleftarrows e^- + e^+ \rightarrow \nu_e + \bar{\nu}_e$ (pair annihilation process)

(iii) γ (Plasmon) $\rightarrow \nu_e + \bar{\nu}_e$ (plasma process)

(iv) $\begin{cases} e^- + (Z, A) \rightarrow (Z-1, A) + \nu_e \\ (Z-1, A) \rightarrow (Z, A) + e^- + \bar{\nu}_e \end{cases}$ (URCA process) (5-49)

(v) $e^- + (Z, A) \rightarrow e^- + (Z, A) + \nu_e + \bar{\nu}_e$ (Bremsstrahlung)

(vi) γ + Coulomb field $\rightarrow \nu_e + \bar{\nu}_e$ (photonuclear process)

(vii) $\gamma + \gamma \rightarrow \gamma + \nu_e + \bar{\nu}_e$ (photon collisions)

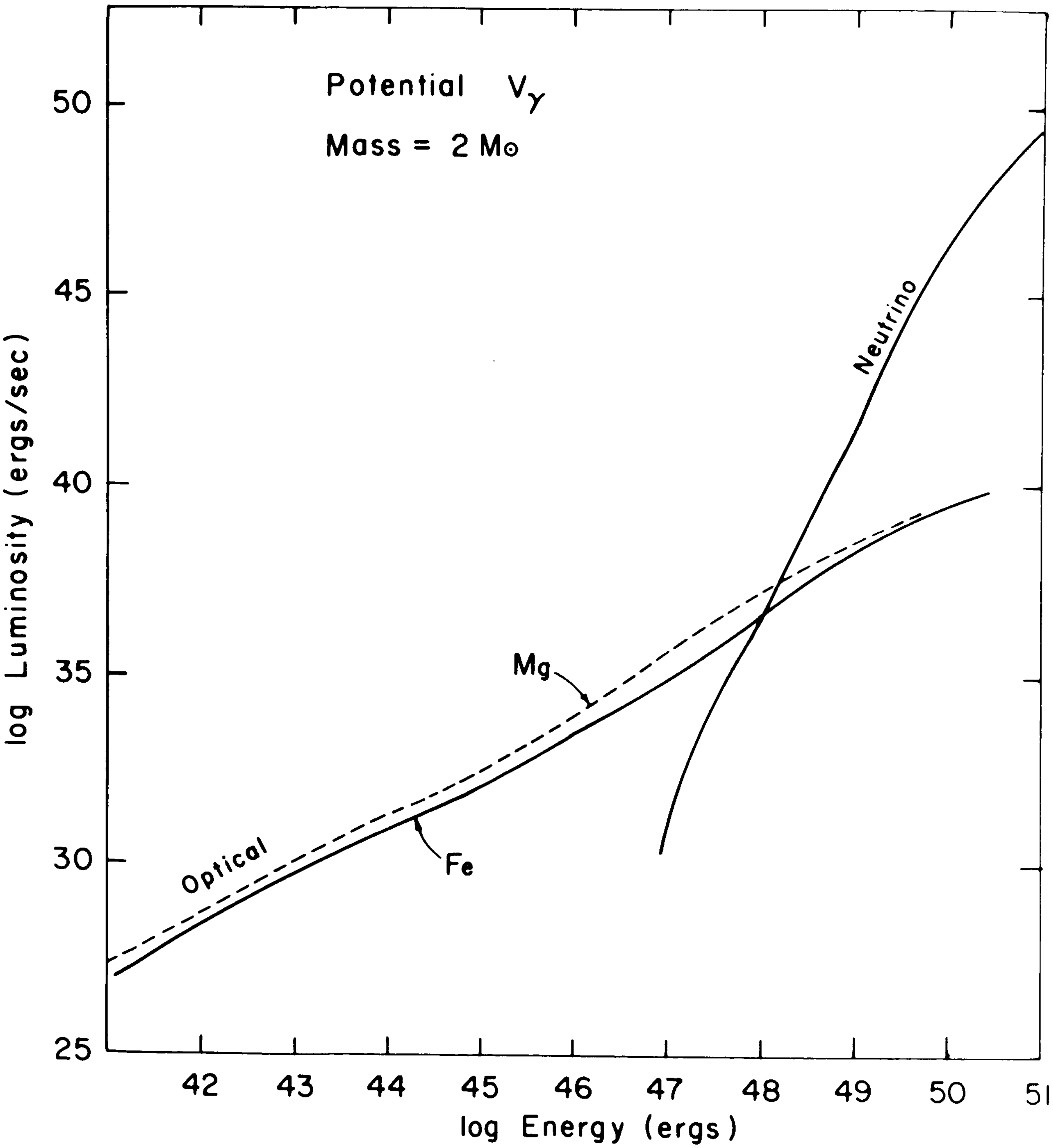
Potential V_γ
Mass = 2 M⊙
log Luminosity (ergs/sec)
50
45
40
35
30
25
42
43
44
45
46
47
48
49
50
51
log Energy (ergs)
Neutrino
Mg
Optical
Fe

Figure 48

Depending on the particular density-temperature combination we encounter, some of these dominate over others, but generally in astrophysics the first four (i-iv) are more important than the last three (v-vii). In relatively low temperature-density regions ($T \lesssim 5 \times 10^{8}\ {}^{\circ}K$, $\rho < 10^{5}\ gm/cm^{3}$) the photo neutrino process is dominant, in the high temperature and low density region ($T > 10^{9}\ {}^{\circ}K$, $\rho < 10^{7}\ gm/cm^{3}$) the pair annihilation process dominates over the rest, while in high density-temperature regions ($\rho > 10^{6}\ gm/cm^{3}$, $T \gtrsim 8 \times 10^{8}\ {}^{\circ}K$) most of these processes are suppressed due to the paucity of empty electron states and usually only the plasma neutrino process remains. The URCA process plays an important role only under special circumstances such as during the dynamic collapse of a star. In a diagram in reference 75, the temperature-density plane is divided into several regions, inside each of which one of the first three processes in (5-49) dominates. According to such diagrams (and also from discussions given in references such as 74) the plasma neutrino process is expected to be the most important mechanism in the cooling of hot neutron stars ($10^{10} \gtrsim T \gtrsim 10^{9}\ {}^{\circ}K$, $\rho > 10^{6}\ gm/cm^{3}$). Let us, therefore, look into this process in somewhat more detail.

The neutrino-pair decay of a free photon is usually forbidden by the energy-momentum conservation law (when $\omega^{2} \leq k^{2}$), but inside an electron gas, the electromagnetic radiation has a spectrum of the form

$$\omega^{2} = \omega_{o}^{2} + k^{2} \tag{5-50}$$

and for $\omega^{2} > k^{2}$, such waves, when quantized, behave like relativistic particles (called "plasmons") of rest mass ω_{o} each of which can decay into a pair. A similar argument applies both to transverse and longitudinal plasmons. In (5-50), k is the wave vector and ω_0, called "plasma frequency," is given by

$$\omega_0^2 = 4\pi e^2 \int d^3\bar{p}\, \frac{f(\bar{p})}{E_p}\left(1 - \frac{1}{3}\frac{\bar{p}^2}{E_p^2}\right) \tag{5-51}$$

where $f(\bar{p})$ is the momentum distribution function for the electrons and

$$E_p = (p^2 + m_e^2)^{1/2} \tag{5-52}$$

For a degenerate Fermi gas, (5-51) reduces to

$$\omega_0^2 = 4e^2 p_F^3 / (3\pi E_F) \tag{5-51'}$$

where p_F is the Fermi momentum and E_F is the Fermi energy

$$E_F = (p_F^2 + m_e^2)^{1/2}$$

Noting that p_F is related to density through

$$p_F = \left[3\pi^2 n_e(\rho)\right]^{1/3} \tag{5-53}$$

we see that ω_0 is fixed for a given ρ or n_e.

The neutrino-pair emission rates per unit volume from transverse and longitudinal plasmons are given in reference 74 as

$$Q_t = 2g^2(3\pi e^2)^{-1}(2\pi)^{-3}\omega_0^6 \sum_{n=1}^{\infty}\int_0^{\infty} \exp(-n\beta\omega)\, k^2\, dk \tag{5-54}$$

$$Q_\ell = \frac{g^2}{3\pi e^2}\,\frac{1}{(2\pi)^3}\,\frac{1}{\exp(\omega_0\beta)-1}\int_0^{\omega_0} dk\, k^2(\omega_0^2 - k^2)^3 \tag{5-55}$$

where $g = 3.08 \times 10^{-12}\, m_e$ is the weak coupling constant, e is the electronic charge and $\beta = (kT)^{-1}$. (5-56)

It should be noted that throughout the above discussion the system of units where $c = \hbar = 1$ has been adopted. The above equations reduce to the following, simpler, forms in c.g.s units:(74)

$$Q_t(\mathrm{ergs/cm^3\text{-}sec}) = 2.96\times10^{22}\, y^6 z^3 \quad (\text{if } \hbar\omega_0 \ll kT)$$
$$= 1.54\times10^{22}\, y^{7.5} z^{1.5}\, e^{-x} \quad (\text{if } \hbar\omega_0 \gg kT) \qquad \text{(5-54')}$$

$$Q_\ell(\mathrm{ergs/cm^3\text{-}sec}) = 3.15\times10^{20}\, y^9 (e^x - 1)^{-1} \qquad \text{(5-55')}$$

where $x = \frac{\hbar\omega_0}{kT} = \omega_0\beta$, $y = \frac{\hbar\omega_0}{m_e c^2} = 6.63\times10^{-12}[n_e(\mathrm{cm^{-3}})]^{1/3}$, (5-57)

$$z = \frac{kT}{m_e c^2} = \frac{T_9}{5.94} \quad \text{where } T_9 \equiv T(^\circ K)/10^9$$

Q_t and Q_ℓ were calculated first, for various different values of electron number density n_e and T, in the range of 10^{24} cm^{-3} $< n_e < 10^{40}$ cm^{-3} and 10^6 °K $< T < 4\times10^{10}$ °K. When $\hbar\,\omega_0 \sim kT$, neither of the approximations in (5-54') apply. Therefore, Q_t has been plotted against n_e at each given T in each of the two limits $x \ll 1$ and $x \gg 1$, and the intermediate region has been interpolated smoothly by hand on the graph. Q_ℓ turns out to be negligible as compared with Q_t throughout the range considered. This result is shown in Figure 49. The number attached to each curve is the corresponding temperature. The decay rate of plasmons at a given temperature T increases with an increase in density at first, but eventually it decreases when extremely high densities are reached, as is to be expected (a maximum at around $\rho \sim 4\times10^{10}\, T_9$ (for $\mu_e \sim 2$)). We see from the above that the emissivity is a function of density only for a given temperature. Therefore, in the isothermal core of neutron stars, Q is fixed at a given density (that is, at a given radial distance from the center). The total neutrino energy loss rate (or neutrino luminosity), L_ν, can therefore be obtained by carrying out the following integration from the center to the surface of the star:

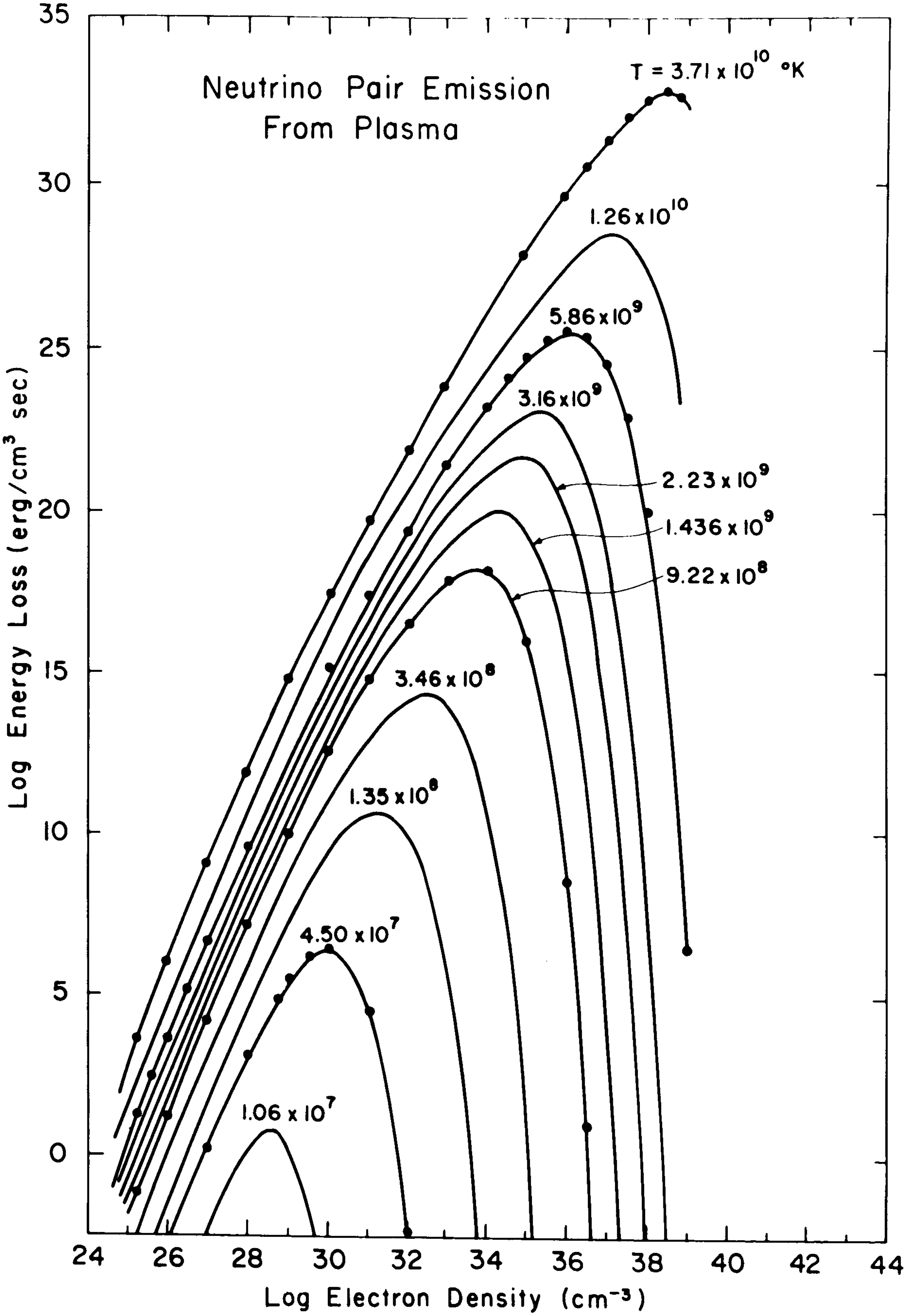
Neutrino Pair Emission
From Plasma
T = 3.71 x 10^10 °K
1.26 x 10^10
5.86 x 10^9
3.16 x 10^9
2.23 x 10^9
1.436 x 10^9
9.22 x 10^8
3.46 x 10^8
1.35 x 10^8
4.50 x 10^7
1.06 x 10^7
Log Energy Loss (erg/cm³ sec)
Log Electron Density (cm⁻³)
35
30
25
20
15
10
5
0
24
26
28
30
32
34
36
38
40
42
44

Figure 49

$$L_\nu = \int_0^R Q(\mathrm{ergs/cm^3\text{-}sec})\, 4\pi \left[r(\mathrm{cm})\right]^3 dr \,;\; Q = Q_t + Q_\ell \qquad (5\text{-}58)$$

In above calculations, n_e, rather than ρ, has been used as a free parameter to represent density, because in the process of converting n_e to ρ we must know the exact composition of each layer in the star. It seems that the assumption $(A/Z) = 2$ has customarily been employed in other papers$^{(74)}$ for this purpose. This assumption is correct for He^4, O^{16}, etc., and is not a bad approximation for heavy elements such as Fe^{56}. However, it is seriously wrong to make this assumption for the neutron core and also for the outer layers where the composition changes very sharply from layer to layer. We have seen in Chapter II how the mean value of A/Z deviates from 2 in high density regions. The core integration program in Chapter IV has been constructed so that at each r, the corresponding n_e, ρ and other interesting physical quantities, can be calculated. By slightly modifying the computer program, the integration (5-58) can be carried out without trouble. That is, the input table listing Q as a function of n_e and T is first constructed from Figure 49, then at each point r, the desired value of Q is computed from the input table just prepared and the interpolation subroutine, and the 7094 computer is instructed to carry out the integration (5-58) step-by-step. n_e is fixed at a given r while T is maintained constant throughout a star at a given age (note that the outermost non-degenerate layers do not contribute to the integral). Neutrino luminosity L_ν has been calculated in this manner for several interesting temperatures ranging between 10^{10} °K and 10^7 °K for each of the six models of the V_β or V_γ type. The result is shown in the third column of Tables 28-33. The values of L_ν when $L_\nu <<< L_{ph}$ (optical) are not shown. In all cases L_ν is negligible as compared with L_{ph} for $T \lesssim 10^8$ °K. Neutrino luminosity is plotted against total energy content on a logarithmic scale for the model (V_γ, 2 $M_\odot$) in Figure 48. Similar graphs are plotted for five other models also. The results are:

(i) At the highest temperature considered (10^{10} °K) neutrino luminosity is about $10^{6 \sim 7}$ times the optical luminosity, (ii) at $T \sim 5 \times 10^9$ °K $L_\nu \sim 10^5\ L_{ph}$, (iii) at $T \sim 3 \times 10^9$ °K $L_\nu \sim 10^{3 \sim 4}$ times L_{ph}, (iv) optical and neutrino luminosity become more or less comparable at slightly less than a billion degrees, (v) neutrino luminosity becomes negligible as compared with the optical luminosity for $T < 5 \times 10^8$ °K, (vi) the detailed properties, however, depend on the different types of model. For instance at the same internal temperature it appears that larger neutrino luminosities are associated with the heavier models, and that for a given weight and temperature the luminosities are, in general, greater for V_γ type models than for V_β type models (Tables 28-33). (vii) As the internal temperature decreases from about 10^{10} °K to 5×10^8 °K, the neutrino luminosity goes down from about $10^{45 \sim 47}$ to $10^{31 \sim 34}$ ergs/sec, depending on the type of model. (viii) For typical hot neutron stars of surface temperature about 2×10^7 °K, neutrino luminosity is about $10^{3 \sim 5}$ times optical luminosity or about $10^{7 \sim 9}$ times the solar luminosity. (ix) When the surface temperature goes down to about 10^7 °K, L_ν goes down to about $10^{3 \sim 4}\ L_\odot$.

After the above calculations had been completed, the following improved approximation formula for Q_t due to Inman and Ruderman(76) became available:

$$Q_t = 1.228 \times 10^{22}\left(\frac{\hbar\omega_0}{m_e c^2}\right)^9 F(x) \quad \text{where } F(x) = \sum_{n=1}^{\infty}\frac{K_2(nx)}{nx} \quad \text{or}$$

$$x^3F(x) = 2\zeta(3) + \frac{1}{2}x^2 \ln x - \frac{1}{4}(2\ln 2 + 1)x^2 + \frac{x^4 \ln x}{96} - \frac{1}{96}\left(\ln 2 - \frac{1}{4} + \ln 2\pi - \frac{\zeta'(2)}{\zeta(2)}\right)x^4 \qquad (5\text{-}58')$$

$$\text{for} \quad x < 2\pi \qquad \left(x = \frac{\hbar\omega_0}{kT}\right)$$

where $\zeta(3) = \sum_{n=1}^{\infty}\left(\frac{1}{n^3}\right)$; $\zeta(2) = \sum_{n=1}^{\infty}\left(\frac{1}{n^2}\right) = \frac{\pi^2}{6}$; $-\zeta'(2) = \sum_{n=1}^{\infty}\frac{\ln 2}{n^2}$

An input table listing F(x) as a function of x in the range $0.02 \leq x \leq 10$ was prepared from (5-58'), and Q_t was calculated again in the same range of n_e and T as before; but this time with the equation (5-58'), the F(x) - x input table, and the interpolation subroutine. Some of the results are shown in Figure 49 by the black dots. The former graphic method using smooth hand interpolation in the intermediate regions is found to be in excellent agreement with the new analytic expression (5-58'), and it can therefore be concluded that further improvement of the results already obtained should not be expected through the use of the new formula (5-58'), in place of the old (5-54') together with the graphical interpolation method as was used previously.

Quite recently, it was discovered that a modified "URCA process" in a degenerate matter may give an important contribution to the neutrino luminosity of neutron stars. According to qualitative estimates made by Chiu and Salpeter,(22)

$$L_{\nu, u_n} \cong 2 \times 10^{36}\left(T_c / 10^9\,^\circ\mathrm{K}\right)^8 \left(\frac{E_{F,n}}{50\ \mathrm{M_{ev}}}\right)^{-2.25}\left(M/M_\odot\right) \quad \text{ergs/sec} \qquad (5\text{-}59)$$

This became known to me after all my work had been finished. The plasma neutrino luminosity estimated by the same authors(22) is

$$L_{\nu,pl} \cong 2\times 10^{36}\left(T_c/10^{9}\,{}^{\circ}K\right)^{10}\left(R/10\,km\right)^{4}\left(M/M_{\odot}\right)^{-1} \quad \text{ergs/sec} \qquad (5\text{-}60)$$

According to these equations, for a typical neutron star with $M = 1\odot, T_c = 10^{9}\,{}^{\circ}K$, $R = 10$ km and a neutron Fermi energy of 50 Mev, the URCA neutrino luminosity in (5-59) and the plasma neutrino luminosity in (5-60) are both equal to the value 2×10^{36} ergs/sec. In this case the effect of the URCA process is not large (because it increases the total neutrino luminosity only from 2×10^{36} to 4×10^{36} ergs/sec). However, by examining my results it appears that the neutrino cooling rate at the critical temperature around $10^{9}\,{}^{\circ}K$ might be greatly affected by the inclusion of the URCA process. Because the URCA process plays an important role in the dynamic collapse of a star, it should not be surprising if it also becomes important during the subsequent cooling. It is desirable that a more detailed formula for the neutrino luminosity due to the URCA process should be derived and applied to my models, so that its quantitative effect on the present results might be determined.

V-7 COOLING TIMES

The cooling time τ is computed from the carefully prepared data of the last sections and from the following relation:

$$\tau = -\int_{U_1}^{U_2} \frac{dU}{L(U)} \qquad (5\text{-}61)$$

where U is the total energy content of a star, or the total internal energy, and $L(U)$ is the total luminosity $(L_{\nu} + L_{ph})$ expressed as a function of U, as in Figure 48. If the above integration is carried out from the initial internal energy U_1 to the final internal energy U_2, then τ gives the time interval during which the star has cooled from a higher temperature T_1 (where the total energy content is U_1) to a lower temperature T_2 (where the total energy content is now U_2). In the actual computation, a graphical method has been used. For a small interval of time Δt in which the change of luminosity is small, $\Delta t \sim \Delta U/\bar{L}$, where $\bar{L}$ is the mean luminosity in this interval. The period of time between the moment the star started to cool until a certain later time (the age or cooling time of the neutron star) is then found by dividing this total period into small intervals and then by replacing the integral of (5-61) by the sum over the small intervals. Then,

$$\tau = \Sigma \left(\Delta U/\bar{L} \right) \tag{5-61'}$$

For this purpose, graphs such as Figure 48, plotted for all six models, were used.

The results for each type of model (V_βI), (V_βII), etc., are tabulated in the last two columns of Tables 28 through 33 for model atmospheres of pure iron and pure magnesium, respectively. The cooling curves are shown in Figures 50 through 53. The detailed behavior of cooling is different for each different type of model (each has different internal nuclear physics, mass, density, radius and composition). But in general the following conclusions can be drawn. (i) Until the surface temperature drops to the range 1 million to 10 million degrees, the star cools off mainly by the neutrino process. Below this point cooling proceeds mainly through optical radiation from the surface. (ii) The time scale is very short at high temperatures. For instance, the period of time during which the surface temperature is about 50 million degrees and the internal temperature is from about 5 to 10 billion degrees lasts only from about a second to a few hours at most even with only the plasma neutrino process of cooling. At higher temperatures (say, $T_{in} \sim 10^{11}$ °K), other neutrino processes such as those involving μ neutrinos become important and the time scale is expected to

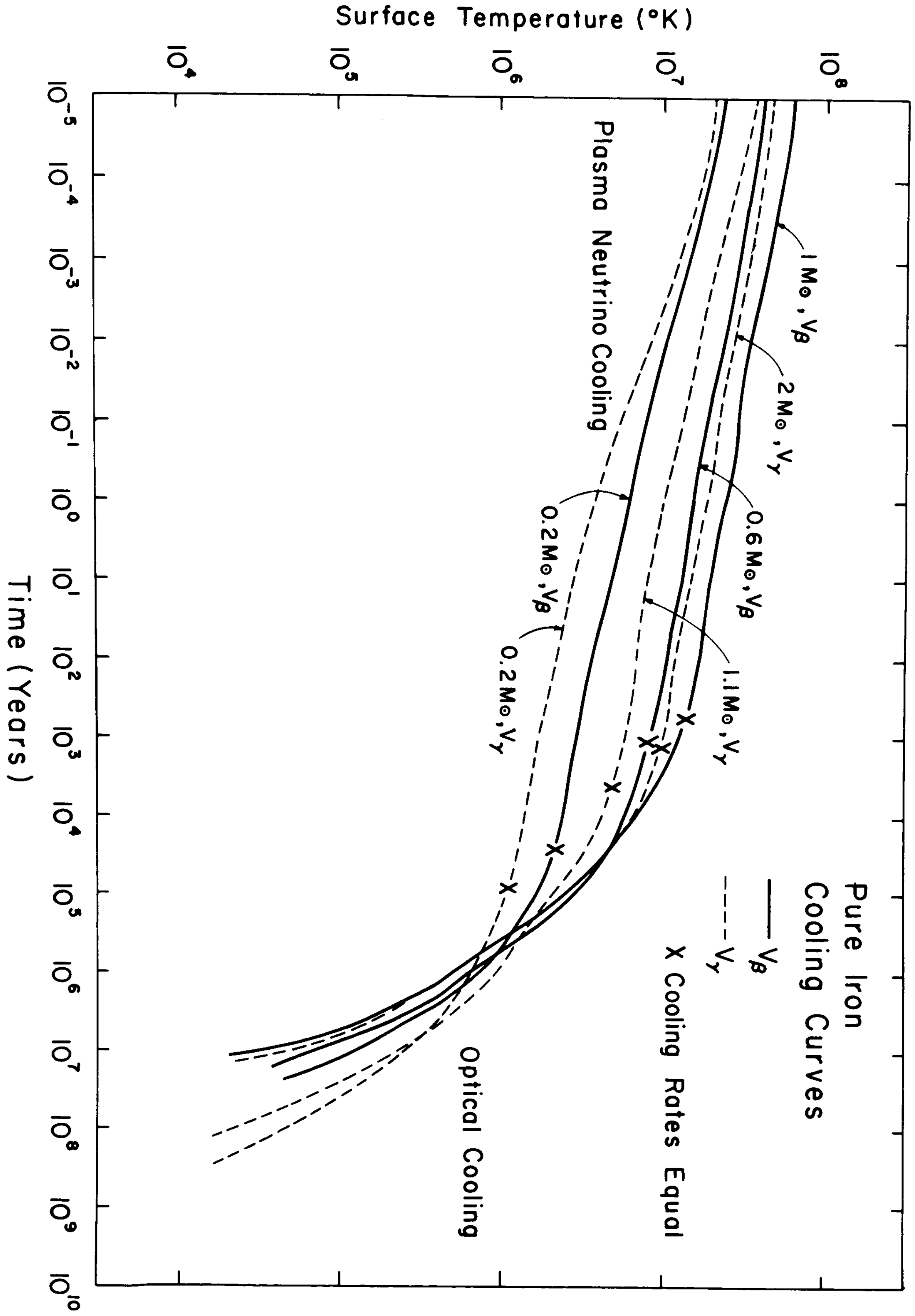
Surface Temperature (°K)
10⁴
10⁵
10⁶
10⁷
10⁸
Time (Years)
10⁻⁵
10⁻⁴
10⁻³
10⁻²
10⁻¹
10⁰
10¹
10²
10³
10⁴
10⁵
10⁶
10⁷
10⁸
10⁹
10¹⁰
Pure Iron Cooling Curves
— ν_β
- - - ν_γ
X Cooling Rates Equal
1 M⊙, ν_β
2 M⊙, ν_γ
0.6 M⊙, ν_β
1.1 M⊙, ν_γ
0.2 M⊙, ν_β
0.2 M⊙, ν_γ
Plasma Neutrino Cooling
Optical Cooling

Figure 50

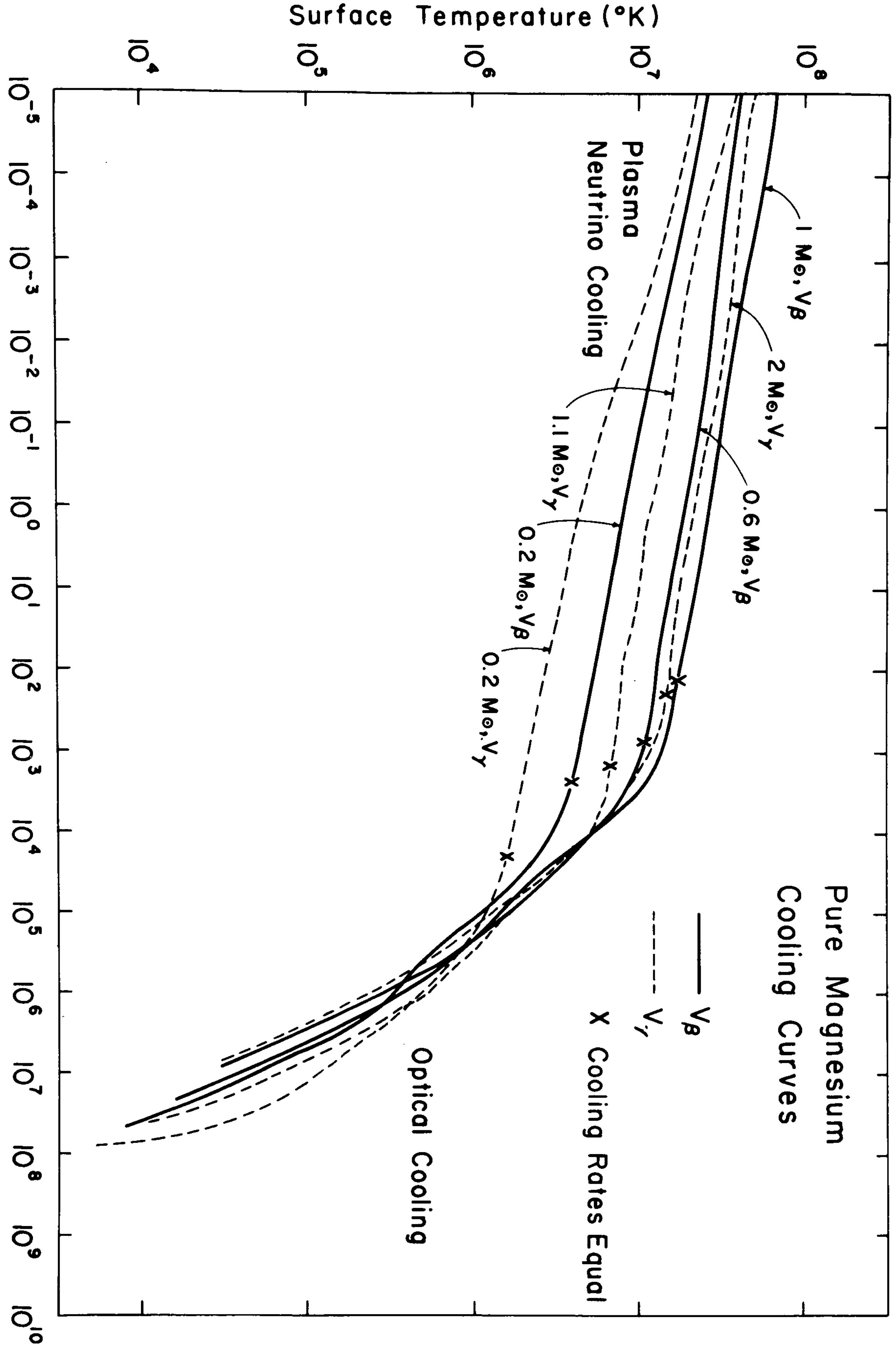
Surface Temperature (°K)
10^4
10^5
10^6
10^7
10^8
Time (Years)
10^-5
10^-4
10^-3
10^-2
10^-1
10^0
10^1
10^2
10^3
10^4
10^5
10^6
10^7
10^8
10^9
10^10
Pure Magnesium Cooling Curves
V_β
V_γ
X Cooling Rates Equal
1 M⊙, V_β
2 M⊙, V_γ
0.6 M⊙, V_β
1.1 M⊙, V_γ
0.2 M⊙, V_β
0.2 M⊙, V_γ
Plasma Neutrino Cooling
Optical Cooling

Figure 51

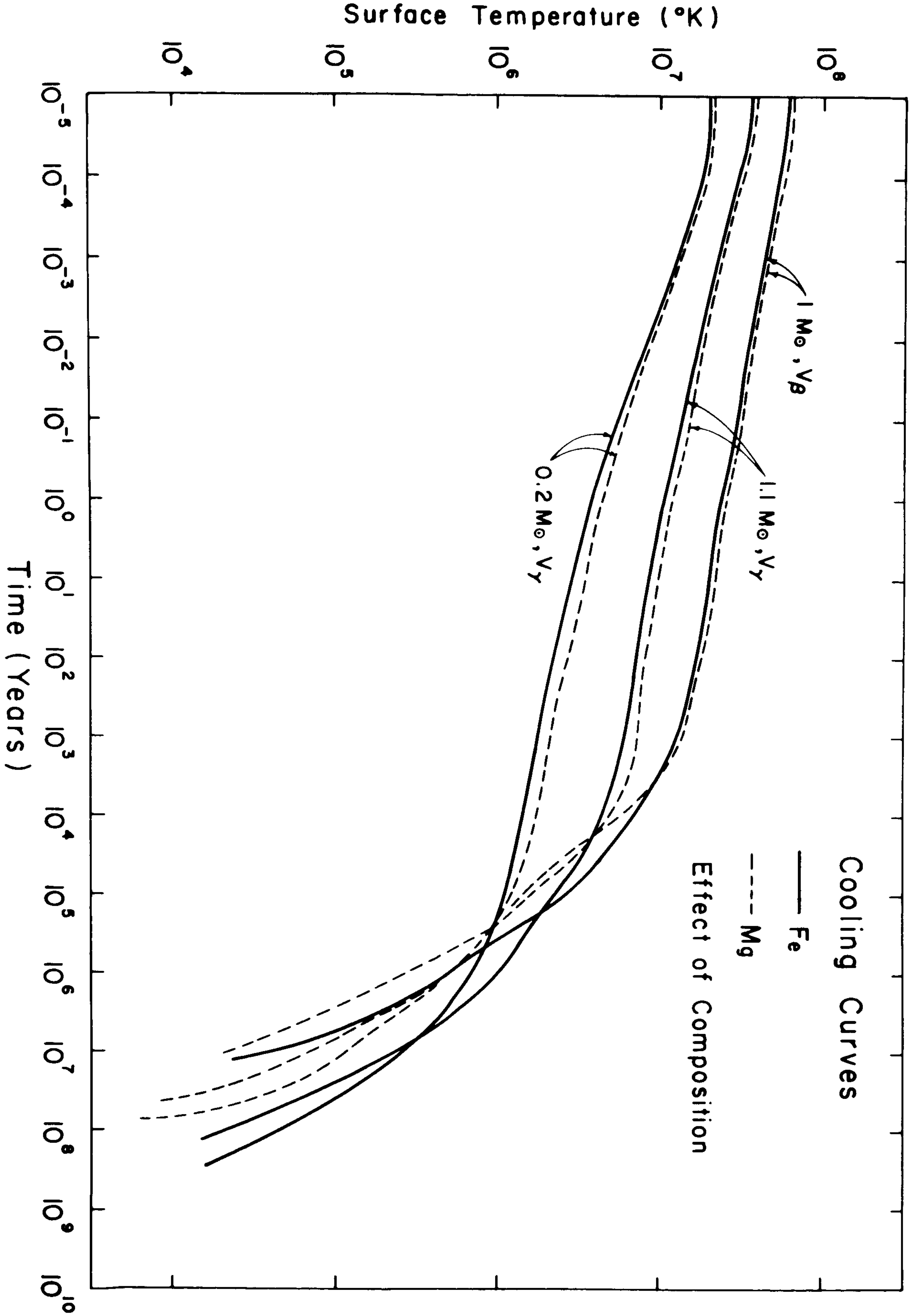
Surface Temperature (°K)
10^4
10^5
10^6
10^7
10^8
Time (Years)
10^{-5}
10^{-4}
10^{-3}
10^{-2}
10^{-1}
10^0
10^1
10^2
10^3
10^4
10^5
10^6
10^7
10^8
10^9
10^{10}
Cooling Curves
—— Fe
- - - Mg
Effect of Composition
1 $M_\odot$, V_β
1.1 $M_\odot$, V_γ
0.2 $M_\odot$, V_γ

Figure 52

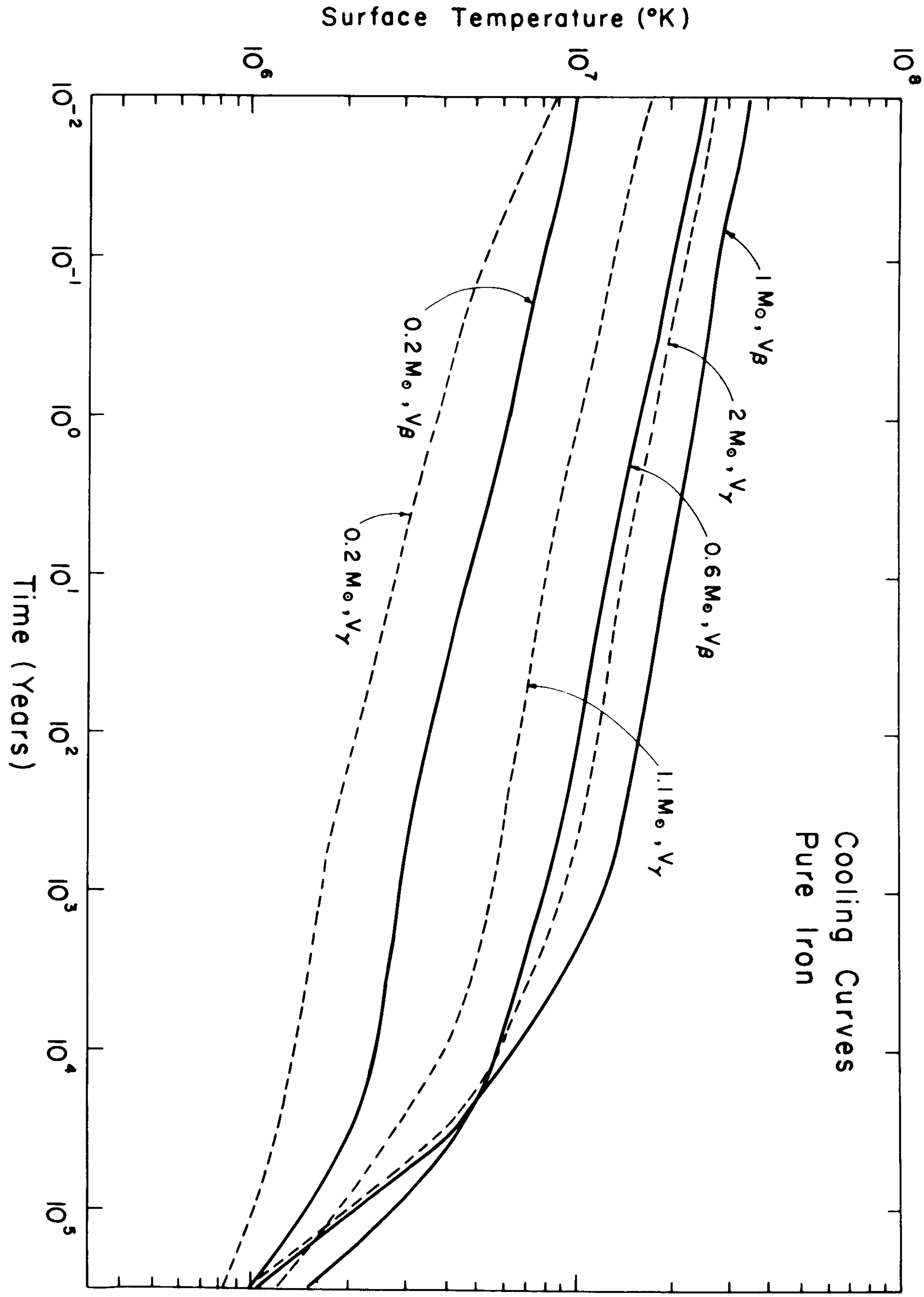
Surface Temperature (°K)
10⁶
10⁷
10⁸
Time (Years)
10⁻²
10⁻¹
10⁰
10¹
10²
10³
10⁴
10⁵
Cooling Curves
Pure Iron
1 M⊙, Vβ
2 M⊙, Vγ
0.6 M⊙, Vβ
1.1 M⊙, Vγ
0.2 M⊙, Vβ
0.2 M⊙, Vγ

Figure 53

become much shorter (with a peak at around $T_{in} \sim 10^{11}$ °K, $\rho \sim 6 \times 10^{11}$ gm/cm^3, and $\tau \sim 10^{-5}$ sec).(17) This result confirms our earlier assumption that all neutron stars (of any kind) hotter than those with $T_e \sim 5 \times 10^7$ °K (that is, $T_{in} \sim 5 \times 10^9$ °K) would cool off too fast to be observed. When the surface temperature becomes about 2×10^7 °K, the cooling rate is still quite high and the stars are from about 10 minutes to 20 years old. Stars with $T_e = 1 \times 10^7$ °K are about 1 day to a few thousand years old, and those with $T_e = 5 \times 10^6$ °K are about a few months to 20,000 years old. However, for all the models considered (all the models possible), it takes about 10^5 to 10^6 years to cool down to the point where $T_e = 10^6$ °K. Hereafter, the difference in the cooling behavior between different types of model is relatively small and after about 10^7 to 5×10^8 years from the time of its birth (through a supernova explosion), the surface temperature of all our models drops to about 10 thousand years. Cox's opacity code broke down at temperatures lower than about 10^4 °K and therefore cooling beyond this point was not followed in this research. However, it is expected that nothing interesting would happen at these low temperatures. A neutron star would most likely continue to cool down, asymptotically approaching zero-temperature. Therefore, the life times of neutron stars are expected to be about 10^8 to 10^9 years. Of course, long before that, they will become too faint ever to be detected. From the discussion in the next section, it is impossible to detect neutron stars cooler than $T_e \sim 10^6$ °K and the life times of detectable neutron stars may therefore be tentatively set at from 10^5 to 10^6 years (the time it would take to cool down to $T_e \sim 10^6$ °K).

Figure 50 shows the cooling curves of our six models with iron atmospheres (solid curves correspond to V_β type models and dashed curves to V_γ type models). The point at which the plasma cooling rate and the optical cooling rate become equal ($L_\nu = L_{ph}$) is shown by a cross for each curve. The figure shows that for the same type of model (either V_β or V_γ), the lighter neutron stars have a lower surface temperature than the heavier ones up to an age of about 10^5 years, but after that heavier neutron stars cool off faster so that the total life times of the heavier stars are somewhat shorter (about $10^7 \sim 10^8$ years) than those of the ligher stars ($10^8 \sim 10^9$ years). Among models of the same mass and same surface temperature, V_γ type models are seen to be much younger than V_β type ones. A graph similar to the ones for Fe atmospheres is shown for Mg atmospheres in Figure 51. This contains the same notation as was previously used, and the general behavior is seen to be also the same. In the discussion of this section, the moment at which a neutron star is formed (or the moment of a supernova explosion) is defined as its time of birth (the point from which its age is counted).

To see better the effects of different composition, cooling curves for the same type of models of the same mass but of different composition are shown in Figure 52. Solid curves represent models with iron atmospheres and dashed curves those with Mg atmospheres. We see that for $T_e > 10^6$ °K, Fe models are somewhat cooler at a given age than the corresponding Mg models, but the reverse occurs when $T_e < 10^6$ °K. Consequently, the total lifetimes of Mg models are somewhat shorter than those of Fe models. This is explained as follows. For the hotter neutron stars ($T_{in} \gtrsim 10^{8 \sim 9}$ °K, $T_e \gtrsim 10^{6 \sim 7}$ °K) which are cooling mainly by a neutrino process, the age of the star is determined by the total internal energy U and the neutrino luminosity L_ν, both of which depend on the internal temperature of the star but which are independent of the atmospheric composition. Therefore, neutron stars of the same internal temperature and other internal properties (mass, nuclear forces, etc.) have the same age. However, neutron stars of the same internal temperature have a higher surface temperature if the atmospheric composition is Mg instead of Fe because the opacity of Mg is generally smaller than that of Fe, as can be seen in Figure 42. However, a cooler neutron star ($T_{in} \lesssim 10^8$ °K, $T_e \lesssim 10^6$ °K) which is cooling by optical radiation from the surface only is more strongly governed by the surface composition, because now luminosity, and not only T_e, depends on the opacity of its atmosphere. The optical luminosity is larger for Mg than for Fe (see Figure 48) at the same U(or T_{in}) because of the lower opacity associated with Mg. Therefore, if one compares the cooling time of two models, identical in every respect except that one has an atmosphere of Mg while the other has one of Fe, the cooling time of the former must necessarily be shorter than that of the latter when the optical luminosity predominates. As a star cools down, this effect of surface composition on luminosity (which shortens the cooling time of Mg models as compared with that of Fe models) eventually becomes more important than its effect on surface temperature (which makes the cooling time of Mg models longer than that of Fe models), and finally τ becomes shorter for the cooler stars with Mg atmospheres than with Fe atmospheres. On comparing Figure 52 with Figures 50 and 51, however, we see that the effect of different composition is rather small compared with the effect of different mass or of different nuclear potential in the interior.

The most important range of temperature from the point of view of one trying to observe the star is $10^6 < T_e < 2 \times 10^7$ °K, as will be seen in the next section. Therefore, this portion of the curves is enlarged in Figure 53. In this critical range, the variation in the calculated age of a neutron star with different nuclear potential is quite large. For instance at $T_e = 10^7$ °K, a star of $1 M_\odot$ may be only about a few years old if a nuclear potential of type V_γ is assumed or it could be as old as 2500 years if a V_β type potential is chosen. At a slightly lower temperature, $T_e = 5 \times 10^6$ °K, models of $0.2\ M_\odot$ (the lightest models) may be only a few months old with V_γ and about several years old with V_β. The variation of age with mass is still more drastic. In the detectable range of surface temperature shown in Figure 53, the possible age of a stable neutron star is seen to be anywhere from about one day to about 10^6 years.

V-8 OBSERVATIONAL PROBLEMS -- DETECTABILITY

a. General Remarks

As mentioned at the beginning the main motive for starting this research was to see whether neutron stars, if they exist, would be detectable. Interesting theoretical data have been accumulated to answer this question.

The conclusion is that (i) it appears practically impossible for earth-bound astronomers to directly observe these stars even through the world's largest telescopes, (ii) some of the neutron stars should be detectable by x-ray telescopes mounted on rockets or artificial satellites above the earth's atmosphere, provided that Planck's radiation formula is still applicable on the surface of such hot stars, but (iii) even above our atmosphere it is almost hopeless to detect these stars outside the narrow range of wave lengths in the soft x-ray regions.

To explain the above conclusions, let us first go back to Table 25. If we assume that neutron stars emit radiation as black bodies, the wave length λ_{max} giving the maximum intensity in the spectrum is simply given by

$$\lambda_{max}\,(\mathrm{cm}) = hc/(4.9651\, k\, T_e) = 0.2918/T_e\,(^{\circ}\mathrm{K}) \qquad (5\text{-}62)$$

This shows that when $T_e \sim 10^6$ to 10^7 °K, the maximum comes in the soft x-ray region, $30 \gtrsim \lambda_{max} > 3$Å, while this maximum shifts to the ultraviolet region when T_e falls to around $10^5 \sim 10^4$ °K.

The earth's atmosphere is transparent to radiation only in the regions 3000 Å $\lesssim \lambda \lesssim$ 7000 Å (visible), 8000 Å $\lesssim \lambda \lesssim$ 12000 Å (infrared), and 1 cm $\lesssim \lambda \lesssim$ 10 meters (microwaves). Interstellar matter consists mainly of hydrogen and interstellar absorption is quite high near the lyman continuum (ultraviolet region) but it is practically negligible outside of this range.

It is seen in Table 25 that the total optical luminosity of hot neutron stars with $T_e > 10^6$ °K ($\lambda_{max} < 30$ Å) is comparable to or higher than the solar luminosity, and that at $T_e \sim 10^7$ °K, most of the energy output is concentrated in the x-ray region around 3 Å. Since interstellar gases are practically transparent to radiation of these wave lengths, quite a large flux of x-rays from such a hot neutron star should be detectable just above our atmosphere (here, for instance, $L \sim 10^3 L_{\odot}$ for $T_e \sim 10^7$ °K). However, as was seen above, our atmosphere is opaque to x-rays and, consequently, most of this high flux does not reach the earth's surface. The fraction of the radiation which passes through our atmospheric window is given by(17)

$$\int_0^{x'} \frac{x^3 dx}{(e^x - 1)} \Big/ \int_0^{\infty} \frac{x^3 dx}{(e^x - 1)} \text{ where } x = h\nu / kT_e \text{ and } x' = \frac{h\nu(\text{visible})}{kT_e}.$$

Then, when $T_e \sim 10^7$ °K, only about 10^{-8} of the total flux would reach an earth-bound telescope. Although the total energy output of a star's surface at this temperature is quite high ($L \sim 10^3\ L_\odot$), its luminosity would appear to be only $10^{-5}\ L_\odot$ to an observer on the ground and therefore too faint to be observed unless the star is practically within the solar system.

Neutron stars hotter than this, $T_{in} \gtrsim 10^{10}$ °K and $T_e \gtrsim 5 \times 10^7$ °K, cool off too fast to be observed ($\tau < 10$ hours) as seen in Section V-7 and they should be excluded from our consideration.

Cooler neutron stars with $T_e < 10^6$ °K are hard to detect even above the earth's atmosphere. Neutron stars with $10^4 < T_e < 10^6$ °K emit radiation with a maximum intensity in the ultraviolet region where, as we saw above, the interstellar absorption is quite high. Consequently, this portion of the spectrum will not reach us. The fraction of radiation with longer wave lengths (to which interstellar gases are almost transparent) is too small to produce an energy flux sufficient to be detected. For instance, at $T_e = 5 \times 10^5$ °K, about 5×10^{-5} of the total flux can reach us. At this temperature the total luminosity of the star is about $10^{-2}\ L_\odot$, and so we will receive only $L \sim 5 \times 10^{-7}\ L_\odot$, whether we are above or below our atmosphere. That is, the chance of our observing these cooler stars ($10^4 < T_e < 10^6$ °K) whose maximum energy output is in the ultraviolet region is even less (both above and below our atmosphere) than that of our observing from the surface of the earth the hotter neutron stars considered earlier, because of the strong interstellar absorption of radiation in the ultraviolet range.

Finally let us consider even colder neutron stars with $T_e \lesssim 10^4\ ^\circ K$. Here the maximum of the Planck's spectrum comes in visible region, but at these temperatures, the total luminosity of the star is less than $10^{-9}\ L_\odot$, worse from the standpoint of being observable than all the previous cases.

We have exhausted, in the above, all possible ranges of temperature which a neutron star can have and are led to the three conclusions summarized at the beginning of this section. Combining the above considerations with the results of the last section (Figures 50 to 53), we see that some of the neutron stars which emit x-rays can surely last long enough to allow us to observe them through rocket-bound telescopes in outer space, provided that these stars can be treated as black bodies and that their mass is not too small. (For instance, Figure 53 shows that a neutron star of $M \sim 0.2 M_\odot$ and $T_e \sim 10^7\ ^\circ K$ can last only for a few days or less.)

It was recently suggested(22) that a large fraction of the ultraviolet light may be converted into visible light (Balmer recombination lines) if a neutron star is surrounded by a gas cloud of density > 20 atoms/cm^3, and that in such a case hot neutron stars ($T_e \sim 10^7\ ^\circ K$) may be just barely seen by terrestrial telescopes.

What is outlined above is further explored in detail in Section V-8c, but before that let us review the experimental background briefly.

b. x-ray Observations

Since it became possible to explore outer space through rocket-bound instruments above the earth's atmosphere, the experimental evidence of x-ray sources outside the solar system have been reported.(18,19,20) From analyzing the results of three flights, Giaconni's group(18) concluded that a strong x-ray source of temperature about 8 million degrees is located near the galactic center. They maintained, furthermore, that this source has an effective wave length of about 3 Å, is not associated with the earth's atmosphere nor with any members of the solar system, and is not ascribable to any form of auroral activity, but is of galactic origin. Besides this major source, two other much weaker x-ray sources were detected, one near the Crab Nebula and the other somewhere between 20 and 30 hr right ascension and between + 10° and + 50° declination.

Friedman's group reported(20) that two new x-ray sources had been detected, one in Scorpius and the other in the direction of the Crab Nebula. The stronger source, in Scorpius, with an angular size less than 5° and with an energy flux of 1.4×10^{-3} ergs/cm^2 - sec - Å with a nearly flat spectrum in the wave length range of 1.5 Å to 8 Å, was located at 16 hr 15 min. right ascension and - 15° declination. The weaker source of flux 2.0×10^{-9} ergs/cm^2-sec - Å in the same frequency interval as the former was found to coincide in its location with the Crab Nebula to within 2°.

No optically prominent features are known to be present at the location of the Scorpius source, nor have any unusual stars, such as radio stars, been found there. This is a region thickly populated with faint stars but with no visible nebulosity. On the contrary, the Crab Nebula is a well known source of visible and radio synchrotron emission.

Fisher(19) reported the results of his scanning of the night sky for possible x-ray emissions, but no agreement is apparent between his results and those of other groups. Friedman's group attributes this to the fact that the detectors used by Fisher are about 13 times less sensitive than theirs, and argues that because of this difference in instrumentation the two sources detected by Friedman's group should be insignificant compared with Fisher's background. The source near the galactic center reported by Giaconni's group(18) is most likely the Scorpius source reported by Friedman's group.(20) A slight discrepancy between the positions reported by these two groups is quite to be expected, considering the very broad field of view used by the former.

The latest x-ray measurement was made during the eclipse of the Crab Nebula on July 7, 1964. It was reported(20') that the size of the x-ray source in the Crab Nebula as estimated from the change in flux during the eclipse is about 1 light year. This eliminates the possibility that the blackbody radiation from a neutron star is the major cause of the total measured x-ray flux from the Crab Nebula, but does not eliminate the possibility that there is a neutron star in the Crab Nebula, as is shown in the next section, V-8c.

c. Discussion

In the 8th column of Tables (28-33), the maximum wave lengths λ_{max}, corrected for gravitational red shift, are listed. All other spectral shifts are negligible (for instance, the doppler width is only about $0.001\ \lambda$).

Assuming that the interstellar absorption is negligible (which is a justifiable approximation in x-ray regions) and that the total measured x-ray flux comes only from a neutron star radiating as a blackbody, the distance d to the x-ray source (a neutron star) is easily calculated through the relation

$$d = \left\{ L/(4\pi F) \right\}^{\frac{1}{2}} \tag{5-63}$$

where L is the total optical luminosity of the star and F is the flux (ergs/cm^2-sec) of x-rays measured just above out atmosphere.

At the present stage, because of the paucity of experimental data it may be dangerous to be too specific in numerical comparisons but I think that by comparing some of the measured quantities with those predicted by the theoretical models one might gain some insight into the problem.

The apparent temperature of the Scorpius source (without the red-shift) was measured to be about 8 million degrees(18b) (Section V-8b). The real temperature is easily found by blue shifting the observed value; that is, the actual surface temperature $T_e = (1 + \varphi)\ 8 \times 10^6\ {}^\circ K$, where $\varphi = \Delta\lambda/\lambda$ is the gravitational red shift. For a known T_e, the corresponding age is found from a $T_c - \tau$ curve such as that shown in Figure 53. The results are listed in the table below. The distance calculated from (5-63) with $F = 10^{-7}$ ergs/cm^2-sec (approximately the measured flux from the Scorpius source) is expressed in parsec (1 parsec = 3.084×10^{18} cm = 3.26 light years).

MODELS		$(1M_\odot, V_\beta)$	$(0.6M_\odot, V_\beta)$	$(0.2M_\odot, V_\beta)$	$(2M_\odot, V_\gamma)$	$(1.1M_\odot, V_\gamma)$	$(0.2M_\odot, V_\gamma)$
$\varphi = \Delta\lambda/\lambda$		0.285	0.156	0.0282	0.301	0.125	0.0131
T_e(real) ($^\circ$K)		1.03×10^7	9.25×10^6	8.23×10^6	1.04×10^7	9.00×10^6	8.12×10^6
AGE	Fe	2400 yrs	300 yrs	10 days	1200 yrs	27 yrs	5 days
τ	Mg	2900 yrs	1950 yrs	1 yr	1600 yrs	26 yrs	3 days
Distance(psc)		~400	~450	~800	~800	~900	~1800
λ_{max} (Å)		3.6	3.45	3.3	3.65	3.4	3.25

According to this table, the maximum intensity comes at around 3.5 Å, the possible age can be anywhere from 3 days to 3000 years, and the corresponding distance from about 2000 to 400 parsec. The wide range in age exists because of differences among the stars being considered: differences in the nuclear and particle physics which govern the interior, differences in the surface composition and most important, differences in mass. The youngest model has $M \sim 0.2\ M_{\odot}$, $R \sim 24$ km, a Mg atmosphere and is of V_{γ} type, while the oldest ($\sim$ 3000 years) has $M \sim 1\ M_{\odot}$, $R \sim 5$ km, a Mg atmosphere and is of type V_{β}.

The Scorpius source **was** used for the above calculations. Therefore, let us look into this source in detail. There is no nebulosity, no visible or radio stars at the location of this source, but a strong x-ray emission was detected. If future observations reveal that it is a point source, it is most likely that it is a neutron star. As noted in Section V-8a, a neutron star, by itself (that is, in the absence of surrounding gases or heavy nebulosity in its vicinity), cannot emit a detectable amount of radiation except in the form of x-rays (no visible, no radio synchrotron emission). Among the several possibilities presented in the above table the models ($0.2\ M_{\odot}$, V_{β}), ($0.2\ M_{\odot}$, V_{γ}) and ($1.1\ M_{\odot}$, V_{γ}) should be eliminated, because for any of these to be the Scorpius source the corresponding supernova explosion should have occured less than 30 years ago, but no supernovae were observed in Scorpius within this century.

It may be interesting to compare the possible age of the Scorpius source presented in the above table with some ancient records. The corresponding supernova explosion could be a celestial event recorded in one of the following years:(23) 134 B.C., 436 A.D., 827 A.D., 891 A.D, and 1585 A.D. Some of these may, however, be comets or ordinary novae. Some of these were seen not quite near the x-ray source, but the accuracy of the location in ancient records is often doubtful and none of these should be eliminated as possibilities.

The event in 827 A.D. appears to be closest to the observed location of the Scorpius source. It was noted by Humbolt (1850), that two Arabian astronomers, Haly and Giofor Ben Mohammed Albumazar, observed a new star in Scorpius as bright as "the moon in her quarters" which lasted for four months, but the date appears to be no more certain than the first half of the ninth century. If this is the supernova explosion which formed a neutron star now emitting a strong x-ray flux in Scorpius, then the age of the star should be about 1200 years, and from the above table the heaviest model (2 $M_{\odot}$, V_{γ}) with an iron atmosphere is seen to agree best with the observations, for which case the source is expected to be about 800 parsec away.

It is strange, however, that such a spectacular event should not be recorded anywhere except in the Arabian records. It is at least not present in the Japanese records, which were thoroughly searched, although its omission here may be due to bad weather such as usually prevails in Japan at the time of year of the Arabian observation. D. M. Dunlop, after examining the original Arabian sources, reported(61) that it is not certain whether this new star observed by Arabs was a supernova or a comet. The above table indicates, however, that it poses no trouble if it were a comet or even if none of the possible supernovae considered above were the mother of the neutron star candidate in Scorpius. For instance, if the neutron star is about 1 $M_{\odot}$, of the V_{β} type, and has a Mg atmosphere, the table shows that the mother supernova should have occured at about 1,000 B.C.,(and would be about 400 parsec away), which is long before any of the ancient supernova events considered above. It is not surprising that no records of such an old event should be available. It should also be noted that we may arrive at a model even older than any of those listed in the preceding table if we use a different possible nuclear potential in the interior, and that it is, therefore, quite possible that the event in question occured in prehistoric times. It is also possible that the neutron star was formed through something much less spectacular than a supernova explosion.

On examining the results shown in Tables 28-33 and Figures 50-53, we notice the complexity involved in the problem. For instance, it seems improper to assign a definite value to the number of neutron stars at a given temperature from just simple statistics and a knowledge of the total number of supernovae in the universe, even if all supernovae end up as neutron stars and even if we neglect all other possible formation mechanisms of neutron stars, because, for instance, we do not know how the remnants of supernova explosions are distributed among possible models and also because the cooling rate depends drastically on the age and the internal properties of the star, such as its mass, radius and the interaction potential present. Consequently the time required for a neutron star to cool down to a given temperature varies very much from model to model. For instance, if $M \sim 0.2\ M_{\odot}$, it takes only a few days to cool down to $T = 10^{7}\ {}^{\circ}K$ after the formation. But if $M \sim 0.6\ M_{\odot}$ and a V_{β} type potential applies, this cooling takes 3,000 years, while if the potential is the V_{γ} type, the same star requires less than a year to cool down to the same temperature.

It is, however, possible to make less restricted estimates. For instance, the neutron stars detectable in the present frequency range ($1.5\ \text{Å} \lesssim \lambda \lesssim 8\ \text{Å}$) cannot be among the lightest ones, because in order that the maximum radiation be in this frequency range the surface temperature T_e must be $2 \times 10^7 \gtrsim T_e \gtrsim 5 \times 10^6\ {}^\circ\text{K}$, but for such temperatures the lightest neutron stars ($\sim 0.2\ M_\odot$) cool too fast to be observed. For instance, it takes for models of $0.2\ M_\odot$ to cool down to $5 \times 10^6\ {}^\circ\text{K}$ (the lower limit in the preceding temperature range) and $\lambda_{max} \sim 7\ \text{Å}$ only a year or less if the potential type is V_γ and less than ten years if it is V_β . (See Figure 53 and Tables 28-33.)

Next, I should like to show that, according to my models, it is quite possible that nothing would be detected at the location of a known ancient supernova, were its remnant to be a neutron star of sufficiently small mass. As an example, let us consider the Crab Nebula, in which a supernova explosion is supposed to have occured in 1054 A.D. This is a strong source of both visible and radio synchrotron emission as well as a region of high nebulosity, which is believed to be due to the existence of massive expanding shells expelled by the supernova explosion in 1054 A.D. The size of the x-ray source in the Crab Nebula was reported to be about one light year (Section V-8b), and this indicates that the major x-ray flux is related to the hot gases in the outer expanding shells. However, this does not eliminate the possibility that there exists a tiny dense neutron star near the center of the Crab Nebula. To visualize the situation, let us tentatively assume that there is a neutron star in the Crab Nebula and examine whether it should be detectable or not. Its surface temperature at present (910 years after the explosion) is determined from the theoretical models. That is, the T_e of various different models at $\tau = 910$ years is read from a $T_e - \tau$ curve such as that shown in Figure 53. From a given T_e, the corresponding λ_{max} (with red shifts) is determined from Tables 28-33. The luminosity of a star at a given T_e has been calculated and plotted already in Section V-6a. Inserting $d = 1100$ parsecs (our distance from the Crab Nevula) and various values of L into equation (5-63) we calculate the total flux coming from the neutron star only. The properties of the hypothetical neutron star in the Crab Nebula (its surface temperature T_e, maximum wave length λ_{max}, internal energy U, optical luminosity L_{ph}, and the flux F_n to be measured just above our atmosphere which comes from the neutron star only and not from the surrounding expanding shells) are listed below, both for models of Fe and Mg atmospheres.

MODELS		$(1M_\odot, V_\beta)$	$(0.6M_\odot, V_\beta)$	$(0.2M_\odot, V_\beta)$	$(2M_\odot, V_\gamma)$	$(1.1M_\odot, V_\gamma)$	$(0.2M_\odot, V_\gamma)$
T_e(°K)		1.23×10^7	8.1×10^6	2.9×10^6	9.33×10^6	5.63×10^6	1.68×10^6
λ_{max}(Å)		~3	~4	~12	~4	~5	~20
log U(ergs)		47.65	47.45	46.92	48.06	47.96	47.28
log L_{ph} (ergs/sec)	Fe	36.68	35.78	34.75	36.76	36.21	34.41
	Mg	37.08	36.38	35.48	37.34	36.60	34.83
Fn (ergs/cm^2-sec)	Fe	3.30×10^{-8}	4.16×10^{-9}	3.88×10^{-10}	3.98×10^{-8}	1.12×10^{-8}	1.77×10^{-10}
	Mg	8.31×10^{-8}	1.65×10^{-8}	2.07×10^{-9}	1.51×10^{-7}	2.75×10^{-8}	4.67×10^{-10}

The above table shows that if the neutron star has $M \gtrsim 0.6\ M_\odot$ for the V_β type and $M \gtrsim 1\ M_\odot$ for the V_γ type, the maximum intensity comes within the range $3\ \text{Å} < \lambda_{max} < 6\ \text{Å}$ and the x-ray flux is $10^{-7} \sim 10^{-8}$ ergs/cm^2-sec which is comparable with the flux measured in the Crab Nebula. But if its mass is about 1/4 to 1/5 solar mass the maximum intensity comes at around $10 < \lambda_{max} < 20\ \text{Å}$, the surface temperature is only a few million degrees and the flux is reduced to about $10^{-9}\sim 10^{-10}$ ergs/cm^2-sec which is too weak for detection. In the above calculations, the interstellar absorption was neglected, but this may not be justified in this wave length range. When an appropriate correction is applied the flux will become even less than the values calculated above. The conclusion is that the neutron star in the Crab Nebula, even if it exists, cannot be detected if its mass is sufficiently small. It is also possible that a medium weight neutron star exists near the center of the Crab Nebula and emits x-rays of flux $\sim 10^{-8}$ ergs/cm^2-sec but that it cannot be singled out because the expanding shells which surround the star also emit similar x-rays, perhaps of somewhat greater intensity.

While neutron stars cool too fast to be observed at the critical stage where $3 \times 10^6 < T_e < 3 \times 10^7$ °K, some of the medium-weight and heavy neutron stars remain luminous for a long time. For instance, a 2 $M_\odot$ neutron star of type V_γ about 400 parsec away and another of 1 $M_\odot$ and type V_β about 100 parsec away both having $T_e = 7 \times 10^6$ °K and $\lambda_{max} \sim 5\mathring{A}$ would produce an output intensity of 10^{-7} ergs/cm^2-sec even as long as 10,000 years after their formation. Most of the medium-weight and heavy neutron stars last as long as $10^{5\sim 6}$ years before they become cooler than $T_e = 10^6$ °K (Figures 50 and 51). It is remarkable that once we get outside of our atmosphere, neutron stars much further away than any of the observable white dwarfs can be within reach of our detectors if they are massive and hot enough. For instance, a massive, hot neutron star of the V_γ type with a mass $\sim 2\ M_\odot$, radius $\sim$ 10 km, $T_e \sim 1 \sim 2 \times 10^7$ °K ($\lambda_{max} \sim 3\ \mathring{A}$), when about 10^3 years old, would, even if it were as far away as 2,000 to 3,000 parsecs, produce a flux of about 10^{-8} ergs/cm^2-sec just above our atmosphere. With the sensitivity of the present instruments, these stars are only just barely detectable. But if the sensitivity were increased by a factor of, say, 10^2, quite a few neutron stars might be "visible."

V-9 CONCLUSION

Whether a given neutron star is detectable or not depends largely on the physical parameters involved, especially its mass. Among the x-ray sources which have already been discovered and those which will be discovered in the future, it is quite possible that some are not neutron stars, while it is also possible that some others are indeed neutron stars. We have seen that while it would be difficult to detect light neutron stars, some of average-weight and massive neutron stars should last long enough to permit their observation.

Should future observations reveal that none of the celestial x-ray sources are neutron stars, this could indicate that the ordinary Planck's radiation formulae are not applicable on the surface of neutron stars because of the extraordinarily high temperatures which obtain there; or it may be that some of the other fundamental assumptions made in this research are wrong. For instance, a neutron star may not be formed through a supernova explosion, or perhaps in such extremely dense matter some peculiar phenomena occur which cannot be explained by the present theories of general relativity and high energy physics. On the other hand, for the very same reason, neutron star problems would provide strong support for some of the existing theories of the lastest stages of stellar evolution, particle physics and general relativity upon which this research is based, should the results of research on neutron stars such as presented here turn out to agree well with future observations. If such agreement is not found, the discrepancies may provide us with clues to some of the puzzles which today exist in the fundamental physical theory.

In any case, improvements in the techniques of detection are quite badly needed. Some possible improvements in x-ray measurement which would help us to distinguish between neutron stars and other x-ray sources and to better understand the properties of neutron stars are: (i) the selection of a different wave length range, especially on the shorter wave length side of the peak. For instance, by choosing $\lambda < 1\,\mathring{A}$ for the Scorpius source with the peak at $\lambda_{max} \sim 3\,\mathring{A}$, we should be able to see a non-flat spectrum (due to a sharp drop of intensity in blackbody spectrum on the shorter wave length side) if the radiation comes from a neutron star; (ii) with sufficiently high sensitivity the intensity discontinuity at K (and L) shell absorption edges might be detected; (iii) by increasing the angular resolution of the instrument one could determine whether the source is a point source or an extended one. A neutron star should be a point source. The position of the absorption edge is a characteristic of the surface composition (for instance, the K-shell absorption comes at $1.3\,\mathring{A}$ for Fe and at $6.3\,\mathring{A}$ for Mg). The shift of the observed position from the expected position is then practically due to the gravitational red shift, which is proportional to M/R. The red shift measurement is very useful, because it gives both the surface composition and the ratio of mass to radius, which can be compared with the prediction of the theoretical models. Beside the above considerations, if some of the x-ray sources are identified with neutron stars, the distance, the age and cooling rate of the star can be calculated by a suitable combination of theoretical and experimental data(especially the measured flux). If, further, the source could be associated with a known supernova explosion of known time and distance, we would have more physical parameters to compare our theoretical models with. In this way, it would be possible to select a few models (or a unique model) from a number of various possible models. One of these methods alone may not be very significant but when as many as possible are used in a suitable combination, the problem of neutron stars may in the future provide a powerful tool for studying some of the fundamental theories in physics and astronomy.

Some possible refinements on the present work might be (a) the development of a better theory of interaction forces between sub-atomic particles, especially at the critical region of 10^{14} gm/cm$^3 \lesssim \rho^c \lesssim 10^{16.5}$ gm/cm^3, (b) the application of degenerate compton scattering to opacity in the high density, high temperature region, (c) the derivation of an accurate URCA neutrino luminosity formula (and similar formulae for any other neutrino processes of appreciable importance if any) which could be applied for the cooling of neutron stars and might indicate some appreciable change in the cooling behavior at the critical point around $T \sim 10^9$ °K (the corresponding $T_e \sim 10^6 - 10^7$ °K), (d) the derivation of an internal energy expression which includes the potential and not only the kinetic term, the application of which may change my final results for total energy content of a neutron star by a factor of about 2, (e) more quantitative work on the diffusion problem, (f) similarly for the convection problem, (g) the inclusion of a degree of partial ionization on the equation of state in atmospheres (this was taken into account in the opacity calculations but in the equation of state it was simply assumed that all electrons are ionized which is a justifiable approximation for the hot models but perhaps not for the cooler ones, and (h) the investigation of cooling behavior at the coldest limit $T_e < 10^4\,{}^{\circ}K$. Most of the improvements suggested above are not necessary at the present stage, because the paucity of observational data does not permit their validity to be checked. However, the first four of the above refinements may produce appreciable changes in the final results of this dissertation.

It should be emphasized that models at the two different possible extremes of neuclear potential and atmospheric composition have been developed in parallel in this research in order to avoid as far as possible the danger of drawing conclusions from too limited models. The main approach taken was, therefore, to set upper and lower limits, which are consistent with physical principles, to the possible models. It seems most likely that an actual neutron star should be represented by a model intermediate between the two extremes.

APPENDIX 1

In a Grand Canonical ensemble, the Grand partition function Z is,(50)

$$Z = e^{-\Omega/\tau} = \sum_{N} e^{(\mu N - \epsilon)/\tau} \qquad \text{(A1-1)}$$

$$\tau \equiv kT \qquad \text{(A1-2)}$$

$$N = nV = -\left(\frac{\partial \Omega}{\partial \mu}\right)_{V,\tau} \qquad \text{(A1-3)}$$

$$\Omega = -\tau \log Z \qquad \text{(A1-4)}$$

μ=chemical potential, N = total number of the particle, n=number density.

For fermions and bosons,

$$\Omega = -\tau \sum_{i} \log(1 + X_i) \text{ with } X_i \equiv e^{(\mu - \epsilon_i)/\tau} = \eta\, e^{-\epsilon_i/\tau} \qquad \text{(A1-5)}$$

where η is defined by

$$\eta \equiv e^{\mu/\tau} \qquad \text{(A1-6)}$$

Then from (A1-2) and (A1-3)

$$nV = -\left.\frac{\partial \Omega}{\partial \eta}\right)_{V,\tau} \frac{\partial \eta}{\partial \mu} = -\frac{\eta}{\tau} \left.\frac{\partial \Omega}{\partial \eta}\right)_{V,\tau} \qquad \text{(A1-7)}$$

Consider an assembly of nuclear matter consisting of nuclei (A, Z), free protons P and free neutrons N in equilibrium, with respective number density n_s for the nuclei (A,Z), n_p for free protons and n_n for free neutrons. Using subscripts s, p, n for physical quantities of the nucleus (A, Z), proton and neutron respectively, the above statistical equilibrium condition applying to each become:

$$n_s = -\frac{1}{V}\,\frac{\eta_s}{\tau}\left(\frac{\partial\Omega_s}{\partial\eta_s}\right)_{V,\tau}$$

$$n_p = -\frac{1}{V}\,\frac{\eta_p}{\tau}\left(\frac{\partial\Omega_p}{\partial\eta_p}\right)_{V,\tau} \qquad \text{(A1-8)}$$

$$n_n = -\frac{1}{V}\,\frac{\eta_n}{\tau}\left(\frac{\partial\Omega_n}{\partial\eta_n}\right)_{V,\tau}$$

because all are in a common box of volume V at the same temperature = kT in equilibrium, with the additional condition

$$\eta_s = \eta_p^{Z_s}\,\eta_n^{N_s}\exp\left(Q_s/kT\right) \text{ where } Q_s \text{ is the} \qquad \text{(A1-9)}$$

binding energy of the nucleus s, namely,

$$Q_s \equiv -c^2\left(M_s - M_p Z - M_n N\right) \qquad \text{(A1-10)}$$

where M_s, M_p, M_n are masses of the nucleus (A, Z), proton and neutron. At this point two approximations are necessary: (1) to a first approximation the energy of the excited states is neglected, and (2) the assumption of a perfect gas is employed, which is justified for heavy nuclei, protons and neutrons in the whole density range to be used in this section, namely for $\rho \lesssim 10^{11}$ gm/cm^3.

For a perfect gas, it is well known that (p. 65 reference 50)

$$\Omega = -\tau e^{\mu/\tau} V/\lambda^3 = -\tau\eta\frac{V}{\lambda^3} \qquad \text{(A1-11)}$$

where

$$\lambda = h/(2\pi MkT)^{1/2} \qquad \text{(A1-12)}$$

so that

$$n = -\frac{1}{V}\left(\frac{\partial\Omega}{\partial\eta}\right)_{V,\tau}\frac{\eta}{\tau} = \frac{\eta}{\lambda^3} \quad \text{for each constituent particle.}$$

Namely, $n_s = \omega_s\dfrac{\eta_s}{\lambda_s^3}$, $n_p = \omega_p\dfrac{\eta_p}{\lambda_p^3}$, $n_n = \omega_n\dfrac{\eta_n}{\lambda_n^3}$ (A1-13) where the partition function including the spin orientation is expressed as

$$\omega = \sum_i (2J_i + 1)\exp(-\epsilon_i/\tau) \text{ over all levels } i. \qquad \text{(A1-14)}$$

From (A1-9) and (A1-13), we get

$$n_s = \left[\omega_s n_p^{Z_s} n_n^{N_s} \exp(Q_s/kT)\right] / \lambda_s^3$$

$$= \frac{\omega_s}{\lambda_s^3}\left(\frac{n_p \lambda_p^3}{\omega_p}\right)^{Z_s}\left(\frac{n_n \lambda_n^3}{\omega_n}\right)^{N_s}\exp(Q_s/kT) \qquad \text{(A1-15)}$$

For protons and neutrons $\omega_p = \omega_n = 2$ noting $I = \frac{1}{2}$ for both, with no excited states. Also noting $\lambda_p = \hbar/(2\pi M kT)^{1/2} = \lambda_n$, $\lambda_s = \hbar/(2\pi A M kT)^{1/2}$ (where M = the atomic mass unit), (A1-15) reduces to

$$n(A.Z) = \left[\frac{\omega(A,Z)}{2^A} n_n^N n_p^Z A^{3/2}\left(\frac{2\pi\hbar^2}{MkT}\right)^{\frac{3}{2}(A-1)} \exp(Q(A,Z)/kT)\right] \qquad \text{(A1-16)}$$

where n_s, Q_s and ω_s are re-expressed as $n(A,Z)$, $Q(A,Z)$, and $\omega(A,Z)$, and the relations $N_s + Z_s = A$, $\tau = kT$, $\hbar = h/2\pi$ are used. $\omega(A,Z)$ is the same form as (A1-14). Subscripts s are dropped.

APPENDIX 2

M was defined as U(R), the solution of (1-8) and (1-9). From (1-8)

$$M = U(R) = \int_0^R 4\pi \mathcal{E}(\rho) r^2 dr \qquad \text{(A2-1)}$$

From (1-45) and (1-37),

$$M_p = \int_0^R 4\pi r^2 \rho_m \sqrt{-g_{rr}(r)}\; dr \qquad \text{(A2-2)}$$

From (1-46), (1-45) and (1-8),

$$\begin{aligned} M_B &= \int_0^R \frac{dM_B}{dr} dr = \int_0^R 4\pi r^2 \rho_m \sqrt{-g_{rr}(r)} dr - \int_0^R 4\pi r^2 \mathcal{E} dr \\ &= M_p - M \end{aligned} \qquad \text{(A2-3)}$$

From (4-7)

$$a \equiv M_B / M_p = 1 - \frac{M}{M_p} \qquad \text{(A2-4)}$$

a_1 was defined as (4-2),

$$a_1 = \Delta M_1 \,/\, (N m_H) = (N m_H - M)/(N m_H) = 1 - M/(N m_H) \qquad \text{(A2-5)}$$

N was defined as (1-44)

$$N = 4\pi \int_0^R \sqrt{-g_{rr}(r)}\; n(r)\, r^2\, dr \qquad \text{(A2-6)}$$

Therefore

$$N m_H = 4\pi \int_0^R \sqrt{-g_{rr}(r)}\; n(r)\, m_H\, r^2 dr \qquad \text{(A2-7)}$$

Note that m_H, proton mass, is a constant. In Section I-4b of Chapter I, ρ_m was defined as

$$\rho_m = \sum_\ell n_\ell M_\ell \qquad \text{(A2-8)}$$

where the sum is taken over all baryons present ℓ. M_ℓ is the mass and n_ℓ is the number density of the ℓth baryon.

If we have neutrons only , $\rho_m = n\, m_H$ (the proton neutron mass difference is neglected). Then (A2-7) becomes

$$N m_H = 4\pi \int_0^R \sqrt{-g_{rr}(r)}\, \rho_m r^2 dr \equiv M_p$$

from (A2-2), and (A2-5) reduces to

$$\alpha_1 = 1 - M / M_p \equiv \alpha$$

while this is not true for mixtures where $\rho_m = \sum_k n_k M_k \neq m_H n$ and hence $N m_H \neq M_p$. In the above, n is the baryon number density and N is the total baryon number of the star.

APPENDIX 3

From the definition of the mean density $\bar{\rho}$, $M = \frac{4}{3}\pi\bar{\rho}R^3$, we have the relation

$$\bar{\rho} \propto \frac{M}{R^3}$$ (where M is the mass and R the radius of a white dwarf) (A3-1)

The average gravitational force within a white dwarf is

$$F = \overline{\rho \frac{GM_r}{r^2}} \propto \frac{M^2}{R^5} \qquad \text{(A3-2)}$$

The pressure P of the degenerate electron gas which supports the star has, from Eq. (3-4a) and (3-4b), the following dependence on ρ, and hence M and R (from above relation).

$$P \propto \rho^{5/3} \propto \frac{M^{5/3}}{R^5} \qquad \text{(non-relativistic)} \qquad \text{(A3-3)}$$

$$P \propto \rho^{4/3} \propto \frac{M^{4/3}}{R^4} \qquad \text{(relativistic)} \qquad \text{(A3-4)}$$

Therefore,

$$\frac{dP}{dr} \propto \frac{M^{5/3}}{R^6} \qquad \text{(non-relativistic)} \qquad \text{(A3-5)}$$

$$\frac{dP}{dr} \propto \frac{M^{4/3}}{R^5} \qquad \text{(relativistic)} \qquad \text{(A3-6)}$$

To satisfy the hydrostatic equilibrium condition $\frac{dP}{dr} = -\frac{GM_r}{r^2}$, (A3-2) and (A3-5) or (A3-6) must be equated. Then we obtain

$$\frac{M^{5/3}}{R^6} = \text{const}\,\frac{M^2}{R^5} \rightarrow M^{1/3} = \text{const}\,R^{-1} \qquad \text{(non-relativistic)} \quad \text{(A3-7)}$$

while

$$\frac{M^{4/3}}{R^5} = \text{const}\,\frac{M^2}{R^5} \rightarrow M^{2/3} = \text{const} \qquad \text{(relativistic)} \qquad \text{(A3-8)}$$

That is, for a non-relativistic electron gas, there is only one fixed value of R that a star of a given mass can have and still be a stable star. If the degenerate gas is relativistic, there is no fixed value of R for a given mass because the R's on the different sides of Eq. (A3-3) cancel each other, and there is no equilibrium configuration in this case.

REFERENCES

1. L. Landau; Physik. Zeits. Sowjetunion, 1, 285 (1932).

2. G. Gamow; Atomic Nuclei and Nuclear Transformations, Oxford (1936), second edition, p. 234.

3. J. R. Oppenheimer and R. Serber; Physical Rev. 54, 540 (1938).

4. J. R. Oppenheimer and G. M. Volkoff; Phys. Rev. 55, 374 (1939).

5.a F. Zwicky; Ap. J. 88, 522 (1938).

5.b F. Zwicky; Phys. Rev. 55, 726 (1939); also Handbuch der Physik (Berlin: Springer-Verlag), 51, 766 (1958).

6. J. R. Oppenheimer and H. Snyder; Phys. Rev., 56, 455 (1939).

7. S. Chandrasekhar; An Introduction to the Study of Stellar Structure, Dover (1957).

8. J. A. Wheeler; paper read at the Solvay Converence, Brussels, published with B. K. Harrison and M. Wakano, in La Structure et l'evolution de l'univers (Brussels; R. Stoops) (1958).

9. A. G. W. Cameron; Ap. J., 130, 884 (1959).

10. T. H. R. Skyrme; Nuclear Physics 9, 615 (1959).

11.a E. E. Salpeter; Annals of Physics 11, 393 (1960).

11.b E. E. Salpeter; Ap. J. 134, 669 (1961).

12. T. Hamada and E. E. Salpeter; Ap. J. 134, 683 (1961).

13. V. A. Ambartsumyan and G. S. Saakyan; AJ, 4, 187 (1960).

14. V. A. Ambartsumyan and G. S. Saakyan; AJ, 5, 601 (1962).

15. V. A. Ambartsumyan and G. S. Saakyan; AJ, 5, 779 (1962).

16. G. S. Saakyan; AJ, 7, 60 (1963).

17. H. Y. Chiu; Annals of Physics 26, 364 (1964).

18.a R. Giacconi, H. Gursky, F. R. Paolini, and B. B. Rossi; Phys. Rev. Letters, 9, 439 (1962).

18.b R. Giacconi, H. Gursky, F. R. Paolini, and B. B. Rossi; Phys. Rev. Letters, 11, 530 (1963).

19. P. C. Fisher and A. F. Meyerott; Ap. J. 139, 123 (1964).

20. H. Friedman; a paper presented at the American Astronomical Society meeting at Washington D.C., Dec. 1963; also S. Bowyer, E. T. Byram, T. A. Chubb, and H. Friedman; Nature 201, 1307 (1964).

20'. H. Friedman; private communication through Dr. A. G. W. Cameron (1964).

21. For instance, G. W. Clark, M. Oda, and P. Morrison, paper presented at the meeting in reference 61 (to be published).

22. H. Y. Chiu and E. E. Salpeter; Phys. Rev. Letters, 12, 412 (1964).

23. D. C. Morton; Nature 201, 1308 (1964).

24. C. W. Misner and H. S. Zapolsky; Phys. Rev. Letters 12, 635 (1964).

25. A. Finzi; Ap. J. 139, 1398 (1964).

26. M. Schwartzschild; Structure and Evolution of the Stars, Princeton U. Press (1958).

27. R. C. Tolman; Relativity, Thermodynamics and Cosmology, Oxford (1962).

28. E. M. Burbidge, G. R. Burbidge, W. A. Fowler, and F. Hoyle; Revs. Modern Phys. 29, 547 (1957).

29. A. G. W. Cameron; Lecture notes at Yale University (1963).

30. F. Hoyle; Monthly Notices, 106, 23 (1946).

31. E. Schatzman; White Dwarfs, North-Holland Publishing Co. (1958).

32.a A. G. W. Cameron; paper read at Symposium presented at the Royal Society of Canada (1959), also Publication of the Astronomical Soc. of the Pacific, Vol. 69, 201 (1957).

32.b A. G. W. Cameron; Ap. J., 129, 676 (1959).

33. A. G. W. Cameron; Ap. J. 130, 429 (1959), Ap. J. 130, 895 (1959), Ap. J. 130, 916 (1959); Physics and chemistry of the earth, Vol. III, 199 Pergamon Press (1960), Fast neutron physics, II, 1699, Interscience Publishers (1963). C. Hayashi, R. Hoshi and D. Sugimoto; Supplement of the Progress of theore. Phys. 22, 1 (1962). S. A. Golgate, W. H. Grasberger and R.H. White, J. Phys.Soc., Japan 17 Suppl.A.III, 157 (1962). R. Stothers; Ap. J. 138, 1085 (1963).

34. A. H. Wapstra, Physica, 18, 2 (1952). A. Green and D. Edwards, Phys. Rev. 91, 46 (1953). I. Talmi and R. Thieberger; Phys. Rev. 103, 718 (1956). R. Thieberger and A. de Shalit, Phys. Rev. 108, 378 (1957).

35. A. E. S. Green, Revs. Modern Phys. 30, 569 (1958).

36. A. G. W. Cameron; Can. J. Phys. 35, 1021 (1957).

37. F. Everling, L. A. König, J. H. E. Mattauch; Nuclear Phys. 18, 529 (1960).

38. E. Feenberg and G. Trigg; Revs. Modern Phys. 22, 399 (1950).

39. J. K. Major and L. C. Biedenharn; Revs. Modern Phys. 26, 321 (1954).

40. A. G. W. Cameron; Ap. J. 130, 452 (1959).

41. J. N. Bahcall; Ap. J. 139, 318 (1964).

42. Landolt-Börnstein; Numerical Data and Functional Relationships in Science and Technology Vol. 1, Energy Levels (1961).

43. M. G. Mayer and J. H. Jensen; Elementary Theory of Nuclear Shell Structure, Wiley and Sons (1960).

44. J. M. Blatt and V. F. Weisskopf; Theoretical Nuclear Physics, Wiley and Sons (1960).

45. A. G. W. Cameron; Can. J. Phys. 36, 1040 (1958). M. A. Preston; Physics of the Nucleus, Addison-Wesley (1962). T. D. Newton; Can. J. Phys. 34, 804 (1956). H. A. Bethe; Revs. Modern Phys. 9, 69 (1937). C. Bloch; Phys. Rev. 93, 1094 (1954).

46. T. Ericson; Advances in Phys. 10, 425 (1960).

47. A. G. W. Cameron; private communication (1963).

48. C. T. Hibdon; Phys. Rev., 114, 179 (1959).

49. (a) J. R. Huizenga; Phys. Rev. 120, 1305 (1960).
(b) J. R. Huizenga; Phys. Rev. 120, 1313 (1960).

50. C. Kittel; Elementary statistical physics, Wiley and Sons (1961).

51. K. A. Brueckner and J.L. Gammel; Phys. Rev. 109, 1023 (1958). K. A. Brueckner, J. L. Gammel, and J. T. Kubis; Phys. Rev. 118, 1095 (1960). P. C. Sood and S. A. Moszkowski; Nuclear Phys. 21, 582 (1960). J. de Swart and C. Dullemond; Bull. Am. Phys. Soc. 6, 269 (1961). R. Jost and W. Kohn; Phys. Rev. 87, 977 (1952).

52. J.S. Levinger and L. M. Simmons; Phys. Rev. 124, 916 (1961).

53. Robert Serber; Revs. Modern Phys. 36, 649 (1964).

54. L. Van Hove; Revs. Modern Phys. 36, 655 (1964).

55. Eugene Jahnke and Fritz Emde; Tables of Functions, Dover (1945). Si(y) is defined as

$$S_i(X)= \int_0^x \frac{\sin t\, dt}{t} = \frac{1}{2}\int_{-x}^{+X} \frac{\sin t\, dt}{t} = x + \frac{x^3}{3!\,3} + \frac{x^5}{5!\,5} + \dots$$

56. L. Landau and E. Lifshitz; The classical theory of fields, Addison-Wesley (1959).

57. Ya. B. Zel'dovich; JETP, 14, 1143 (1962).

58. L. Landau and E. Lifshitz, Mechanics of Continuous Media, Gostekhizdat (1953).

59. S.S. Schweber and H.A. Bethe; Mesons and Fields, Vol. I, Row, Peterson (1955).

60. H.Y. Chiu and W. F. Hoffmann; Gravitation and Relativity, Benjamin (1964).

61. Symposium on neutron stars and celestrial x-ray sources, March 20, 1964, Goddard Institute for Space Studies, New York.

62. M. Rudkjöbing; Pub. Köbenhavns Obs., No. 160 (1952).

63. L. Landau and E. Lifshitz; Statistical Physics, Addison-Wesley (1958).

64. F. B. Hildebrand; Introduction to Numerical Analysis, McGraw-Hill (1956).

65. S. Chandrasekhar; Phys. Rev. Letters 12, 114 (1964).
S. Chandrasekhar; Phys. Rev. Letters, 12, 437 (1964).

66. R. W. Fuller and J.A. Wheeler; Phys. Rev. 128, 919 (1962). F. Hoyle and W. A. Fowler; Monthly Notices 125, 169 (1963); Nature 197, 533 (1963). W. A. Fowler; Revs. Modern Phys. 36, 545 (1964).

67. G. R. Burbidge; Ap. J. 137, 995 (1963).

68. D. H. Sampson; Ap. J. 129, 734 (1959).

69. D. Ezer and A. G. W. Cameron; Icarus 1, 422 (1962).

70. H. Y. Chiu and S. Tsuruta; Thermodynamic properties of hot matter (unpublished); also S. Tsuruta and H. Y. Chiu; Astron. J. 67, 284 (1962).

71. K. A. Brueckner; Phys. Rev. 118, 1095 (1960); also V. F. Weisskopf, Nuclear Physics 3, 423 (1957).

72. For instance, a recent discussion in J. Bernstein, M. Ruderman and G. Feinberg; Phys. Rev. 132, 1227 (1963).

73. H. Y. Chiu and R. Stabler; Phys. Rev. 122, 1317 (1961). V. I. Ritus; JETP 14, 915 (1961). H. Y. Chiu and P. Morrison; Phys. Rev. Letters 5, 573 (1960). H. Y. Chiu; Phys. Rev. 123, 1040 (1961). G. Gamow and M. Shönberg; Phys. Rev. 59, 539 (1941). B. M. Pontecorvo; JETP 9, 1148 (1959). G. Gandel'man and V. Pineau, JETP 10, 764 (1960). L. Rosenberg; Phys. Rev. 129, 2786 (1963). S. Matinyan and N. Tailosani; JETP 14, 1195 (1962). N. Van Hieu and E. P. Shabalin; JETP 17, 681 (1963).

74. J. B. Adams, M. A. Ruderman and C. H. Woo, Phys. Rev. 129, 1383 (1963).

75. H. Reeves; Ap. J. 138, 79 (1963).

76. C. L. Inman and M. A. Ruderman; Preprint from the Institute for Space Studies (1964).